# Durham E-Theses

## *The electrical properties of zinc silicate composite films on silicon*

Salam, Rahim

**How to cite:**

**Use policy**

*Yang bersama-sama disisi ku disini ;*

*isteri ku*

*dan*

*anak ku.*

THE ELECTRICAL PROPERTIES OF ZINC SILICATE

COMPOSITE FILMS ON SILICON

by

Rahim Salam, B.Sc.

a thesis submitted in accordance with the regulations

for the degree of Doctor of Philosophy in the

University of Durham.

1980

# ABSTRACT

This thesis describes work on the growth and electrical properties of thin luminescent films of zinc silicate phosphor, $Zn_2SiO_4$ : Mn, formed from the solid-state reaction of $ZnF_2$:Mn and $SiO_2$ at $1000^{\circ}C$, on n-type silicon substrates. The film formed in this way consists of zinc silicate separated from the silicon by a non-luminescent interfacial layer. Electrical measurements were made on metal-insulator-silicon (MIS) capacitors formed by photolithography using both the composite and the interfacial film as the insulator.

The film properties vary with the growth conditions. Three types of films, defined by the gas ambient for the reaction, were investigated. High frequency capacitance-voltage measurements on the composite films showed good MIS-type characteristics but with flat-band voltages that changed with electrical stress. These changes, together with measurements made on the interfacial layers, were used to study the formation of space-charge within the films. Films formed in short reaction times in $N_2$ and those with longer reaction times in 10% of $O_2$ in $N_2$, showed polarization when negatively stressed at $10^5$ v/cm and above. This was explained by the build-up of negative space-charge at the dielectric-dielectric interface, due to the separation of $Zn^{2+}$ cations from the immobile $(SiO_4)^{4-}$ anions in the silicate, close to the interface.

Films formed by a long reaction time in ultra-pure $N_2$, showed the above type of polarization phenomenon only in a very thin outer layer. However, in the bulk, polarization was probably due to charge accumulation at crystallite boundaries. In general, there is no strong evidence of electron injection into the silicate films.

## ACKNOWLEDGEMENTS

# CONTENTS

INTRODUCTION

1.1     Light-emission from Silicon-based Devices

This thesis is concerned with the investigation of the electrical properties of a possible light emitting thin film on silicon.  Incorporation of such films with silicon integrated circuit technology might find application as integrated electronic display devices or for optical couplings between chips or in integrated optics.  The question of whether visible and controllable light can ever be emitted from silicon integrated chip structures is also of considerable academic interest.

Electronic displays based on solid-state devices have found many applications in present day scientific instruments, watches, calculators, etc.  Many of these display devices use light-emitting diodes (LED's), which exploit some of the electronic properties of semiconducting III-V compounds, especially $GaAs_x : P_{1-x}$ or GaP.  Devices from such materials have the advantage of low power operation and give high resolution in daylight.  On the other hand, liquid crystal displays, which have an even lower power dissipation have the disadvantage of requiring an external light source for illumination.  The majority of LED's utilise the mechanism of radiative recombination of excess carriers which have been injected from a forward biased p-n junction and for this to occur the band-gap of the material has to correspond to wavelengths in the visible range of the spectrum (1) .  Silicon has a band-gap of 1.1 eV which corresponds to the infra-red, and therefore it is not directly of use for display devices using the radiative recombination mechanism.  Furthermore, silicon has an indirect band-gap and therefore a non-radiative transition is normally involved.

Other forms of solid-state display device use thin electroluminescent films deposited on to suitable electrodes which will omit visible radiation with a.c. or d.c. excitation.  Display panels have
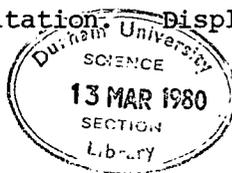
already found several technological applications mainly using zinc sulphide semiconductors, although very little of their operating mechanism is, as yet, completely understood.

Present day devices for performing drive, decoding, memory functions, etc., are fabricated by the monolithic integrated circuit techniques on silicon substrates but since the display devices use materials other than silicon, external connections have to be made to complete a display system. The relative high costs of such interconnections and their high failure probability makes them a governing factor in limiting the complexity and costs of present display systems. It was realized in the Department in 1966 that if a thin film, with light emitting capability, can be formed on a silicon substrate also containing the associated circuitry, then complex integrated interconnections could be made using standard silicon technology. There are considerable problems with semiconducting thin films on silicon and a substitute is to use a phosphor film excited by the injection of high energy electrons from the silicon leading to impact ionization or resonance transfer electroluminescence.

The idea of monolithic displays has almost been overtaken by advances in the driving methods for both LED's and liquid crystals. The real problem is because of the miniaturization in silicon integrated chips. For a monolithic display which has to be about 5-10 mm across, it has to be extremely bright in order to be readable. However, optical couplings between chips could still be of interest, and small light emitting areas opposite silicon photodetectors or coupled via optical film could be of importance in the future. Light emitting films could be of increasing interest for integrated optical devices. There is also the scientific question of whether light from a solid silicon-based structure could be achieved.

This thesis forms part of a wider study of possible electro-luminescent films for the applications described. The material considered is zinc-silicate, doped with manganese, which in its natural occuring form is known as 'willemite'. The formation of thin willemite films on silicon has been successfully initiated by Edwards (2) in this Department. This chapter will present some of the general properties of 'willemite' and the results of previous investigations of such 'willemite' films.

## 1.2    General Properties of Willemite

Willemite is a naturally occuring luminescent mineral composed of zinc orthosilicate. In this thesis the word 'willemite' will always refer to the synthetic luminescent zinc silicate film incorporated with manganese. In powder form this material has long been used for the screens of cathode-ray tubes giving the green light output with a peak emission of 5250 $\overset{o}{A}$. The broad structureless emission band centred about this peak is typical of $Mn^{2+}$ ion in the rhombohedral crystal structure of $\alpha$-$Zn_2SiO_4$, and it is practically independent of the method of excitation.

The first detailed X-ray examination of willemite was undertaken by Bragg and Zachariasen (3) in 1930. The structure of willemite is based on a rhombohedral space lattice with a unit cell composing of 42 atoms from six $Zn_2SiO_4$ groups. In general, the basic building block of silicate consists of a silicon atom surrounded by four oxygen atoms at the corners of a tetrahedra. Because of the large unit cell and rhombohedral space lattice on which willemite is based, it is quite difficult to get a clear picture of the atomic arrangement in the structure. However, from the work of Bragg (4), the structure is basically formed by the interlinking of $SiO_4$ tetrahedra and $ZnO_4$ tetrahedra in such a way that each atom of the $SiO_4$ group also forms part of two neighbouring tetrahedra

3

Chemical Name :           $\alpha$-Zinc Silicate, $Zn_2SiO_4$ : Mn.

Crystal Structure :       Rhombohedral, based on silicate tetragonal

                          network.

                          Silicate radical, $(SiO_4)^{4-}$, ionically bonded

                          to zinc metallic cation, $Zn^{2+}$.

Dopant :                  Manganese. $Mn^{2+}$ ions replacing $Zn^{2+}$ ions in

                          lattice site.

Energy Band-gap :         5.4-5.5 eV (optical).

Radiative Emission :      Green.  Peak at $5230\overset{o}{A}$ (for 1% Mn).

                          Decay time $\sim 10^{-2}$ sec.

Luminescence Mechanism : Transition of 3d electrons in $Mn^{2+}$ ion.

                          From $^4G$ excited state to $^6S$ Ground state.

Energy Levels :
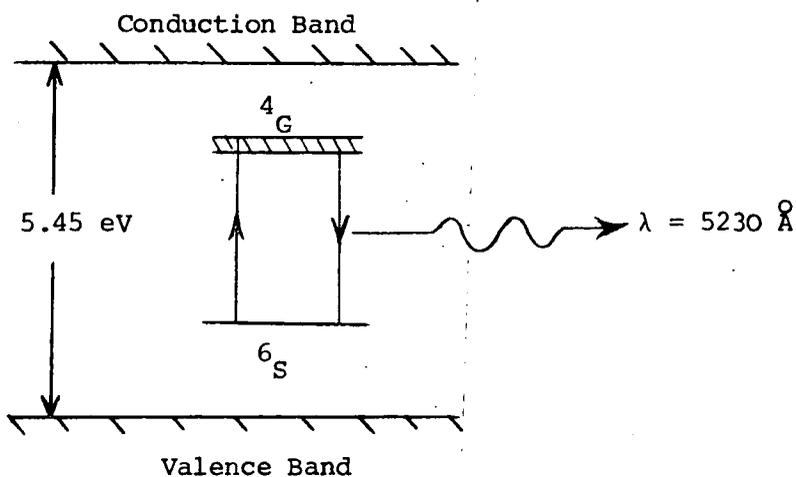


Table 1.1  Properties of Willemite $(Zn_2SiO_4)$

around zinc atoms. The strongly bound $SiO_4$ group in zinc orthosilicate is due to the mixed covalent-ionic band that occurs between the Si atom and its four surrounding O atoms. This results in a radical $SiO_4$ group with a net charge of -4, i.e. $(SiO_4)^{-4}$, which is ionically bonded to $Zn^{2+}$ ions. Zinc silicate phosphors are made by incorporating manganese ions into the crystal lattice, the $Mn^{2+}$ ions replacing the zinc, with a slight expansion of the lattice because of the slightly larger $Mn^{2+}$ ion. Klick and Schulman [5] proved conclusively that it is the excitation of these $Mn^{2+}$ ions which is responsible for the peak in emission spectrum at 5250 $\overset{o}{A}$. Zinc orthosilicate has an optical band-gap of 5.4-5.5 eV and a summary of its properties is given in Table 1.1.

Almost all the extensive work on willemite reported in the literature refers to synthetic powder samples and there appears to have been very little done on thin films. Feldman and O'Hara [6] developed a technique for forming willemite thin films by evaporating the phosphor on to silica glass and then firing it at $1100^{o}$ C for half an hour in oxygen. More recent work by di Giacomo [7] described two methods for depositing polycrystalline thin film of willemite on quartz, sapphire and silicon wafers having initial oxides of about 1 μm in thickness. The first method was a vapour phase process using $MnCl_2$ as dopant while the second was the normal evaporation and firing process. Neither method was very successful in producing good quality films, especially the latter, where there were problems of decomposition.

Edwards [2] has successfully developed a simple technique for preparing thin films of willemite on silicon substrates. The idea is to make use of silicon dioxide, which is thermally grown with ease on silicon, as one of the constituent materials. The other constituent is $ZnF_2$ : Mn (doped with manganese) deposited on the $SiO_2$ by vacuum evaporation. A subsequent heat treatment at a high temperature ($900^{o}$ C- $1000^{o}$C) in nitrogen causes the films to react forming a high

4

quality film of willemite. The $ZnF_2$ : Mn is used instead of any other
zinc compound (e.g. $ZnCl_2$) because both $ZnF_2$ and $MnF_2$ have very nearly the
same vapour pressures and melting points ($872^\circ$ C and $856^\circ$ C respectively)
so that the powder can be evaporated and condensed without loss of the
activator. Zinc fluoride is one of the very few phosphors that can be
deposited by evaporation without losing its yellow luminescence.

The chemical reaction as postulated by Edwards, takes the form
of

$$2ZnF_2 : Mn + 2SiO_2 \rightarrow Zn_2SiO_4 : Mn + SiF_4$$
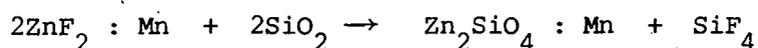
where the $SiF_4$ is given off because of its volatility. In order to
achieve high fields with low voltages, Edwards decided to investigate
films formed from initial oxide films of thicknesses of 1000 $\overset{o}{A}$ or less.
The films always gave uniform green cathodoluminescent emission with peak
emission at 5250 $\overset{o}{A}$. The films were found to be strongly adherent to
the silicon, and stable and they have not deteriorated after many years in
ordinary air. Transmission electron microscope studies of these thin
willemite films revealed the presence of islands of crystallites of
converted oxide surrounded by unreacted oxide in regions where there
was insufficient $ZnF_2$. The willemite films were also shown to be
polycrystalline by using the reflection diffraction technique and it
was also proved that they have the correct crystal structure of $\alpha$-$Zn_2SiO_4$.

1.3     Luminescence of Willemite Thin Films

Luminescence is caused by radiative transitions associated with
either the bulk material, imperfections and/or single or multiple
activators. Energy for luminescence has to be provided by some sort of
external excitation. From the point of view of excitation and emission
mechanisms, willemite is one of the simpler materials for achieving
luminescence, although there appears to have little inherent in the
detailed study of its energy transport processes.

The origin of the green emission from willemite has been the subject of a considerable amount of theory which has been reviewed by Klick (8), Garlick (9) and Klick and Schulman (5). From its spectral features, the transitions are found to be entirely within the $Mn^{2+}$ ion between the $^4G$ excited state of the 3d electrons, in which four of them have parallel spins and one antiparallel, and the $^6S$ ground state in which all five electrons have parallel spins. The energy difference between these two states is 2.37 eV and there is a long decay time ($\sim 10^{-2}$ sec) for the radiative transition to take place. The green luminescence of willemite is observable with as little as 0.1% of Mn incorporated in the zinc silicate, or as much as 20% Mn although the output in intensity is then very much reduced. The peak output occurs at about 1% Mn doping which is normally used.

Because of the single impurity activation and simplicity in understanding its emission mechanism, willemite seems to be a very likely material for achieving electroluminescence. In his review of the various types of luminescence mechanisms, Morant (10) also presented the possible ways of achieving luminescence in willemite by electrical excitation. The four ways in which the 3d electrons of $Mn^{2+}$ can be raised to an excited state are :-

(a) the resonance excitation (exciton transfer) from electron-hole recombination occuring within about 100 Å of the $Mn^{2+}$

(b) the inelastic collision of a hot conduction electron or an injected electron,

(c) the trapping of a hole which subsequently recombines with an electron transferring its energy to the ion, and

(d) the absorption of an externally applied radiation.

The last case applies only to photoluminescence and the other three to cathodoluminescence or electroluminescence. With electrical

6
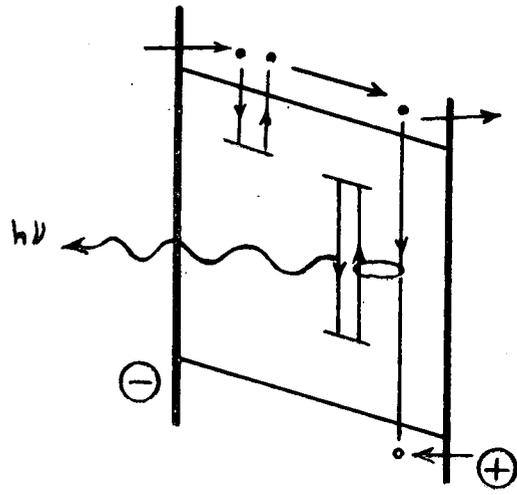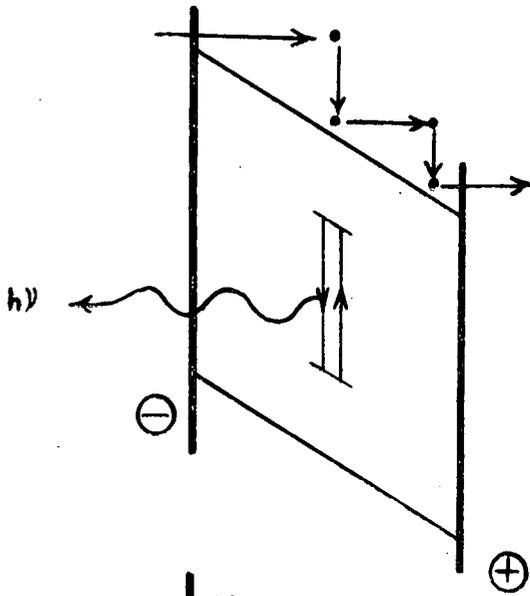
Bipolar Injection

Unipolar Injection &
Impact Excitation
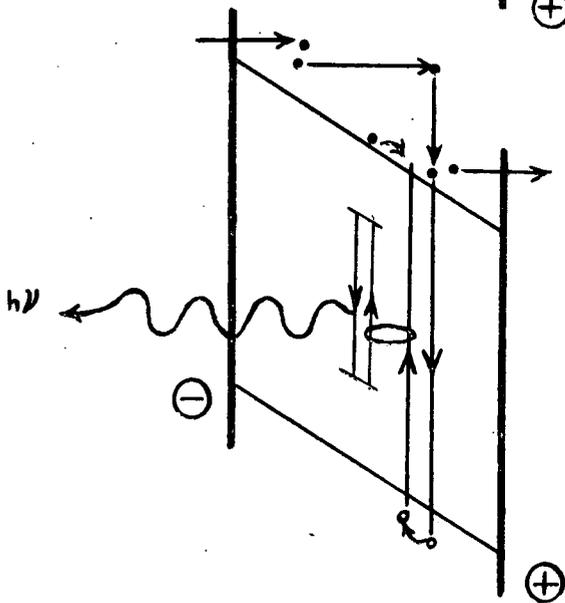
Unipolar Injection &
Impact Ionization

Figure 1.1  Electroluminescent processes applicable to
willemite [after Morant (10)]

excitation any of the three mechanisms may occur simultaneously, and there will always be competition between non-radiative energy losses and excitation energy which ultimately determines the efficiency. Cases (a) and (b) are most likely if electroluminescence is to be obtained in willemite thin films because (c) is improbable due to the low mobility of holes as well as space-charge effects that can arise from trapping.

To achieve electroluminescence by either of the first two cases, Morant (10) has classified the methods of excitation into three ; namely bipolar injection followed by recombination, unipolar injection followed by impact excitation, and unipolar injection followed by impact ionization (see Fig. 1.1). In a wide band-gap material which probably has a very low electron mobility, excitation by means of bipolar injection followed by recombination is expected to be most inefficient. Hence the most likely efficient electroluminescent mechanism in willemite thin films seems to be unipolar injection. This might be achieved by using a thin film willemite on n-type silicon, in the form of an MIS-type structure, where the metal electrode has to be transparent for the light emission to escape. By biasing with a positive voltage, a high field could be created in the willemite enabling electrons injected from the silicon to excite the 3d electrons of $Mn^{2+}$ ions by collision ionization (Edwards (2) ). It was hoped that light emission could be achieved in this manner.

1.4     Review of Previous Experimental Work

Edwards' early experimental work on willemite thin films on silicon was affected by ionic contamination, uncontrollable processing and irreproducible electrical results. Capacitance-voltage and conduction measurements varied from one capacitor to another. Because of the lack of control in the processing, Edwards concluded that the initial oxide

grown prior to the formation of willemite films was already contaminated with either sodium or hydrogen ions. There was also evidence for the formation of negative space-charge in his willemite films. Cathodo-luminescence was always observed but not photoluminescence, i.e. when irradiated with ultra-violet light at either room temperature or liquid nitrogen temperature. Edwards observed some d.c. electroluminescence in his MIS-type willemite structures at fields of about $2 \times 10^6$ v/cm, which was on the verge of dielectric breakdown occurring at localized spots in the electrodes. It was proposed that the corresponding high current of about 100 μA was a result of hot electrons leading to collision ioniza-tion, the same electrons being responsible for impact collision with $Mn^{2+}$ ions which gave the green emission.

Later work by Husain (11) was mainly concerned with the investiga-tion of the electrical properties of willemite thin films on metal electrodes. The metal chosen was platinum since it is less likely to be affected by the willemite reaction-bake process, and in the absence of solid platinum, a thin film had to be deposited on an insulating substrate of quartz. Willemite films were also deposited on alumina and sapphire substrates but there were problems of substrate cracking and the films peeling off. The willemite was formed from a silicon monoxide film deposited on the platinum so that it may be rather different from that formed on silicon. However, current variability as well as the existence of a residual film were also observed in those films. Husain's current measurements were inconsistent and irreproducible. Weak electroluminescence was also observed but again, only at very high fields, and this supported the electron injection model of Edwards.

In more thorough measurements on improved willemite MIS-type structures, Davies (12) found a decrease in the slope of the C-V plot. This decrease in slope was explained by the non-uniformity of the willemite

films, especially at the interfaces with the silicon and the metal electrode.    The distortion of C-V characteristics because of non-uniformity in the dielectric has been reported for other films by Crowell (13), Nicollian and Goetzberger (14), and Snow and Dumesuil (15). Based on this idea, Davies proposed that the area of the willemite MIS-type capacitor is divided into elemental capacitors experiencing varying degrees of electron injection.  Each localized elemental capacitor will have its individual C-V characteristic as expected for a normal MIS-type structure and the net characteristic, when the individual characteristics are added up, will result in a lowering of the measured C-V slope.  This effect of slope lowering in C-V plots has been dealt with in detail, theoretically, by Brews and Lopez (16).   Davies also showed the existence of a remnant oxide layer in between the willemite and the silicon by etching experiments and it is this remnant layer which he proposed as the determining factor for the high applied voltages required for electron injection from the silicon into the dielectric.  Further investigation by Davies led to the discovery of an outer insulating layer, a few tens of Angstroms in thickness, on the surface of the willemite, possibly derived from unreacted constituents, e.g. ZnO and $ZnF_2$.  This led to the invention of Davies of the "degrotting" or post-etching process for the removal of this unwanted layer by a post-reaction chemical cleaning.

The remnant oxide layer, or residual film, was thought to be responsible for the scattering of electrons that are injected from the silicon into the willemite, thus reducing the efficiency of luminescence. For this reason, it is important to achieve an almost negligible residual film when forming the willemite films.

In the subsequent work by Errington (17) on the rate of growth of willemite films on silicon, it was found that for reaction-bake times in excess of two minutes in nitrogen, the thickness of oxide used up in

Residual Film

p-silicon　　　　n+　　　Willemite　Aluminium
　　　　　　　　-sili-
　　　　　　　　con

$h\nu$

Depletion
Region
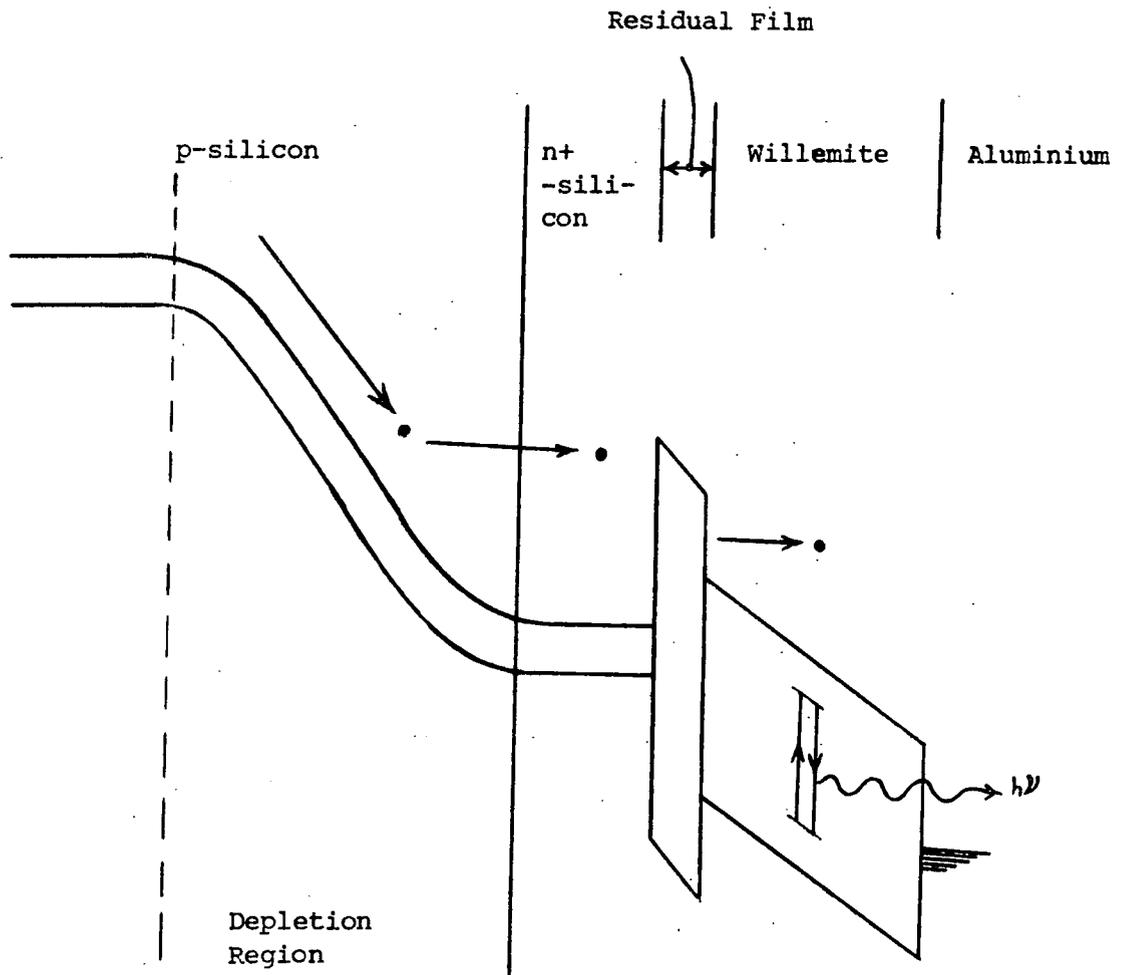
Figure 1.2　　Electron injection structure for achieving

electroluminescence in willemite using a

reversed biased $pn^{+}$-junction

after Campbell (18)

the reaction is proportional to the square root of the reaction time. This seems to be in accordance with Fick's diffusion law for a constant source concentration into a semi-infinite body. By varying the thicknesses of initial oxide and zinc fluoride as well as the reaction time and temperature, Errington tried to find conditions for the elimination of the residual oxide film. However the smallest thickness was found to be about 50 $\overset{o}{A}$ in conditions which also cause problems of thinness of the willemite. For willemite thick enough to be brightly cathodoluminescent, the residual film thickness was at least 300 $\overset{o}{A}$ . Errington also measured the refractive index of the residual oxide film, from ellipsometer measurements. This showed values varying from 1.80 to about 2.60, depending on the time of bake within a range of up to 20 min., and much greater than that of thermal oxide ( n = 1.46).

On the basis of the weak light output and extremely high fields required to achieve luminescence, Campbell (17) fabricated a $pn^{+}$ structure underlying the films (see Fig 1.2). The objective of such a structure, instead of the usual singly doped silicon, is to achieve a large concentration of energetic hot electrons from avalanching when the $pn^{+}$ structure is reverse biased. Hence, in such condition, the probability of very high concentration of electrons for impact collision to excite the $Mn^{2+}$ ions is increased. Electron injection from the $pn^{+}$ structure in fact comes from microplasmas which has switching properties. Campbell also deduced that the residual oxide films were responsible for limiting the injection efficiency of high energy electrons. Campbell also prepared willemite films by heating non-oxidized silicon having deposited $ZnF_2$:Mn at 850$^o$ C in wet oxygen atmosphere. The films were, however, of poorer quality and displayed less bright cathodoluminescent properties with a more yellow light emission.

## 1.5    Outline of Present Research

As has been pointed out in Section 1.4, some of the major problems facing previous workers in the area of willemite thin films were due to lack of reproducibility.  Although many processing improvements were made between 1969 and 1976, it was thought that the main cause of inconsistent results was still the lack of control in the processing techniques, with possible contamination of the willemite films. Furthermore, the reaction process could have caused the uneven formation of willemite crystallites dispersed throughout the film plus the possibility of defects and grain-boundaries causing major obstacles for achieving homogeneous films.   It was hoped that if many test structures could be fabricated on a miniaturized scale and with the use of a high quality processing then film homogeneity of the willemite might be improved.

The objective of the present work was to carry out a more intensive study on the physical parameters involved in the formation and electrical properties of willemite films, with the hope of achieving electron injection and electroluminescence.   For this reason, the investigation does not only involve the electrical characteristics of the willemite film but also those of the underlying silicon and the residual oxide film (known only as the residual film in this thesis).   Integrated circuit techniques were used, as far as possible, for the fabrication of the test samples.  Their design, the fabrication technique and the methods of electrical measurements are described in Chapter 2.   This leads in Chapter 3 to a review of the relevant theories involved in the analysis of electrical results, with particular emphasis on the Metal-Insulator-Semiconductor (MIS) capacitance-voltage characteristics.

The research work was divided into three phases, concerned with different types of willemite film produced by different conditions imposed during the reaction-bake processes.   The first phase was for

willemite films produced by a short reaction-bake time ($\sim$ 20 min) in nitrogen. This type of willemite is typical of the films investigated by former workers. The electrical results and their analysis are presented in Chapter 4. In the second phase of the work oxygen was deliberately introduced in a known proportion in the ambient during the reaction process. It was proposed by Errington (17) that a negligible residual film might be achieved, by having the silicon oxidized in situ, in this way. Results for this type of willemite film, which also had a long reaction-bake time ($\sim$ 20 hrs), are presented in Chapter 5. The long reaction time was used because Hurd and Johnston (19) have shown that it will give a much more uniform distribution of the material constituents in the willemite film. For the preparation of the third type of willemite film similar conditions were used, except for ultra-pure nitrogen as the ambient during the reaction. Chapter 6 gives the results and analysis for this final phase of the work.

The properties and characteristics of all the three types of willemite film and of the resulting MIS structures are reviewed and discussed in Chapter 7, with emphasis especially on the influence of reaction-bake conditions on the electrical characteristics. Chapter 8 concludes this thesis with conclusions and some suggestions for further work.

# REFERENCES

## CHAPTER 1

1.  C.H.Gooch, "Injection Electroluminescent Devices",
    John Wiley & Sons, (1973).

2.  G.S.Edwards, Ph.D. Thesis, Durham University (1970) ;
    A.N.Rushby - J.Mat. Sci., $\underline{6}$, 225 (1971) ; and
    M.J.Morant - Sol.St.Elec., $\underline{16}$, 173 (1972).

3.  W.L.Bragg and W.H.Zachariasen - Zeit.f.Krish., $\underline{8}$, 518 (1930).

4.  W.L.Bragg - "Atomic Structures of Minerals", London (1937).

5.  C.C.Klick and J.H.Schulman - J.Opt.Soc.Amer., $\underline{42}$ , 910 (1952)

6.  C.Feldman and M.O'Hara - J.Opt.Soc.,Amer., $\underline{48}$, 816 (1958).

7.  G.M.di Giacomo - J.Electrochem.Soc., $\underline{116}$, 313 (1969).

8.  C.C. Klick - Brit.J.Appl.Phys., Suppl, $\underline{4}$,74 (1955).

9.  G.F.J. Garlick - "Luminescent Materials", Oxford University
    Press (1949).

10. M.J.Morant - "The Luminescent Properties of Willemite",
    Departmental Reports (1972).

11. M.R.Husain - Ph.D. Thesis, Durham University (1973).

12. G.D.Davies - M.Phil.Thesis, ~~Durham~~ London University (1975).

13. C.R.Crowell - Appl.Phys.Letts, $\underline{8}$, 328 (1966).

14. E.H.Nicollian and A. Goetzberger - Bell Syst.Tech. J., $\underline{46}$ ,
    1055 (1967).

15. E.H. Snow and B.E. Deal - J.Appl.Phys, $\underline{37}$, 2123 (1966).

16. J.R.Brews and A.D.Lopez - Sol.St.Elec., $\underline{16}$, 1267 (1973).

17. D. Errington - unpublished.

18. R. N. Campbell - Ph.D. Thesis, Durham University (1977).

19. J.M.Hurd and R.E.Johnston - private communication.

SAMPLE PREPARATION AND MEASURING TECHNIQUES

## 2.1 Introduction

A review of the previous work on willemite presented in the previous chapter, showed lack of reproducibility possibly due to lack of control in processing. With this in mind, it was decided to fabricate all test structures in this work by monolithic integrated circuit techniques. For such purposes, the fabrication of test structures should therefore be as far as possible like that of some other well-established Metal-Insulator-Semiconductor (MIS) type structures.

Most work on MIS structures has been performed on the silicon-silicon dioxide system and an excellent description on the physics and technology involved is given by Grove (1). For the MOS system one can deduce information about surface and interfacial states, charge movement within the insulator and also effects of charge-trapping (2-4). Applying similar methods to our willemite films, should give some insight into their physical characteristics.

The first half of this chapter is devoted to a description of the design and fabrication of test structures for these electrical measurements. In the second half, the optical and electrical measuring techniques that were used during the course of this investigation are described. Most electrical measurements were the normal ones of capacitance-voltage, with d.c. conduction measurements in specific circumstances only. The optical measurements were basically for determining film thickness and refractive index and this was done using the ellipsometer. Occasional measurements, other than those mentioned here, will be described in the relevant chapters.

## 2.2 Design of Test Structures

Fabricating films on silicon so as to obtain MIS-type structures

involves various stages of processing summarized in the flow diagram

presented in Fig.2.1.  The normal MOS fabrication procedure with the

relevant technology involved is well presented by Allison (6) and the

present procedure is similar.  All test structures in this work used

1.5 - 2.0 Ωcm, n-type silicon substrates of 3.8 cm diameter and 0.266 cm

thickness.  It was decided to fabricate the structures in the form of an

array of five by five matrix of chips in the centre of the slice where the

inter-chip separation is 0.23 mm.  Each chip is in the form of a square of

size 1.69 mm.  The purpose of fabricating these chips in the central part

of the slice was to avoid edge defects of the slice.  On each chip, there

were three different structures (see Fig. 2.2), namely the composite,

residual film and the bare silicon, and when metal contacts are laid down

on top of these structures one ends up with a set of three different cap-

acitors.  The composite structure consists of a metal contact on a combined

willemite-residual film above the silicon substrate (see Fig. 2.3(a)), while

the residual film capacitor (Fig. 2.3(b)) has its willemite film removed.

The bare silicon metallized areas in the two corners of each chip have both

of the overlying films removed and in fact are rectifying metal-semiconductor

structures.  These structures are labelled by CW, CO and SB as in Fig. 2.2,

representing the composite, residual film and bare silicon capacitors

respectively.  For both the composite and residual film structures there

are three capacitors of different areas on each chip, with the largest

measuring $1.036 \times 10^{-3}$ $cm^2$.  However, there are only two metal-silicon

structures per chip, each with an area of $6.890 \times 10^{-4}$ $cm^2$.  With eight

capacitors per chip, one then has a total of two hundred capacitors availabe

on one silicon slice.  This method therefore enables one to study the repro-

ducibility of the electrical characteristics so that the physical interpre-

tation can be more reliable.  The chip layouts have been reduced by about

one hundred and twenty times from the size of the original drawing and
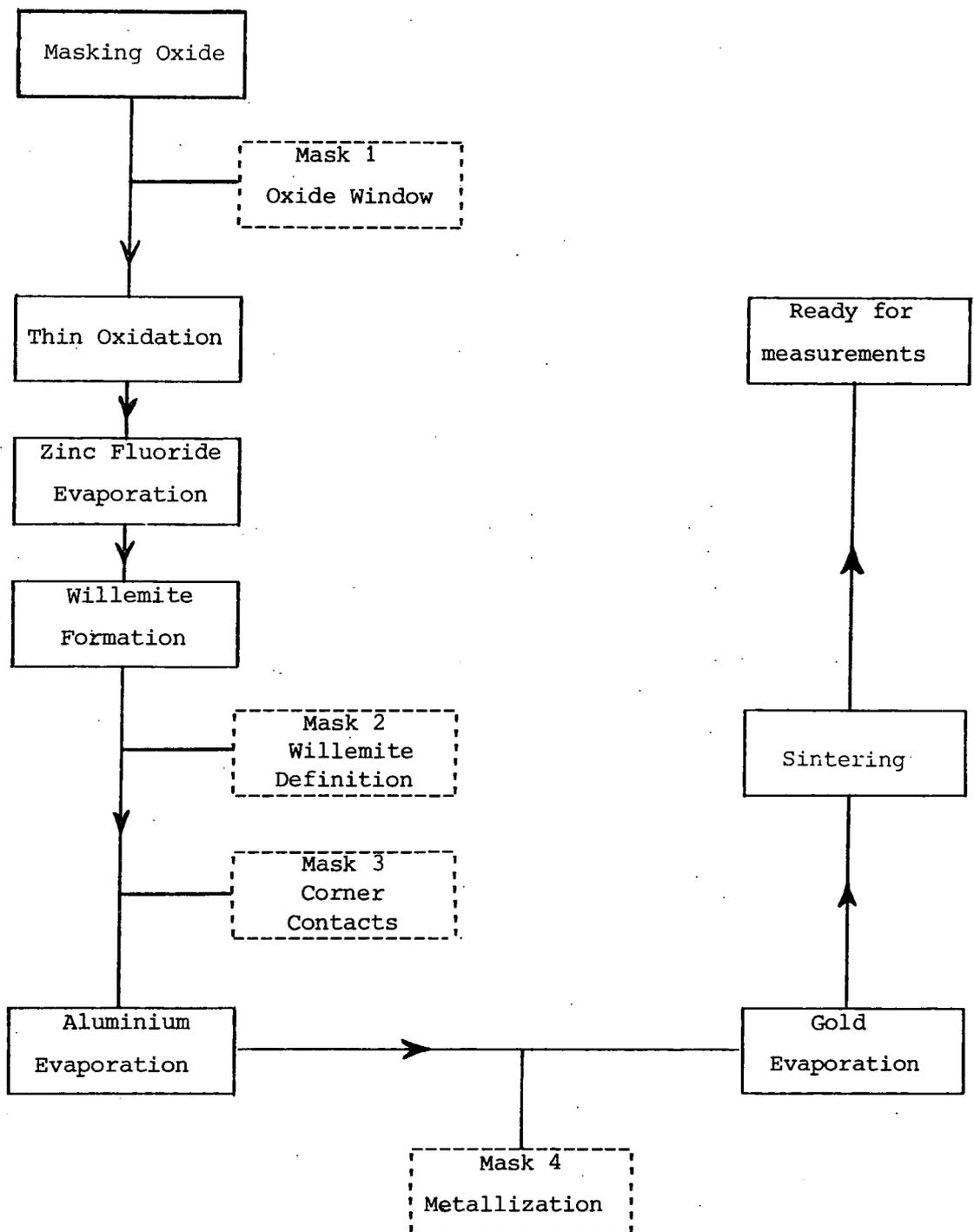
Figure 2.1:   Chart Flow Diagram of main stages
              of fabrication in the production
              of an experimental slice.
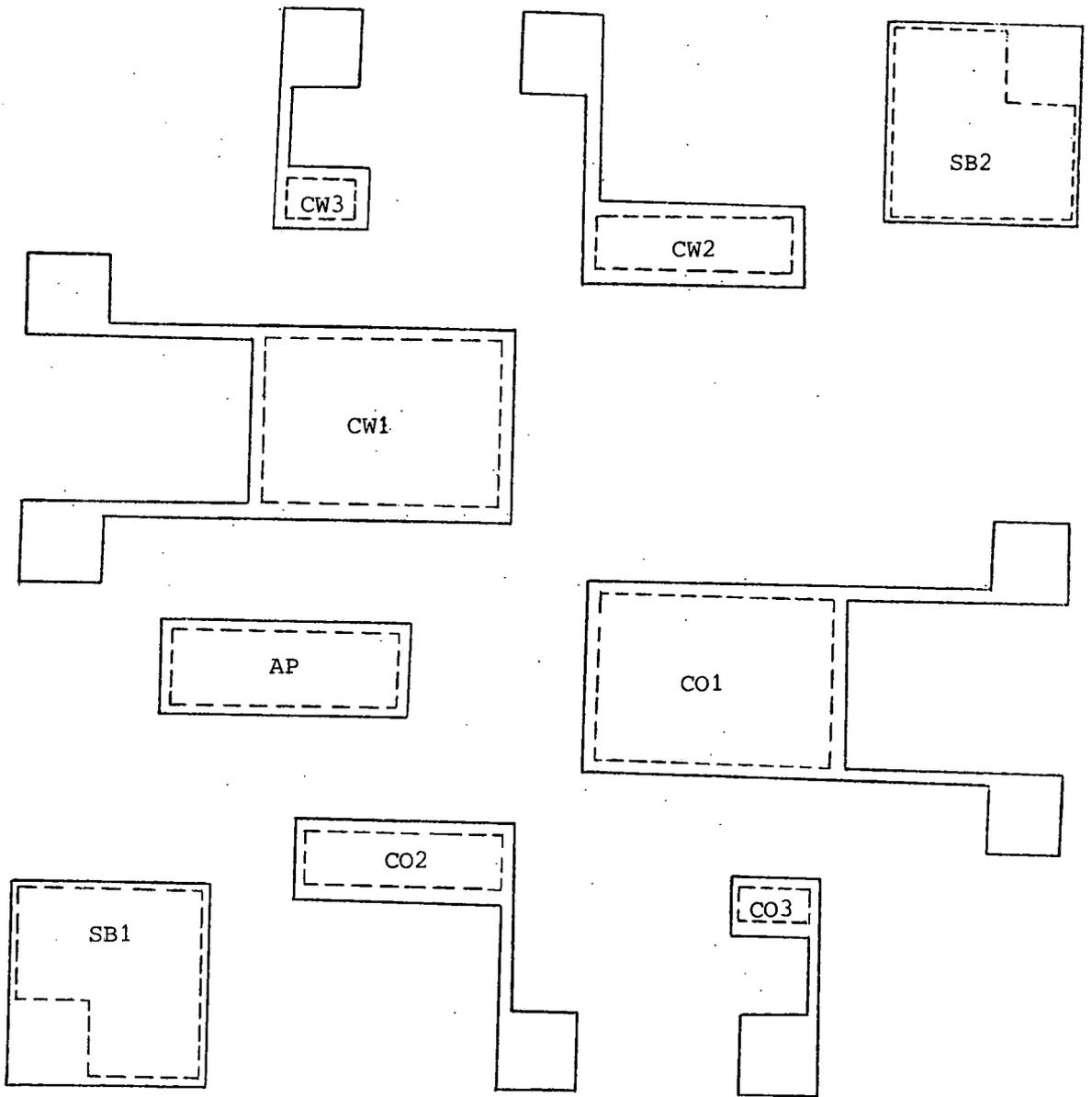
Fig. 2.2: Layout of final chip. Dashed lines enclose effective areas of capacitors.

willemite

To bonding pad

n-type

<111>

silicon

(a)

masking oxide

aluminium metallization

residual film

To bonding pad

n-type

<111>

silicon

(b)
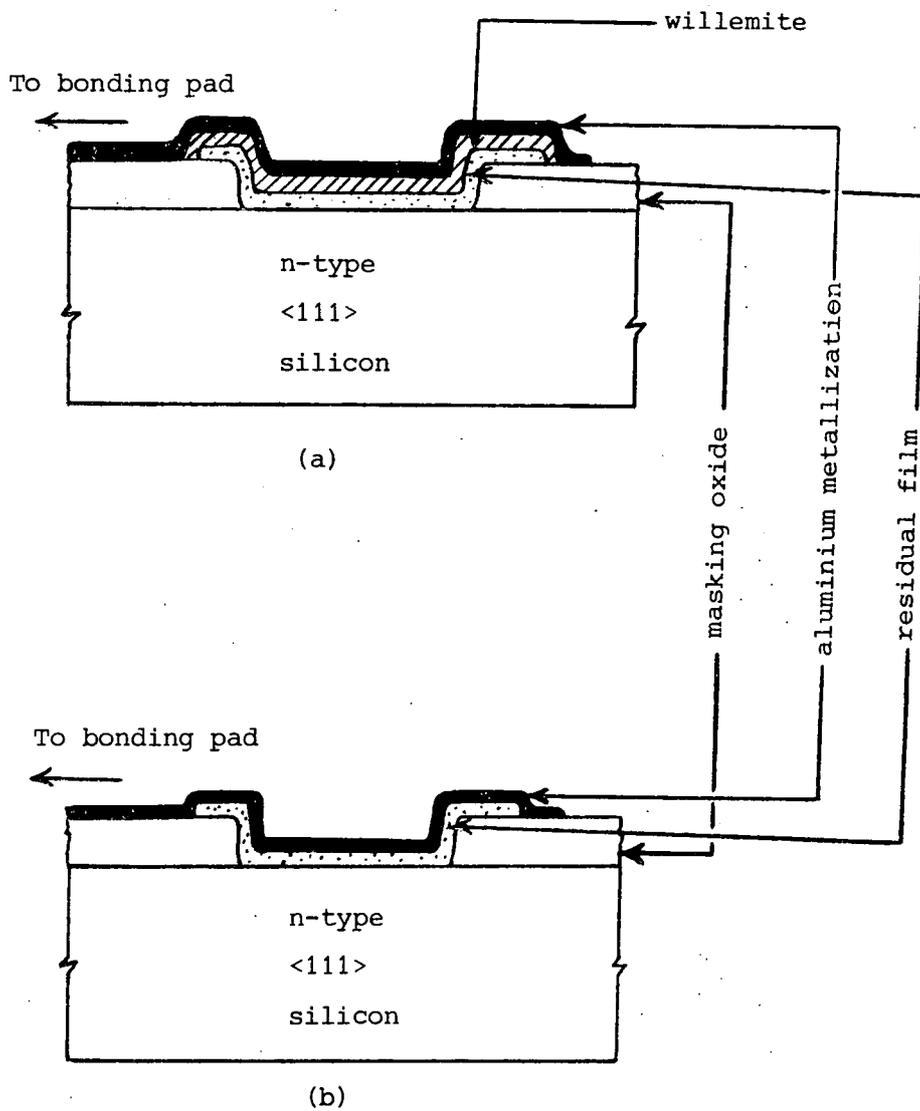
Fig. 2.3: Cross-sectional view of (a) composite
structure and (b) residual film structure.
Diagrams are not to scale.

this ability to miniaturize the chip increased the probability of getting defect-free devices.

A cross-section of two of the capacitors is given in Fig. 2.3(a) and (b). It is worth describing some of the advantages of such structures. Firstly there is the masking oxide (from wet oxidation), about 1.50 μm thick, over the entire silicon slice. The capacitor films, of the order of a few hundred Angstrom thickness, are grown in areas from which this oxide has been removed. Such a structure can reduce the intense edge field effects compared with normal dot-evaporated capacitors. It has also been found that the oxide surface can contribute surface conduction (2) by contamination with ionic charges which may invert or accumulate, depending on the type of silicon, the silicon surface below it. With a thick masking oxide, this can be greatly reduced, since its capacitance is only $7.7 \times 10^3$ pF/cm$^2$ as compared to a device capacitance of $6.9 \times 10^4$ pF/cm$^2$. The masking oxide is also capable of reducing the possible effect of contamination at the silicon-oxide interface. All these factors can well contribute to better definition of the effective area of the capacitors.

In Fig. 2.2, the effective areas of the capacitors are shown by dotted lines and Fig. 2.3 illustrates them in a cross-section. The aluminium metallization overlaps over the edges of the capacitors, again to prevent any lateral conduction from taking place, and the effect of the willemite or residual film overlapping the oxide windows results in a more uniform electrical field at the edges. All electrical connections to the top of the devices are of aluminium, the areas of which are bordered by the dark lines in Fig. 2.2. Bonding pads for probing the devices from the outside are of 130 μm by 130 μm square in dimension, which are sufficiently large for micro-probing but small enough not to contribute much of their stray capacitances of 0.39 pF each. Connections from the capacitors to the bonding pads are made by aluminium strips which are 15 μm in width. Cap-acitors that are made of composite and residual film structures each have

15

two electrical connections to bonding pads. The resistance between these pads provides a good way of testing whether the resistivity is sufficiently low for a good electrical connection to be made on the capacitor.

## 2.3    Sample Preparation and Fabrication

Integrated circuit fabrication by the photolithographic technique is an established technology and many articles have been written on it. For the present case, we are mainly interested in the fabrication of thin films based on such technology. Excellent descriptions of the growth of thin oxide films on silicon are given by Burger and Donovan (5), Wolf (6) and Grove (1). Processing and fabrication were carried out in a class 10,000 clean room with class 100 laminar flow benches for critical operations, and in order to prevent any form of cross-contamination strict restrictions of allowing one beaker per solvent etc. were observed. Washing and cleaning was done with Ultrar iso-propyl-alcohol or deionized water and in fact all solutions used were high purity Ultrar chemicals supplied by Hopkins and Williams.

All devices were fabricated during the course of this work on n-type, <111> silicon having a resistivity of 1.5 - 2.0 Ω.cm., unless otherwise mentioned. The silicon slices were 1.5 ins. (3.81 cm.) in diameter and 0.266 mm. thick. There were four masking stages involved:-  (1) for defining the window in the masking oxide,  (2) for willemite definition, (3) corner contact definite,  and (4) definition of metallization pattern. The masks were labelled 1,2,3 and 4 respectively and the function of each will be explained as the discussion on fabrication proceeds.

Initial cleaning of the silicon slices followed a standard procedure, (see Appendix I). The slices were then inserted into a furnace for about 10 minutes at a temperature of $1000^{\circ}C$ in dry oxygen, so as to achieve a good quality thermal oxide on the silicon.  Following this was

a wet-oxidation stage, carried out in a separate furnace tube with steam passing through it. Steam oxidizes the silicon surface at a much faster rate than oxygen, but the resulting oxide is of inferior electrical quality to that of dry oxidation. Setting the temperature of the furnace at $1000^{\circ}$C and baking the slices for one hour gave a masking oxide over the entire substrate of a thickness of about 1.5 μm. The role of the thin oxide layer in the first stage of oxidation was to obtain an oxide-silicon interface with minimum defects (2-4). The thick masking oxide has a dual role; the electrical isolation of devices as mentioned in the previous section and protection from contamination of the silicon surface. For the purpose of fabricating the capacitors, suitable areas in the masking oxide have to be defined and the oxide etched off. The technique is to apply a uniform coating of photoresist over the entire slice, exposing it to ultra-violet light through the oxide-window mask and then developing the photoresist. The action of the ultra-violet light is to harden the photo-resist. Unexposed areas remain soft and are removed with ease by the photoresist developer. Hence the unexposed areas, as determined by the mask, are removed and the underlying oxide is then etched off by using a solution of 1 : 10 mixture of hydrofluoric acid in water. Using the photo-resist remover, the remaining photoresist is then washed off, and then the slices are finally cleaned with iso-propyl-alcohol. This is a standard photolithographic process as used in each masking stage.

Immediately following the etching of the capacitor windows in the thick oxide was the growth of the thin, thermal oxide. This oxide, which is of thickness between 200 $\overset{\circ}{A}$ and 500 $\overset{\circ}{A}$, is one of the constituents required in the formation of thin willemite films as was described in the previous chapter. The oxidation was carried out in a dry oxygen atmosphere at $1000^{\circ}$C, except where stated later, the period of oxidation being dependent on the oxide thicknesses required.

17

The next stage of fabrication, i.e. the zinc fluoride evaporation, involved the use of a high-quality high vacuum system consisting of rotary and diffusion pumps with a large liquid nitrogen trap (3), and thermal evaporation facilities. The source for the thermal evaporation of zinc fluoride was a platinum 'pepper-pot' loaded with zinc fluoride powder, $ZnF_2$:Mn, containing 1% manganese. The silicon slices were mounted in the chamber at a distance of about 11.0 cm above the source and with the oxidized surface facing downwards. After evacuating the chamber to a pressure of $10^{-6}$ torr, the source was heated to about $800^{o}C$ for a few minutes for degassing. The evaporation was done an hour later when the pressure was less than $10^{-6}$ torr. The source temperature was allowed to stabilize at $865^{o}C \pm 5^{o}C$ before the shutter covering the substrate was opened. A time of about six minutes of evaporation was usually sufficient. Within the chamber, adjacent to the substrate, was installed the quartz crystal head of a film thickness monitor. This enabled one to control the thickness of the zinc fluoride films deposited on to the silicon oxide. Another method of measuring the zinc fluoride thickness was by a test piece of silicon, 1 cm by 2 cm, mounted on the edge of the substrate holder and which was later measured by ellipsometry. The evaporated zinc fluoride films were usually between 500 $\overset{o}{A}$ aND 1100 $\overset{o}{A}$ thick.

The third stage in making the test capacitor was the solid-state reaction for the formation of the willemite films, colloquially called 'willemization'. A special furnace was prepared for this purpose and profiled to give a peak temperature of $1000^{o}C$. The ambient gas and the time of 'willemization' depended on the type of willemite film required. In Table 2.1, the general features of three different types of willemite films are given. Type-A willemite was that studied by previous workers. Type-B was first fabricated by the author and Type-C was as proposed by Hurd and Johnston (12). The details of the fabrication techniques and the

| Willemite Type | Reaction Ambient | Reaction Time | Thin Oxide Thickness (Å) | Zinc Fluoride (Å) | Optical Microscope Examination | |
|---|---|---|---|---|---|---|
| | | | | | Willemite Surface | Residual Film Surface |
| Type-A | Dry $N_2$ | 20 min. | ∿600 | ∿550 Å | Coarse, violet, crystallites embedded in a tan background | Fine grain, Homogeneous. |
| Type-B | 10% of dry $O_2$ in dry $N_2$ | 20 hours | ∿200 | ∿1000 Å | Fine, bluish crystallites embedded in a light yellow background. Crystallites were numerous. | Dendritic or cellular patterns in light yellow background. |
| Type-C | Ultra-pure pure dry $N_2$ | 20 hours | ∿500 | ∿500 | Dendritic, cellular patterns. Fine grains similar to Type B. | Undefined |

Table 2.1:   General Classification of the Types of

Willemite Films Investigated.

resulting characteristics will be discussed in three chapters in the later part of this thesis.

The second masking stage was carried out using the willemite definition mask. Photoresist application and ultra-violet light exposure were the same as described previously. Before the removal of the photo-resist but after the developing, the slice was immersed in a dilute solution of 1 : 10 acetic acid to water in order to etch the willemite except where required for the composite capacitors. After the photoresist removal, the slice underwent a 'degrotting' process as initiated by Davies (2). This is a cleaning process for the willemite surface achieved by using very dilute sodium hydroxide solution (1 in 5 parts of water) which is supposed to dissolve surface layers, such as zinc oxide, formed during the 'willemization' process.

The third masking step, the definition of the corner contacts, was merely to make metal to semiconductor structures at two opposite corners of each chip. These later played an important role when reassessing the electrical characteristics of the silicon surface after undergoing the fabrication processes. By defining the areas with the mask, the residual film was etched using 10% HF solution. The slice was then cleaned and mounted in the chamber of an ultra-high vacuum system for the metallization. The system, a Varian ~~Metal~~ Model 927, had sorption, ion and sublimation pumps capable of achieving a vacuum of $10^{-9}$ torr. For our purposes, only the ion and sorption pumps were used for aluminium evaporation at a pressure of less than $10^{-7}$ torr. A 4 keV electron beam evaporation source was used. The thickness of the evaporated aluminium was a few microns.

The final stage of photoresist was for defining the metallization areas. Areas other than that of the devices, connecting strips and bonding pads were etched by using dilute sodium hydroxide. This was used in preference to orthophosphoric acid to prevent any possibility of etching

19

the willemite, which is attacked by most acids.  After washing in iso-
propyl-alcohol and drying, the slice was then annealed for about 10 minutes
in a dry nitrogen atmosphere at a furnace temperature of $470^{\circ}$C.

The final stage of processing was to make the back contact to the
slice.  The unpolished side of the silicon slice was lapped with 3 $\mu$m
grain-size diamond paste and the slice was then cleaned in iso-propyl-
alcohol and mounted in a small vacuum system for the evaporation of gold
at a pressure of $10^{-6}$ torr.  The gold was evaporated on to the back part
of the slice through a mask to give two strips at 0.5 cm apart with each
strip measuring 2.5 x 0.5 cm.  This was then followed by sintering in dry
$N_2$ in a furnace at $435^{\circ}$C for 10 minutes to drive in the gold and form an
ohmic contact.  In order to check that a good ohmic back contact had been
made, the resistance between the two gold strips was always measured on
completing the processing of the slice.  The bulk resistance through the
slice was about 200 $\Omega$  when reasonably good ohmic contacts had been made.


2.4    Instrumentation and Measuring Techniques

In this section a description of the instrumentation techniques
used during the course of this work will be given.  The instruments mentioned
here will only pertain to the most widely used techniques which are con-
sidered to be of basic importance to the physical studies of our films.
Instruments and techniques which were less frequently used will be described
in less detail in their respective sections later in the thesis.

Ellipsometry

One of the most basic techniques for measuring the thickness and
refractive index of thin films on silicon substrates is ellipsometry, used
whenever the thin films are non-absorbing and the substrate highly reflecting.
Theoretically speaking, when elliptically polarized light is incident at an

angle on a highly reflecting substrate with a thin film on it, conditions can be found for it to become linearly polarized after reflection. An elliptically polarized state of the incident light is achieved by placing a compensator (or quarter-wave plate) in the path of a linearly polarized beam. Thus an ellipsometer contains a polarizer, compensator, the reflecting substrate and analyzer in the path of the light. The instrument is set to give an intensity minimum at the analyzer by adjustment of the polarizer and analyzer orientations. Two ellipsometric parameters, $\psi$ and $\Delta$ , evaluated from the polarizer and analyzer readings respectively, are then used to calculate the refractive index and thickness of the film. Both the refractive index and the thickness are characteristic of the film and are also related to a complex function dependent upon the light wavelength, incident angle and the substrate's reflectivity (Appendix II). Mc Crackin et al (13) have given a thorough description of the experimental and computational technique used with an ellipsometer, while Archer (14) has made detailed studies of thin films on silicon substrates. The ellipsometer for our work, constructed by Errington in this department, utilizes a monochromatic green light source ( $\lambda$ = 5461 Å) incident at an angle of $70^{\circ}$ to the substrate normal. Such a setting is claimed by Archer (14) to give an accuracy of $\pm 5$ Å, but our accuracy seems to be approximately $\pm 20$ Å, the discrepancies being due to certain very sensitive alignment procedures, film non-uniformity and substrate irregularity. Nevertheless our results on oxide films on silicon give good thickness agreement, within the quoted accuracy, when compared with capacitance measurements.

The main advantage of ellipsometry is that it is non-destructive. The accuracy achieved is easily an order of magnitude better than that of the conventional interferometer. With the recent development of electronically operated ellipsometers, much more flexibility and accuracy can be obtained and a thorough presentation of the subject is given by Azzam and Bashara (16).

## Electrical Measurements

The most widely used electrical technique for assessing the physical properties of the films is that of the capacitance-voltage (C-V) plot. For such measurements we have used a conductance-capacitance-voltage (G-C-V) analogue instrument, built in this Department by Martin (11). The instrument measures capacitance from 1.0 pF to 10 μF and admittances from 1 m℧ to 100 ℧, over a frequency range of 10 to 500 kHz, which is adequate for most purposes. A sweep voltage of both positive and negative polarity was supplied to the sample by the plotter with a maximum amplitude which was variable up to 20 volts. Superimposed on this slowly varying voltage was a 100 m V (r.m.s.) a.c. signal derived from a Farnell LFM3 Signal Generator. The outputs from the G-C-V plotter, which are a measure of capacitance and conductance against voltage, were directly connected to a Bryans X-Y plotter. Also present on the G-C-V plotter was a facility for controlling the sweep speed, from 27.13 mV/min up to a fast ramp of 5.34 V/sec. However, most of the measurements were performed in the slower sweep speeds of around 300 mV/min, so as to allow sufficient time for the device to respond. Capacitance calibration was provided by a calibration unit containing silvered-mica capacitors each with 0.5 pF tolerance and high value resistors.

For frequencies higher than that of the plotter, a Wayne-Kerr Model B601 radio frequency (RF) bridge was used. The frequency range of this instrument is 5 kHz to 5 MHz with capacitance ranges of 225, 22.5 and 2.25 pF at full-scale. The quoted sensitivity of the bridge is 0.1 pF but a practical value of only 0.25 pF can easily be resolved. The bridge source of 7 mV (r.m.s.) or less was provided by an Advance B4B oscillator while the detector was an Eddystone Model 830 communications receiver. Connected between the d.c. power supply and the bridge was an L-C circuit as shown in Fig. 2.4. The inductor consisting of two RF coils of 128 mH inductance each is necessary to isolate the d.c. power supply from the RF measuring

circuit, while the 1000 pF silvered-mica capacitor is to prevent d.c. current flow through the bridge circuit. The RF bridge was used mainly for Schottky mercury-probe or very thin film MIS measurements.

When studying insulator systems with very low d.c. conduction such as the MIS system, it is necessary to use a highly sensitive current-measuring instrument. For this purpose we made use of a Vibron Electrometer Model 33C and a Convertor Unit Model B33C having nominal resistors from $10^5$ to $10^{12}$ ohms. The sample is connected in series with a selected resistor in the convertor unit and on applying a d.c. voltage the same current flows through the sample and the resistor. The potential across the known resistor is measured by the electrometer enabling the current to be calculated. The electrometer is capable of measuring currents down to $10^{-14}$ amps when the resistor is set at $10^{12}$ ohms. Such a sensitivity however can be obscured by stray charges and careful measurements by taking background current into consideration have to be made. Current values of $10^{-13}$ amps or higher seem to be adequate to discriminate between the sample current and the effects of stray charges. A discharge switch on the electrometer also helps since charges accumulated in the circuit can be drained off after each measurement. The d.c. supply for current measurements was obtained from a Farnell L30AT stabilised power supply unit.

### Probe Gear

Lastly, the probing technique for making electrical contacts on to bonding pads will be described. With extremely small areas, electrical contacts were made by lowering steel microprobes on to the pads under electronic control. This was to avoid any accidental damage that could happen to the capacitors if it were done manually. An Electroglas Inc. Wafer Prober was mounted on a metal frame in a laminar flow cabinet, thus providing a clean probing environment. The prober slice platform has X-Y
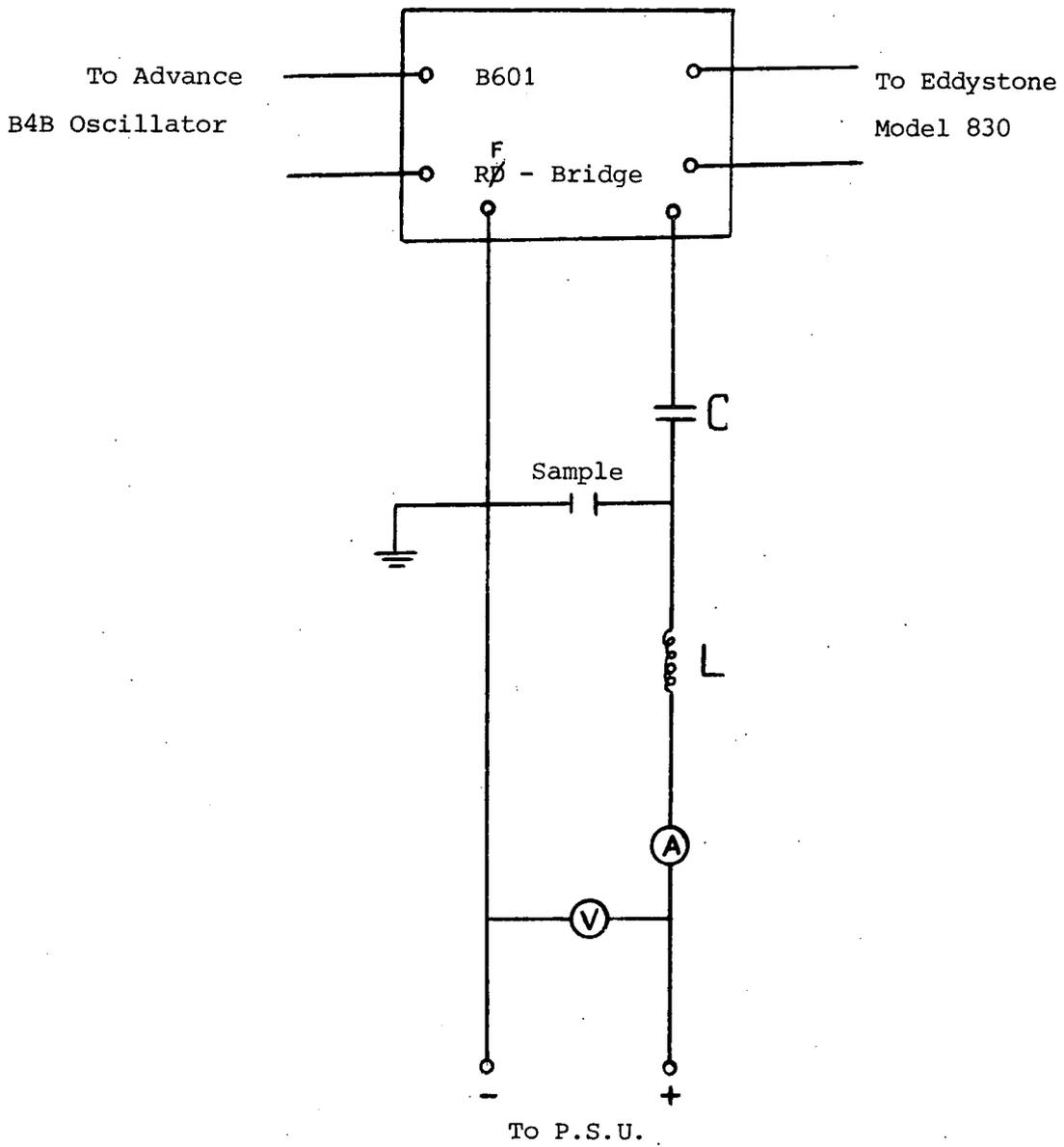
Fig. 2.4:    RF-Bridge set-up for capacitance

measurements
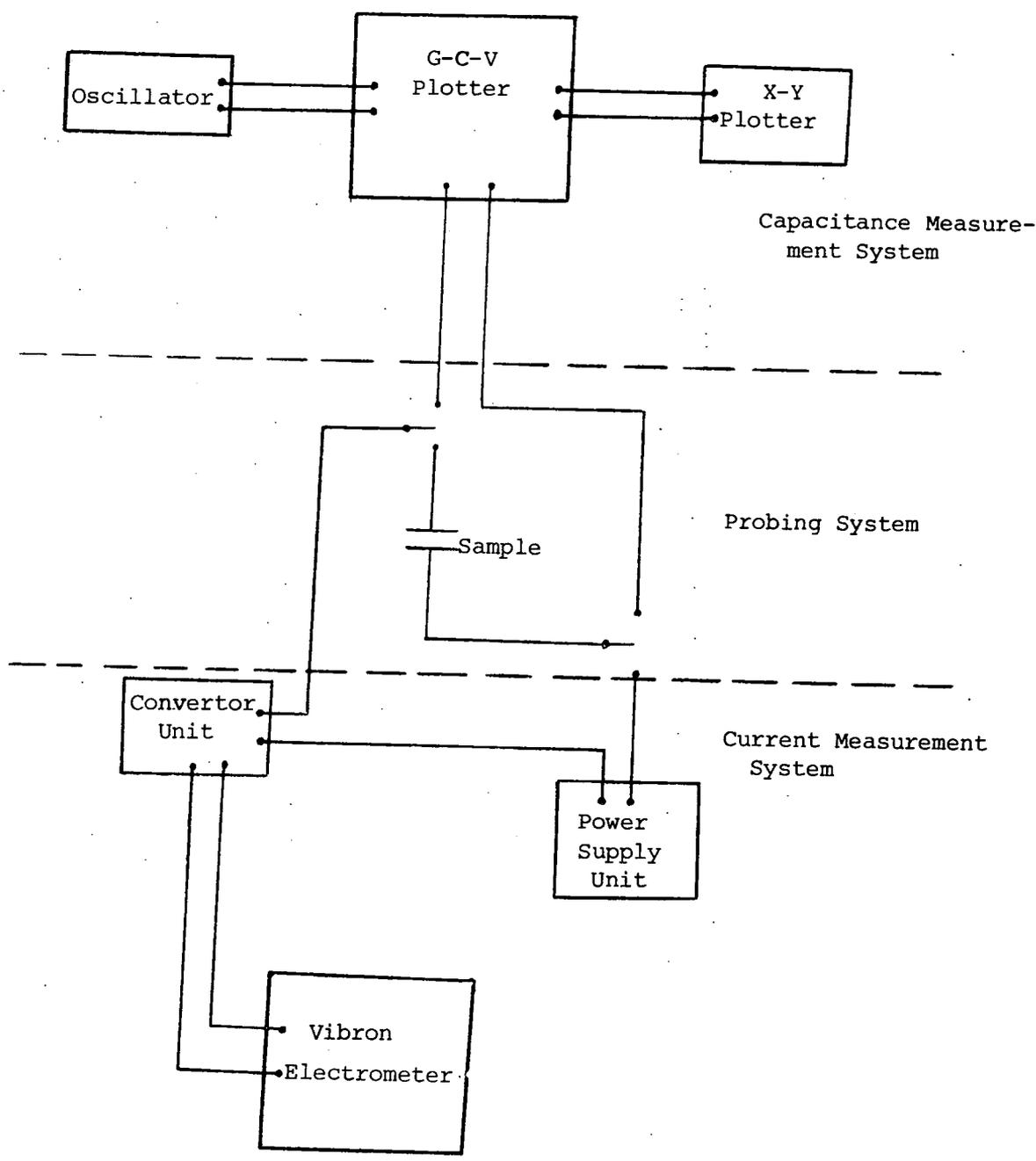
Fig. 2.5: Schematic representation of the equipment for capacitance and current measurements.

electrically controlled movement plus rotation.  The ten steel probes each with a tip radius of 10 μm have sideways and vertical adjustments and electrical connections to the outside.  A vacuum chuck held the slice firmly on the platform so as to give good electrical contact between the gold back contact on the silicon and the platform itself.  The mechanisms for the X-Y movements and probe lowering are controlled by an electronic unit, the Electroglas Inc. 920SS Controller.  This unit enables one to manoeuvre the probes to within 25 μm without any difficulty, so again lessening the possibility of the capacitors being damaged by inaccurate probing.

Finally, a general experimental set-up for the measurements is presented in the form of a block diagram in Fig. 2.5.  The instrumentation technique is shown separated into three parts, namely the capacitance measurement, probing and current measurement.  Such a set-up provides rapid changes that can be made from capacitance to conduction measurements, without the need to move the slice around.

REFERENCES

CHAPTER  2

1.   A S Grove,  'Physics and Technology of Semiconductor Devices',
     Wiley and Sons  (1967)

2.   M M Atalla,  E Tannebaum  and  E J Scheibner,  Bell. Syst. Tech. J.
     $\underline{38}$  749-783  (1959)

3.   A S Grove,  B E Deal,  E H Snow  and  C T Sah,  Sol. St. Elec.
     $\underline{8}$   145-163  (1965)

4.   E H Nicollian  and  A Goetzberger,  Appl. Phys. Letts.  $\underline{7}$
     216-219  (1965)

5.   R M Burger  and  R P Donovan,  'Fundamentals of Silicon Integrated
     Device Technology'  Prentice Hall    1967

6.   H F Wolfe,  'Silicon Data,  A Handbook in Graphs'  Pergamon Press
     1969

7.   J Allison,  'Electronic Integrated Circuits,  Their Technology
     and Design'  McGraw Hill  1975

8.   G S Edwards,  Ph.D. Thesis  Durham  (1970)

9.   G D Davies,   M. Phil. Thesis  Durham  (1975)

10.  M R Husain,   Ph.D. Thesis  Durham  (1973)

11.  P G Martin,   M.Sc. Thesis  Durham  (1970)

12.  J M Hurd  and  R E Johnston,  private communication

13.  F L McCrackin et al,  J. Res. Nat. B. Stds. A  $\underline{67A}$    363-377  (1973)

14.  R J Archer,  J. Opt. Soc. Am.  $\underline{52}$  970-977  (1962)

15.  D Errington,  Unpublished

16.  K A Azzam  and  N M Bashara,  'Ellipsometry and Polarized Light'
     North Holland  (1977)

CHAPTER   3

REVIEW OF RELEVANT THEORIES

3.1     Introduction

The purpose of this chapter is to give a review of the theoretical
background required for understanding the capacitance-voltage characteristics
of the willemite and residual film structures.  Although details are not
given, an attempt is made to clarify the physics by presenting a qualitative
picture of the concepts involved and using mathematical expressions only
when necessary.  These are the main expressions to be used in the interpre-
tation of the results in the following chapters.

Section 3.2 presents the theory of the ideal Schottky barrier,
together with some possible effects that can cause experiments to deviate
from theory.  Following this is a section on the theory of Schottky barriers
with deep trapping levels with emphasis on the capacitance-voltage relation-
ship only.  A thorough description of the physical concepts of capacitance-
voltage of the Metal-Insulator-Semiconductor (MIS) structure is presented
in Section 3.4.  This forms the essence of a major part of the experimental
work carried out by the author during the course of this research.  The
final section is devoted to double-dielectric MIS structures.  Since theories
of such structures are so widely dispersed, depending on various mechanisms
proposed, only a general review is attempted in this section.  A few other
theoretical ideas used in this investigation are given when used in the
relevant chapters, rather than in the present chapter.


3.2     The Schottky Barrier

A metal in contact with a semiconductor can have rectifying character-
istics which depend on the properties of the metal and the semiconductor.
Such a metal-semiconductor contact is known as a Schottky barrier because
of the formation of an energy barrier near the metal-semiconductor interface.

If an n-type semiconductor with a work function $\phi_s$ is brought into contact with a metal of work function $\phi_m$, such that $\phi_s$ is less than $\phi_m$, electrons will flow from the semiconductor into the metal (Fig. 3.1(a)). Both the metal and semiconductor Fermi levels are then forced to coincide in order to achieve equilibrium, and when this is accomplished the surface region of the semiconductor is left with only positive donors. These positive charges are balanced by extra conduction electrons in the surface of the metal and since the density of electrons in the metal is much higher than the semiconductor donor density, the resulting field will drop almost entirely across the semiconductor. The space-charge or 'depletion' region that is formed occupies a distance w between the surface of the semiconductor and the neutral region in the bulk. Electrons going from the metal to the semiconductor now have to surmount an energy barrier $\phi_b$, the barrier height of the Schottky barrier. A Schottky barrier on a p-type semiconductor can be made similar except that the condition is that $\phi_m$ has to be less than $\phi_s$.

For an ideal Schottky barrier, assuming that the current-limiting process is the transfer of electrons across the interface, Bethe's thermionic-emission theory gives the forward-bias current density:-

$$J = A^* T^2 \exp\left(\frac{-q\phi_b}{kT}\right) \left\{ \exp\left(\frac{qV}{kT}\right) - 1 \right\} \qquad (3.1)$$

where     V is the applied voltage,

$\phi_b$ the barrier height

T the temperature,

q the electronic charge

A* the Richardson's constant, and

$A^* = \left(m^*/m_o\right) \; 1.2 \times 10^{+6} \; A \; m^{-2} \; K^{-2}$

where m* and $m_o$ are the effective and rest masses of electrons respectively.

(a)



Vacuum Level

$\phi_m$

$\phi_b$

$\chi_s$

W

$V_d$

$\zeta$

$E_c$

$E_F$

$E_v$

Metal

Semiconductor

(b)



$1/C^2$

slope $= \left( \dfrac{2}{K_s \varepsilon_0 q N_d} \right)$

$V_D$

$V_r$
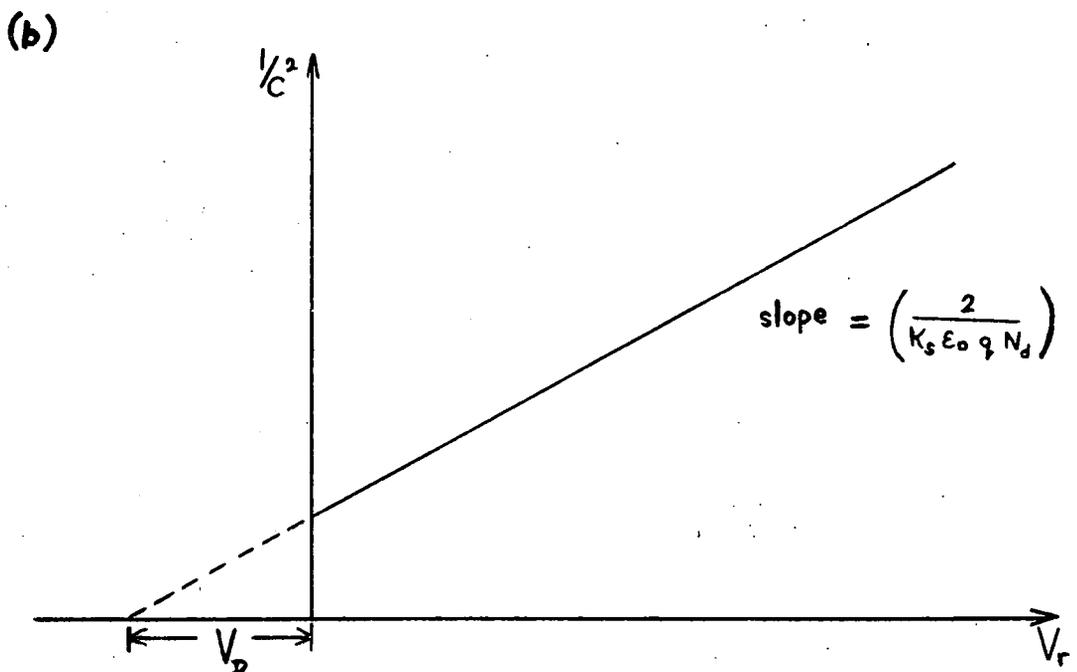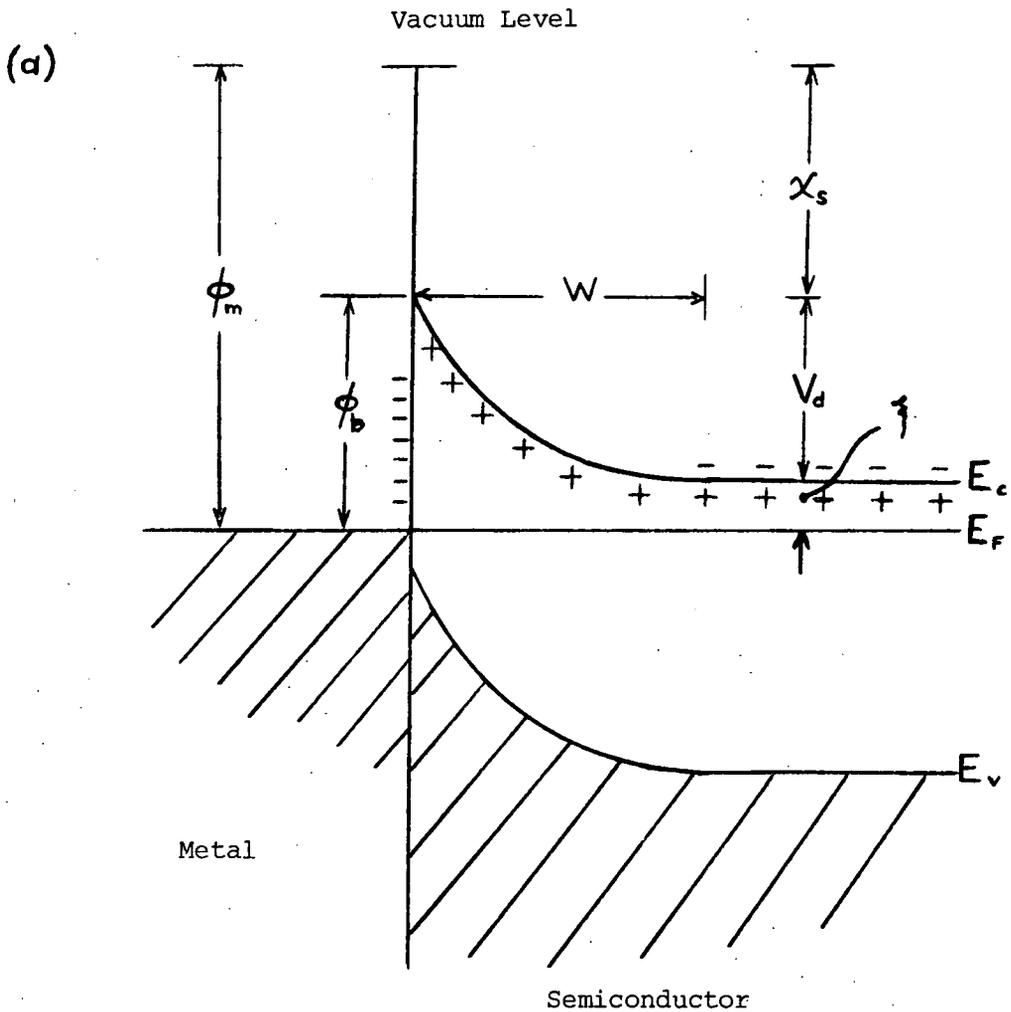
Figure 3.1:   (a) Band diagram of an n-type Schottky barrier.
The value of the semiconductor work function
is given by $\phi_s = \chi_s + \zeta$

(b) A $C^{-2}$ vs Vr plot from the capacitance-voltage
characteristic of a Schottky Barrier.

The theory also gives the saturation current density in the reverse bias direction:-

$$J = A^* T^2 \exp\left(\frac{-q\phi_b}{kT}\right) \qquad (3.2)$$

In most practical cases deviations from both relationships are bound to be observed. The barrier height $\phi_b$ is normally voltage dependent due to image-force lowering or the presence of an interfacial layer between the metal and semiconductor, and if $\phi_b$ is large electron-hole recombination current will then be the limiting factor. The series resistance from the bulk semiconductor will also take up a fraction of the applied voltage and this will bend the $\log I$ by $V$ plot towards saturation at higher forward bias voltages. These factors can also contribute to the non-saturation of the reverse bias current which gradually increases until breakdown is observed. Thinning of the barrier so as to allow tunnelling in reverse bias can also cause the current to increase. Practical Schottky barriers also show the existence of 'surface states' which are discrete energy levels at the surface of the semiconductor. Depending on the sign of their charge the surface states can have a shielding effect on the donors from the electrons in the metal, thus dominant in controlling the barrier height (see Rhoderick (1)).

The depletion region in a Schottky barrier behaves in some respects like a parallel-plate capacitor. In reverse bias the capacitance per unit area is given by

$$C = \left(\frac{K_s \epsilon_o q N_d}{2}\right)^{\frac{1}{2}} \left(V_D + V_r\right)^{-\frac{1}{2}} \qquad (3.3)$$

where $V_D$ is the diffusion voltage (see Fig. 3.1)

$V_r$ is the reverse bias voltage,

$K_s$ the dielectric constant of the semiconductor and

$\epsilon_o$ the permittivity of free-space.

If $N_d$ is assumed to be uniform and $V_D$ is independent of bias, a $C^{-2}$ by $V_r$ plot should give a linear relationship which can yield information on the barrier parameters. From the slope the value of $N_d$ can be evaluated and if the line is extrapolated backwards (Fig. 3.1(b)), the intersection on the voltage-axis gives the value of $V_D$. For a non-uniformly doped semi-conductor the $C^{-2}$ by $V$ plot is non-linear but the slope at any point still indicates the donor concentration at the edge of the depletion layer. This enables an impurity profile from the semiconductor surface inwards to be obtained.

## 3.3   Deep-levels in Semiconductors

When localized electron states are situated around the centre of the band gap a semiconductor is said to contain deep-levels. Basically there exist two types of deep-levels, namely the donor- and acceptor-type traps. The donor-type are neutral when filled with electrons and positive when empty, while the acceptor-type are negative when filled and neutral when empty. Since these traps are situated far from the conduction or valence band, they are not ionized at room temperature. The occupation of a trap within a depletion layer depends primarily on its position with respect to the Fermi level.

Deep-levels can originate from impurity-complexes or impurity-vacancy complexes such that the impurity can be interstitial or substitutional within the host semiconductor. Practical effects due to deep-levels have led to numerous theories and experimental techniques being developed to investigate them. A good review on the subject is given by Milnes (2). Some of the conventional techniques like thermally stimulated current (TSC) and thermo-luminescent (TL) involve tedious experimental-fitting to theory although they have the advantage of yielding fundamental parameters like drift-mobility, capture cross-section, activation energy etc. Others like the

Fernherer and Goetzberger MOS technique (3) or the junction-capacitance method (4,5), yield only the trap depth and density though involving little computation. In this section, the last technique only will be described with specific reference to the theory of Sah and Reddi (5) for a $p^{+}$-n junction (or n-type Schottky barrier).

In the general case, the occupation of the traps is determined by Shockley-Read-Hall statistics according to which the probability of an electron occupying a trap is dependent upon the emission rate of electrons and holes into the conduction or valence band respectively. Thus the junction-capacitance of a $p^{+}$-n (or Schottky barrier) structure becomes strongly dependent on the measuring frequency. To describe this in detail, the model proposed by Sah and Reddi is based on the non-uniform charge distribution due to an acceptor-type trap in an n-type semiconductor within the depletion region (Fig. 3.2). The depletion layer consists of a space-charge region y and a transition region (w-y). Within the space-charge region the charge comes only from the donor concentration $N_D$, since traps lying above the Fermi-level are empty and neutral. On the other hand, the transition region has contributions from both donors and traps, altering the concentration to $(N_D - N_T)$ where $N_T$ is the trap concentration. This situation is illustrated in the lower half of Fig. 3.2 where the non-uniformity is represented by a 'staircase' function. When a small voltage is applied, charges at y and w will be uncovered. At w, free carriers are swept away, and at y, electrons are emitted into the conduction band from the traps. This results in a net change in charge $\Delta Q$ for which the capacitance $C = \Delta Q / \Delta V$ is determined. If the measuring frequency $\omega$ is high, such that the traps cannot respond to the rapidly varying signal voltage, then charging and discharging of the acceptors occurs only at the edge of the transition region $x \doteq w$. In other words, $\tau_t(w) \ll \omega^{-1} \ll \tau_t(y)$, where $\tau_t$ is the time constant of the trapping centres associated with their positions in the depletion region.
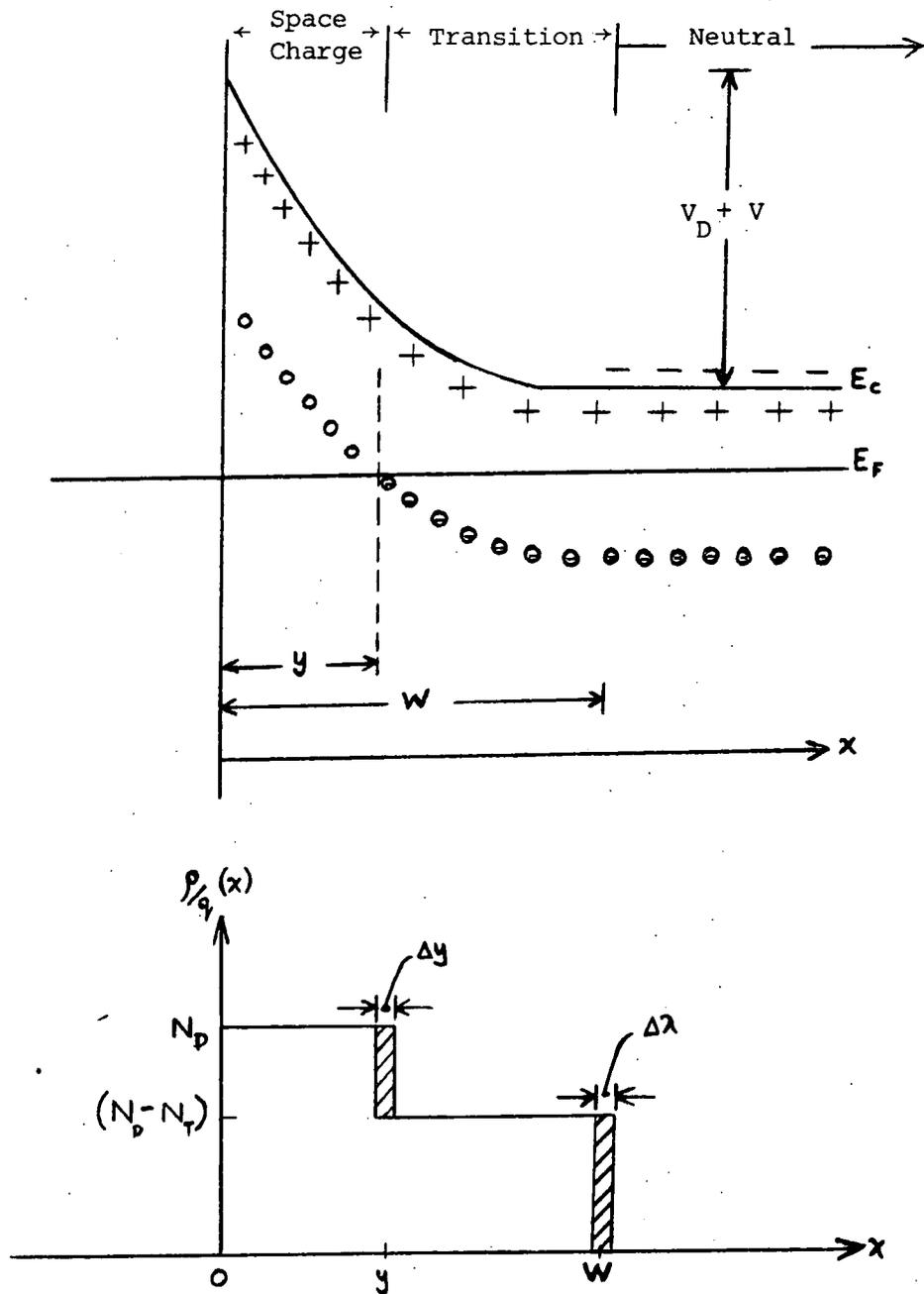
Figure 3.2: Effects of deep acceptor-levels in an n-type semiconductor at reverse bias for a $p^+$-n (Schottky Barrier) structure.

Working on this basis Sah and Reddi derived the relationships ,

$$C_{dc} = \left\{ \left( \frac{q \varepsilon N_D}{2} \right) \left[ V_D - V - \left( \frac{N_T}{N_D} \right) \phi_t \right]^{-1} \right\}^{\frac{1}{2}} \qquad (3.4)$$

and

$$C_{ac} = \sqrt{\frac{q \varepsilon}{2}} \left\{ \sqrt{\frac{\phi_b}{(N_D - N_T)} \left( \frac{N_T}{N_D} \right)} + \sqrt{\left[ V_D - V - \left( \frac{N_T}{N_D} \right) \phi_t \right] / N_D} \right\}^{-1} \qquad (3.5)$$

where $C_{dc}$ and $C_{ac}$ are the dc and ac capacitances respectively, the other symbols have the meanings given previously and

$$\phi_t = (E_F - E_t)/q .$$

Some important observations can be made from the equations (3.4) and (3.5).

(i) For a high trapping concentration, i.e. $N_T \sim N_D$ , the capacitance $C_{ac}$ for low reverse bias is reduced substantially below that of the zero-trap case.

(ii) $C_{ac} < C_{dc}$ at all bias voltages and $C_{ac} \rightarrow C_{dc}$ at large reverse bias.

(iii) If $N_T \rightarrow 0$ both $C_{dc}$ and $C_{ac}$ will approach the ideal junction-capacitance case as in equation (3.3) giving a linear $C^{-2}$ by V plot.

The model is valid as long as $N_T < N_D$ and the applied voltage is in reverse bias. Knowing the trap depth, hence $\phi_t$, a theoretical capacitance-voltage curve can be fitted to the experimental plot, enabling the value of $N_T$ to be worked out. The trap concentration need not necessarily be uniform because it is calculated for any point x = y only. In this way a profile of $N_T$ into the semiconductor can also be obtained. A similar approach can be used for donor-type traps in n-type semiconductors to derive the capacitance-voltage relationship where the mathematical treatment is given in Appendix III.

## 3.4   Metal-Insulator-Semiconductor (MIS) Structures

Following the successful growth of high-quality oxide films on silicon in the early 1960's, it was proposed that a Metal-Oxide-Semiconductor (MOS) structure could be used as a voltage dependent capacitor (6). The main interest in MOS capacitors at that time was in trying to understand the surface properties of silicon. Grove et al (7) were probably the first to provide a complete picture of the MOS capacitor both experimentally and theoretically. Similar ideas can be used more generally for Metal-Insulator-Semiconductor (MIS) structures, with any insulating film on a semiconductor with a metal top contact. On an energy band diagram this system is visualised as having a large barrier height between the semiconductor and insulator conduction band edges when the system is in thermal equilibrium. Electrons cannot surmount this barrier unless externally stimulated, hence there will be no net charge flowing between the metal and semiconductor. However, if the insulator is thin enough (100 Å or less) quantum mechanical tunnelling can take place between the metal and semiconductor.

Fig. 3.3(a) depicts the relative energy bands of an n-type ideal MIS structure in thermal equilibrium. Notice that the Fermi levels of the semi-conductor, insulator and metal are all aligned; the Fermi level of the insulator being assumed to be at its intrinsic energy level. When a positive voltage is applied to the metal with respect to the semiconductor the semiconductor surface will accumulate electrons and most of the voltage will be taken up by the insulator (Fig. 3.3(b)). Electrons are attracted towards the vicinity of the insulator-semiconductor interface and this pile-up of charges causes the field to drop almost entirely across the insulator. Such a situation is known as the accumulation mode. For small negative bias, electrons are repelled from the vicinity of the interface leaving behind a positive space charge region of uncompensated ionized donors (Fig. 3.3(c)). Since in this mode the concentration of carriers is negligible in comparison
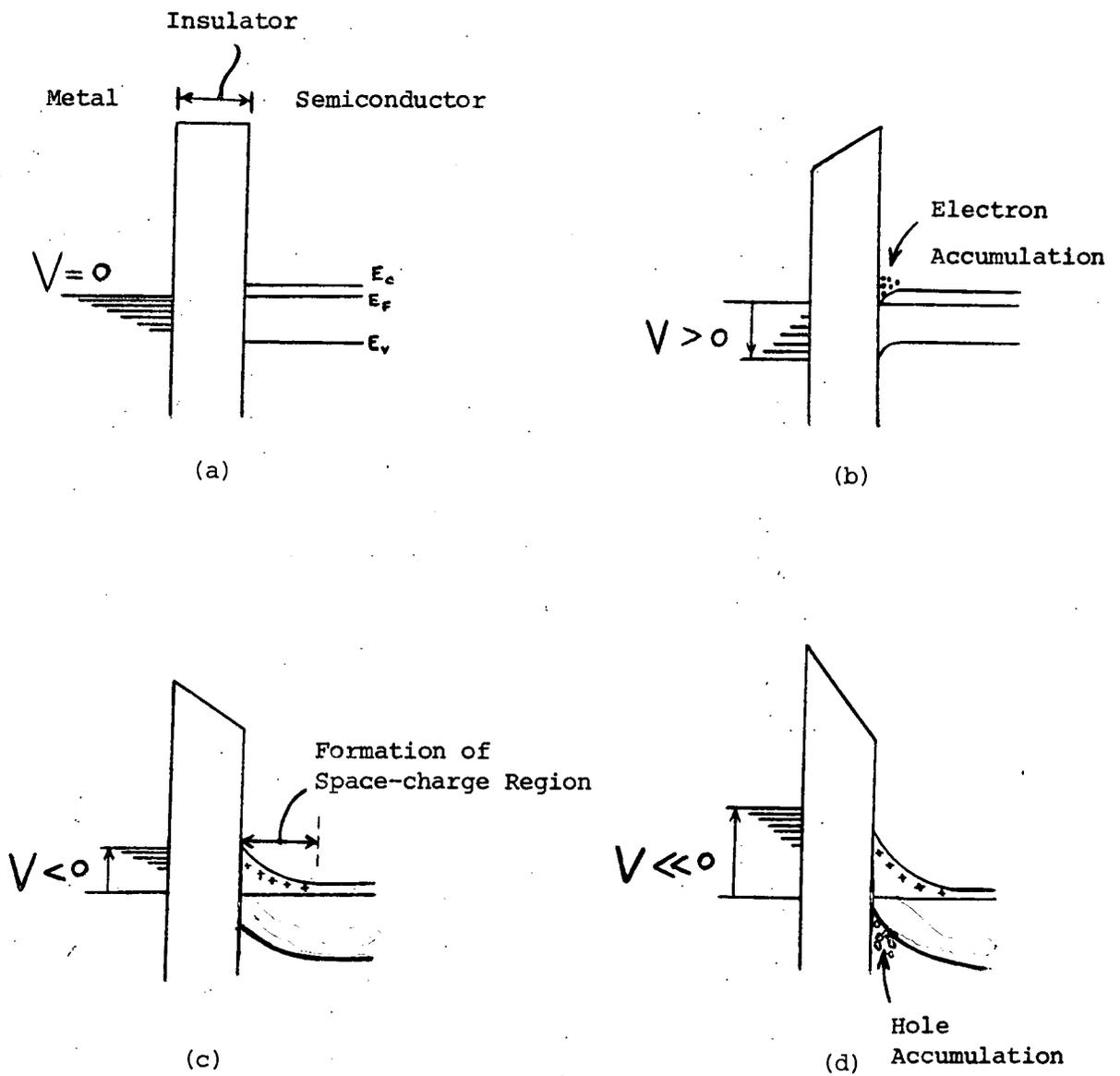
Figure 3.3:    Band diagrams for the various modes of an
               ideal n-type semiconductor MIS structure:

               (a) Thermal equilibrium

               (b) Accumulation

               (c) Depletion

               (d) Inversion

to the impurity concentration, it is referred to as the depletion mode. With further increase in the negative metal bias (Fig. 3.3(d)) holes (the minority carriers in this case) are attracted to the interface so that while some of the semiconductor charge still consists of the charge of the ionized donors, there is also positive charge due to the holes. This situation is referred to as the inversion mode, i.e. an accumulation of minority carriers has altered the electrical polarity of the semiconductor surface.

Consider the effect of rapidly changing the metal bias between the equilibrium situations shown in Fig. 3.3(c) and 3.3(d). It is evident that for the charge distribution to follow such a change, holes must be generated and transported to the surface, and electrons must be removed from the edge of the depletion layer. It is clear that the capacitance following such a bias change will depend on the relative rates of the bias change and of the re-arrangement of the charge within the semiconductor. If the bias change is slow, the charges within the semiconductor will be able to rearrange in phase and be essentially in equilibrium with the instantaneous d.c. bias. In such a case an analysis based on the assumption of equilibrium in a semiconductor yields good results. On the other hand, for a high frequency a.c. measurement such as that of the small signal capacitance, whether or not the equilibrium analysis is applicable will depend on the frequency of the measurement and the rate of carrier rearrangement. Majority carriers can be easily removed from the bulk of the semiconductor with a time constant of the order of the dielectric relaxation time ($\sim 10^{-12}$ sec.), so the question is now reduced to whether or not minority carriers can be generated and/or transported at a sufficiently rapid rate to keep up with the variation in applied bias. This factor will be taken up in a later part of the discussion.

The small signal capacitance-voltage (C-V) characteristic of the MIS structure has been extensively used for the comparison of theory and

32

experiment. A qualitative description of the ideal MIS C-V curve is given here. The total capacitance of the structure is made up of the insulator capacitance, which is assumed to be constant, and a voltage dependent semiconductor capacitance. As has been mentioned earlier, in the accumulation mode electrons are drawn towards the surface of the semiconductor and the situation is comparable to that of a parallel plate capacitor. The total capacitance is thus equal to the insulator capacitance since the semiconductor bulk is neutral and not contributing any charge (Fig. 3.4)). In the depletion mode the space-charge region that is formed in the semiconductor contributes its own capacitance which is voltage dependent since the depletion width varies with voltage. Thus the total capacitance is that of the insulating film in series with the depletion capacitance. This results in a decrease in the total capacitance and, as more of the semiconductor gets depleted with increasing bias, a rapid reduction of the capacitance is observed. In Fig. 3.4 the depletion mode is featured by a sharp drop in capacitance giving rise to a steep C-V gradient which is typical for an ideal MIS structure. With bias greater than that for the onset of inversion, i.e. when the minority carriers (holes in this case) start accumulating at the surface, the situation depends on the measuring frequency. Consider first a small low frequency a.c. signal superimposed on the d.c. bias. If the measuring frequency is sufficiently low for the rate of minority carriers (holes) to keep up with the small signal variation, charge exchange with the inversion layer can occur. The accumulation of holes at the interface increases with voltage and the charge in the inversion layer effectively shields the depletion region from any increase in field. As the charge storage becomes dominated by the inversion layer the capacitance will approach that of the insulator (see curve (a) in Fig. 3.4). On the other hand, if the frequency is high the hole generation cannot follow the varying signal and charge exchange with the inversion layer cannot occur. The capacitance
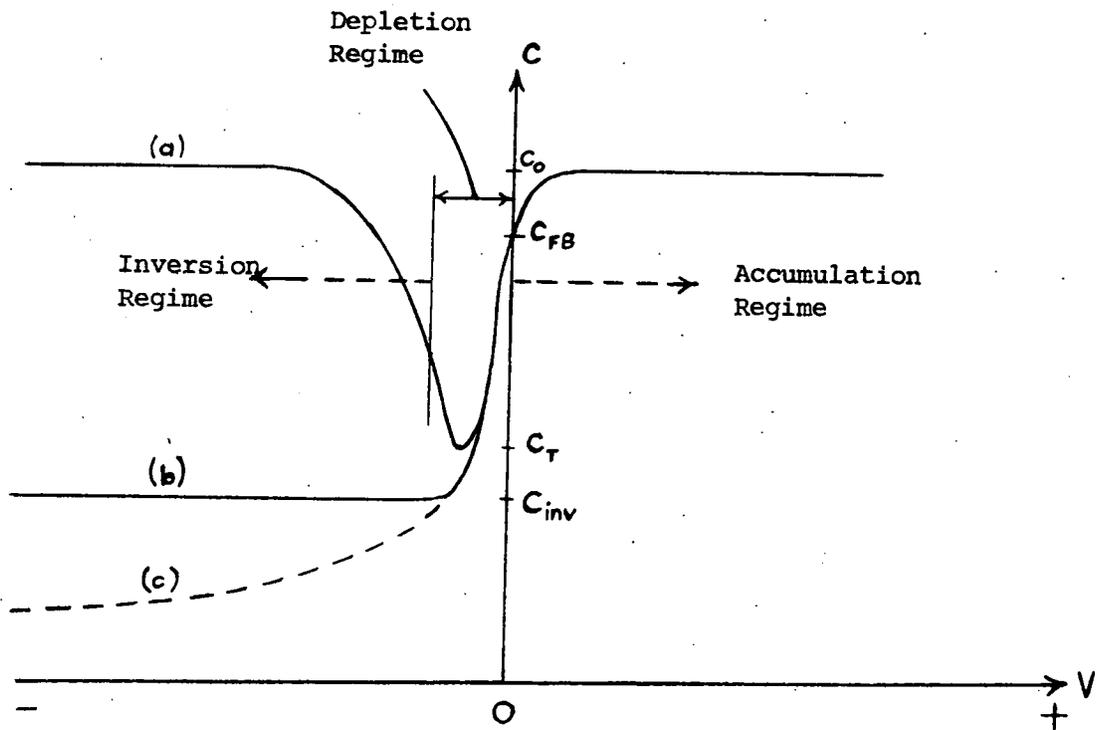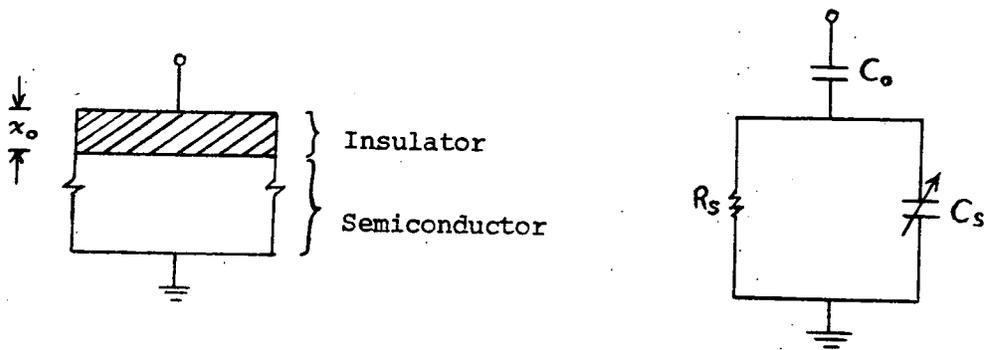
Figure 3.4:    The equivalent circuit and theoretical capacitance-
voltage relationship for an ideal MIS structure.

is then further reduced eventually becoming constant in what is known as the strong inversion situation (curve (b) in Fig. 3.4). Another condition which can occur is the deep-depletion mode, i.e. where the strong inversion case does not occur and the capacitance keeps on decreasing with increasing negative bias (curve (c) in Fig. 3.4). This occurs if the insulator becomes leaky or the device is switched rapidly from the accumulation into the inversion mode thus not allowing sufficient time for the generation of holes to form an inversion layer.

In the above discussion the space charge within the semiconductor is induced by the application of a bias between a metal and the semiconductor. However, such a space charge may also be induced by charges in surface states or by a work function difference between the metal and the semiconductor. Assuming the absence of an external voltage, the effect of a work function difference is to induce an electric dipole consisting of a surface charge in the metal at the metal-insulator interface and a space charge extending into the semiconductor near the insulator-semiconductor interface. In addition, the charge in the surface states will induce charges of opposite polarity in the metal and in the semiconductor. Both these effects tend to shift the C-V curves in the depletion region along the voltage-axis.

For the device in accumulation the insulator capacitance per unit area $C_o$ can be evaluated by the normal parallel plate capacitor expression. On the other hand, the depletion capacitance is more complicated because it is is the resultant of two capacitors, one being voltage-dependent. Taking into account the metal-semiconductor work-function difference $\phi_{ms}$ and the charge contribution from surface-states $Q_{ss}$, the normalized depletion capacitance for an n-type MIS structure is given by Grove et al (7) as

E

Surface                n-type semiconductor

$\phi_s$

$E_c$

$E_F$

$\phi_F$

$E_v$

x
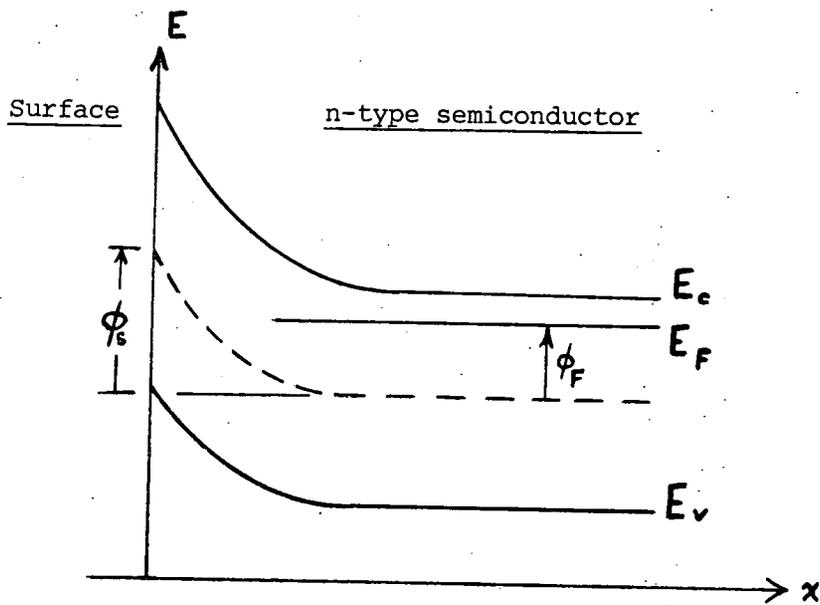
Figure 3.5:   Energy band diagram for the analysis of the
              surface charge and potential difference in
              a semiconductor.

Metal        Insulator        Semiconductor

$\rho(x)$

Volume charges
in insulator

x

Charge on
metal

Accumulation
layer
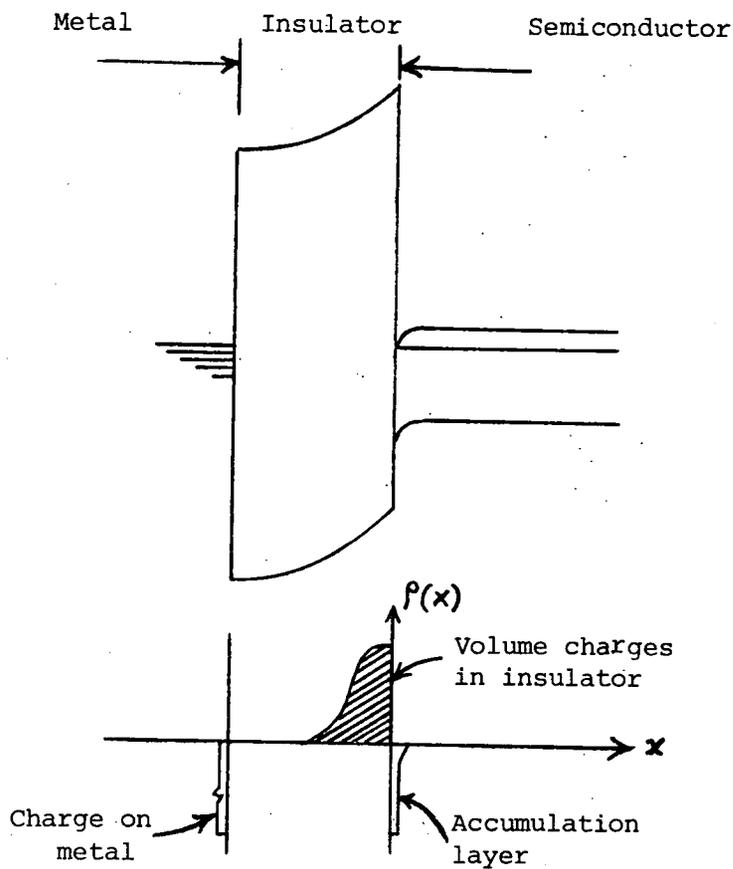
Figure 3.6:   Electrostatic potential and charge density
              for an MIS structure in the presence of
              positive insulator charge density adjacent
              to the insulator-semiconductor interface.

$$\frac{C}{C_o} = \left[ 1 - \frac{2\kappa_o^2 \, \varepsilon_o}{q \, N_D \, \kappa_s \, \chi_o^2} \left( V_G - \phi_{ms} + \frac{Q_{ss}}{C_o} \right) \right]^{-\frac{1}{2}} \qquad (3.6)$$

where

$V_G$ is the applied voltage

$\kappa_s$, $\kappa_o$ are the dielectric constants of the semiconductor and

insulator respectively, and

$\chi_o$ is the insulator thickness.

The metal-semiconductor work-function can be evaluated from the

equation

$$\phi_{ms} = \phi_m - \left( \chi + \frac{Eg}{2} - \phi_F \right) \qquad (3.7)$$

where     $\phi_m$ is the metal work-function,

$\chi$ is the semiconductor electron affinity while

Eg and $\phi_F$ are its band-gap and Fermi level respectively.

Equation (3.6) predicts a displacement of $(-\phi_{ms} + Q_{ss}/C_o)$ along

the voltage axis of a capacitance-voltage plot. By knowing the value of

$\phi_{ms}$ from equation (3.7), the charge of the surface states can be evaluated

from the displacement.

Inversion occurs when the surface potential of the semiconductor

is $\phi_s > \phi_F$ (Fig. 3.5). For strong inversion ($\phi_s \simeq 2\phi_F$), the minimum cap-

acitance per unit area as given by Cobbold (8) is

$$C_{min} = \left( \frac{q \, N_D \, \kappa_s \, \varepsilon_o}{4 \, |\phi_F|} \right)^{\frac{1}{2}} \qquad (3.8)$$

where     $\phi_F = Ei - Ef$.

Another important feature of an MIS structure is the flat-band

condition. This occurs when the bands in the semiconductor are forced to

straighten such that the semiconductor surface is at zero potential. The

corresponding capacitance of the system is known as the flat-band capacitance

and, if the insulator and semiconductor parameters are known, it can be evaluated from the expression given by Goetzberger and Sze (9) as

$$C_{FB} = (\kappa_o \varepsilon_o) \left[ x_o + \left( \frac{\kappa_o}{\kappa_s} \right) \left( \frac{kT \, \kappa_s \, \varepsilon_o}{q^2 \, N_D} \right)^{\frac{1}{2}} \right]^{-1}$$ (3.9)

For unknown insulator parameters, the flat-band capacitance can be deduced from the high frequency C-V curve (Lehovec (10)). If $C_o$ and $C_{min}$ are the measured accumulation and strong inversion capacitances respectively, then the normalized flat-band capacitance is

$$\frac{C_{FB}}{C_o} = 1 - \frac{(C_o - C_{min})}{\left[ 2\sqrt{\ln \frac{N_D}{n_i}} - 1 \right] \cdot C_{min} + C_o}$$ (3.10)

where      $n_i$ is the semiconductor intrinsic carrier concentration.

For silicon at room temperature, the expression in square brackets is approximated by Lehovec to a numerical value of 6 and this can be used in a crude approximation for deducing the flat-band capacitance. Otherwise if the donor concentration is known, the flat-band capacitance can be calculated accurately from equation (3.10). The significance of the flat-band capacitance is that it enables us to extract the experimental value of the flat-band voltage from the C-V curve. As described above, the value is the displacement, $( -\phi_{ms} + Q_{ss}/C_o )$.

In practice, the characteristics of MIS structures are usually found to deviate from the ideal discussed so far. Some of the most commonly encountered effects are summarized as follows:-

(a)      Charges in the insulator

Charges in insulators can be classified into two types. Firstly, there are fixed charges in the insulator bulk and/or in the vicinity of its

interfaces. These charges may be characteristic of the insulator itself or they may be due to the preparation technique. The second types are the mobile ionic charges which can come about from contamination. As can be seen from Fig. 3.6, the insulator charges induce further charge at the semiconductor surface (accumulation in this case). The built-in field due to bulk charges also bends the insulator bands as shown. This causes the flatband voltage to be shifted further on the voltage-axis by an amount depending on the net magnitude and polarity of the charges. A further change in the C-V curve is due to the movement of the insulator charge in an applied field. Since the ionic charges are heavy in comparison to electronic charges, they only move slowly and as a result hysteresis in C-V measurements is often encountered (7).

(b)    Lateral current flow

Surfaces having a permanent inversion layer due to charges in the insulator and/or on the surface can cause lateral current flow. Assuming the charges to be positive and the semiconductor p-type, an inversion layer can be induced in the semiconductor immediately underneath the insulator, including those not covered by the metal.

The effect is to form a depletion capacitance in an area much larger than that of the metal electrode which increases the semiconductor capacitance. Such an effect, known as the a.c. lateral current flow, is very much a function of frequency as described by Nicollian and Goetzberger (11).

(c)    Temperature and illumination

With the device displaying strong inversion, the high frequency characteristic can be forced to change to the low frequency type if there

is a sufficiently elevated temperature and/or illumination. Such external influences increase the carrier generation rate in the semiconductor bulk and facilitate the transition from high to low frequency behaviour.

## 3.5 Double-dielectric MIS Structures

A more complicated type of MIS system is formed by having two different insulators on a semiconductor, such a structure being known as the Metal-Insulator-Insulator-Semiconductor (MIIS) system. The physics of the semiconductor in this system is very similar to that of the MIS, but the insulators have to be treated differently, primarily because of the modification in the electrostatics. Studies on double-layered dielectrics have been widely performed on Metal-$Si_3N_4$-$SiO_2$-Si (MNOS) and Metal-$Al_2O_3$-$SiO_2$-Si (MAOS) structures; the importance lying in their ability to trap or empty electronic charges within the insulators. The introduction of extra charges alters the flat-band voltage and if included in an MIS-type transistor its switching voltage can be varied. This is the principle of one category of memory devices and Balk (12) in his review of this subject has pointed out some of the important physical features.

If an external voltage is applied to an MIIS system the field distribution in the films will be governed by their dielectric properties. For a charge-free system the field at the insulator-insulator interface is determined by the continuity of dielectric flux. If trapping centres exist within the insulators (either in the bulk or at the interface), the flow of currents in the individual insulator may be unequal leading to a build-up of charge. Assuming that the density of trapping states can sufficiently accommodate the built-up charge $Q_i$, the shift in flat-band voltage (compared to the charge-free case) can be expressed by

$$\Delta V_{FB} = - \frac{Q_i X}{\kappa \epsilon_o} \qquad (3.11)$$

38

where $\chi$, $\kappa$ are the thickness and dielectric constant of the outer insulator (nearest to metal).

In this case the trapping sites are assumed to be at the insulator-insulator interface but more generally one can include bulk trapping in the insulators. Apart from trapping effects, the shift in flat-band can also originate from other forms of charge contribution like the creation of surface-states by high fields or the polarization of mobile ions in the insulators. If all these factors are taken into account, the change in flat-band voltage can be a very complicated function of the dielectric properties, field and time, hence a more rigourous treatment is required rather than that of equation (3.11). Hu et al (13) have worked out qual-itatively the directions of hysteresis arising from electron/hole injection from the metal and/or semiconductor during the complete cycle of a C-V sweep of an MNOS structure. The model proposed assumes charge trapping and emptying processes occurring in the silicon nitride via a Poole-Frenkel conduction mechanism during the d.c. sweep. In another study on n-type MNOS structures, Jepperson et al (14) reported C-V shifts towards more negative flat-band voltages after subjecting devices to high fields in negative bias. The results are interpreted in terms of surface states created by the high field and charge injection into the nitride.

Full interpretation of the experimentally observed conduction behaviour in a MIIS system requires knowledge of its band structure. Since trapping states are common in wide band gap materials, the positions of these levels are important when assessing charge injection models. The metal-insulator barrier heights are equally important since they determine the mechanism of conduction from metal into insulator or vice versa. As has been mentioned earlier, the most important parameter of a MIIS system is the flat-band voltage. To observe the memory effects of such devices, a plot of the flat-band voltage against the constant d.c. stress voltage (for

a given time) can reveal hysteresis. Another useful feature is the charging time, i.e. the time needed to achieve a given flat-band shift when a constant d.c. voltage is applied to the device, which is important in determining whether charge can be retained indefinitely (see (15)).

REFERENCES

CHAPTER  3

1.  E H Rhoderick,  'Metal-Semiconductor Contacts',  Oxford  (1978)

2.  A G Milnes,  'Deep Impurities in Semiconductors',  John-Wiley  (1973)

3.  W Fahrner  and  A Goetzberger,  App. Phys. Letts.  21  329-331  (1972)

4.  L C Kimerling,  J. Appl. Phys.  45  1839-1845  (1974)

5.  C T Sah  and  V G K Reddi,  IEEE Trans. Elec. Dev.  ED-11  345-349  (1964)

6.  R Linder,  Bell. Syst. Tech. J.  41  803  (1962)

7.  A S Grove,  B E Deal,  E H Snow  and  C T Sah,  Sol. St. Elec.  8
       145-163  (1965)

8.  R S C Cobbald,  'Theory and Applications of Field-Effect Transistors'
       pp.181-230,  John-Wiley  (1970)

9.  A Goetzberger  and  S M Sze,  'Applied Solid State Science, Vol.1'
       ed. by R Wolfe,  Academic Press (1969)

10.  K Lehovec,  Sol. St. Elec.  11  135-137  (1968)

11.  E H Nicollian  and  A Goetzberger,  IEEE Trans. Elec. Dev.  ED-12
       108-117  (1965)

12.  P Balk, 'Solid State Devices 1973' p. 52    Institute of Physics
       Conference Series,  London

13.  S M Hu,  D R Kerr  and  L V Gregor,  App. Phys. Letts.  10  97-99  (1967)

14.  K O Jepperson  and  C M Svensson,  J. Appl. Phys.  48  2004-2014  (1977)

15.  P Balk  and  F Stephany,  J. Electrochem. Soc.  118  1634-1638  (1971)

# CHAPTER 4

## INVESTIGATION AND DISCUSSION OF TYPE-A WILLEMITE
### (Short Reaction Time)

### 4.1    Introduction

Edward's original work established that thin films of willemite ($Zn_2SiO_4$:Mn) could be formed on a silicon substrate by the conversion of a thermally grown silicon dioxide film, as described in Chapter 1.  It was shown that the willemite had high light emitting capability when bombarded with high energy electrons but that it only exhibited weak electroluminescence (EL) if a high field was applied across the film.  Edward's investigation showed the existence of mobile positive ions in his films, thus overriding other electrical properties.  Further work by Davies (1)   reduced this problem by having better control of the processing technique.  His results indicated that electron injection into the willemite was controlled by thin insulating films at the silicon-willemite interface, (possibly $SiO_2$) and/or at the willemite-aluminium interface, (possibly $Al_2O_3$, ZnO or unreacted $ZnF_2$). As a result of this, a post reaction etching process, i.e. the removal of unwanted constituents from the surface of the willemite, was introduced. Also, the aluminium is now always deposited in a far better vacuum system than in Davies' work.  The combined effect of these improvements in pro-cessing is that it is now believed that the outer insulating layer has been completely eliminated, enabling a direct connection to be made between the willemite film and the aluminium metallization.

However the insulating film between the willemite and the silicon is far more important.  This layer is known as a 'residual film' because it is still present after etching off the willemite in 10% glacial acetic acid.  The residual film is distinguished from the willemite by being non-luminescent and acid resistant.  It has a definite thickness, and refractive index and the investigation of its electrical properties is described in Section 4.4.

In earlier work by Errington (2) it was shown that the silicon-willemite interfacial film always exists even for willemite formed in nitrogen, and with a wide range of initial thicknesses of oxide and zinc fluoride.

It is the objective of this chapter to describe further investigations carried out on willemite films similar to those used earlier and now called Type-A Willemite. Chapters 5 and 6 will describe the investigation of rather different films called Type-B and C Willemite. The earlier sections of the present chapter describe the technique of preparation and examination of the films. Later sections are devoted to the electrical results obtained on the residual and composite films with some analysis. A discussion of the electrical properties of the composite willemite MIS-type structure as a whole is given in the last section of the chapter.

## 4.2 Preparation of Type-A Willemite

The general technique for processing silicon slices for fabricating the electrical test structures were described in Chapter 2. In addition to the electrical test slices, test chips (or control samples) were made at the same time. These measured 1.0 x 1.5 sq. mm, and were from the same type of silicon. They underwent similar treatment to the device slices but without photolithography. The test chips were used for optical examination and for thickness measurements of the initial oxide, composite, and residual films on the ellipsometer. Thermal oxide growth and zinc fluoride evaporation were carried out as in Section 2.3 and with precautions against contamination, especially in the oxide growth, carefully observed.

The most important features of Type-A willemite preparation are its reaction-bake conditions. As has been mentioned earlier, a special furnace was prepared, flushed with dry nitrogen and set at $1000^{\circ}$C. The reaction-bake

process was carried out for 20 min at atmospheric pressure, with an extra 2-3 min. allowed for the slices to reach peak temperature. Earlier, Errington (2) had experimented with different reaction times up to a maximum of 25 min, plus various oxide to fluoride thickness ratios. All his films showed cathodoluminescence but there were differences in the residual film thicknesses. The results were interpreted in terms of the ease with which zinc ions could penetrate the initial layer of willemite that was formed early in the reaction. During this later or transition stage, the dissolution of silicon oxide which is required for the reaction was thought to continue but at a decreasing rate due to crystallites of willemite acting as barriers. Davies (1) also discovered the existence of an insulating layer, possibly ZnO and unreacted $ZnF_2$, at the surface of the film and he used dilute ammonium fluoride to etch off this top layer. It was later realized by the author that since ZnO is not soluble in ammonium fluoride, a weak solution of 20% sodium hydroxide has to be used instead. The etch was followed by immediate washing and cleaning in flowing deionized water for 30 min. To avoid undercutting of the willemite, the etchant used after aluminium metallization was again a weak solution of sodium hydroxide rather than orthophosphoric acid which would normally be used. This is because willemite is easily attacked by most acids. To reduce ionic contamination, the metallisation etch was again done quickly with immediate washing.

Throughout the processing, strict precautions were observed regarding any likely sources of contamination. Washing and cleaning was always done with IPA or deionized water and the slices were handled only with special metal tweezers and stored in glass petri dishes. The photoresist treatment, fixing and developing were all carried out in a class 100 laminar flow bench, which further increases the cleanliness of the processing environment.

## 4.3    Film Examination

Examination of the films on the test chips was carried out using an ellipsometer, optical microscope and a scanning electron microscope (SEM). All the Type-A willemite films prepared revealed strong green cathodo-luminescence when bombarded with electrons in an evacuated pot.  The ellipsometer can measure the approximate thickness and refractive index of the films.  Composite films had refractive indices ranging from 1.68 to 1.72;  the variation being accounted for by changes in the relative thick-nesses of willemite to residual film and by the varying uniformity of the films.  For thin residual films (see Table 4.1), say less than 100 $\overset{\circ}{A}$, the refractive index is about 2.80, while thicker residual films (see Table 4.2) have values of around 1.50.  These values can be compared with those for the oxides of silicon;  1.46 for silicon dioxide and 2.20 for silicon monoxide.

Table 4.1 illustrates results for films prepared in the manner suggested by Errington  (2).   It can be seen that when the zinc fluoride film is much thicker than the oxide, relatively thick, easily etched top layer will result (clearly for the case of T1).  Presumably the suggestion by Davies (4.1) that one of the constituents of the  top layer is unreacted zinc fluoride may be possible.

Visual examination was done with the optical microscope.  The surface of the Type-A willemite always appears to be textured with pink or blue crystallites on a violet background.  It is not easy to decide whether the texture is a consequence of topographical or optical effects.  The grains of individual crystallites are readily observable at high magnification, with preferred nucleation of the crystallites occurring around regions of defects of impurities.  For reasonably large defects such as pin-holes, the nucleation gave rise to 'crater-like' features in the willemite films. These 'crater-like' features are made up of various different colours and

| Type of Film | T1 | T2 | T3 |
|---|---|---|---|
| Initial Oxide | 591 | 594 | 402 |
| Zinc fluoride | 1852 | 1053 | 1448 |
| Composite (without post-etch) | 928 | 905 | 628 |
| Composite (with post-etch) | 659 | 838 | 569 |
| Residual | 74 | 57 | 77 |
| Willemite | 605 | 781 | 492 |
| Top layer | 269 | 67 | 59 |

Table 4.1: Film thicknesses (in $\overset{o}{A}$) on test chips, T1, T2 and T3, for Type-A willemite based on Errington's recommended parameters. Time of bake is 20 mins, at $1000^{o}C$ temperature in atmospheric dry nitrogen.

| Experimental Slice | SL1 | SL4 | SL6 |
|---|---|---|---|
| Initial Oxide | 930 | 318 | 609 |
| Zinc fluoride | 663 | 197 | 553 |
| Composite (without post-etch) | 930 | – | 713 |
| Composite (with post-etch) | 920 | 861 | 694 |
| Residual | 376 | 636 | 342 |
| Willemite | 544 | 225 | 352 |
| Top layer | 10 | – | 19 |

Table 4.2: The film thicknesses (in $\overset{o}{A}$) for Type-A willemite as measured on three difference experimental slices.
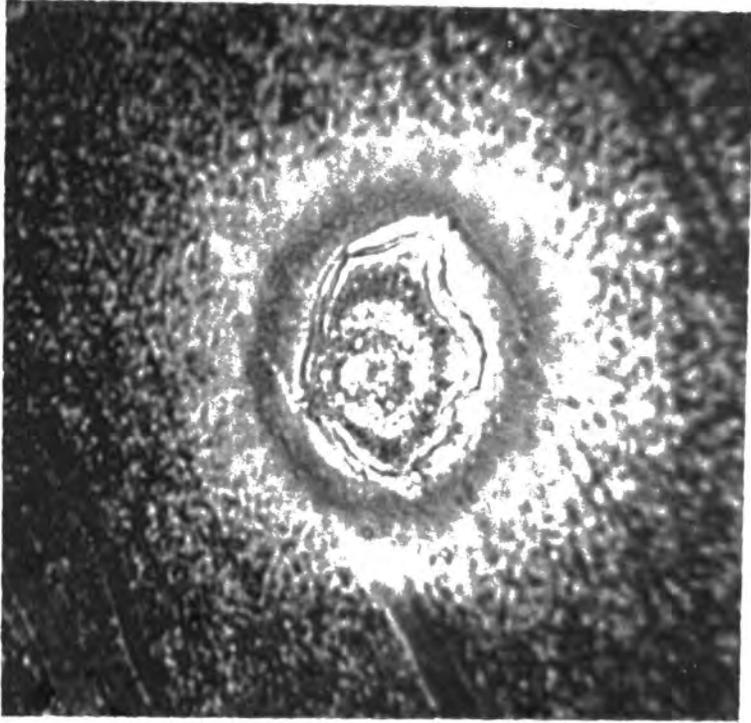
Plate 4.1

grain-sizes which are all well-arranged in a circular manner (see Plate 4.1). This feature may have been caused by tangential surface tension of the constituent materials around a defect centre when in the molten state. However, observations of the residual film did not reveal any related defects in the generally glassy-like appearance.

The SEM examination of both the composite and residual films was usually carried out in the secondary emission mode. The contrast obtained for the willemite is better than for the residual film since the latter tends to darken after a prolonged exposure. Even high magnification (capable of resolving to about 0.1 μm), and tilting the test chips to extremes, did not reveal any significant non-uniformity of the willemite surface, apart from the 'crater-like' features at defects. This indicates that overall, the willemite is uniform and the 'crater-like' features are actually bumps rather than dips.

Grooves were prepared in some composite films, by etching off the willemite along a narrow strip, for examining the edge between the willemite and the residual film. Unfortunately, even at high magnifications, there were no outstanding features that could be seen in the SEM, which may indicate that the change from the willemite to the residual film is gradual rather than a sharp edge.

Cathodoluminescent mode examination in the SEM showed positive results for the willemite films, but not for the residual films. However no other features could be seen in the cathodoluminescent mode.


## 4.4 Electrical Results for the Residual Film

The film thicknesses for Type-A willemite on the slices that were used in electrical measurements are shown in Table 4.2. It must be mentioned here that the residual film thickness was deliberately made much greater than the minimum suggested by Errington (Table 4.1). Very thin

films (less than 100 Å) are known to give rise to quantum mechanical tunnelling and if this is dominant other properties of the film may be masked. Residual film thicknesses for the electrical measurements are greater than 300 Å, well in excess of those for direct tunnelling to occur.

Capacitance and conductance measurements were carried out in ambient room light since no noticeable differences can be observed from those in the dark, but neverthless dc conduction measurements were made in the dark.

A typical capacitance/conductance-voltage characteristic of the residual film is shown in Figure 4.1. The measuring frequency was 100 kHz unless otherwise specified. In forward bias, i.e. when the metal polarity is made more positive with respect to the semiconductor, a slight increase in capacitance is observed which saturates between 60 and 90 mV at a value of Co = 111.14 pF. The value of Co is attributed to be the high frequency residual film capacitance and for a thickness of 341 Å over an area of $1.03 \times 10^{-3}$ cm$^2$ the dielectric constant of the film works out to be $\kappa_o$ = 4.17. For values greater than 90 mV there is a rapid drop in capacitance which is considered to be due to failure of the G-C-V plotter to measure capacitance in parallel with high conduction.

In reverse bias (metal made more negative than the semiconductor), the capacitance decreases quite rapidly up to - 0.52 V which will be shown in Section 4.4 to correspond with $V_{FB}$, followed by a more normal depletion-type characteristic for higher voltages. Correspondingly a rapid drop in conductance also occurs until, at a voltage of -0.20 V, it starts to rise again, achieving a peak conductance value of 2.33 µV close to the voltage $V_{FB}$. For voltages greater than $V_{FB}$ the conductance drops rapidly until at about -1.0 V and beyond, becomes virtually negligible.

Measurement at 1 kHz and at greater voltages than shown in Figure 4.1 reveals an increase in the conductance starting at -4.35 V, again rising
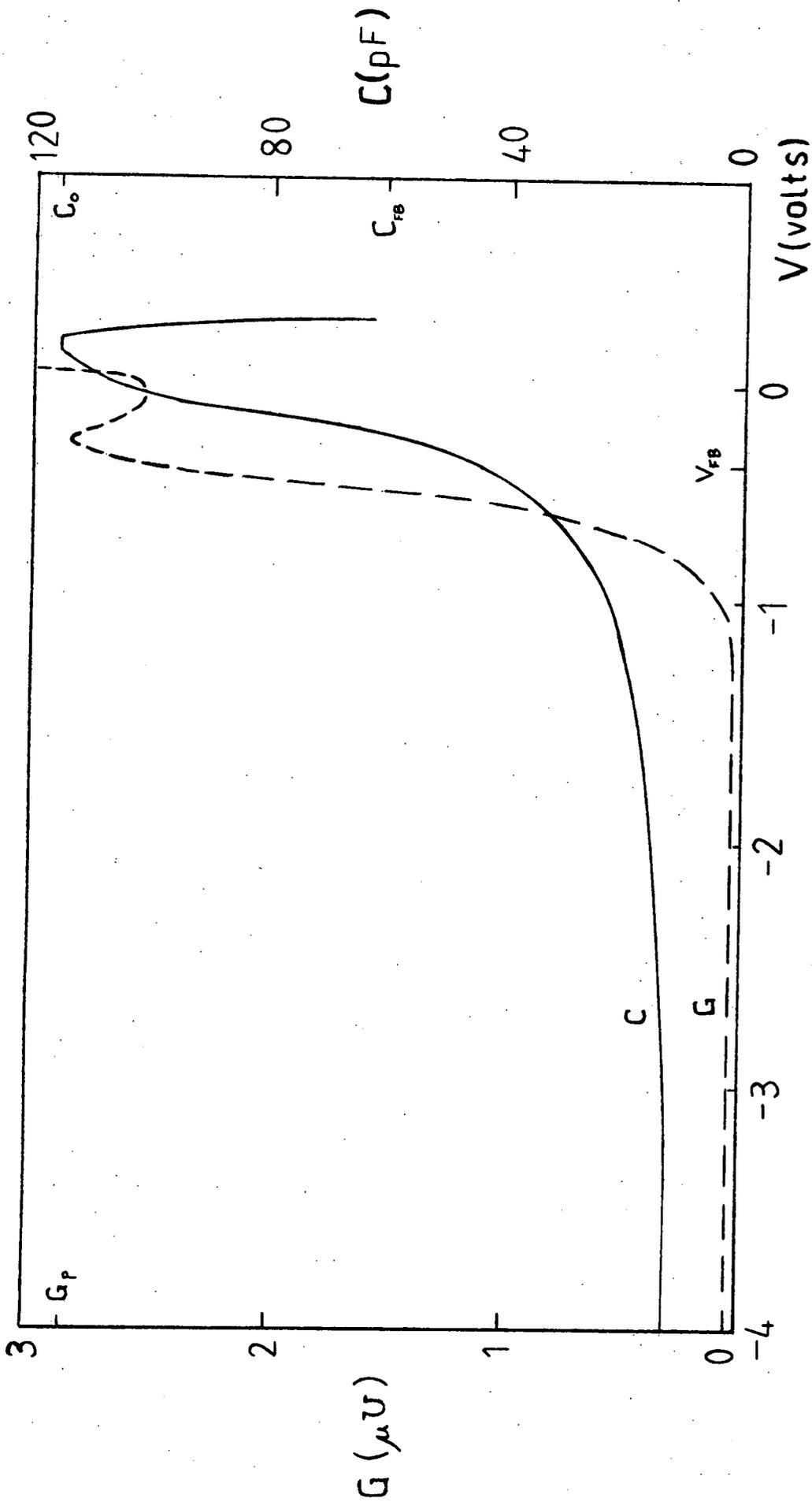
Figure 4.1: Capacitance/conductance vs voltage plot of a residual film.

$C_o$ = 116.7 pF, $C_{FB}$ = 59.3 pF and $G_p$ = 2.33 $\mu\mho$. Measuring frequency is 100 kHz, Ramp rate 35 mV/sec.
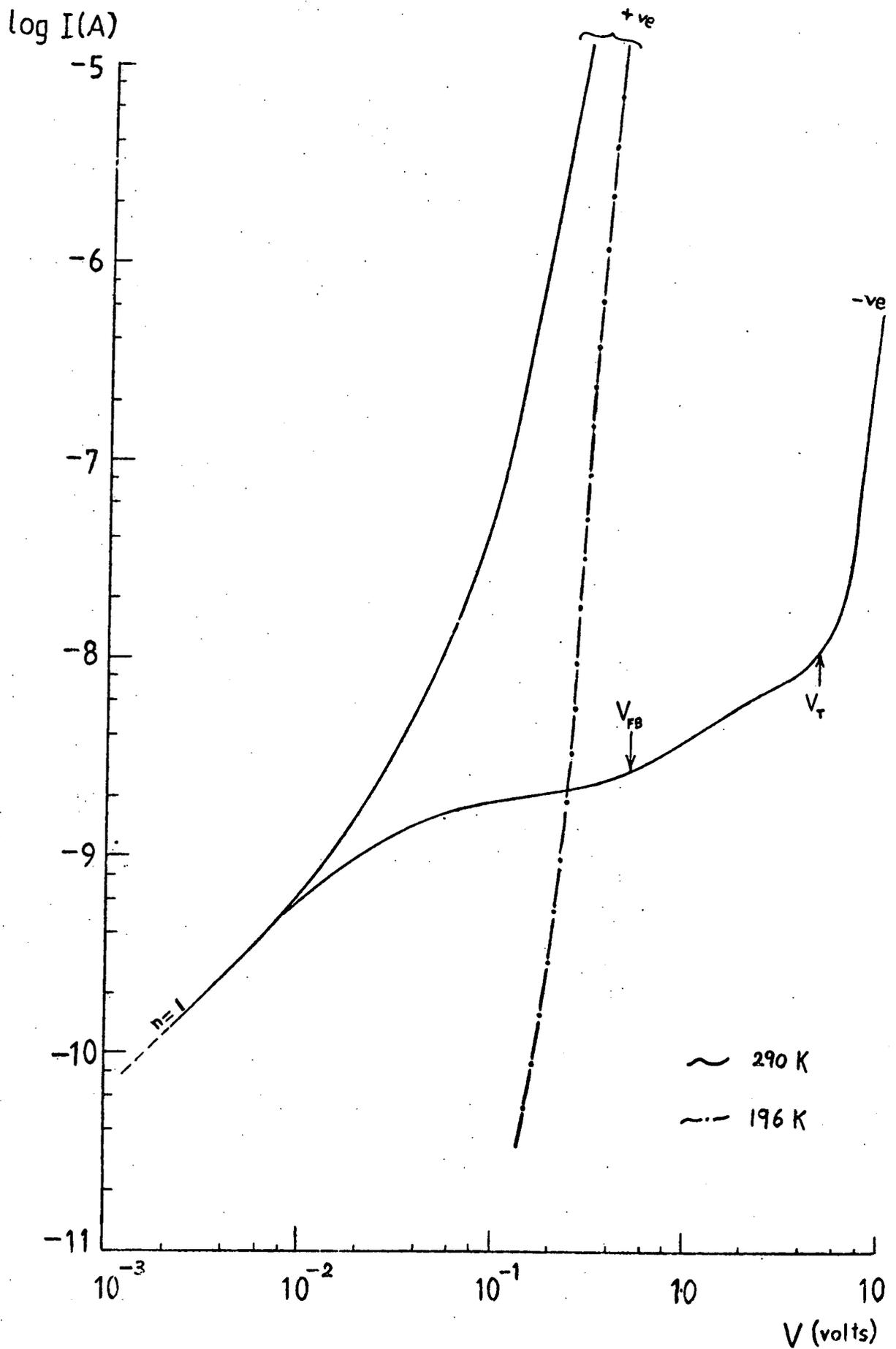
Figure 4.2: Current-voltage characteristic of the residual film for both positive and negative bias.

rapidly with further reverse bias. At 100 kHz this rise in conductance is not observed until the voltage is -7.75 V.

The dc conduction characteristic is shown in Figure 4.2 for both forward and reverse bias. At very small voltages (less than 10 mV) an ohmic relationship is observed in both directions of bias. Voltages greater than 10 mV give a rapid rise in the forward current leading to a strong power law relationship ($\log J \sim V^n$) from 100 mV onwards with a value of n = 6.8. In reverse bias the ohmic region is followed by a sublinear region up to -0.52 V and a more rapid rise from this voltage to -4.40 V. Beyond -4.40 V the current rises even more rapidly in a power-law relationship coinciding with the increase in conductance observed at 1 kHz.

Transforming the capacitance-voltage curve of Figure 4.1 on to a $1/C^2$ - V plot reveals a characteristic very different from that of a Schottky barrier (Figure 4.3). For reverse voltages, less than $V_{FB}$, $1/C^2$ appears constant for both high and low frequencies. With higher reverse voltages the $1/C^2$ plots fit two straight lines with changes of slopes occurring at -1.31 V and -1.55 V for the 1 kHz and 100 kHz curves respectively. The two curves diverge from one another as the reverse voltage is increased.

To try to explain the capacitance characteristics, some work was also done on the underlying silicon after the formation of the Type-A willemite. After the removal of both the willemite and the residual films with hydrofluoric acid etch, aluminium was deposited on the bare silicon to form a metal-semiconductor contact. A typical result for the $1/C^2$ - V for the resulting Schottky barrier is plotted in Figure 4.4. The experimental points are found to be much lower than the calculated curve for an ideal Schottky barrier (indicated by $N_T$ = 0) having the expected parameters of an area of 6.89 x $10^{-4}$ $cm^2$, a doping concentration

47
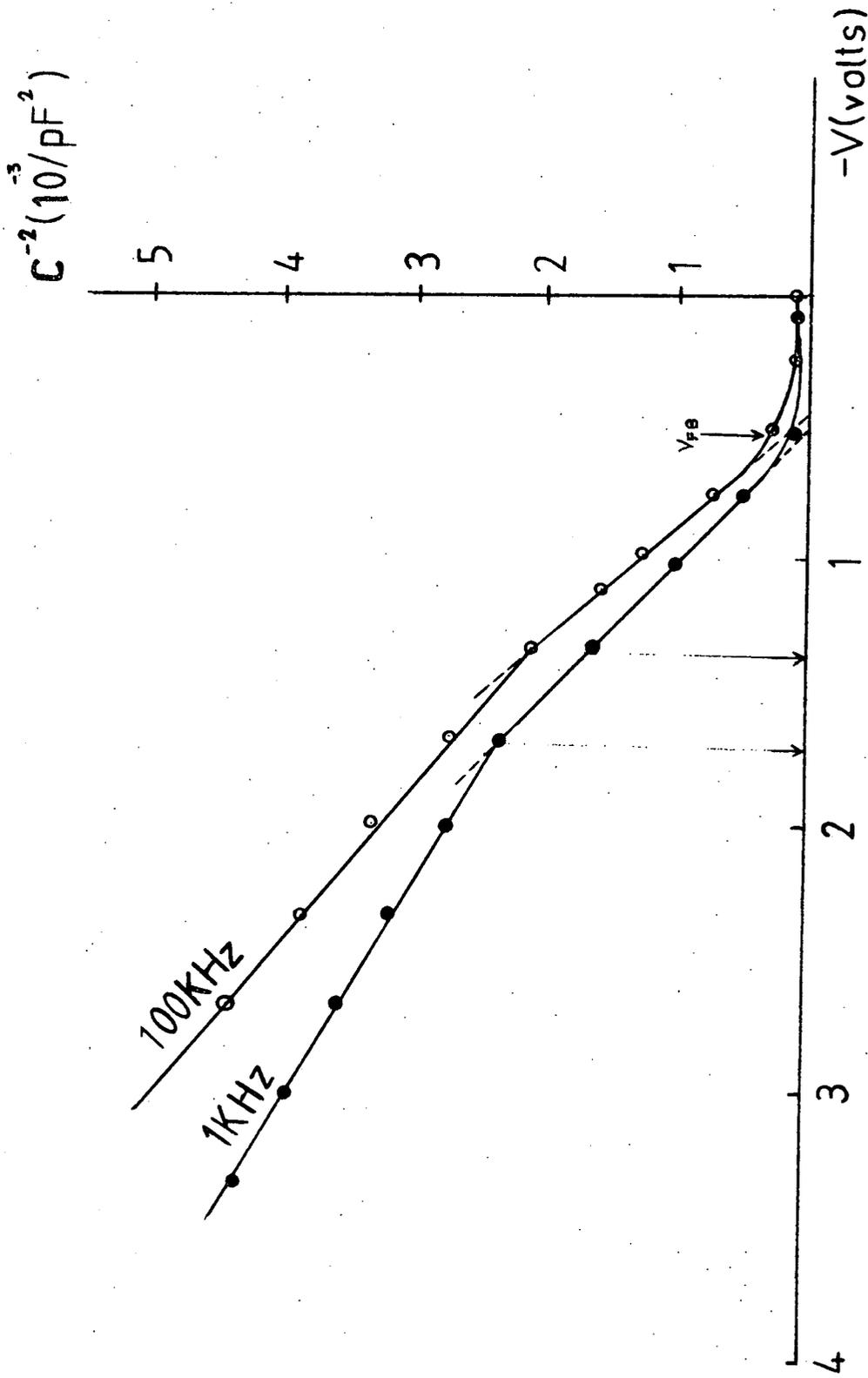
Figure 4.3: A $1/C^2$ vs V plot for a residual film at two different frequencies. Arrows on the voltage axis indicate the points of intersection of the slopes, -1.35 v for 100 kHz and -1.70 v for 1 kHz. $V_{FB}$ = -0.52 v.
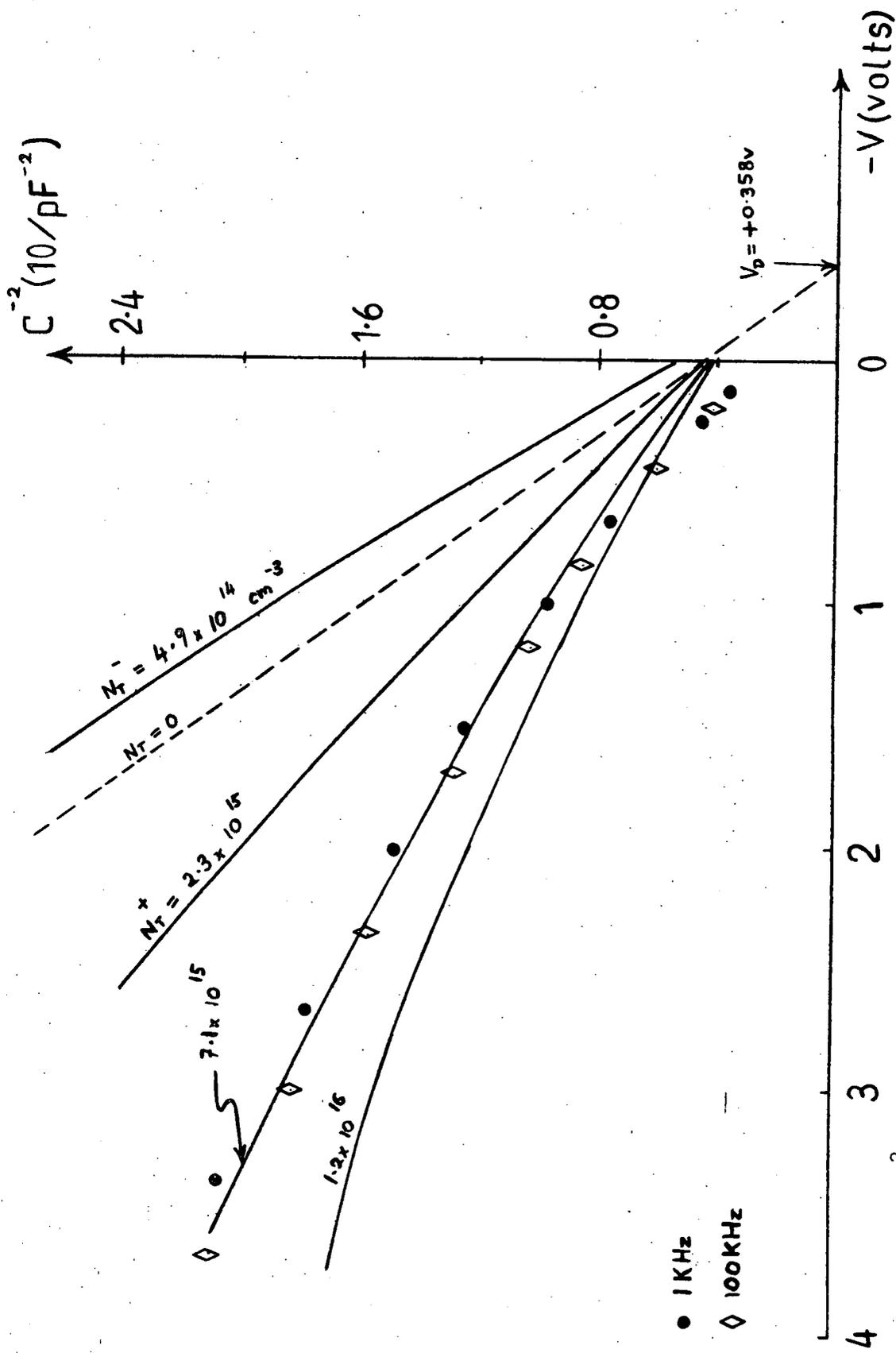
Figure 4.4: A $1/C^2$ vs V plot for Schottky barrier on the underlying silicon from Type-A willemite. Experimental points and theoretical curves. $N_T = 0$ curve is for ideal case. $N_T^+$ and $N_T^-$ are theoretical curves respectively for varying concentrations of donors and acceptors.

of $2.3 \times 10^{15}$ cm$^{-3}$ and a metal-semiconductor barrier height of 0.65 eV (Sze (5)). Assuming that the lack in agreement is due to contributions from deep-impurity trapping levels in the silicon, theoretical curves based on the Sah-Reddi Theory (see Section 3.3), were calculated for both donor and acceptor-type traps with varying uniform concentrations. The donor-type trapping curves (indicated by $N_T^+$) are calculated for a single manganese level at 0.53 eV above the valence band of the silicon using equation (A3.8) (from Appendix III), while the acceptor-type trapping curves (indicated by $N_T^-$) are for zinc at 0.55 eV from the conduction band using equation (3.5). It is seen from the experimental results that there is evidence of some considerable concentration of donor-type deep-impurities in the silicon since an acceptor-type level will yield curves above the ideal case. At low reverse voltages there is no deviation between the high and low frequency values of $1/C^2$ but at higher voltages the value for 1 kHz is higher than for 100 kHz.


## 4.5    Analysis of Residual Film Results

As mentioned in Section 4.2, the existence of the residual film after etching off the willemite has been confirmed by ellipsometric measurements, yielding thicknesses larger than 300 Å. It is necessary to deduce as much as possible about the properties of the structure from the electrical measurements described in Section 4.4. The characteristics are somewhat similar to those of a Schottky barrier with the possibility of the film being sufficiently conducting to form a Schottky barrier in the silicon. If this is so, the measured capacitance should then agree with that from Schottky barrier theory as given in Section 3.2. From the C-V results of Figure 4.1, the capacitance at zero voltage is well in excess of 100 pF, while the theoretically calculated value for a Schottky barrier in the same

silicon over the same area ($1.03 \times 10^{-3}$ cm$^2$) gives a capacitance of only about 10 pF which makes a simple Schottky barrier model unlikely.

Another possibility is that the film is insulating but with pinholes or other defects which enable Schottky barriers to form over small areas where the metallization and silicon effectively touch. If this were so the results would surely not be so reproducible over a large number of similar structures. Also the measured capacitance would be expected to be less than the theoretical value of 10 pF for the entire capacitor area, whereas it is much greater. With these discrepancies, it is quite clear that a Schottky barrier model for the residual film structure has to be discarded.

A third possibility is that the residual film is an insulator without gross defects so that we then have an MIS structure model where the maximum capacitance $C_o$, as in Figure 4.1, can be taken to be the high frequency capacitance of the film. This results in an effective dielectric constant $\kappa_o$ of 4.16 for a film 341 $\overset{o}{A}$ thick. For such a structure, the flat-band capacitance can be calculated from Sze (5) to be

$$C'_{FB} = \kappa_o \epsilon_o A \left[ d_o + \frac{\kappa_o}{\kappa_s} \left( \frac{kT \, \kappa_s \, \epsilon_o}{q^2 \, N_D} \right)^{\frac{1}{2}} \right]^{-1} \tag{4.1}$$

where $d_o$ is the film thickness,

$\kappa_s$ the dielectric constant of silicon,

A the capacitor area, and

$N_d$ the donor concentration, known from the resistivity of the silicon.

Using a value of $2.3 \times 10^{15}$ cm$^{-3}$ for $N_D$, $\kappa_s = 11.7$ and the rest of the parameters as quoted earlier, the calculated value of $C'_{FB}$ using equation (4.1), is 59.30 pF; corresponding to a flat-band voltage $V_{FB} = -0.52$ V. The total charge $Q_o$ present in the residual film can

then be calculated from the relationship

$$V_{FB} = \phi_{ms} - Q_o/C_o{'} \tag{4.2}$$

For aluminium and n-type silicon, $\phi_{ms}$ = -0.70 volts (5), which results in $Q_o$ = 2.7 x $10^{-9}$ C $cm^{-2}$ corresponding to an area density of positive charge of 1.7 x $10^{11}$ $cm^{-2}$. This indicates a high concentration of positive trapped charge so that any speculation about the band diagram of the residual film has to allow for band bending. Another consequence of the large positive charge is to draw electrons towards the semiconductor surface so accumulating it even in thermal equilibrium.

In accumulation the silicon can just be regarded as another electrode for the residual film where the carriers are readily supplied by the silicon (see Figure 4.5). Thus in such a situation the forward bias characteristics are primarily those of the residual film. In normal circumstances, the insulator in an MIS structure is regarded to be non-conducting and trap-free, but because of the high trapping centres in the residual film, appreciable conduction is assumed to take place via these centres. Further confirmation from ac conductivity measurements will shall be discussed later in this section. From the forward bias dc conduction curves of Figure 4.2 measured at room temperature, the threshold voltage at which the linear part of the curve begins is about 90 mV, coinciding with the voltage at which failure in capacitance measurement occurs. Such a power-law relationship, log I $\sim$ $V^n$, has been reported by Jonscher (6) for amorphous materials displaying a hopping conduction mechanism where the value of n can be anything between 6 and 14. The value of n from the linear part of the experimental curve at 290°K is 6.8. Below room temperature the power law is obeyed over a much wider range of current, about four orders of magnitude for the curve at 196°K.

**(a)**

C.B.

$E_F$

$E_T$

V.B.

$V > O$

$E_{FM}$

n-TYPE SILICON      RESIDUAL
                    FILM        METAL

**(b)**

C.B.

$E_F$

$E_T$

V.B.

$E_{FM}$

$V < O$
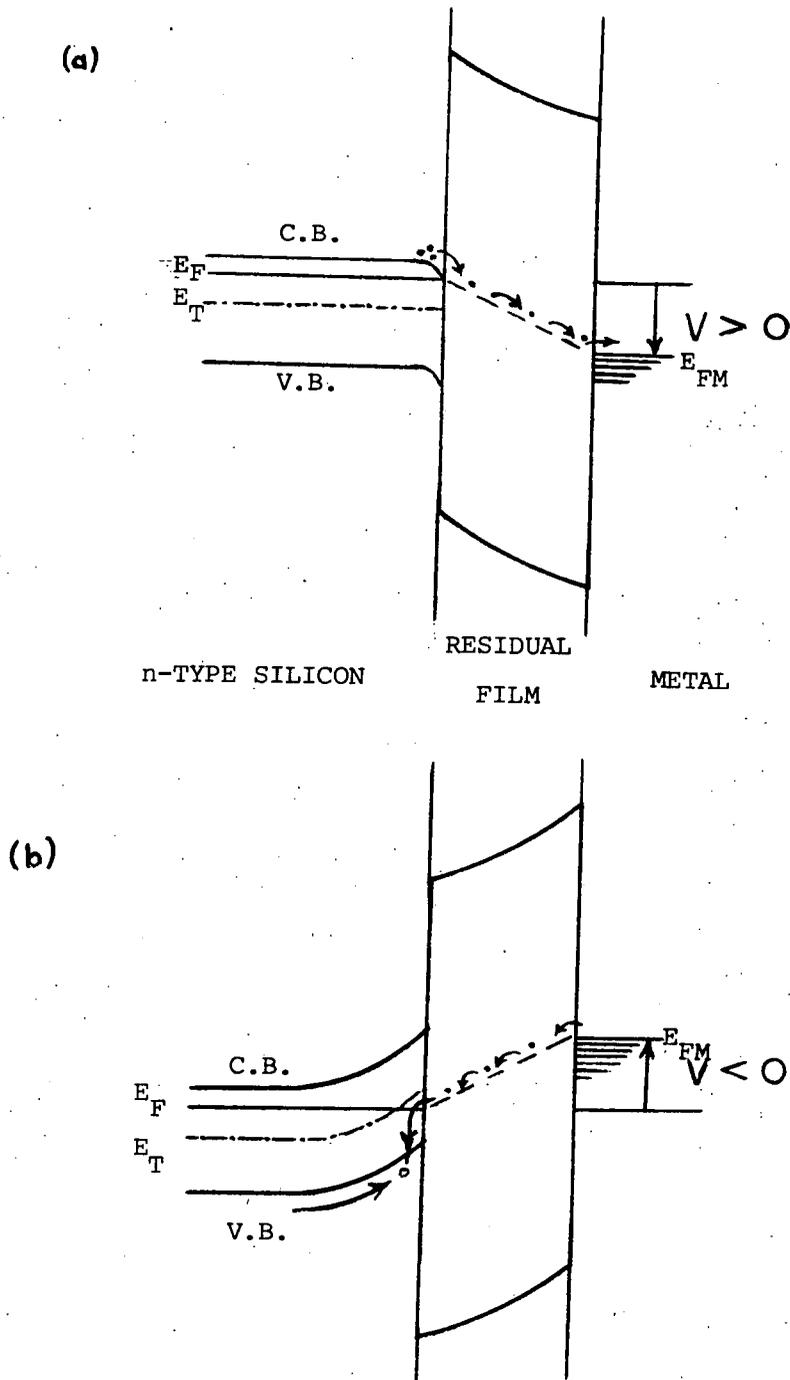
Figure 4.5: Proposed band diagrams for the residual film structure
(a) in accumulation, and (b) in deep-depletion.
Arrows within the film indicate the process of tunnel-
hopping. $E_F$ and $E_T$ are the Fermi-level and the deep
trapping levels in the silicon respectively. $E_{FM}$ is
the metal Fermi Level with respect to that when in
thermal equilibrium.
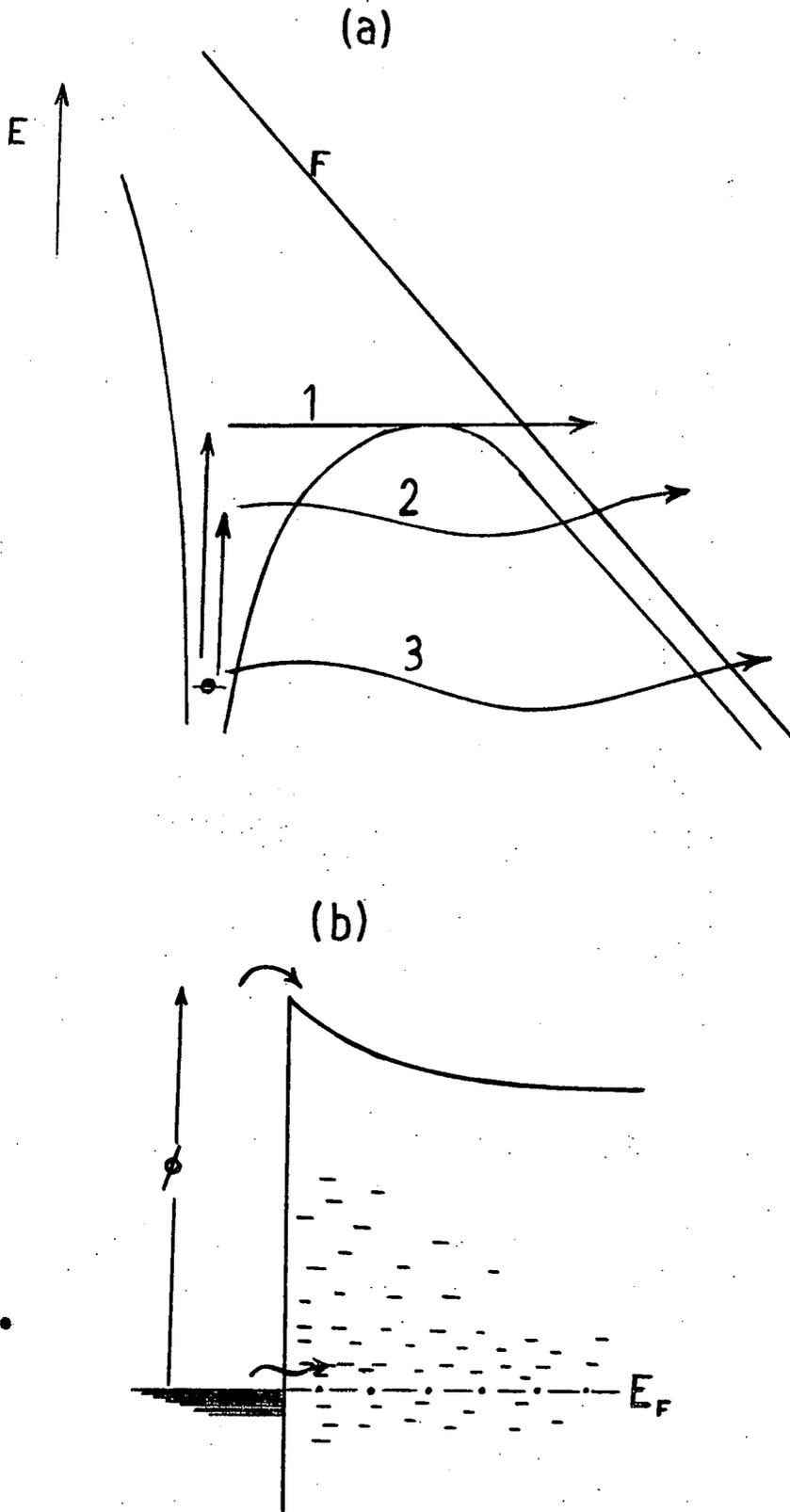
Figure 4.6: Mechanisms for hopping conduction after Jonscher
and Hill (7).

(a) High-field emission from a donor-type centre for
(i) thermal emission over a barrier, (ii) thermally
assisted tunnelling and (iii) pure tunnelling.

(b) Direct injection of electrons from metal into
localized states instead of surmounting the
barrier $\phi$.
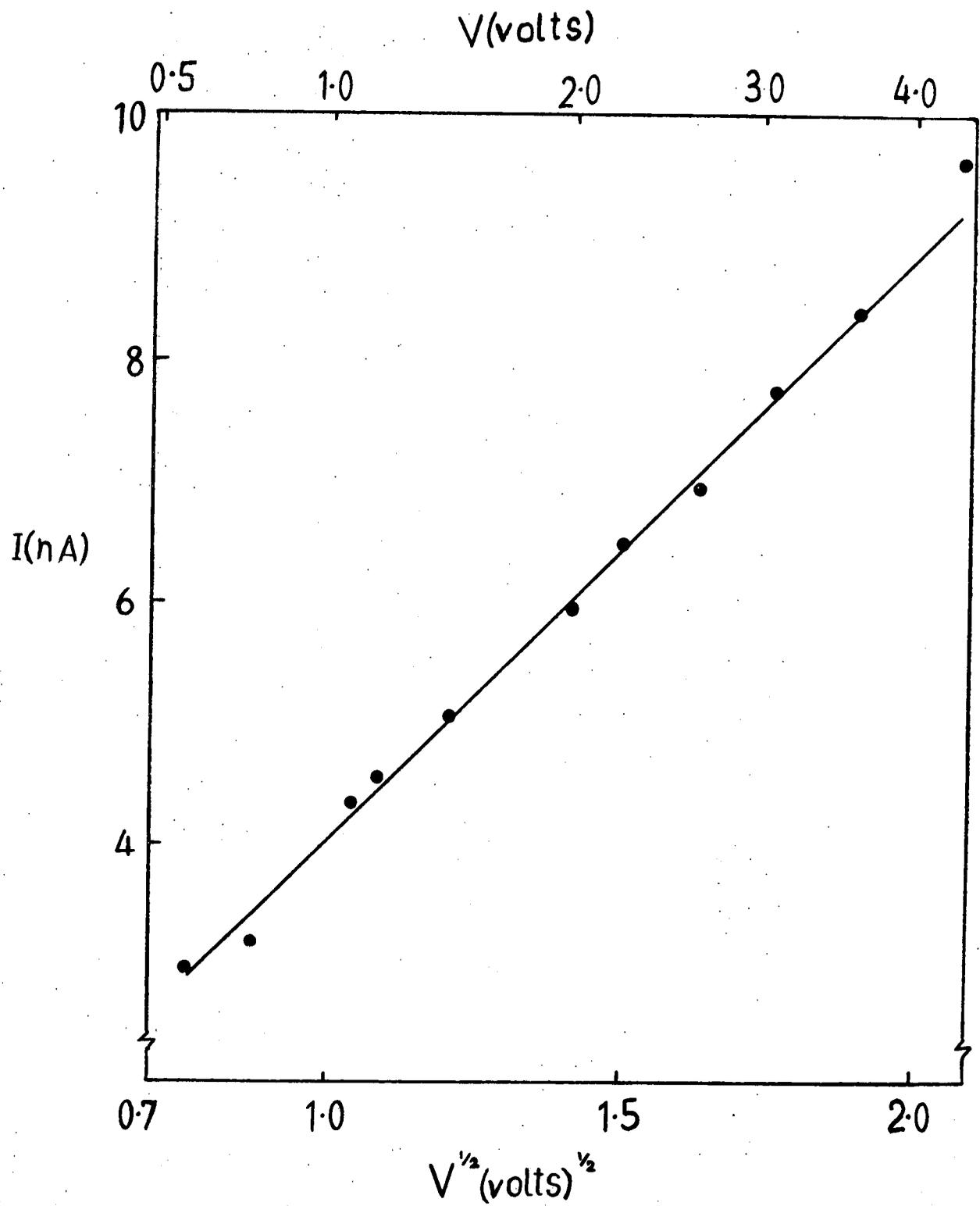
Figure 4.7: Plot of I vs $V^{\frac{1}{2}}$ for voltages between $V_{FB}$ and $V_{T}$ of Figure 4.2.

Furthermore, the activation energy of hopping conduction is reported to be very low ($\sim 10^{-2}$ eV) (6) since conduction takes place between localized energy levels close to the Fermi level rather than the free-carrier bands (7). The onset of high field hopping conduction is found by Jonscher (8) to be about $2.5 \times 10^4$ V/cm and this is comparable to the field of $2.6 \times 10^4$ V/cm at the threshold voltage of 90 mV for the power-law characteristic of the residual film. High field conduction can occur either by Poole-Frenkel excitation of carriers over potential barriers from localized states, or by thermally assisted tunnelling through the top of the field-lowered barriers (see Figure 4.6(a)).

Another feature reminiscent of hopping conduction is the dependence of ac conductivity on frequency, taking the form $\sigma \sim \omega^s$ where $0.8 < s < 1.1$ (6). For a voltage of -0.2 V, the ac conductivities measured at 1 kHz and 100 kHz give a value of s = 1.04. Because of the high density of localized states, direct conduction from the electrode into these states is likely (Fig 4.6(b) ) and further work by Jonscher (7) has established that the conduction is electrode independent. Work on silicon monoxide by Servini and Jonscher (9) and Klein and Lisak (10) has shown that conduction at high fields is a Poole-Frenkel hopping process between localized centres. Bearing in mind that the residual film is probably some combination of oxides of silicon, it is therefore very likely that the mechanism for conduction is by a hopping process.

In reverse bias, the ohmic region of the dc conduction is followed by a strong sublinear characteristic up to the flat-band voltage $V_{FB}$. Presumably this is due to electrons being prevented from getting into the semiconductor from the localized levels of the residual film by repulsion from the negative charge already present in the accumulated surface of the silicon. The repulsive behaviour gives rise to an increase in resistivity, hence explaining the drop in the slope of the log I vs log V plot.

Here, capacitance is mainly being contributed by the residual film (see Figure 4.1), but the drop in capacitance with further increase in reverse voltage is possibly attributed to the film becoming more conducting as field-assisted trapping conduction becomes dominant. For reverse voltages between $V_{FB}$ and $V_T$, the sub-linear characteristic still prevails but this time with an increase in current. When a plot of current against the square root of the applied voltage is made, the experimental points are found to follow a linear relationship (Figure 4.7). Here the field that is required to allow a large number of electrons to pass through the residual film has been surpassed so that most of the applied voltage is dropped across the silicon. With the silicon surface in depletion, holes generated in the bulk are swept towards the surface, recombining with electrons from the residual film in the vicinity of the surface. This leads to a 'recombination front' being formed in the semiconductor surface. In his theoretical model for such a phenomenon, Queisser (11) has indicated that it can give rise to a current of $I \sim V^{\frac{1}{2}}$ provided the dielectric relaxation time exceeds the minority-carrier lifetime. Such an effect is contrary to the conventional semiconductor physics case where the dielectric relaxation time is usually smaller. Similarly the generation process of holes in the bulk of the semiconductor can also be a current limiting factor. Since the width of the depletion region (i.e. the generation region) increases approximately as $V^{\frac{1}{2}}$ the current would be expected to vary with the square root of voltage (12).

The shape of the $1/C^2$ - V plot of the residual film and its frequency dependence (see Figure 4.3) suggests that there is not likely to be a simple relationship. Possible contributions towards the frequency dependence are from the residual film, the deep donor-type levels in the silicon and the electron-hole generation process in the bulk. At low

frequency less conduction is expected to occur via the hopping process in the residual film, which means that fewer electrons are available at the interface. On the other hand the low frequency allows more holes to be swept towards the surface. Similarly more of the deep donor-type traps can become ionized increasing the density of positive centres. The net result is an increase of the positive charge within the space-charge region which tends to increase the capacitance and explaining the lower values at 1 kHz compared with 100 kHz in the $1/C^2$ against V plot. Presumably the trapping centres play the more dominant role because if the electron and hole concentrations were drastically different (i.e. more holes than electrons) then accumulation of holes would occur and an inversion plateau should be observed in the capacitance characteristic. Since no inversion is observed the recombination rate must be too fast to be affected by the range of measurement frequencies used.

The 'knee' characteristic (i.e. the change in slope) in the $1/C^2$ - V curves can again be explained in terms of the role played by the donor-type traps. At flat-band voltage all the traps are filled and uncharged, but as the voltage becomes more negative a point is reached where the trapping level crosses the Fermi-level, beyond which the centres become ionised, leaving fixed, positive centres. From this cross-over voltage onwards the charge of the trapping centres will add to that of the donors in the semiconductor, effectively changing from a low to a higher net doping concentration. This is consistent with the change from a steep to a more gradual slope in the $1/C^2$ vs V plot.

If deep-levels are neglected then the theoretical value for the inversion capacitance, Sze (5), is given by

$$C'_{inv} = A \left( \frac{\kappa_s \, \epsilon_o \, q \, Nd}{4\chi_B} \right)^{\frac{1}{2}} \qquad (4.3)$$

53

where $\chi_B = |E_f - E_i|$ and the other symbols are the usual parameters. With $\chi_B = 0.357$ eV, $N_D = 2.3 \times 10^{15}$ cm$^{-3}$, A = $1.05 \times 10^{-3}$ cm$^2$, the calculated inversion capacitance is found to be 19.82 pF, which would be reached at a voltage of -1.54 V. This voltage would be less negative if deep donor-levels are taken into account. By coincidence the theoretical inversion voltage of -1.54 V is comparable to the voltage of -1.55 where the 1 kHz $1/C^2$ - V plot changes. By assuming the surface potential $\phi_s$ of the silicon to be approximately equal to the difference between this voltage and the flat-band voltage ($\phi_s \simeq |V_C - V_{FB}|$ ), the value of $\phi_s$ can be predicted. As in previous cases, it is assumed here that the applied voltage is dropped entirely across the silicon. From $V_C = -1.55$ V and $V_{FB} = -0.52$ V, we find that $\phi_s \simeq 1.03$ V. This is much larger than expected because $\phi_s$ should be equivalent to the difference between the silicon Fermi-level and the trapping level. Assuming that the trap-levels are at the intrinsic level, $\phi_s = |E_F - E_i| = 0.257$ V. As can be seen, the voltage for the change in slope is very much greater than this, which can possibly be explained as follows. When the trapping level crosses the Fermi level, at $\phi_s = 0.257$ V, electrons are expected to be released from the traps into the silicon conduction band such that the donor-type traps become positive. This situation may not arise because the released electrons are immediately replaced by electrons coming from the residual film. Such trap-filling and emptying processes are usually observed to depend on the time constant of the traps and measuring frequency.

The unexpected rise in dc current for voltages more than $V_T = -4.40$ V can be explained by the following. At these voltages, the semiconductor is forced into the deep-depletion mode with a lot of band bending near the interface. The high field at the interface can then lower the barrier

54

(possibly by image force lowering) as well as making the distance between the bands at the edge thin enough for tunnelling. Electrons from the localized levels in the residual film will then be able to pass directly into the silicon conduction band contributing to an increased current density. The ac conduction measurements at 1 kHz also show a sudden increase in conductivity from -4.40 V onwards, thus supporting the dc results.

From the discussion above it can be concluded that the electrical properties of the residual film can be satisfactorily explained by a modified MIS model. Since nothing is known about the energy bands of the residual film, a wide band-gap, comparable to that of silicon dioxide, with localized energy states at mid-gap has been assumed. As discussed in Section 4.2, the residual film is some form of an oxide of silicon, and its dielectric constant of 4.17 lies between the value of 3.9 for silicon dioxide and 5.0 for silicon monoxide which is consistent with the refractive index values. The discussion has led to a model of tunnel-hopping conduction through the residual film, rather than direct tunnelling. A similar model has been successfully used by Dubey et al (12) for explaining the properties of anodic oxide MOS structures. In the accumulation mode, Figure 4.5(a), the voltage drop is entirely across the residual film which virtually limits the current; the role of the silicon here is only that of an electrode. However in reverse bias, Figure 4.5(b), the silicon plays a more dominant role, being the current limiting factor over a wide range of voltage. Electrons from the metal, which can move easily by tunnel-hopping within the residual film, then face a recombination front in the semiconductor at the vicinity of the interface region. It appears that this model can provide a reasonable explanation for all the experimental results.

## 4.6    Electrical results for the Composite Films

Compared with the residual films the composite willemite films are far more insulating and the majority of the measurements are of the C-V characteristics.

The composite willemite MIS structures have very good MIS-type C-V characteristics, with strong inversion and accumulation and a reasonably steep slope in the depletion regime.  Figure 4.8 shows a typical example of such a characteristic from slice SL6 where the first half-cycle of the sweep is from positive to negative voltage starting at + 3.0 V.  The accumulation capacitance in the initial curve is $C_{max} = 87.7$ pF, which can be assumed to be the effective capacitance of the composite film itself.  Strong inversion occurs at a capacitance of 20.0 pF, which is in agreement with a calculated value of 19.8 pF using equation (3.8) with a donor concentration of $2.3 \times 10^{15}$ $cm^{-3}$.  The flat-band capacitance, as calculated from equation (3.10), gives $C_{FB} = 59.9$ pF, corresponding to an initial flat-band voltage of $V_{FB_0} = - 1.23$ V.  The depletion characteristic is as one would expect to find in typical practical MOS structures, but in this case the slope is less steep than the ideal curve.  The displacement of the C-V curve along the voltage-axis, resulting in a negative flat-band voltage, indicates the existence of positive charges within the film even initially.

An outstanding feature of the C-V characteristics of the composite film is the hysteresis observed when a complete cycle is measured.  After going into strong inversion up to -3.0 V in the forward sweep, the return sweep always has its onset voltage for inversion pulled towards a less negative value.  The gradient of the C-V curve is also reduced, stretching out the curve in the depletion region.  Therefore, with a maximum positive measuring voltage of +3.0 V, it is sometimes hard to tell whether accumulation will definitely occur, although there is always a tendency towards
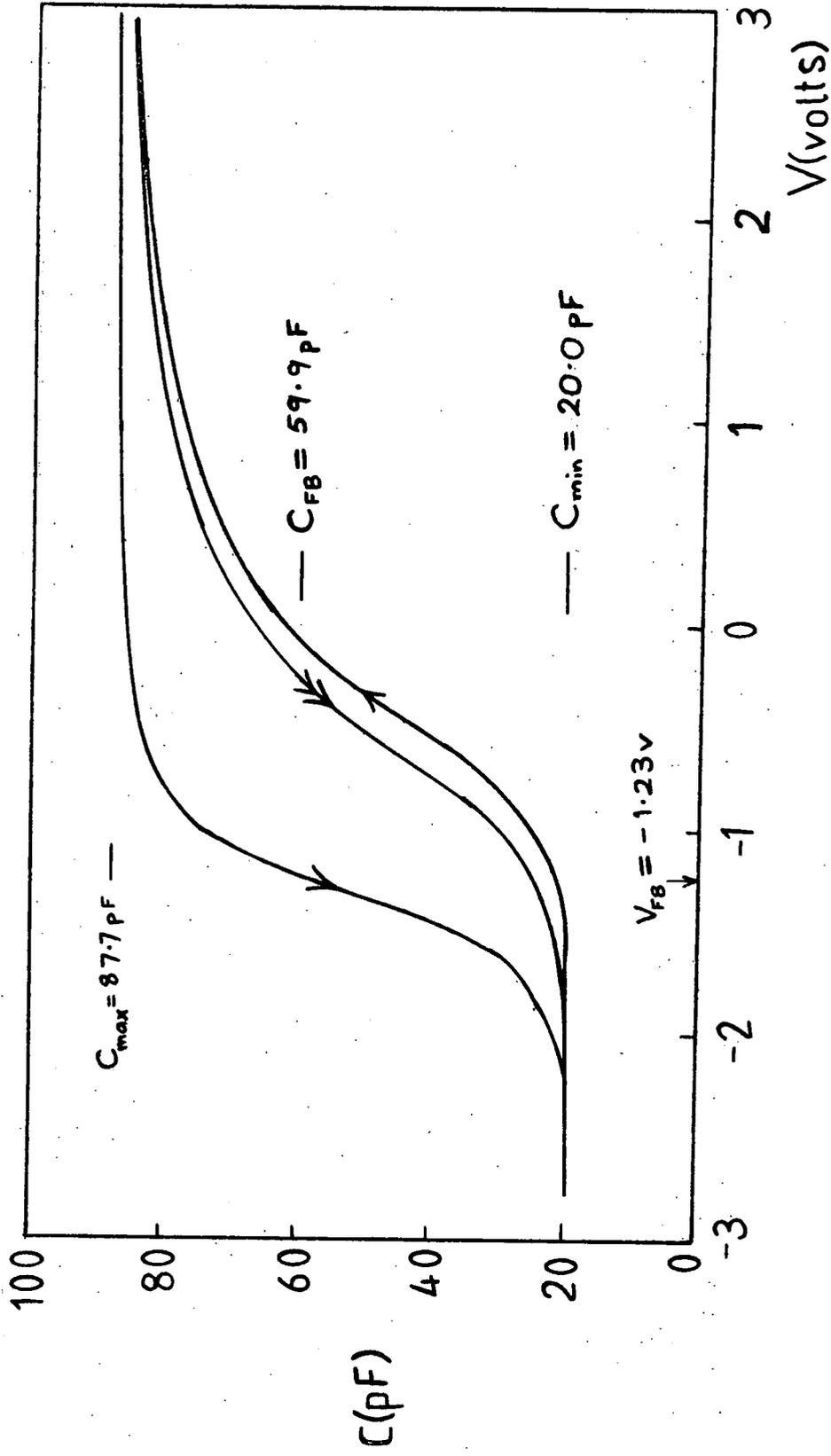
Figure 4.8: The capacitance-voltage characteristics of a composite willemite MIS structure Ramp voltage rate 26 mV/sec. Measuring frequency 100 kHz. The arrows show the direction of sweep starting from $V_G$ = +3.0 volts.
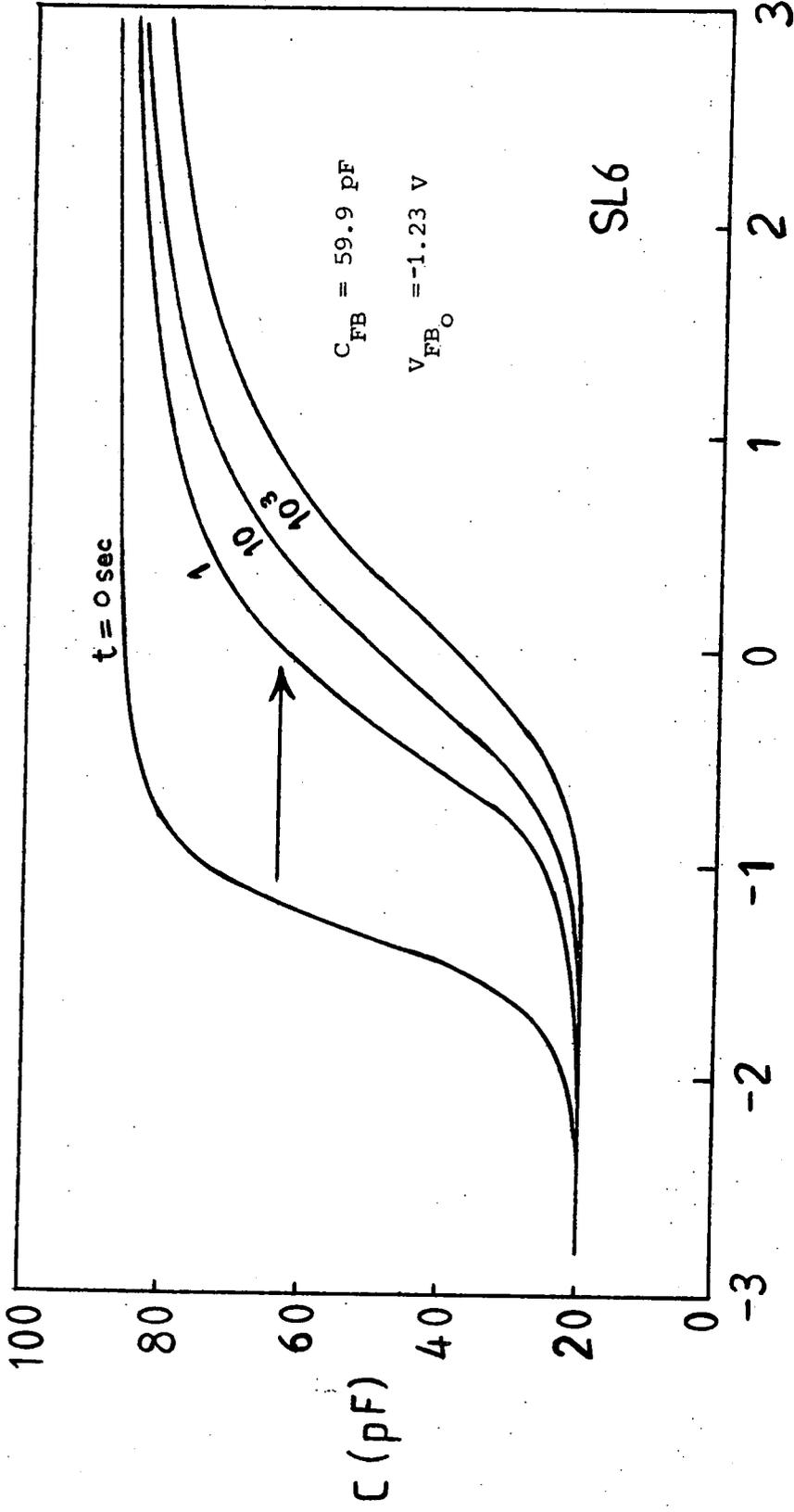
Figure 4.9: The C-V curves of a composite willemite MIS after different times of stress. Stress voltage $V_s$ is -4.0 volts. Arrow indicates direction of shift.

accumulation in the return sweep. The most conclusive point that can be made here is that there is always a shift in the flat-band voltage towards a less negative quantity following a negative bias sweep. In this case the shift arising from the hysteresis is about 1.12 V.

To help identify the cause of the shift, measurements for both directions of sweep voltage (i.e. positive to negative and vice versa) starting at different values of voltage bias were carried out on fresh structures. It was found out that positive sweep voltages do not give any shifts of the C-V curve, while those in the negative region have a large effect. The deduction that can be made from these observations is that a negative voltage has the effect of neutralizing positive charges and/or creating negative space-charge regions within the film.

The effect of the magnitude of the negative voltage on the C-V shift is more difficult to measure because of the ever-changing voltage during the sweep, making it complicated. For example, in Figure 4.8, the forward sweep C-V curve in the second cycle indicated by double arrows, is shifted slightly towards the left of the previous return sweep, showing that there is a small amount of recovery. Although the effect is small compared with the first hysteresis, the pattern of the C-V curves is similar to those arising from positive ions movements within the film as has been proposed by Grove et al (21) for MOS structures.

Figure 4.9 illustrates the change in the C-V curves when the sample was stressed with a voltage of -4.0 V for different durations of time. Measurements were carried out in the first cycle of the forward sweep from +3.0 V to -3.0 V. It should be noted that the possibility of even small negative measuring voltages contributing to the flat-band shifts cannot be totally omitted. For this reason the maximum negative measuring voltage was limited to -3.0 V which is less than the stress voltage of -4.0 V.

It can be seen that the largest change in the flat-band voltage occurs during the first second of the applied stress. This large change is followed by smaller shifts which gradually tend towards a saturation condition after a very long period of stresses. Simultaneously with the shift in the C-V curve is the reduction in the depletion region slope, implying some correlation between the three parameters.

A prolonged stress of -4.0 V for about $10^4$ sec eventually led to what is called the 'breakdown' in the MIS-type characteristic; as illustrated in Figure 4.10. The term 'breakdown' used here is not in the actual sense of a total dielectric breakdown, but rather the incapability of the structure from sustaining charge equilibrium. This phenomenon is identified by losses in strong inversion characteristic in the negative regime of measuring voltages and accumulation characteristics in the ~~positive~~ positive regime. (See curve (b) of Figure 4.10). At the onset of this phenomenon, there is still a tendency to inversion as illustrated by the existence of a plateau in curve (b). If further stressing is carried out the C-V characteristic will ultimately become that of the residual film, implying a loss in the insulating property of the overlying willemite film.

In order to study the variation of flat-band voltage with stress amplitude and stress time, a more careful procedure has to be followed. This is done by first finding the average flat-band capacitance, $C_{FB}$ for several composite structures. The C-V curve of a fresh structure was then measured for a small voltage range around the expected flat-band value. A constant dc negative voltage $V_S$, i.e. the stress voltage, was applied to the structures for a given time and the above measuring procedure repeated. For stress durations of less than 1 sec an Advance Instruments PG 58 Pulse Generator was used to apply the stress. By progressively increasing the time of the stress, the change in flat-band

58
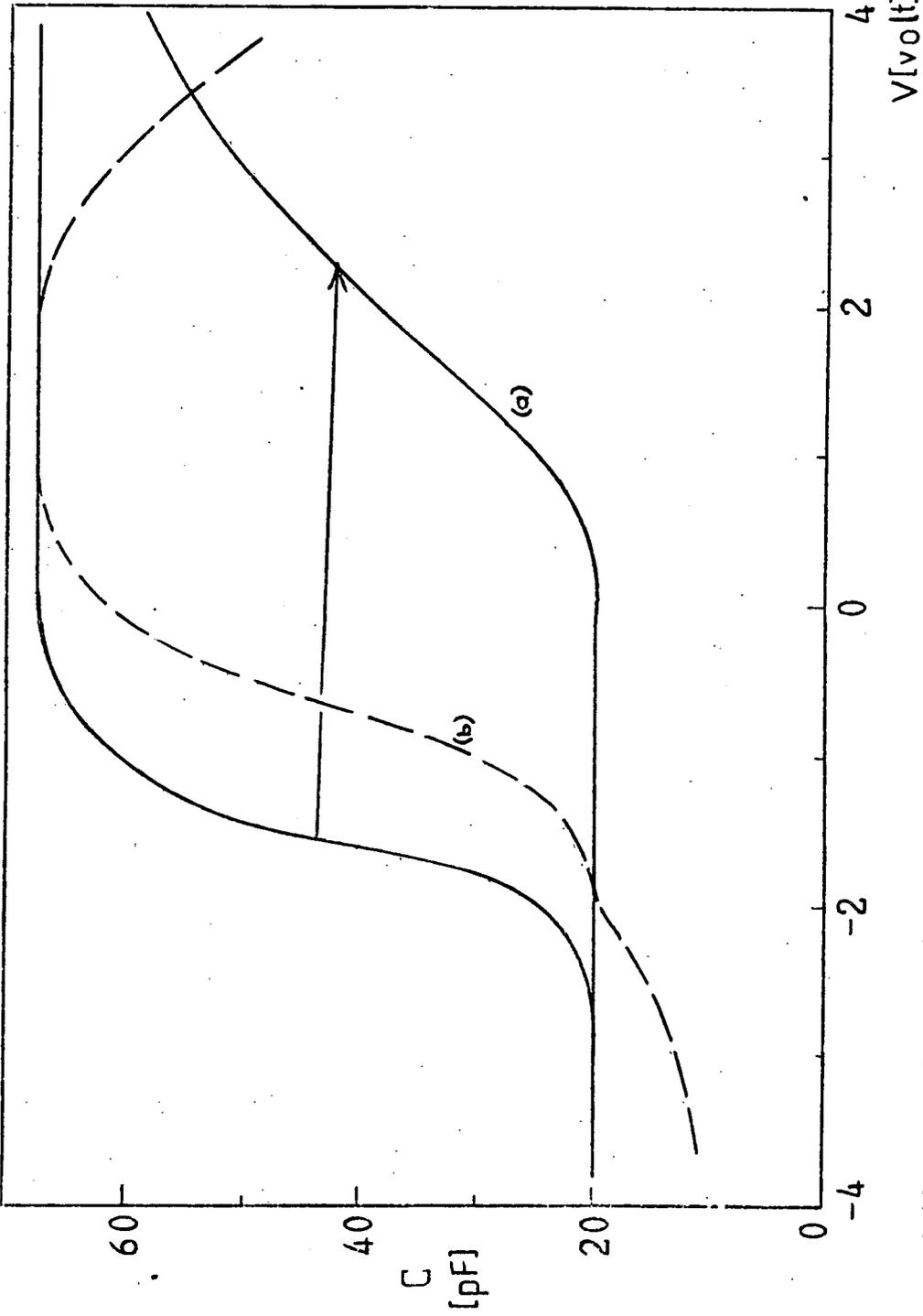
Figure 4.10: C-V characteristics of the composite film (a) after a long duration of stress, and (b) during the process of 'breakdown'. Note the loss in accumulation and inversion capability in curve (b) at high voltages.
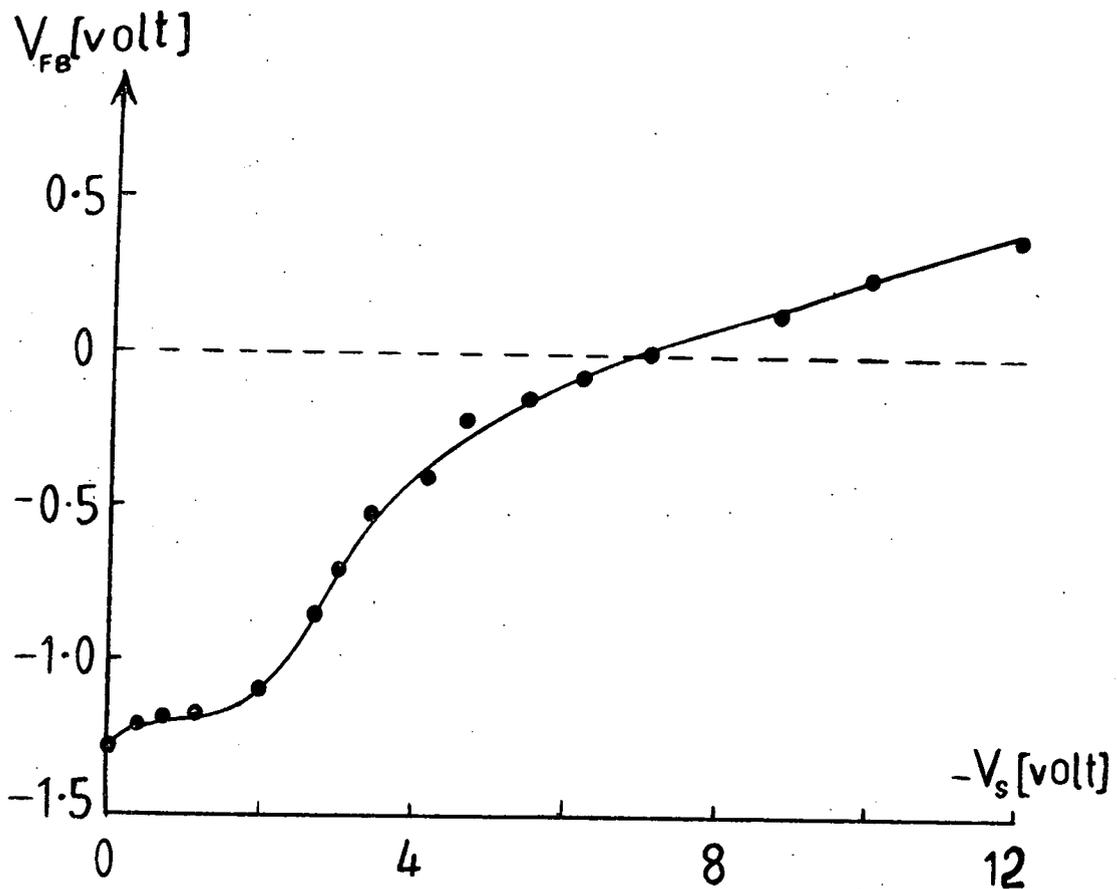
Figure 4.11:   Flat-band voltage vs. negative stress voltage.
Stress time, 1 sec.   Initial flat-band voltage
$V_{FB_o}$ = -1.27 v.
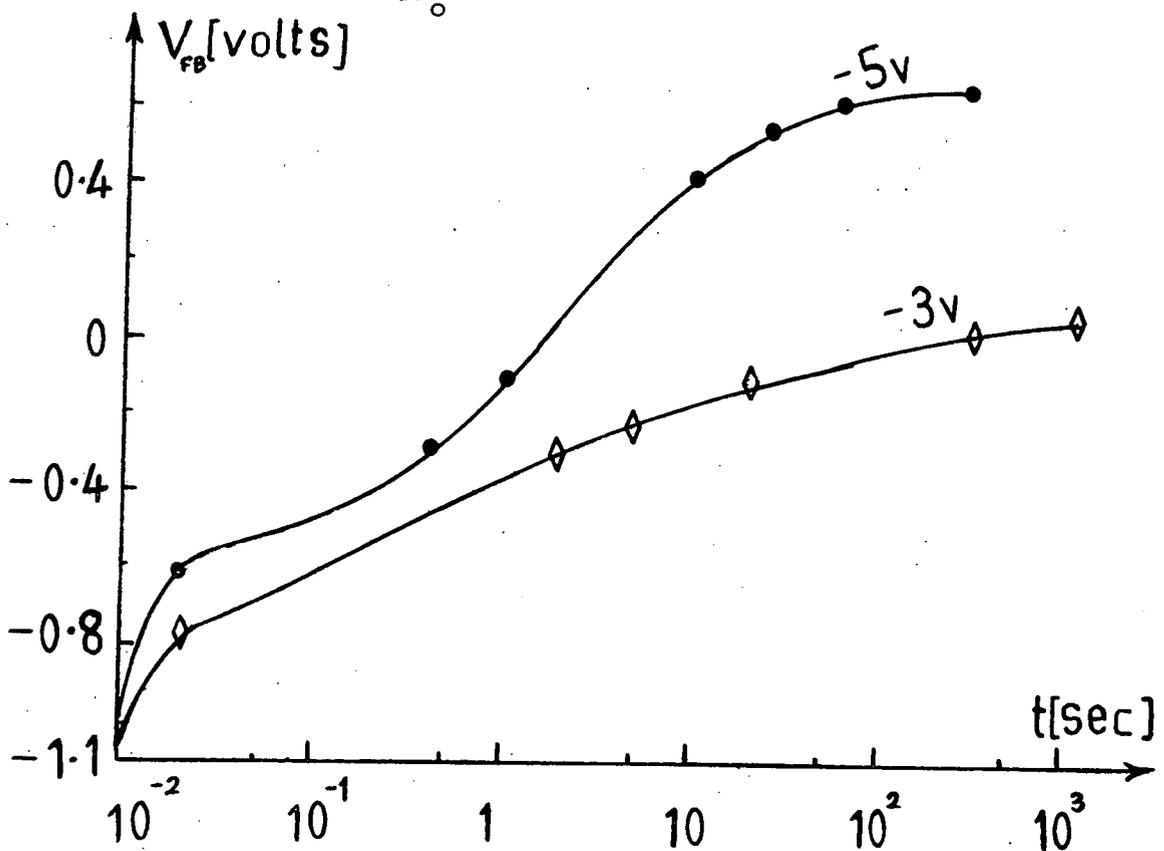


Figure 4.12:   Flat-band voltage vs. stress time for two
different stress voltages.

voltage with stress time was thus observed. In an alternative experiment the stress time was held constant while the stress voltage was varied. Although this method is not very accurate, it was also able to measure changes in flat-band voltage without much interference due to the C-V measuring voltage. Furthermore, it is sufficiently accurate as long as the stress voltage magnitude was kept higher than the initial flat-band voltage $V_{FB_O}$. Greater inaccuracy occurs for low stress voltages, i.e. values close to the initial flat-band voltage of about -1.27 V.

Results for the variation of flat-band voltage with stress voltage are given in Figure 4.11. Increasing negative dc voltages were applied consecutively to the composite structure for one sec with interruptions in between to carry out measurement of $V_{FB}$. The initial flat-band voltage $V_{FB_O}$ is at -1.27 V, implying the existence of positive charge already in the film. This is followed by a very small change in $V_{FB}$ for values of $V_s$ up to -1.70 V. Within this region of $V_s$ the change in flat-band voltage is slightly over 0.1 V, virtually a constant. From $V_s = -1.70$ V to about -3.80 V, there is a rapid change of flat-band voltage towards less negative values. Up to this point the value of $V_{FB}$ is still negative, indicating that the effective stress so far has not been able to alter the polarity of the net charge in the composite film, i.e. the film still contains net positive charge. The change in flat-band voltage over this region is about 0.85 V, giving an average slope of 0.4 for the gradient. Values of $V_s$ greater than -3.80 V yield progressively smaller changes in flat-band voltage, with an approximately linear relationship between the shift and the stress voltages. The change in flat-band voltage over 6.20 V of stress voltage is about 0.55 V, equivalent to a slope of 0.09 for the gradient. A polarity change from negative to positive in $V_{FB}$ occurs at $V_s = -7.0$ V, implying that stress voltage

above this value are capable of creating net negative charges within the film. The maximum amplitude of $V_s$ that can be applied before the C-V characteristic goes into 'breakdown' is -14.0 v.

Another important test that was carried out after a large negative stress had shifted the curve to a positive flat-band voltage value was to try to recover its initial negative flat-band voltage. The attempted recovery process was carried out by applying positive stress voltages. Although different magnitudes and durations of positive stressing were tried, there was only very slight recovery towards less positive flat-band voltages and the flat-band voltage could never be made negative after once being forced positive. Again the 'breakdown' phenomenon occurred if very high positive voltages were applied in the attempted recovery process. If the stressed sample was left for 24 hours an open-circuit recovery of about 0.2 V was observed which was again insufficient to make $V_{FB}$ return to a negative value.

As has been mentioned earlier, the shift in flat-band voltage is also a function of time as shown approximately in Figure 4.9. More accurate measurements were made using a technique similar to that for finding the effect of voltage stress. The value of $V_s$ was fixed while the structure was pulsed either manually or electronically for different durations of time. Flat-band voltage measurements were made after each pulse. Figure 4.12 shows the shift in $V_{FB}$ with time for two different stress magnitudes. The horizontal axis here is the true total stress time, i.e. the sum of the nominal stress times applied. It can be seen that for $V_s = -5.0$ V, a shorter time is required to achieve a given flat-band shift compared to $V_s = -3.0$ V, the difference being more remarkable for stress times in excess of 1 sec. It looks as if there is a tendency for the -5.0 V stress curve to saturate with time, and in fact for a stress

time of $10^4$ sec, the C-V curve goes into the typical 'breakdown' characteristic. Presumably this indicates that the net charge within the film has reached a maximum value, and that any further action in trying to add further charges is prevented by repulsion due to the internal built-in field arising from the space-charge already in existence. At the lower end of the logarithmic time-axis, though not shown in Figure 4.12, the flat-band shift for -5.0 V stress was also observed for times as short as a few microseconds, but for -3.0 V stress, the shift only started for times greater than 60 µs. Another point of interest is the time required to achieve a value of zero for the flat-band voltage. For a -5.0 V stress, this time is about 1.5 sec. but for a -3.0 V stress it is about 150 sec. This is a difference of two orders of magnitude in the stress time for a difference of only 2.0 V in the stress voltage. In other words, it takes about a hundred times longer to neutralize the positive space-charge within the composite film with a -3.0 V stress voltage than with -5.0 V.

Since results from C-V measurements have shown that the measurement itself may alter the electrical properties of the composite film, it was to be expected that the same problems would be encountered in dc conduction measurements. Nevertheless current measurements were carried out carefully with small increasing steps of voltage (a few millivolts) each applied for about half a minute. The purpose of the long measurement time was to observe if there is any fluctuation or decay in the current. The current characteristic for negative applied voltages is shown in Figure 4.13 from which it is seen that the current starts to be appreciable at around -1.10 V. This threshold voltage happens to coincide with the flat-band voltage $V_{FB}$ from C-V measurements, although it is slightly smaller. The current starts to saturate at around -1.70 V and
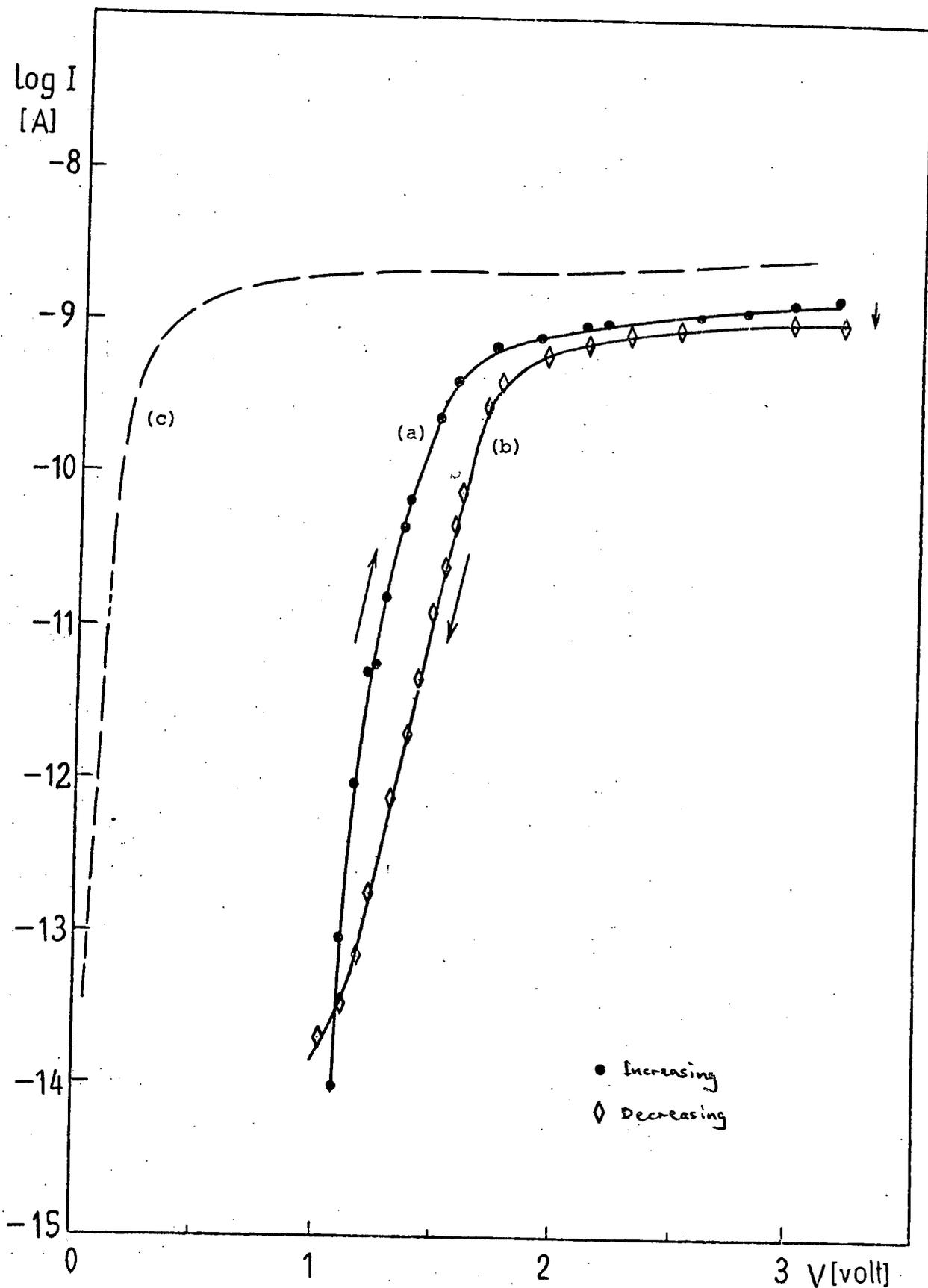
Figure 4.13:    Current-voltage characteristic of Type-A willemite
composite film with negative bias.   Arrows indicate
direction of current measurement, (a) increasing
and (b) decreasing.   Curve (c) resembles
characteristic of residual film.

| Experimental Slice | SL1 | SL6 |
|---|---|---|
| Composite, $d_T$ $(\overset{o}{A})$ | 920 | 693 |
| Residual Films, $d_o$ $(\overset{o}{A})$ | 376 | 341 |
| Willemite, $d_W$ $(\overset{o}{A})$ | 544 | 352 |
| $C_{max}$ (pF) | 68.0 | 87.7 |
| $C_{min}$ (pF) | 21.2 | 20.0 |
| $C_{FB}$ (pF) | 52.9 | 59.1 |
| $V_{FB_o}$ (volts) | -1.24 | -1.23 |

Table 4.3: Typical results of film thicknesses from two slices of Type-A willemite processed separately.

the saturation current is about $10^{-9}$ A. The voltage range over which the current saturates corresponds to the range of stress voltages which cause the dramatic changes in flat-band voltage in Figure 4.11.

Another feature to take notice of is the direction of changing voltage during the current measurement. In Figure 4.13, curve (a) is for measurements made with increasing negative voltages while curve (b) is for the return measurements with decreasing negative voltages. It can be seen that curve (b) is shifted towards the right of curve (a), implying that a higher voltage is required in the second case in order to achieve the same current (i.e. the current decays). If very high voltage stresses or prolonged measurements are carried out, the whole current-voltage characteristics of curve (b) are, however, shifted very much towards lower values in the voltage axis (curve (c) in Figure 4.11), with a slight increase in the saturation current also. This implies that the composite film is now more conducting, and in fact if measurements were carried out over a long time (a few hours), the conduction characteristic ultimately approaches that of the residual film. However, the direction of shifts along the voltage-axis leading to the 'breakdown' phenomenon in the C-V curve is opposite to the dc conduction case cited here. In the C-V case, the shift due to the effect of negative voltages is first positive going and then negative, followed by the 'breakdown' phenomenon (see Figure 4.10). Presumably the process leading to the 'breakdown' phenomenon found in the C-V characteristics corresponds to that of the I-V measuring process.

Conduction measurements with positive voltages are inconsistent but again there is a threshold voltage for appreciable current flow. However in this case the threshold voltage is found to be variable from 0.2 V onwards. Above the threshold the current rises very, very rapidly finally approaching the forward current characteristic of the residual

film.  It is possible that the consecutive application of positive
voltages for some time can cause the composite film to approach
'breakdown.'

## 4.7   Analysis of Composite Film Results

Table 4.3 presents film thicknesses and some of the capacitance
results for Type-A willemite composite film structures fabricated on dif-
ferent silicon slices.  The residual film thicknesses from both slices
are comparable but there is a difference of about 200 $\overset{o}{A}$ in the willemite
film thickness.  Values of the accumulation capacitance  are given in
the column headed $C_{max}$, and from these values and the thicknesses, the
effective dielectric constant of the composite film $\kappa_c$ is calculated
as 6.68 and 6.64 for slices SL1 and SL6 respectively.  Using a dielectric
constant value of 4.16 for the residual films, the respective dielectric
constant $\kappa_w$ of the willemite film for slices SL1 and SL6 is found to be
12.19 and 15.52.  These values are rather higher than might be expected.

The capacitance in strong inversion given by $C_{min}$ are comparable
for both slices and so are their initial flat-band voltages.  Such results
demonstrate the consistency in the properties of Type-A composite willemite
films prepared in the same manner at different times with the present
technique.  As has been mentioned previously, the negative value of the
initial flat-band voltage $V_{FB_o}$ indicates the existence of positive charges
within the composite film.  Calculations carried out using equation (4.2)
give a bulk charge density of $2.8 \times 10^{11}$ cm$^{-2}$ which surprisingly agrees
well with the bulk charge density of $1.7 \times 10^{11}$ cm$^{-2}$ for the residual
film, particularly as there is a scatter of about 0.2 V in the value of
$V_{FB_o}$.  This agreement shows that the positive charges in the composite
film  reside mainly in the residual film.  In other words, it appears

that the fresh film of willemite itself after processing and prior to any measurement is electrically neutral.

Hysteresis effects found in C-V measurements, as in Figure 4.8, and the flat-band voltage shifts with stress time, as in Figure 4.9, show that only negative voltages applied to the metal are responsible. There are two possible causes of the flat-band shifts in this direction Either (a) negative charges are being introduced into the films, or (b) there is movement of mobile positive charge in the films away from the silicon and towards the metal. Possible mechanisms for the shift can be categorized into two, namely electronic and ionic, and each possibly will be treated individually.

When a negative voltage is applied to the metal, the two electronic processes that can give rise to a negative space-charge are (i) the extraction of holes from the willemite into the metal, and (ii) the injection of electrons from the metal into the willemite. The discussion of the charge movement is here being confined to the metal and willemite only because a strong inversion characteristic in the C-V curve is always observed, thus ruling out any appreciable charge exchange between the silicon and the composite film. Considering that willemite is a wide band-gap material (Eg $\sim$ 5.5 eV), the concept of hole conduction and trapping within the forbidden gap is very dubious and Jonscher and Hill (7) have pointed out that hole processes can be ruled out for large gap materials. Hence the mechanism of hole extraction from the willemite into the metal ~~wille-mite~~ is not discussed. The plausible electronic mechanism that will be discussed here is, therefore, that of electron injection from the metal into the willemite.

The threshold voltage at which flat-band shifts become appreciable is -1.70 V and taking into account the voltage drop across the silicon

as well, the corresponding field across the composite film is approximately
1.7 x $10^5$ V/cm. If the mechanism of electron transfer in the willemite
is by Poole-Frenkel conduction the field that would normally be required
is about an order of magnitude higher than this. Electron injection has
been observed at a threshold field of 1.5 x $10^6$ V/cm for a MAOS structure
by Balk and Stephany (13) and at $10^6$ V/cm for a MNOS structure by Tsujide
et al (14). For the sake of argument, assume that the trapping centres
are donor-type with Fermi-level of the dielectric at mid-gap and that the
barrier height of the traps with respect to the metal Fermi-level is
0.5 eV. If the tunnelling distance through the forbidden gap is about
50 $\overset{O}{A}$, then for Poole-Frenkel conduction to take place the field has to be
about $10^6$ V/cm. Presumably such a mechanism is unlikely in view of the
fact that the measuring field in our case is much lower. An alternative
mechanism for electron injection into the willemite is by hopping conduc-
tion, involving the direct tunnelling of electrons between localized
states with energy levels situated around mid-gap. Although the field
required for this to occur is only moderate, about $10^4$ - $10^5$ V/cm, the
density of localized states has to be rather high, of the order of $10^{18}$ $cm^{-3}$
or more. Zinc silicate, being a glassy material, seems to be a good can-
didate for hopping conduction since a number of other glass materials have
been found to exhibit such a mechanism (15). Unfortunately, for moderate
field strengths, conduction by this mechanism is normally observed at low
temperatures (see Jonscher (7)). Therefore there is considerable doubt
as to whether the trapping of electrons in the willemite could account
for the flat-band shifts observed.

The second category for negative space-charge formation near the silicon is from ions. Positive and negative ion concentrations may be changed locally by the movement of mobile impurity species within the willemite, as occurs for sodium ions in aluminium oxide, see Abbott and Kamins (16), or by the polarization of the dielectric itself, as for phosphosilicate glass (Snow and Deal (17)). In most dielectrics, the mobile impurity species are positive ions often sodium, potassium or hydrogen. However, positive ion movement from impurity species can definitely be eliminated as the dominant feature here because, as has been discovered, the value of $V_{FB}$ can in fact be made positive with sufficient negative stress. If the effect of this stress was to draw positive impurity ions away from the silicon and towards the negative electrode of the metal, $V_{FB}$ would certainly become less and less negative, but it could never be made positive even if all the impurity ions are transferred to the metal-film interface in this way. On the other hand, if the impurity species are assumed to be negative then, with negative bias, they would be expected to be driven closer towards the silicon and resulting in a more positive $V_{FB}$ value as found. However, negative impurity ions would mean that the initial flat-band voltage value $V_{FB_o}$ would be positive which does not apply to this type of structure.

Abbott and Kamins (16) have found symmetry in C-V curves about the initial flat-band voltage when stresses of both polarities were applied to their $Al_2O_3$ composite films containing sodium impurities. For the willemite composite structure, the flat-band shifts are non-symmetrical about $V_{FB_o}$, and in fact there is no shift at all with positive stress voltage. Hence for all these reasons, movement of impurity ions cannot explain the experimental results, although small effects of positive ion movement can be detected from the slight hysteresis at the second cycle of the C-V curve as illustrated in Figure 4.8.

The second alternative, which seems more likely, is that the shift
in the C-V curve is due to the polarization of the willemite itself.  Such
polarization can lead to the formation of a space-charge within the com-
posite film which in turn induces charges of opposite polarity in the
semiconductor so shifting the flat-band voltage.  The two types of polar-
ization which may be possible here are due to molecular polarizability
and/or interfacial polarizability.  The former is due to the displacement
of positive and negative charge centres or the orientation of dipole
moments when a field is applied, while the latter is due to charge
accumulation at trapping centres or defects so as to induce an image charge
in the nearby electrode.  For the composite structure, if the polarization
phenomenon occurs in the willemite, it is difficult to choose between the
two mechanisms but by using the double-dielectric MIS-type structure model
suggested by Snow and Dumesnil (18), on whose analysis the following
discussion is based, a good understanding of the polarization phenomena
is possible.

The willemite film has been shown to be electrically neutral initially
but it is assumed to have a uniform concentration of N mobile cations each
with charge q compensated by an equal concentration of fixed anions with
charge $-q$.  Upon application of a negative voltage, the mobile cations
will drift towards the metal where they discharge or pile-up, leaving
behind a negative space charge of density $-qN$, near the willemite-residual
film interface.  The negative space-charge in the willemite will at first
compensate the positive centres present in the residual film but with
lengthened stress time and as the space-charge grows, all the positive
centres will become compensated for and extra positive charge will then
be induced in the semiconductor (holes and dopant ions in this case).
The effect can be seen in Figure 4.9 where the flat-band voltage reaches

67

a saturation with a positive value of $V_{FB}$ after a long duration of stress, indicating the existence of a net negative charge in the composite film. On the other hand, the positive space-charge layer being narrow and near the outer electrode, induces all its image charge in the metal. Figure 4.14 depicts the situation for the charge distribution, electric field and potential after achieving saturation in $V_{FB}$ with the stress voltage. By neglecting the charge $Q_O$ and using Poisson's equation, Snow and Dumesnil (18) derived the saturation voltage $\Delta V_{SAT}$ in terms of $V_s$ :-

$$\Delta V_{SAT} = -\left( \frac{\kappa_O}{\kappa_w} \frac{dw}{do} \right) V_s \tag{4.4}$$

where the value of N has been assumed to be very large ( $> 10^{19}$ cm$^{-3}$ ) With some algebra, equation (4.4) can be transformed to give $\Delta V_{SAT}$ in terms of the effective dielectric constant of the composite film $K_c$ and its thickness $d_c$, i.e.

$$\Delta V_{SAT} = -\left[ \frac{\kappa_O}{\kappa_c} \frac{dc}{do} - 1 \right] V_s \tag{4.5}$$

Figure 4.15 shows the experimental points for flat-band saturation voltage plotted against the stress voltage. The straight line drawn has a slope of 0.412. With $\kappa_O = 4.17$ derived from Section 4.4 and equating the slope factor to the square bracket term of equation (4.5), the value of $\kappa_c$ is found to be 6.0, which is comparable to $\kappa_c = 6.64$ as derived from the accumulation capacitance calculation. The discrepancy may be due to neglecting $Q_O$ in the derivation of equation (4.5). Another possibility is that whereas the line drawn in Figure 4.15 passes through the origin, the experimental measurements show a threshold voltage at -1.70 V below which there is little change of $V_{FB}$. Another factor is that the voltage drop across the silicon itself has also been neglected.

SILICON    RESIDUAL    WILLEMITE        METAL
           FILM

$Q_s$

$Q_o$

$-Q_w$

$x$ ←

$d$

$Q_w = -N_q d$

$Q_G$

$d_o$    $d_w$

$P$

$E$

$x$ ←

$\dfrac{Q_w}{K_w \mathcal{E}_o}$

$V$

$x$ ←

$V_s$
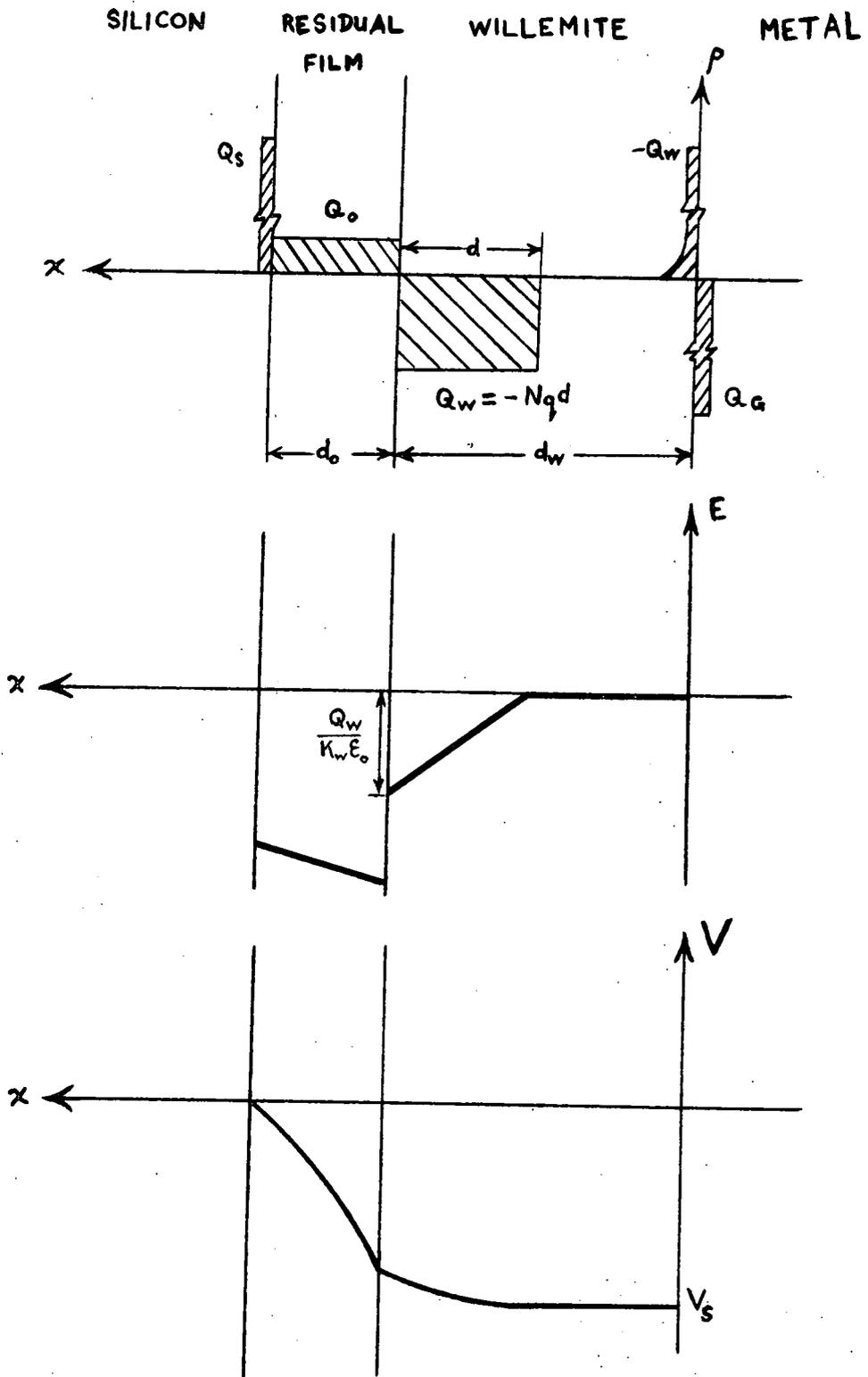
Figure 4.14:    The proposed charge, electric field and potential
                distributions with application of a stress voltage
                $V_s < 0$ sufficient to achieve a saturation in
                polarization.
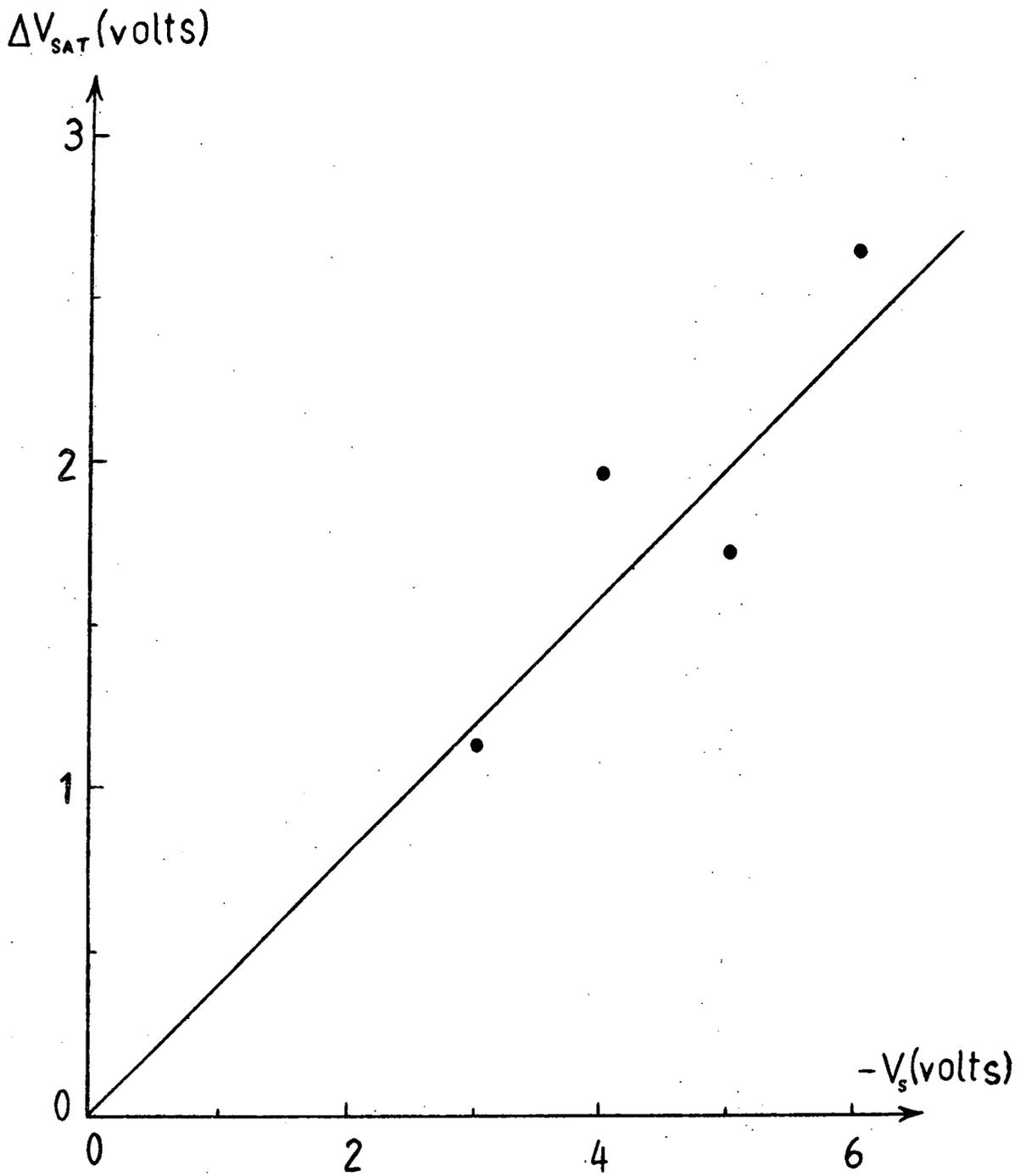
Figure 4.15: Plot of flat-band voltage shift at saturation, $\Delta V_{SAT}$, against the stress voltage $V_S$.
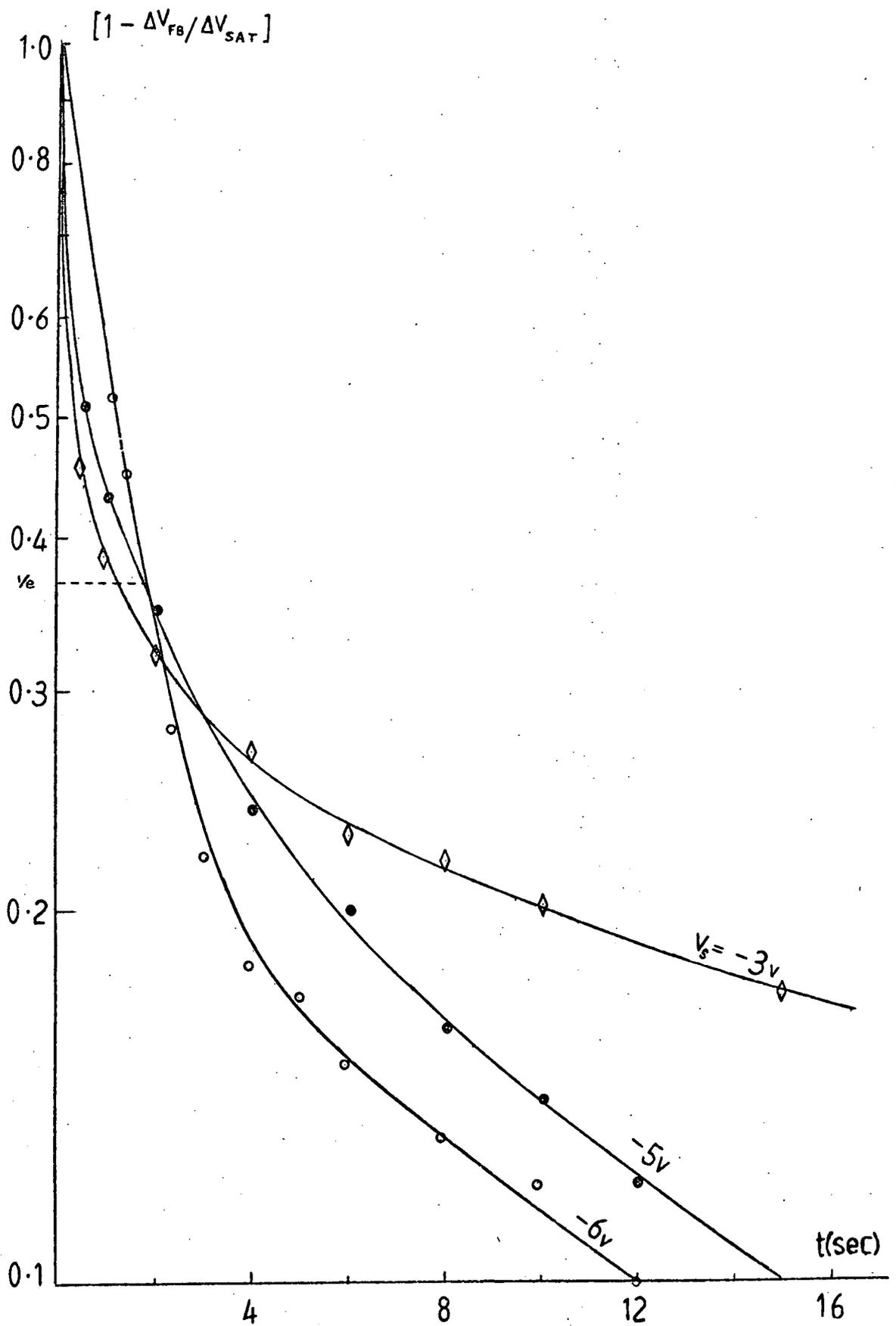
Figure 4.16: Plot of $(1 - V_{FB}/V_{SAT})$ against time from equation (4.6) for three different stress voltages. Points are derived from Figure 4.12 and $\tau$ is defined corresponding to the value of $1/e$.

From the kinetics of space-charge formation, Snow and Dumesnil also arrive at a relationship for the flat-band voltage shift with time:-

$$\Delta V_{FB} = \left( \frac{\kappa_o \, d_w}{\kappa_w \, do} \right) V_s \left[ 1 - \exp\left( -\frac{t}{\tau} \right) \right] \qquad (4.6)$$

where t is the total time of stress.

Here $\tau$ is the time constant of the space-charge defined by

$$\tau = \left[ \varepsilon_o kT \left( \kappa_w + \kappa_o \, \frac{d_w}{d_o} \right) \right] \bigg/ (Nq^2 D) \qquad (4.7)$$

where D is the diffusion coefficient for the mobile ions.

Knowing the value of $\Delta V_{SAT}$ for a given $V_s$, a plot of $\log(1 - \Delta V_{FB}/\Delta V_{SAT})$ against time of stress should therefore give a straight line. From Figure 4.12, the values of $\Delta V_{FB}$ with stress time can be extracted and $\Delta V_{SAT}$ is taken to be 1.13 V for $V_s = -3.0$ V, 1.73 V for $V_s = 5.0$ V and 2.65 V for $V_s = -6.0$ V. The resulting plot is presented in Figure 4.16 but the linear relationship is not found. This deviation from linearity has also been found by Snow and Dumesnil for their borosilicate glass films, and they explain it by that fact that as the polarization builds up the field in the bulk of the dielectric drops from about $10^5$ V/cm to near zero Since the mobility depends on the field, a curvature in the plot will occur because of the field changes with time. For the case of the willemite film, the formation of negative space-charge is in fact very much enhanced by the presence of the positive charges in the residual films, so explaining the strong curvature observed. Furthermore there is a change in the direction of the internal field at the dielectric-dielectric interface between the initial and the final situations. Neglecting the curvature of the lines plotted in Figure 4.16, the time constant for the formation of this space-charge may be found approximately from the corresponding value

69

of $1/e$ for $(1 - V_{FB}/V_{SAT})$. Thus $\tau$ is found to be 1.15 sec, 1.65 sec and 1.80 sec. for values of $V_s$ of -3.0 V, -5.0 V and -6.0 V respectively. Using equation (4.7) and an average value of 1.53 sec for $\tau$, the diffusion coefficient of the mobile ions can be estimated by assuming appropriate values for the other parameters. At room temperature and using $\kappa_w = 15.50$, $\kappa_o = 4.16$, the relative thicknesses of willemite and residual film for slice SL6 from Table 4.3 and $N \simeq 10^{19}$ $cm^{-3}$, the value of D is approximately $10^{-14}$ $cm^2$/sec. This value is higher than the value of $10^{-19}$ $cm^2$/sec at $200^{\circ}C$ for $Na^{2+}$ ions in borosilicate glass estimated by Snow and Dumesnil. This may be reasonable for the willemite in view of the comparative ease with which the C-V curves can be shifted at room temperature.

The threshold value of $V_s = -1.70$ V at which appreciable shifts in flat-band first occur corresponds to the voltage at which the dc current is found to rise suddenly to the saturation value of $10^{-9}$ A. This current may be principally due to the movement of ions plus some contribution from electrons moving into the willemite from the metal. Since strong inversion is still possible, even when $V_{FB}$ has gone into saturation, it is certain that holes accumulating at the surface are not being replenished This would imply that only a negligible number of electrons can be traversing the whole length of the composite film from the metal to the silicon.

The drastic lowering in the gradient of the C-V curves which occurs with the $V_{FB}$ shift can be explained by the polarization of the willemite being inhomogeneous. If the polarization occurs preferentially at certain parts of the willemite film area, then the observed $V_{FB}$ will be a suitable average of values corresponding to the polarized and non-polarized areas. If the inhomogeneity occurs over very small areas, the average for each capacitor will be the same, as observed. Such inhomogeneity in the flat-band distribution will cause a stretching out of C-V curves on the voltage

axis as has been described by Brews (19). It is not surprising that such

inhomogeneity arises in the willemite because film examination, as described

in Section 4.3, has shown the ~~greasy~~ grainy and coarse texture of willemite

crystallites. A similar effect was also found in the work on willemite by

Davies (1).

The above discussion has concentrated on the effects of negative

applied voltages on the position and shape of the C-V curve. With positive

applied voltages there is hardly any shift in the flat-band voltage until

'breakdown' occurs, as reported in the last section. Such a phenomenon can

be viewed on the following lines. The movement of negative ions towards

the metal electrode is totally dismissed since they are already assumed to

be immobile. Other alternatives are electron accumulation at the silicon

surface and the movement of mobile positive charges towards the residual

film interface. The latter cannot easily happen for two reasons. Firstly,

since polarization is expected to take place near the vicinity of the

dielectric-dielectric interface, any movement of positive ions, towards

this interface can only result in a very slight displacement. It may be

that such a small displacement is not sufficient to reveal any effective

space-charge in the condition that the residual film is non-penetrable by

the mobile positive ions. The second factor, probably the more dominant,

is the role played by the fixed positive charge centres in the residual

film. Any tendency trying to create a positive space-charge near the

interface will be suppressed by these fixed centres, repelling any mobile

positive charges. In fact it is the same fixed positive centres that are

also responsible for enhancing the formation of the negative space-charge

with the negative bias. Higher positive voltage only creates an intense

repulsive field at the interface which can create lattice strains and

ultimately the 'breakdown' phenomena in the willemite.

71

## 4.8 General Discussion of Type-A Willemite Films

The formation of Type-A willemite by baking for 20 min. at $1000^{O}C$ results in a three-layer structure, namely the underlying silicon, the residual film and the willemite itself. Basically the silicon still has most of its initial properties, apart from the addition of deep levels within the band-gap. From the starting materials, $ZnF_2$:Mn and $SiO_2$, the two most likely candidates to form these deep levels are manganese and zinc ions, but this raises the question of which of the two is most likely to get into the silicon first during the reaction-bake. It also raises the question of the diffusion of these ions through $SiO_2$ which will also depend on their respective segregation coefficients. Zinc has a maximum solid solubility of $6 \times 10^{16}$ $cm^{-3}$ in silicon and it forms two acceptor-type levels at 0.55 and 0.31 eV from the valence band, while manganese, with a solid solubility of $2 \times 10^{16}$ $cm^{-3}$, has a single donor-type level at 0.53 eV. In Figure 4.4, the Schottky barrier $1/C^2$ - Vplot shows the effect of varying concentrations of zinc and manganese using the Sah-Reddi Theory described in Chapter 3. It is found that the experimental points fit the theory in the direction of donor-type levels, i.e. the actual $1/C^2$ values are lower than the ideal case. This indicates that the deep-levels are due to manganese rather than zinc and fitting the experimental points to the theoretical curve yields an approximate donor-type trap density of $7.1 \times 10^{15}$ $cm^{-3}$, which is still less than the maximum solid solubility value of $2 \times 10^{16}$ $cm^{-3}$. Since there is no data available for either the diffusion or segregation coefficient of manganese in silicon or $SiO_2$, it is difficult to know how manganese would compete with zinc diffusing into the silicon. In spite of the 1% manganese in the initial zinc fluoride, as compared to the larger proportion of zinc, it appears that more manganese than zinc gets into the silicon during the short reaction time of 20 minutes. This could only be possible if at $1000^{O}C$, manganese

diffuses through $SiO_2$ at a very much faster ~~role~~ rate than zinc. There appears to be no reason why this should not be so.

The theoretical curves of Figure 4.4 assume uniform donor concentrations throughout the silicon. The deviations of the experimental points from the $N_T^+ = 7.1 \times 10^{15}$ cm$^{-3}$ curve at low reverse bias could, therefore, be due to non-uniformity.

The introduction of manganese in the silicon does not markedly affect the general properties of the composite structure, where the inversion capacitance calculated without deep levels is comparable to the experimental value. On the other hand, the deep levels play an important role as recombination centres near the interface with the residual film and of course the semiconductor's minority carrier lifetime is expected to be changed because of this.

Previous work on the reaction-bake for forming willemite speculated that the reaction might take the form of

$$2ZnF_2 : Mn + 2SiO_2 \rightarrow Zn_2SiO_4 + SiF_4 \uparrow$$
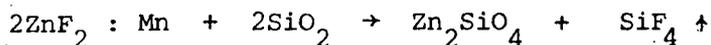
Also, Errington ( 2 ) has proved that the presence of oxygen in the atmosphere can continue oxidizing the silicon during the reaction-bake process. This shows that oxygen can pass through both willemite and silicon oxide during the reaction.

Reactions for the formation of silicate glasses are generally not as simple as the above because the rate-determining factor is dependent on so many parameters like the diffusion of various anions and cations within the lattice of the silicate, the bonding nature of the ions or influence of ionic fluxes. The ions $Si^{4+}$ and $O^{2-}$ can diffuse very rapidly through a silicate structure, but unbounded cations like $Zn^{2+}$ or

$Mn^{2+}$ would be the rate-determining factor because the diffusion rate of these cations far exceed those of $Si^{4+}$ or $0^{2-}$ (20). For these reasons it seems more likely that the willemite forming reaction is in two stages rather than one, taking the form:-

$$2ZnF_2 : Mn + SiO_2 \rightarrow 2ZnO : Mn + SiF_4 \uparrow$$

$$2ZnO : Mn + SiO_2 \rightarrow Zn_2SiO_4 : Mn$$
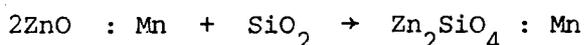
In such a case, the zinc oxide presumably dissociates into zinc and oxygen ($ZnO \rightleftharpoons Zn^{2+} + 0^{2-}$) which diffuse through the silicate to react with the underlying $SiO_2$ and finally forms willemite. For this reason it can be expected that the residual film, largely made up of a network of silicon and oxygen, contains embedded $Zn^{2+}$ and/or $Mn^{2+}$ ions. The present electrical results show that there is a high density of positive centres in the residual film which supports this proposal. These centres may also be responsible for providing localized states in the residual film by becoming coulombic electron trapping sites or by causing trapping sites out of structural defects. Visual observations of the residual film under the microscope showed that the residual film has a very fine granular structure, presumably polycrystalline, and that there are no flaws or defects to be found. Under the SEM secondary emission mode with an electron energy of 25 keV or less, again, there were no special features of the image, although sufficient contrast was obtained. The grain size is very fine, which would imply that the residual film is polycrystalline.

To deduce the properties of Type-A willemite from the electrical measurements made on the composite structure is highly complicated, but from knowledge of the residual film, a reasonable model can be postulated. As mentioned in the previous section, there is no definite means for distinguishing between electronic trapping and polarization effects at

moderate field strengths.  However, at high fields, say greater than $10^6$ V/cm, a certain amount of electronic conduction would be expected. Unfortunately this high field electronic conduction cannot be observed because of the so-called 'breakdown' phenomenon taking place first.  This phenomenon will be mentioned in a later part of this section.  In all conduction measurements involving high fields, the composite structure met with the same fate, i.e. the current characteristic tended towards that of the residual film structure and never recovered.  Another phenomenon related to the current measurements is the critical voltage at which the rapid rise in current occurs.  Davies (1) attributed this to the voltage at which the number of electrons injected from the metal into the willemite become appreciable.  From the polarization model proposed for moderate field strengths, the critical voltage of about -1.27 V may correspond to the field required to displace the mobile cations from the immobile anions. The critical voltage used here is analogous to the concept of activation energy for ions in dielectrics as applied by Abbots and Kamins (16) and Snow and Dumesnil (17) to sodium ions in $Al_2O_3$ and lead ions in borosilicate glass respectively.  In the former case, the activation energy is approximately 0.60 - 1.00 eV while the latter has a value of 1.05 eV.

An extensive survey of the structural properties of willemite films has been carried out by Edwards.  The basic structure is formed by interlinking of $SiO_4$ tetrahedra to $ZnO_4$, the $(SiO_4)^{4-}$ forming a radical anion while the $Zn^{2+}$ acts as its cation.  The Si-O atoms are covalently bonded while cations and anions are ionically bonded.  Sutton (20) in his review on space-charge polarisation in silicates, indicated a rigid glassy  network of the silicon-oxygen tetrahedra while metallic ions are more loosely bound and reside in relatively large cavities in the network.  Consequently, the energy barrier for the motion of these cations from cavity to cavity

is relatively low so that current flow occurs under an electric field by a statistical drift of these ions through the network cavities. It can be assumed $Zn^{2+}$ and $Mn^{2+}$ are the metallic cations moving within the cavities in the case of willemite, and the very low critical field required may indicate that they are loosely bonded to the silicate tetrahedra network. Presumably, with a negative voltage, $Zn^{2+}$ and/or $Mn^{2+}$ ions are freed from the $(SiO_4)^{4-}$ radicals thus leaving a negative space-charge in the willemite as observed. Under the influence of the applied field, mobile cations will find their way to the metal by drifting from cavity to cavity by the most probable paths. Since a random distribution of willemite crystallites exists throughout the entire film then it can be expected that there will be a lateral non-unformity in the polarization and this is shown by the reduced slope of the C-V curves with increasing flat-band shift. It is not known whether the cations pile-up or are discharged by the metal on reaching the electrode. Non-stoichiometry of the willemite is expected to occur most markedly in the vicinity of the willemite-residual film interface, and the cations here may be loosly bonded. For this reason, polarization at the interface is thought to be dominant in the willemite film. Usually such a type of polarization is known as interfacial polarization and in fact in this case its occurrence is very much influenced by the presence of positive centres in the residual film.

As the negative space-charge is formed by polarization of the willemite the interaction between this negative space-charge and the positive centres in the residual film, possibly $Zn^{2+}$ and/or $Mn^{2+}$ cations, will create a built-in field. This internal field, shown in Figure 4.17(b), will cause very large mechanical strain in the lattice of the silicate network which ultimately can give way to localized conduction effects in the willemite. Perhaps this is how the 'breakdown' phenomena occur, although the actual mechanism, as in most cases of dielectrics, is not well-understood.
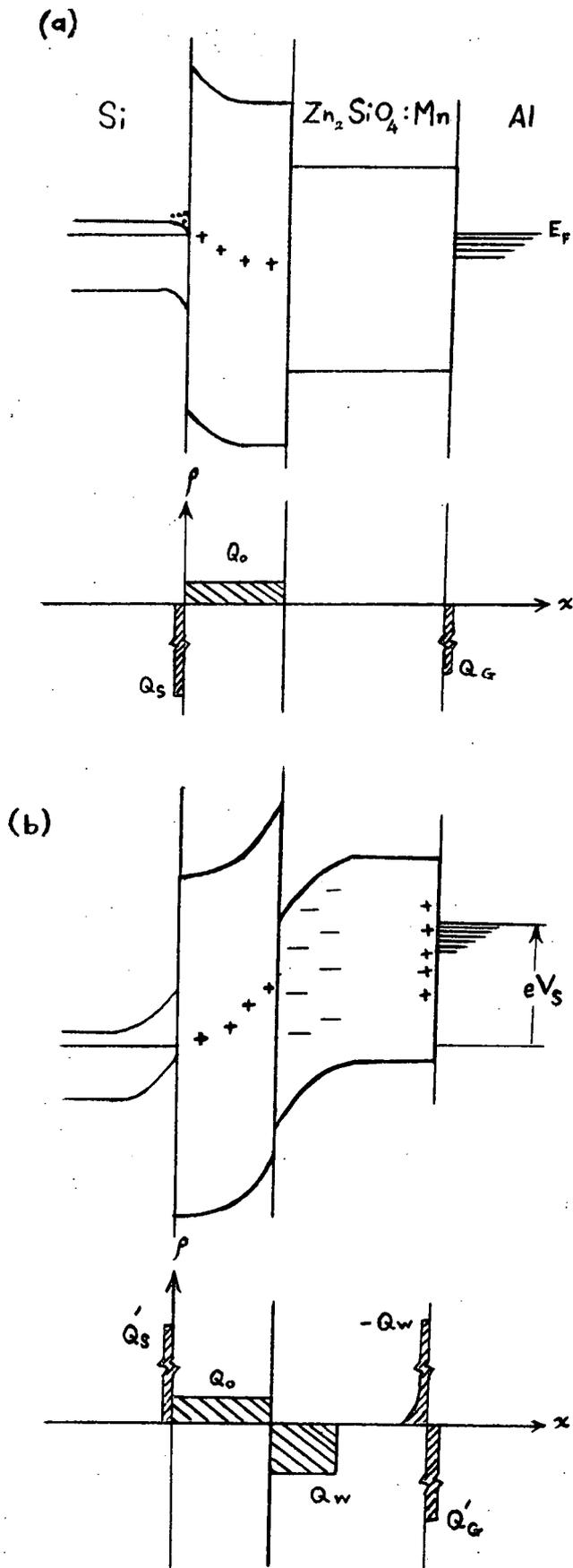
Figure 4.17:   Proposed band diagrams and charge distributions for a
composite willemite structure (a) initially, and (b)
after achieving flat-band saturation.

Figure 4.16(a) illustrates a proposed initial situation in the composite
structure band diagrams.  The silicon surface is accumulated due to the
residual film positive centres while the willemite,which is assumed to be
initially neutral, has no band bendings.  After a saturation in polariza-
tion has been achieved, the bands are depicted by Figure 4.16(b), where
the silicon surface is now in depletion and the internal field causes a
high degree of band bending in the willemite at the residual film interface.


## 4.9    Conclusion

The technique for the reaction-bake formation of Type-A willemite
has been described in the early part of this chapter, followed by the results
of a visual and SEM examination of the films.  The composite willemite films
are found to be cathodoluminescent while the residual films are not.

The electrical properties of the underlying silicon and the residual
film have been described.  The silicon is found to contain deep donor-type
levels making it more n-type while the residual film is an insulator with
a high density of positive centres which contribute to the field-assisted
tunnel-hopping high-field conduction mechanism.

The electrical properties of the basically insulating composite
willemite films are described in the later part of the chapter.  Polarization
was found to be a dominant feature in Type-A willemite although electronic
conduction cannot be totally dismissed.  The polarization may be due to the
dissosociation of $Zn^{2+}$ and/or $Mn^{2+}$ cations from the $(SiO_4)^{4-}$ radicals.
A breakdown phenomenon in the composite film has been attributed to the
internal field caused by positive centres in the residual film and negative
space-charge arising from polarization.

The electrical properties of Type-A willemite will be compared with
those of Types-B and C in the general discussion, Chapter 7.

REFERENCES

CHAPTER   4

1.  G D Davies,  M. Phil. Thesis   Durham  (1970)

2.  D A Errington,  unpublished

3.  H F Wolf,  'Silicon Semiconductor Data',  Pergamon Press (1969)

4.  R M Burger  and  R P Donovan,  'Fundamentals of Silicon Integrated
        Device Technology, Vol.I'   Prentice-Hall (1967)

5.  S M Sze,  'Physics of Semiconductor Devices'  John Wiley & Sons (1969)

6.  A K Jonscher,  Thin Sol. Films   1   213 (1967)

7.  A K Jonscher  amd  R M Hill,  Thin. Sol. Films   8  169  (1975)

8.  A K Jonscher.  J  Phys. C:  Sol. St. Phys.   4   1331 (1971)

9.  A Serviori  and  A K Jonscher,  Thin Sol. Films   3  341 (1969)

10.  N Klein  and  Z Lisak,  Proc. IEEE   54  979 (1968)

11.  H J Queisser,  Sol. St. Dev.  Proc. Conf.  Inst. Phys.   London (1972)

12.  P K Dubey,  V A Filikov  and  J G Simmons,  Thin Sol. Films   33
        49 (1976)

13.  P Balk  and  F Stephany,  J. Electrochem. Soc.   118  1634 (1971)

14.  T Tsujide,  S Nakanuma  and  Y Ikushima,  J. Electrochem. Soc.   117
        703  (1970)

15.  N  F Mott,  J. Non-Cryst. Sol.   8-10  1-18 (1972)

16.  R A Abbott  and  T I Kamins,  Sol. St. Elec.   13  565-576 (1970)

17.  E H Snow  and  B E Deal,  J. Electrochem. Soc.   113  263 (1966)

18.  E H Snow  and  M E Dumesnil,  J. Appl. Phys.   37  2123 (1966)

19.  J R Brews  and  A D Lopez,  Sol. St. Elec.   16  1267-1277 (1973)

20.  P M Sutton,  J. Am. Cer. Soc.   47   188 (1964)

21.  A S Grove,  B E Deal,  E H Snow  and  C T Sah ,  Sol. St. Elec.
        8   145-163 (1965)

# CHAPTER 5

## INVESTIGATION AND DISCUSSION OF TYPE-B WILLEMITE
(Long Reaction Time - $N_2/O_2$)

### 5.1    Introduction

In the last chapter the results were described for Type-A willemite produced with a short reaction-bake time, approximately 20 min., in an ambient of dry nitrogen.    The results have shown the influence of the residual film, as first discovered by Davies (1), between the silicon and the willemite.    This film is presumably a consequence of an incomplete reaction although there is no definite experimental evidence for this. However, in a separate work Hurd and Johnston (2) have discovered that for a complete reaction to take place, the reaction-bake time has to be extended to approximately 20 hrs.    In this chapter, and the next, the properties of willemite formed by a reaction-bake time in excess of 20 hrs will be described.    In accordance with a suggestion by Dr. Hurd it was decided to incorporate a 10% oxygen in nitrogen atmosphere with this long reaction time.    The willemite prepared in this way will be termed 'Type-B willemite'.

In this chapter, all the investigations on Type-B willemite will be presented.    The early part of the chapter describes the parameters and processing involved in the preparation of composite structures from this type of willemite.    Details of the preparation technique otherwise required will not be repeated since they are very similar to those for Type-A willemite.    Section 5.2 also describes the examination of the films by ellipsometry, optical microscopy and the SEM.    Electrical results, mainly C-V measurements, are presented in the following section.    The later sections of this chapter are used for the analysis and  discussion of the electrical results.

5.2     Preparation and Examination of Type-B Willemite

The object of incorporating 10% oxygen in the reaction atmosphere for this type of willemite is to obtain the in situ formation of $SiO_2$, which can then react with the $ZnF_2$. The flow of oxygen into the furnace was measured on a separate flowmeter and adjusted to 10% of the total gas flow. As mentioned in the last chapter, the reaction furnace was set at $1000^{\circ}C$ and profiled to achieve a flat-zone about 6 cm long.

Some preliminary films were produced for thickness measurements. These had various thicknesses of initial oxide and it was found that even with negligible initial oxide, the resulting residual film was about 200 Å thick. It was decided that the initial oxide thickness for the electrical test slices should be about 200 Å , so as to have a reasonably good film-to-silicon interface.

As described in Chapter 2, the oxidation of silicon slices and evaporation of $ZnF_2$ are standard procedures. After the willemite furnace had been prepared, the slices were gradually introduced into the furnace so that from room temperature to the peak temperature of $1000^{\circ}C$ it took a time of about 10 min. This procedure is to avoid any possible stress in the films that may be caused by a sudden exposure to a high temperature. The reaction bake was carried out for about 20 hrs, but it cannot be denied that small fluctuations in the oxygen flow and the temperature may have occurred during this time. Extracting the slices from the furnace was simply the reverse of the introduction procedure. The post reaction cleaning of the willemite surface was by dilute NaOH solution and the willemite etching was done by a weak solution of either acetic or hydrochloric acid. In processing, the experimental slices were accompanied by test chips used for film thickness measurements, and optical and SEM examinations.

The film thicknesses of three experimental slices are presented in Table 5.1. It can be seen that the initial oxide thicknesses were

79

| Experimental slice | SL4 | SL7 | SL10 |
|---|---|---|---|
| Initial Oxide | 233 | 203 | 216 |
| Zinc Fluoride | 197 | 571 | 770 |
| Composite, $d_T$ | 861 | 854 | 935 |
| Residual Film, $d_o$ | 636 | 257 | 226 |
| Willemite $d_w = d_T - d_o$ | 225 | 597 | 709 |

TABLE 5.1    Film thicknesses in $\overset{o}{A}$ on three experimental

slices, as measured with the ellipsometer.
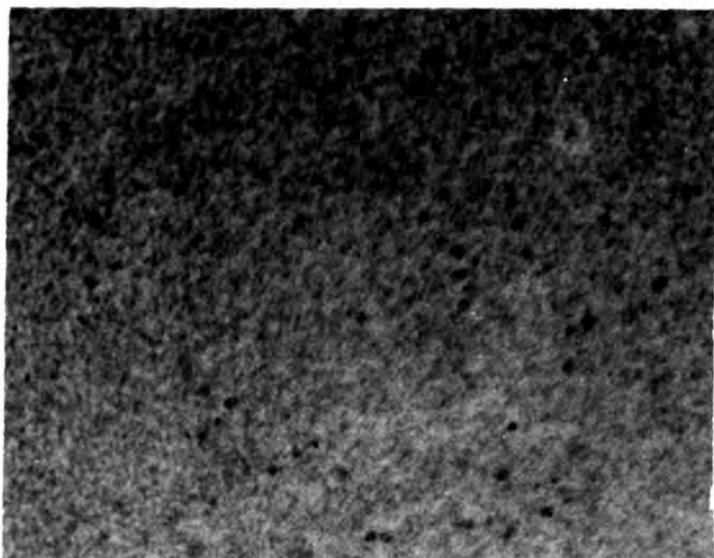
Plate 5.1    A 560x photomicrograph of Type-B
             willemite.  Lower part is towards
             edge of film.
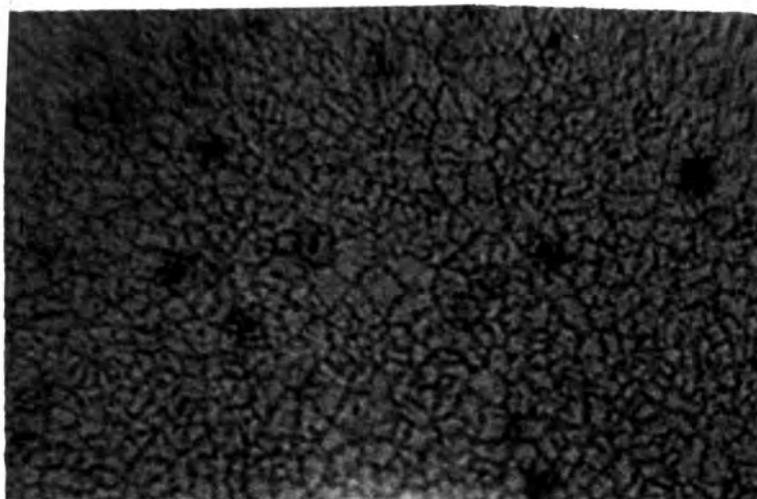


Plate 5.2    A 560x photomicrograph of the
             residual film from Type-B willemite.

slightly over 200 Å while the thicknesses of zinc fluoride is seen to vary from 197 Å for SL4 to 770 Å for SL10. Nevertheless, irrespective of the zinc fluoride thickness, the total thickness of the composite film on all three slices was found to be 850-950 Å . Because of the very thin zinc fluoride film, slice SL4 is found to have a residual film of about 636 Å while the other two have residual film thicknesses of slightly over 200 Å. Slice SL4 therefore has the thinnest willemite film and a thick residual film which may be due to the fact that with very little zinc fluoride, oxidation of the silicon is enhanced during the reaction-bake process. It must be recalled here that the oxygen present in the ambient leads to the further oxidation of the silicon during the reaction while it is being attacked at a rate which depends on the thickness of the zinc fluoride. In other words, the thicker the zinc fluoride the thicker will be the willemite film and the thinner the residual film. Average refractive indices of the composite films range from 1.56 for SL4 to 1.85 for SL10 with the residual films having values of 1.61 and 2.14 respectively.

Unlike Type-A willemite, the willemite films prepared in this case have a much finer grain structure as seen under the optical microscope. Fine,bluish dendritic features were observed and it was confirmed by the SEM that this feature was not topographical (e.g. dips or bumps) but due to differences in refractive index. These dendritic features existed in the form of cellular structures as shown in Plate 5.1. The edges of the willemite films had coarser crystallites which were more dispersed and closely resembled the features of Type-A willemite in their grain size and colour. This edge effect may have been caused by a more inhomogeneous flow of the constituent materials in molten form towards the edges during the reaction-bake process.

Cathodoluminescent tests on Type-B willemite using the Tesla discharge gave very good bright green light emission thus confirming

the luminescent properties of this type of willemite films. On the other hand, use of the cathodoluminescent mode in the SEM resulted in a rapid darkening of the image implying a charge retention capability of the willemite. In other words, films of Type-B willemite are good insulators. In the SEM secondary emission mode, the Type-B willemite films gave higher images contrast than Type-A willemite. This was observed by placing the two types of willemite side by side during the investigation. This shows that the secondary emission coefficient must be greater in Type-B than in Type-A films.

After etching off the willemite, the residual films were not cathodoluminescent. Dendritic features, like those in the willemite, were also observed in the residual films but with brown colouration instead of blue. These dendrites appeared in a background of very fine grained yellow material. On etching off the residual film with concentrated HF, the dendritic features were still found in the underlying silicon, as shown in Plate 5.2. Suspecting that the crystalline structure of the silicon surface may have been disrupted by the processing, electron channelling pattern (ECP) tests were carried out in the SEM on the residual silicon, together with a fresh piece of silicon acting as a control. This test can determine features of the semiconductor crystallinity up to 50 $\overset{\circ}{A}$ beneath the surface. The control silicon gave a very strong ECP image with well-defined lines while the residual silicon under test revealed slightly diffused lines although its ECP image was still recognizable. It must therefore be concluded that the silicon surface is still crystalline after the formation of Type-B willemite with the slightly off-set image being due to the incorporation of additional elements in the silicon surface.

## 5.3 Electrical Results

The electrical properties of Type B willemite were studied by similar methods to Type-A, with measurements on both composite and residual films. In addition the change in the silicon due to the long reaction, as shown by the existence of dendritic features in the surface, aroused interest in knowing more about the resulting electrical properties. For this reason a separate investigation of deep levels in the silicon was made by means of the metal-semiconductor rectifying characteristic using the mercury probe technique. After etching off the composite willemite film, gold contacts were evaporated on to the unpolished side of the silicon and sintered at 450°C in nitrogen for about 10 min. A thin oxide, for rectifying purpose, was grown by reacting the silicon in a mixture of 10% ultrar $H_2O_2$. The test piece was then placed with its surface of interest downwards on to a Perspex block with a capillary column containing 99.999% pure mercury forming a rectifying top contact. The sample was held firmly in place by two steel probes pressing downwards on to the gold. Reverse-bias capacitance measurements were made with a Wayne-Kerr RF-bridge at a frequency of 5MHz following the procedures laid down in Chapter 2. The results were compared with those for a control sample of silicon that had not been used as a willemite substrate.

A $1/c^2 - v_r$ plot of the capacitance measurements is presented in Fig 5.1 and compared with theory using $N_d = 2.3 \times 10^{15}$ cm$^{-3}$ and $V_D = 0.253v$ for the mercury-silicon Schottky barrier. The experimental points for the control silicon fit well with the calculated ideal curve, hence showing the reliability of the measuring technique. It can be seen that the experimental points for the test silicon are considerably above those for the ideal case, indicating the existence of deep acceptor-type traps in the silicon. This result is the opposite to that for
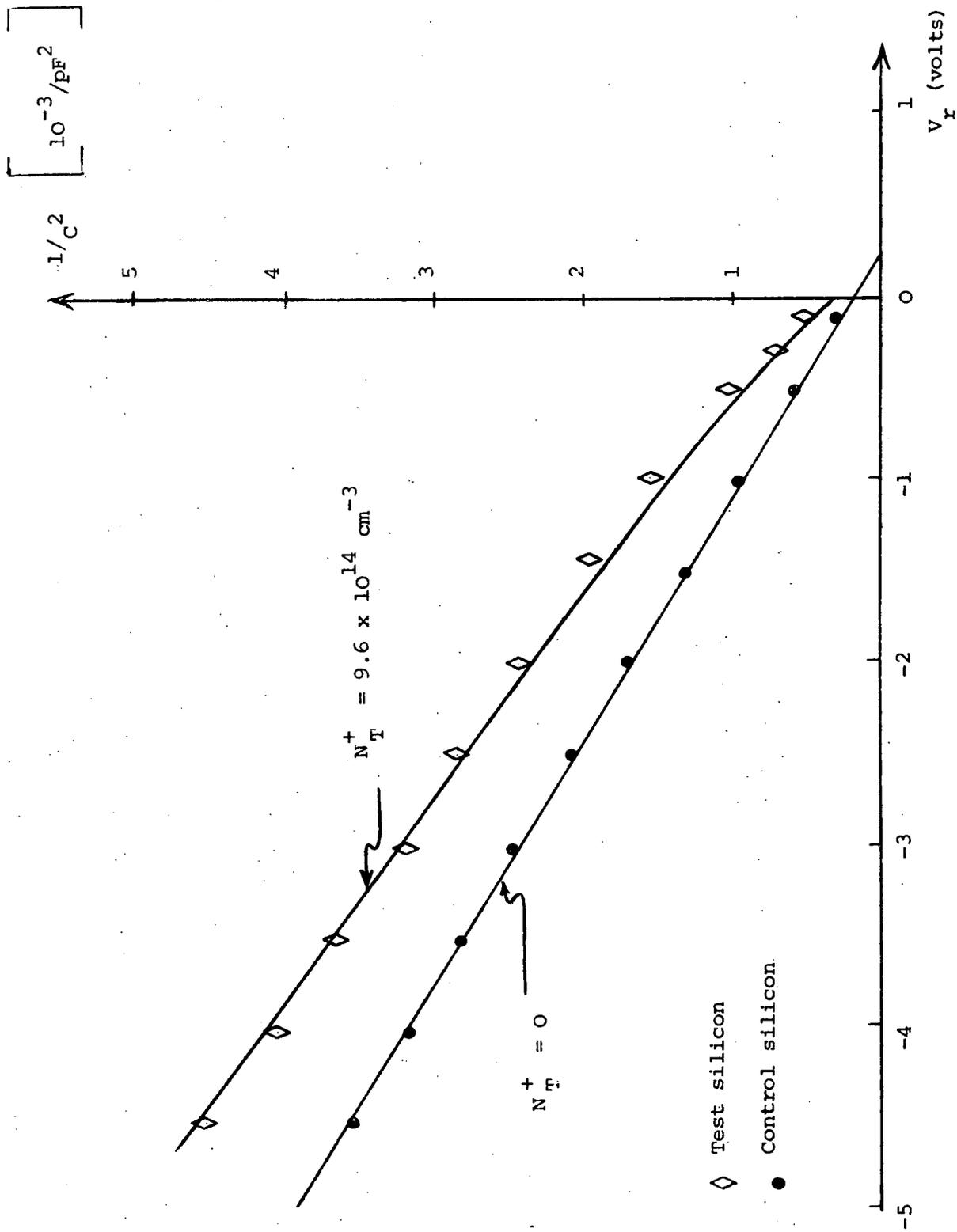
Fig 5.1   A Schottky barrier-type plot for rectifying contacts on the silicon after etching off the willemite composite film. Lines are from theory for silicon without deep levels and with acceptor-type traps due to zinc. Measuring frequency, 5MHz, Area, 2.69 x 10$^{-3}$ cm$^2$. Doping concentration, $N_d$ = 2.3 x 10$^{15}$ cm$^{-3}$.

| | Experimental Slice | SL7 | SL10 | SL4 |
|---|---|---|---|---|
| Structure | | | | |
| Composite Film | $d_T$ (Å) | 854 | 935 | 861 |
| | $C_{max}$ (pF) | 68.9 | 55.1 | 36.1 |
| | $C_{min}$ (pF) | 18.5 | 17.2 | 13.0 |
| | $C_{FB}$ (pF) | 49.6 | 40.3 | 28.8 |
| | $V_{FBo}$ (volts) | -0.884 | -1.077 | -0.900 |
| | $\kappa_T$ | 6.42 | 5.62 | 3.39 |
| Residual Film | $d_o$ (Å) | 257 | 226 | 636 |
| | $C_{max}$ (pF) | 104.0 | 119.7 | 73.8 |
| | $C_{min}$ (pF) | 20.9 | 19.6 | 18.6 |
| | $C_{FB}$ (pF) | 66.3 | 69.1 | 51.9 |
| | $V_{FBo}$ (volts) | -0.515 | -0.802 | -0.980 |
| | $\kappa_o$ | 2.91 | 2.95 | 5.12 |

TABLE 5.2    Typical results from 3 different slices of the composite and residual film structures.

Type-A willemite where the traps are donor-like.   There therefore seems
to be some correlation between the presence of the dendritic features in
the silicon surface and the deep acceptor-type traps observed in these
measurements.   A detailed analysis of these results will be taken up in
the next section.

Most of the electrical measurements refer to the Type-B willemite
films which will be classified into two types depending on the respective
thicknesses of the willemite and residual films.   The first category has
the willemite thicker than the residual film while the second was the
reverse situation.   In both cases the residual films were far more
insulating than for Type-A willemite and the d.c. conduction was too low.
to measure accurately.   The electrical results are therefore entirely
based on C-V measurements and the effects of electrical stress on changing
these characteristics.

## A. Composite Structures with dw> do

Results presented in this category refer to measurements made
from slices SL7 and SL10 processed in different batches.   From Table 5.1,
both the (dw/do) ratios of slices SL7 and SL10 were found to be greater
than unity as described in Section 5.2.   In general, the C-V curves of
both the composite and residual film structures from both slices have
typical MIS-type characteristics.   A summary of their MIS parameters is
presented in Table 5.2 where $C_{max}$ and $C_{min}$ represent the accumulation
and strong inversion capacitances respectively, and $C_{FB}$ is the flat-band
capacitance calculated from equation (3.10).   From the total thickness $d_T$
and the value of $C_{max}$, the effective dielectric constant of the composite
film is about 6.4 for SL7 and 5.6 for SL10.   The initial flat-band voltages
$V_{FBO}$ are -0.884v and -1.077v for SL7 and SL10 respectively, the more
negative value being for the thicker film.

Generally speaking, the C-V curves for the present composite willemite films in this category behave similarly to those of Type-A willemite. The hysterisis for a full cycle C-V measurement is found to depend on sweep speed, time and the maximum measuring voltage. Shifts in flat-band voltages also tend towards more positive ~~possible~~ values when negative voltages are applied to the metal electrodes. This feature is illustrated in Fig. 5.2(a) where, with consecutive increase in a 2 min duration negative stress voltage to the metal electrode, the C-V curves are seen to shift toward the right along the voltage-axis. As for Type-A willemite, the C-V shifts are accompanied by lowering of the slope resulting in a stretching-out effect in the depletion regime.

A difference in the characteristics is found, however, in the residual films for Type-A and Type-B willemite. For Type-B the residual film is far more insulating and similar stress-induced shifts in the C-V curves are observed, although the magnitude of the change in the flat-band voltage, $\Delta V_{FB}$, is much smaller than for the composite film. The residual film C-V shift is illustrated in Fig. 5.2 (b). Since both curves in Fig. 5.2 (a) and 5.2 (b) are for a 2 min stress time, a direct comparison in their magnitudes can be made. For the composite film with $V_s = -4.0v$, $\Delta V_{FB}$ is found to be about 1.32v while under the same stress voltage, the residual film has a shift of only 0.27v. Correspondingly, the lowering of the slope of the C-V curves in Fig 5.2(b) is less than in Fig 5.2(a). As will be discussed in Section 5.4 the implication is that the creation of negative space-charge in the composite film is predominantly in the willemite rather than the residual film. Neither the composite nor the residual films have any noticeable shift in their flat-band voltages when positive stress voltages are applied.

A preliminary illustration of the change occuring in the composite film C-V curves with stress duration is given in Fig 5.3.
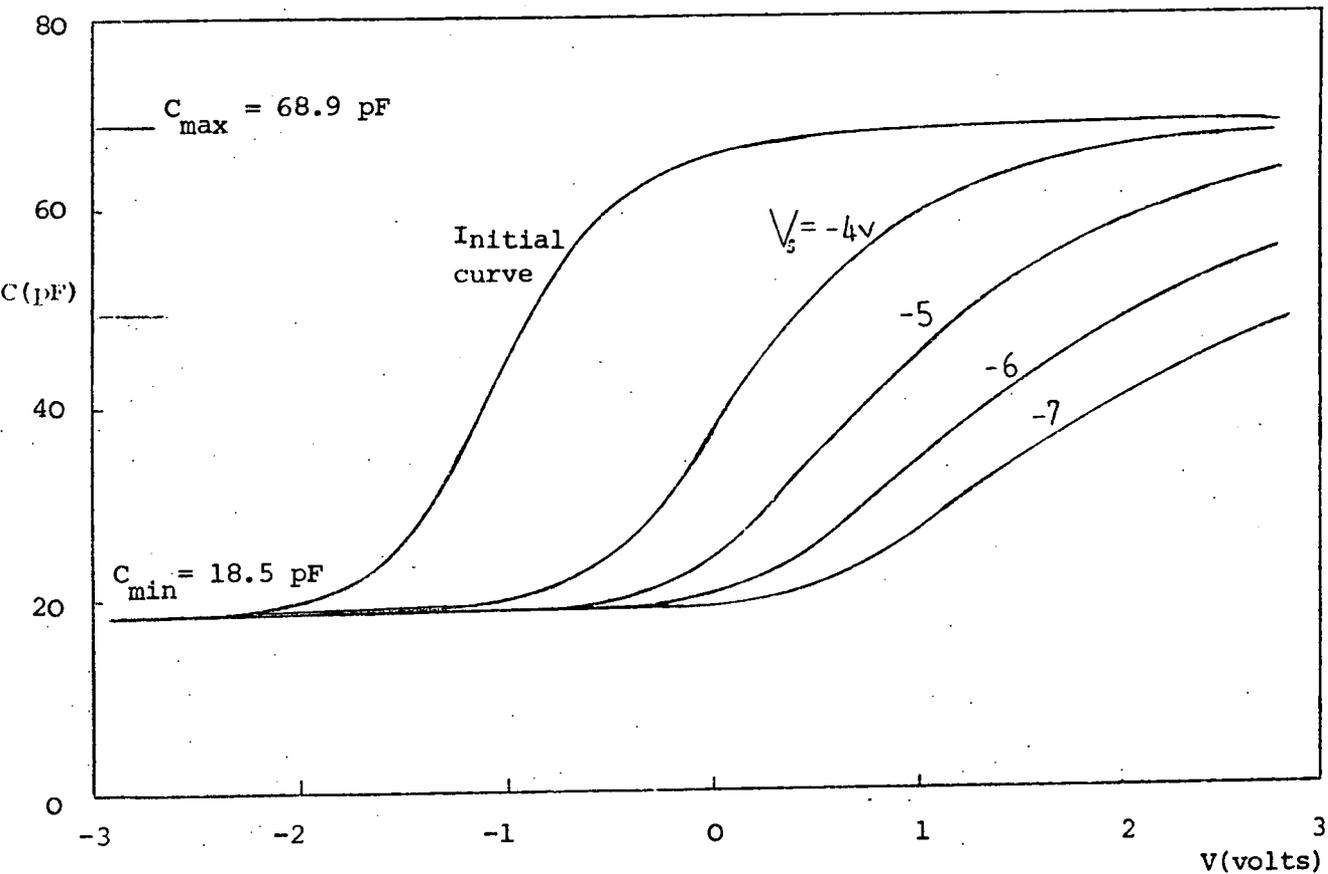
Fig 5.2 (a)    A typical C-V plot for a Type-B willemite composite structure
with increasing negative stress voltage. Stress time, 2 min.
Case of dw > do.
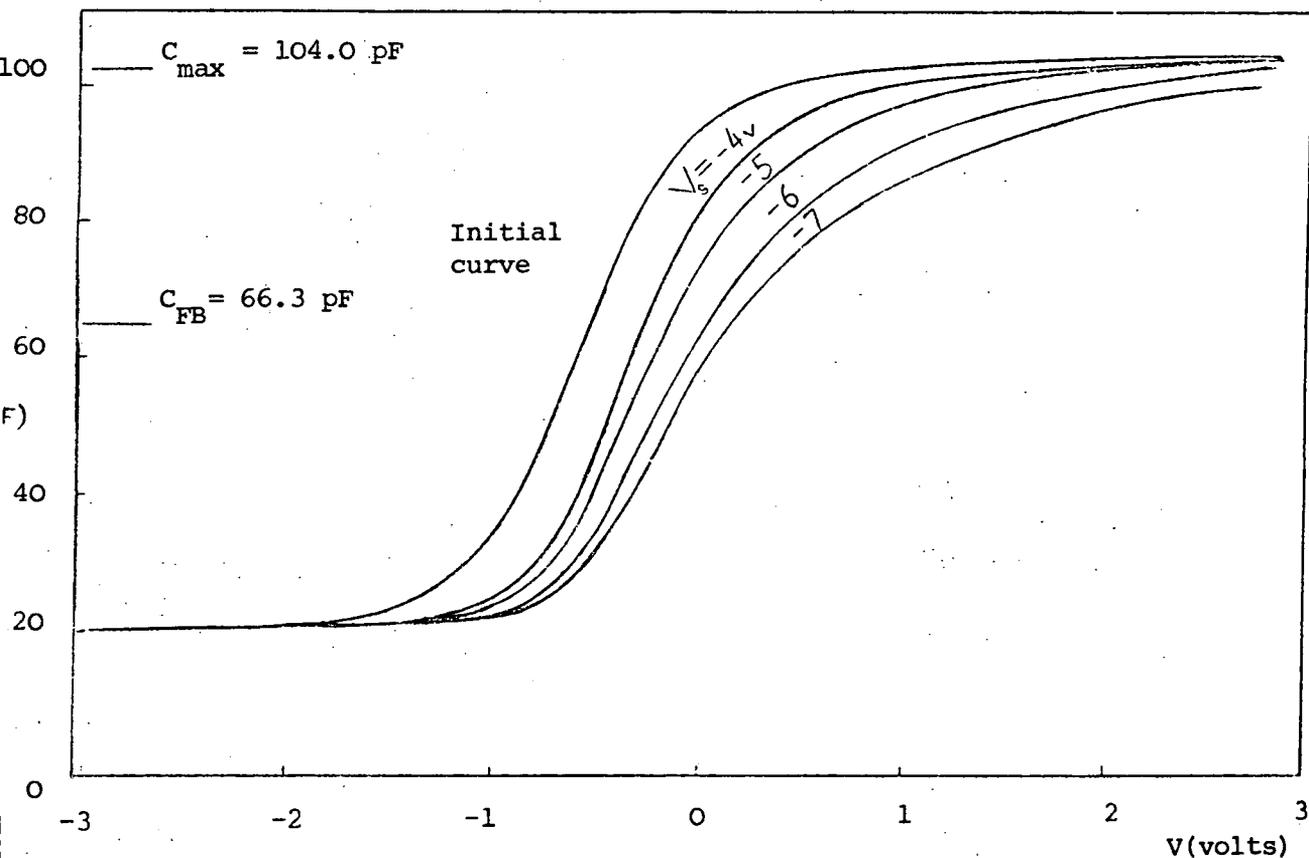


Fig 5.2 (b)    A typical C-V plot for a Type-B residual film structure
with increasing negative stress voltage. Stress voltage,
2 min.    Case of dw > do.
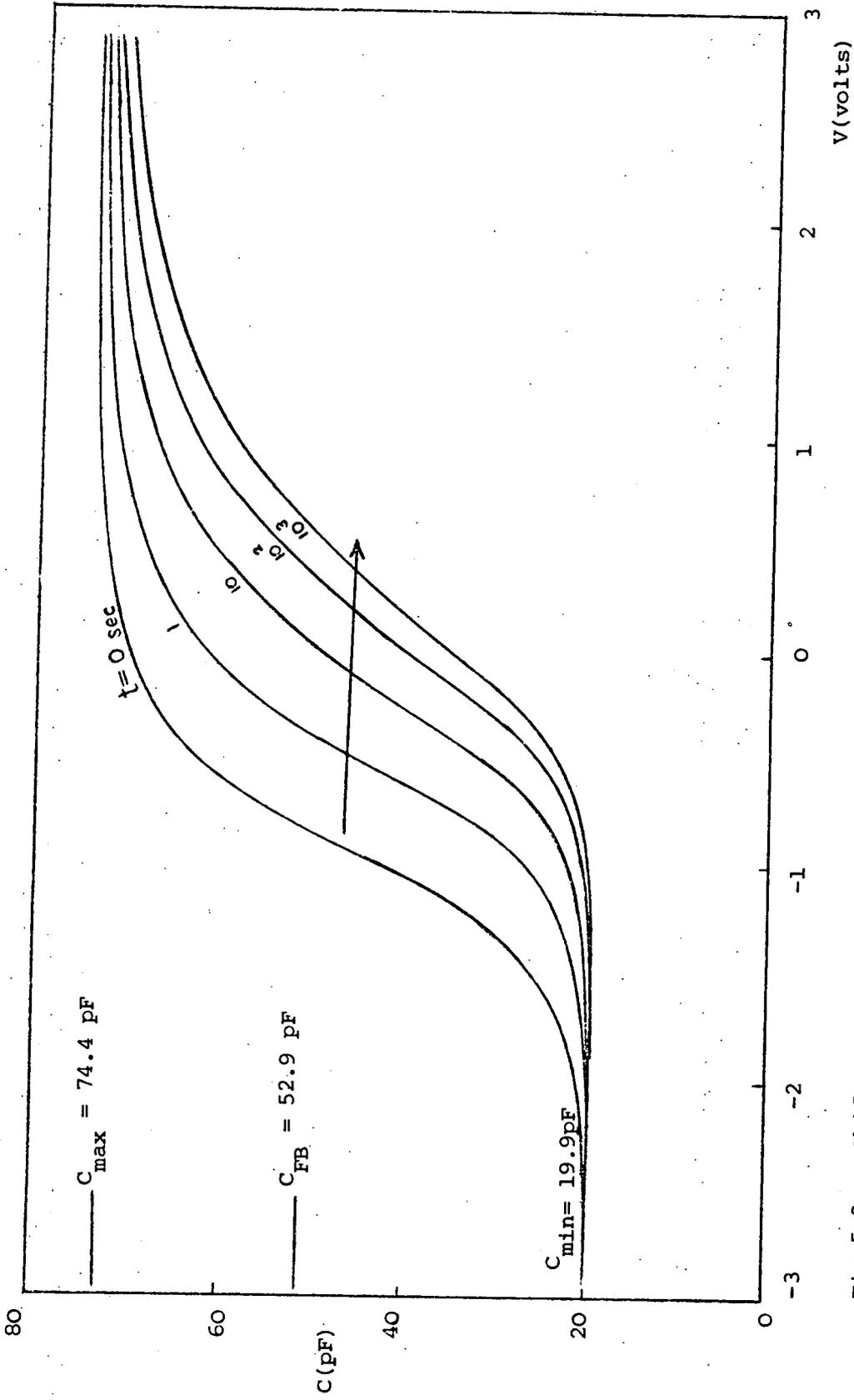
Fig 5.3    Shifts in the C-V curve of composite films with time of stress. Stress voltage, -4.0v.    Measurement done from positive to negative polarity.

The stress voltage in this case is -4.0v and the pattern of the shift is very similar to that for Type-A willemite except that it is slower, especially for short duration of stress. After the first second of stress, the value of $\Delta V_{FB}$ is 0.45v but which is insufficient to convert the polarity of the flat-band voltage to a positive quantity. For the residual film, the time taken to attain a given shift is much longer still. For example, after a stress duration of $10^3$ sec with $V_s$ = -4.0v, the shift in the flat-band voltage of the residual film is 0.37v while the composite film has $\Delta V_{FB}$ = 1.42v. Again, it can be deduced from this that the process creating negative space-charge in the composite film seems to be dominantly in the willemite rather than the residual film.

So far, the discussion of Type-B willemite structures has been confined to moderate field strengths, i.e. less than $10^6$ v/cm. However, some work extending into higher fields has also been carried out. Fig 5.4 shows the effect of high stress voltages on shifting the C-V curve. This shows moderate and high field effects denoted by Regions I and II respectively. It should be noted here that with a negative bias applied to the metal electrode, part of this voltage is dropped across the silicon. In the strong inversion case the drop is approximately 0.5v and therefore negligible compared to the larger stress voltages. For negative values of Vs, Region I of Fig 5.4 shows $\Delta V_{FB}$ rising gradually, with a tendency to saturate after 7.0v. The maximum change in flat-band voltage is less than 1.0v. Region II is defined for stress voltages greater than 10.0v, which corresponds to a field of approximately $10^6$ v/cm. In negative bias, $\Delta V_{FB}$ is seen to rise rapidly for Vs > 10.0v, followed by a slight saturation for voltages between -17.0 and -18.0 v. Surprisingly, for any further increase in stress voltage, $\Delta V_{FB}$ is seen to decrease. Such results can be interpreted in terms of the space-charge distribution in the film. For Region II, the build-up of negative space-charge in the composite film is very rapid continuing until a maximum in the build-up
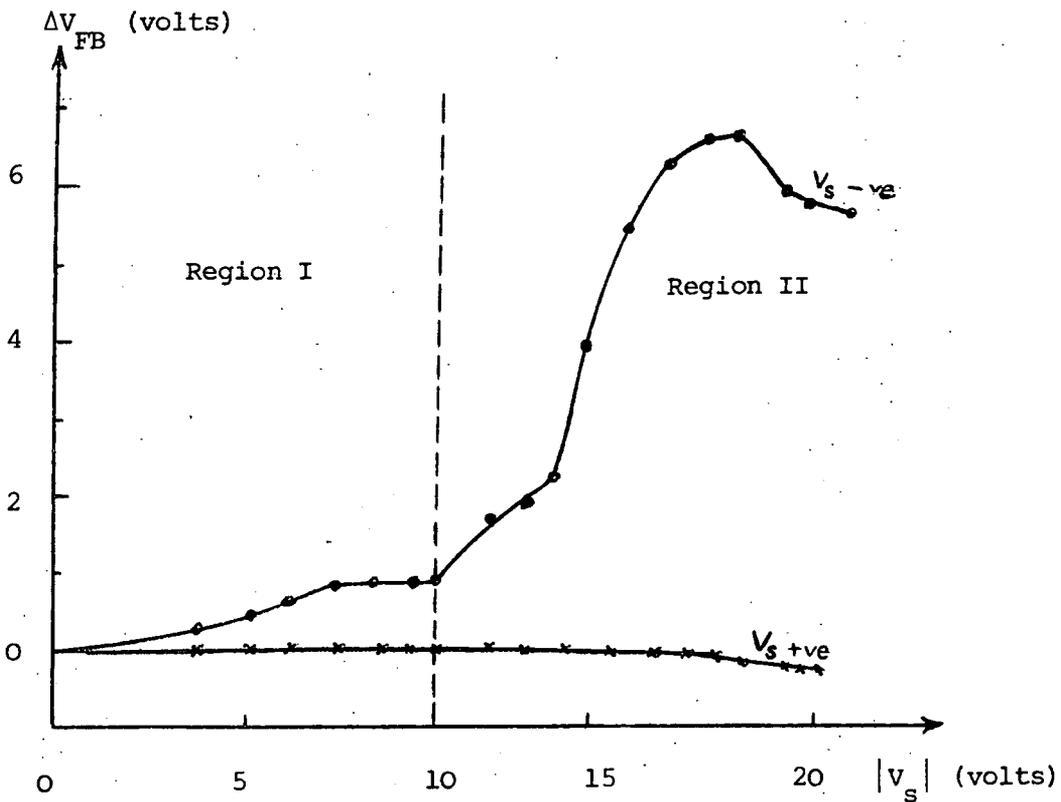
__Fig 5.4__    Change in flat-band voltage with stress voltages of both
polarities.  Stress time, 1 sec ; initial flat-band
voltage, -1.08v.  Regions I and II represent moderate
and high field regions respectively.
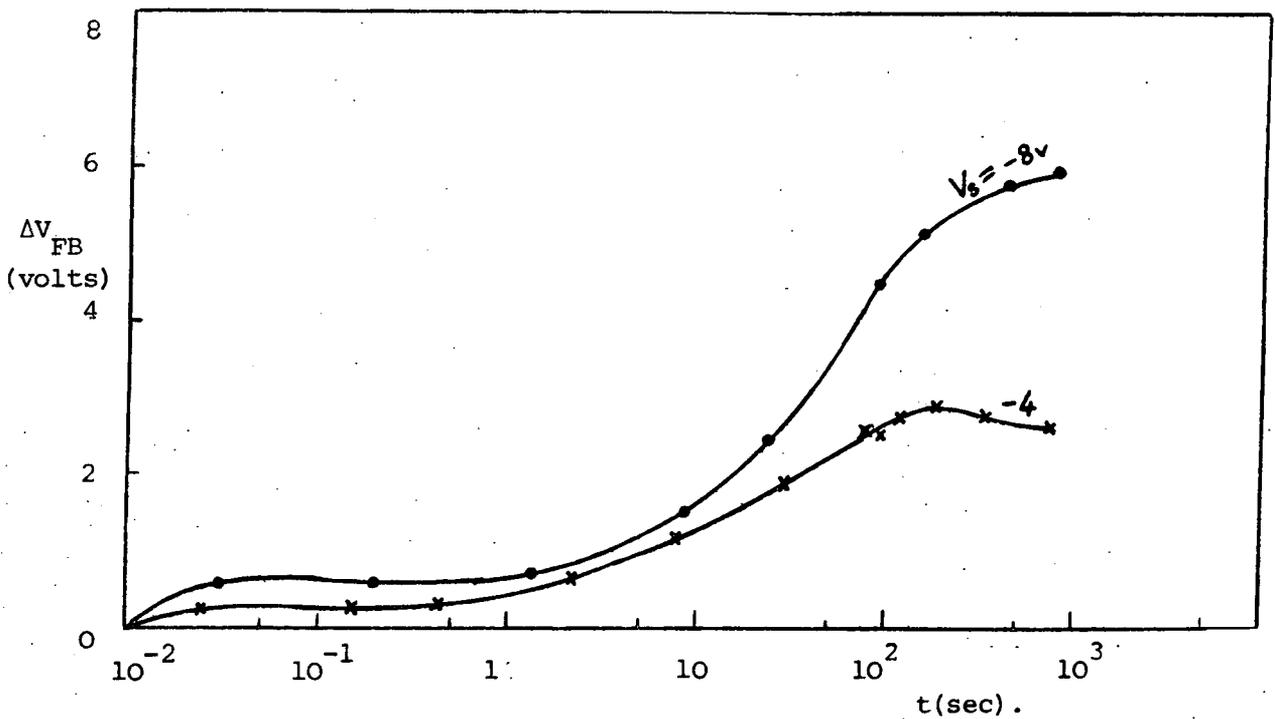


__Fig 5.5__    Change in flat-band voltage of the composite structure with
stress duration for two different stress voltages.
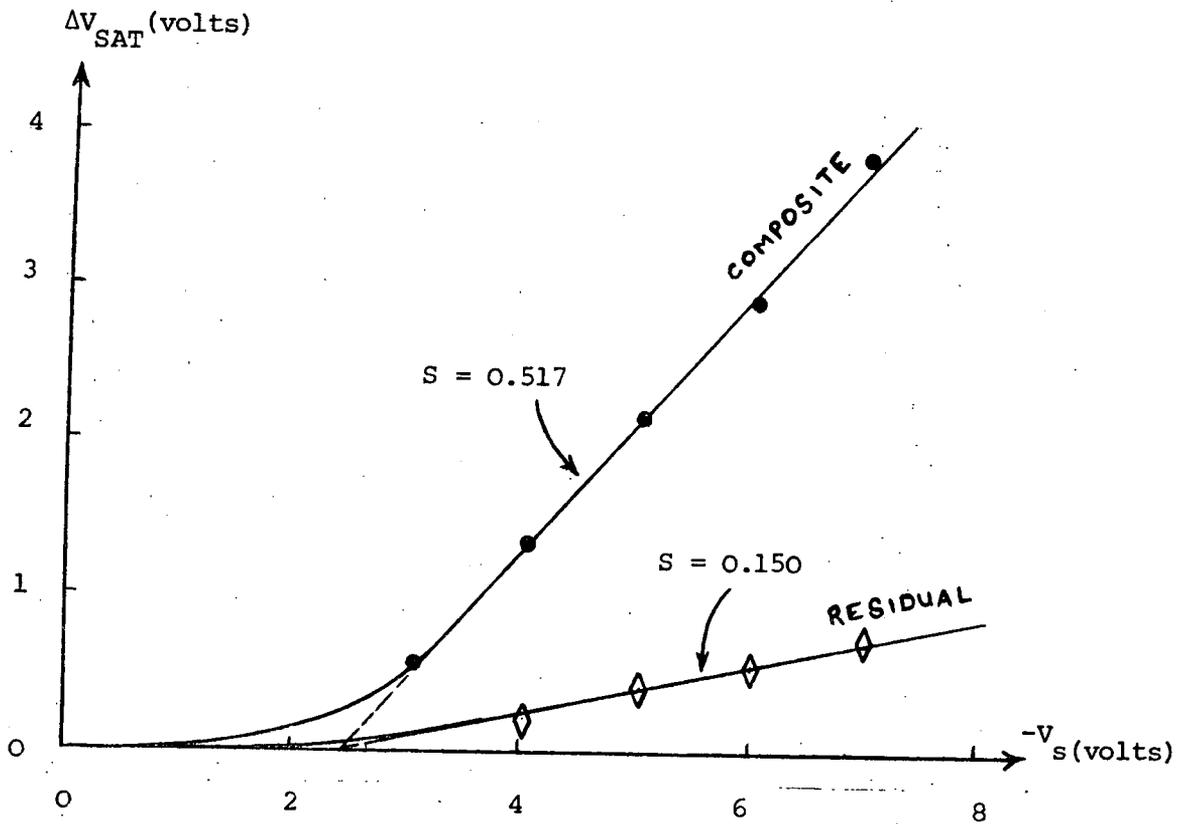
**Fig 5.6** Plot of flat-band saturation voltage against stress voltage for composite and residual film structures of Type-B willemite. Initial flat-band voltages :- composite -1.08v, residual film -0.88v.
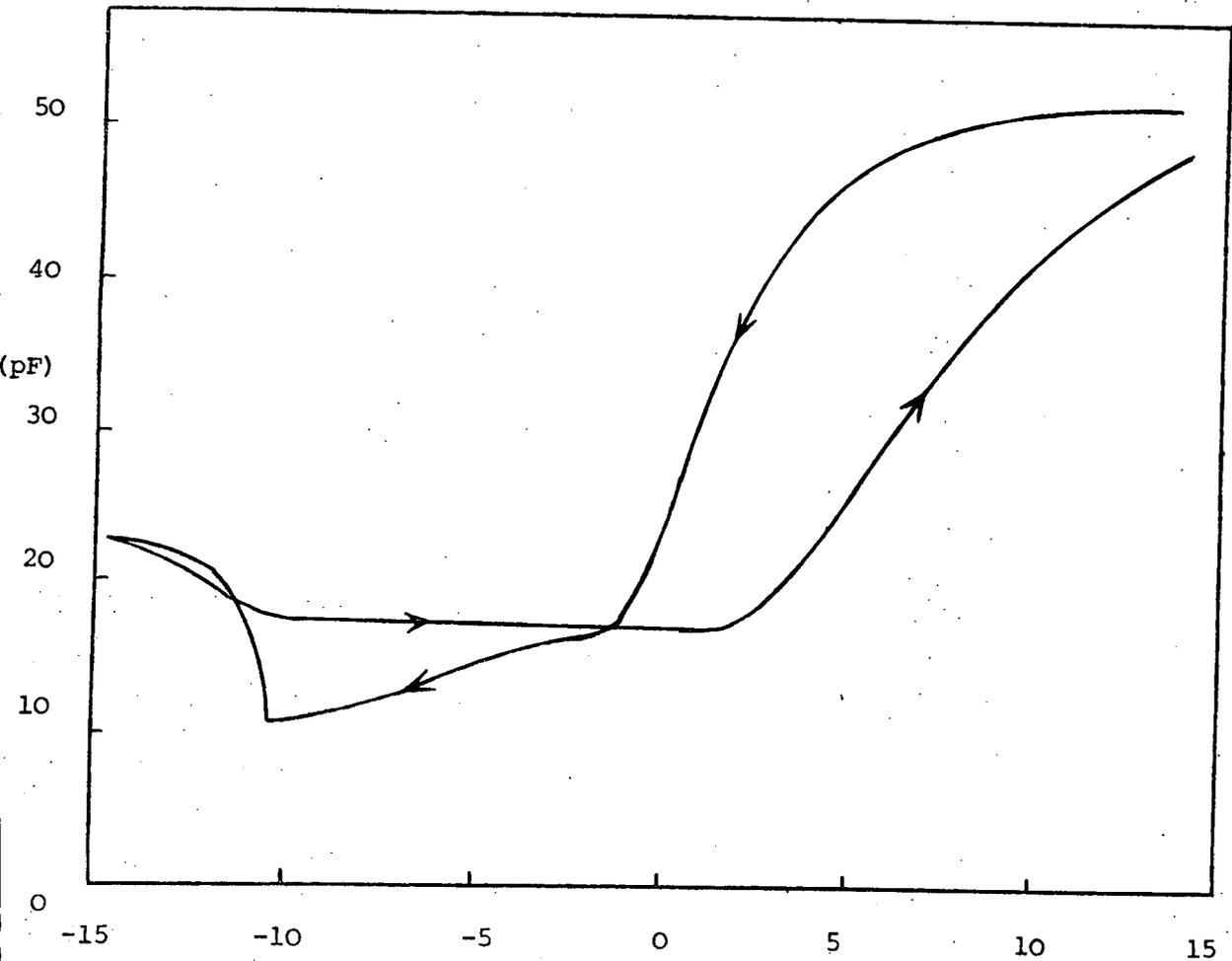


**Fig 5.7** High field C-V characteristics of Type-B composite structure. $V_s$ = -12.0v applied prior to measurement. Arrows indicate direction of sweep, starting at +15.0v.

is reached. The highest applied voltages must result in a loss of some of the negative space-charge that has been built-up previously. The fact that positive stress voltages do not produce any appreciable flat-band shifts is confirmed by the result shown in Fig. 5.4.

The flat-band saturation voltage, i.e. the value of maximum $\Delta V_{FB}$ for a given stress magnitude, against the stress voltage plot of Fig 5.6 shows a good linear relationship for both composite and residual film structures above about 3 volts. The slope of the line for the composite structure is 0.517 while that for the residual film is 0.150.

Fig 5.5 presents measurements of the change in flat-band voltage for the composite structure with duration of stress. For both stress voltages, -4.0v and -8.0v., $\Delta V_{FB}$ increases only slightly until at about 1 sec. where the increase appears to be more rapid on a log scale. Ultimately, $\Delta V_{FB}$ reaches a saturation value. With -4.0v stress this occurs at 160 sec. and with -8.0v at $10^3$ sec. It should be noted that the results presented in Fig. 5.5 are for the case of moderate fields, Region I, only.

A further feature was observed in the C-V curves of the composite structure with high applied fields. This effect happens after the structure is subjected to a high stress, either positive or negative, for some considerable time. For example Fig 5.7 shows a typical C-V curve for a composite film that has previously been subjected to a stress voltage of -12.0v for 1 sec. so as to achieve a positive value of $V_{FB}$. The C-V measurement covers a range of ±15.0v, starting from +15.0v. In the forward sweep, instead of going from depletion into inversion, the capacitance of the structure keeps on decreasing with increasing negative voltage until at about -10.5v when it suddenly increases again. This increase is accompanied by some considerable conductance of a few $\mu\Omega^{-1}$ rising with the sweep voltage

between -10.0v and -15.0v and back again.   In the return sweep the
capacitance is quite similar until -10.5 v, after which its value
remains constant at 17.2pF right up to +1.8v.   This is a strong inversion
characteristics as opposed to the deep-depletion characteristic in the
forward sweep.   In terms of the semiconductor, it can be deduced that
in the forward sweep the silicon surface is unable to accumulate holes
until after the high negative voltage has been applied.   This change
is probably related to the appreciable conductance observed between
-15.0v and -10.0v.   Later, the return sweep also produces a more
positive flat-band voltage, a value of 9.4v as compared to 2.7v for the
forward sweep.   This must be due to a net increase in the negative space
charge within the composite film after the structure has been exposed to
the high negative measuring voltage.

The variation of the capacitance of the residual film with
frequency over the range 1-300 kHz was also measured.   Fig 5.8 presents
the result plotted for the two dc bias voltages of 0.5 and 4.0v i.e. in
accumulation mode.   The dielectric constant calculated for a film thick-
ness of 226 $\overset{o}{A}$ and an area of $1.03 \times 10^{-3}$ $cm^2$ is about 3.53 at 1 kHz
dropping to about 3.33 at 30 kHz and above.

One feature absent in Type-B compared to Type-A willemite is
the "breakdown" phenomenon which was never observed with the former even
though extremely high fields of up to about $2 \times 10^6$ v/cm were subjected
to the structure.   In the absence of this phenomenon it was possible to
measure the recovery of the flat-band voltage after shifting it with a
negative applied stress.   The recovery was far more rapid if a positive
voltage was applied.   Alternatively the sample could be heated to return
the flat-band voltage in a negative direction.   Results of experiments
of both types will be presented.
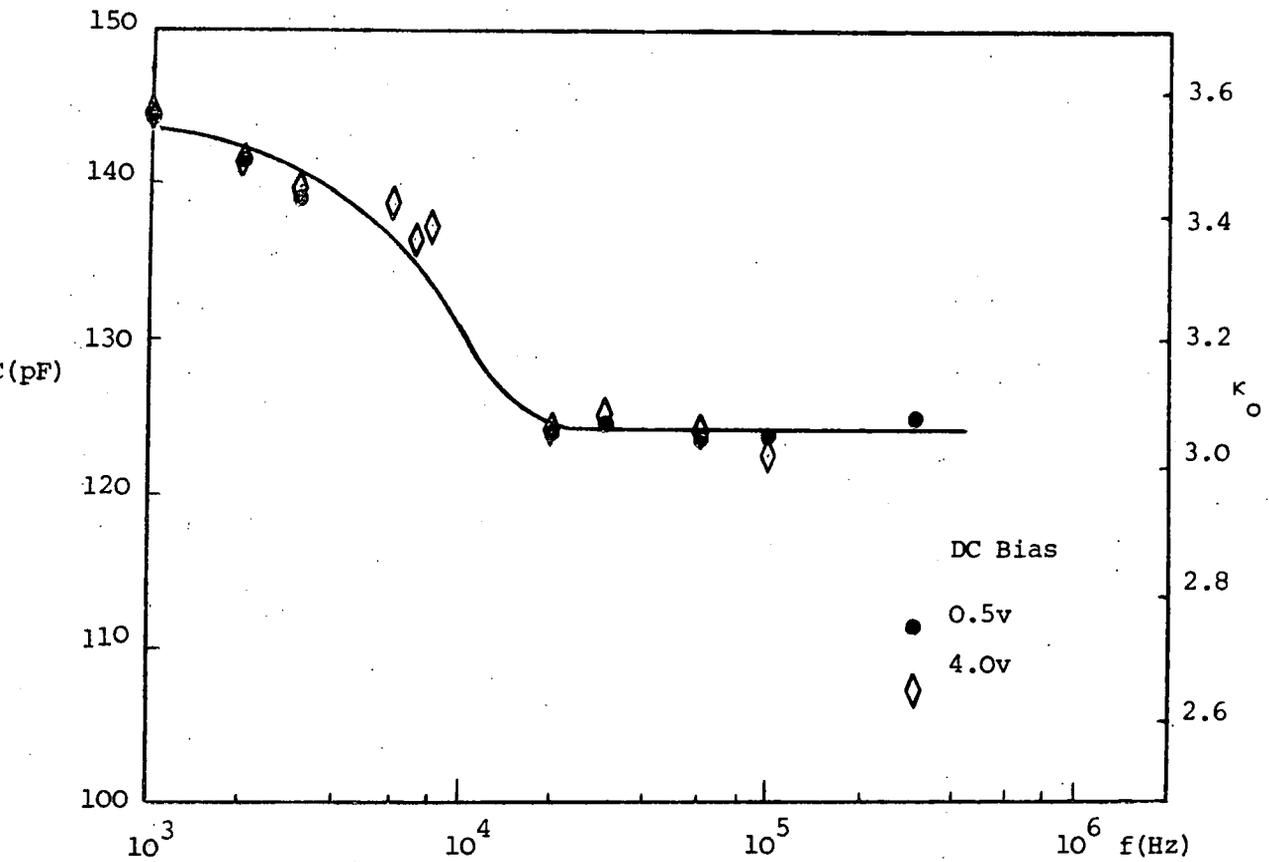
Fig 5.8    Variation of capacitance of the residual film with
           frequency for two different applied voltages.
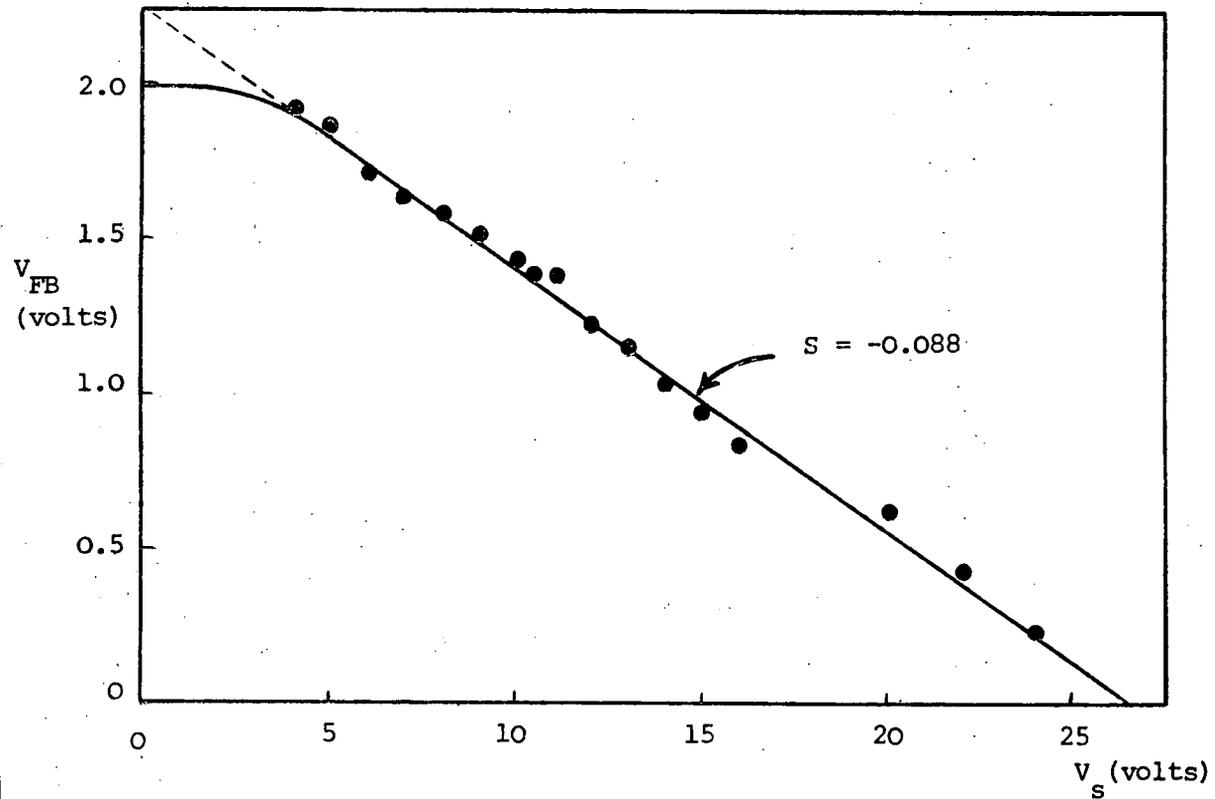


Fig 5.9    Recovery of flat-band voltage with positive stress
           voltage.    Initially $\Delta V_{FB}$ = +3.0v after negative stress.
           Duration of stress, 1 sec, for each step.
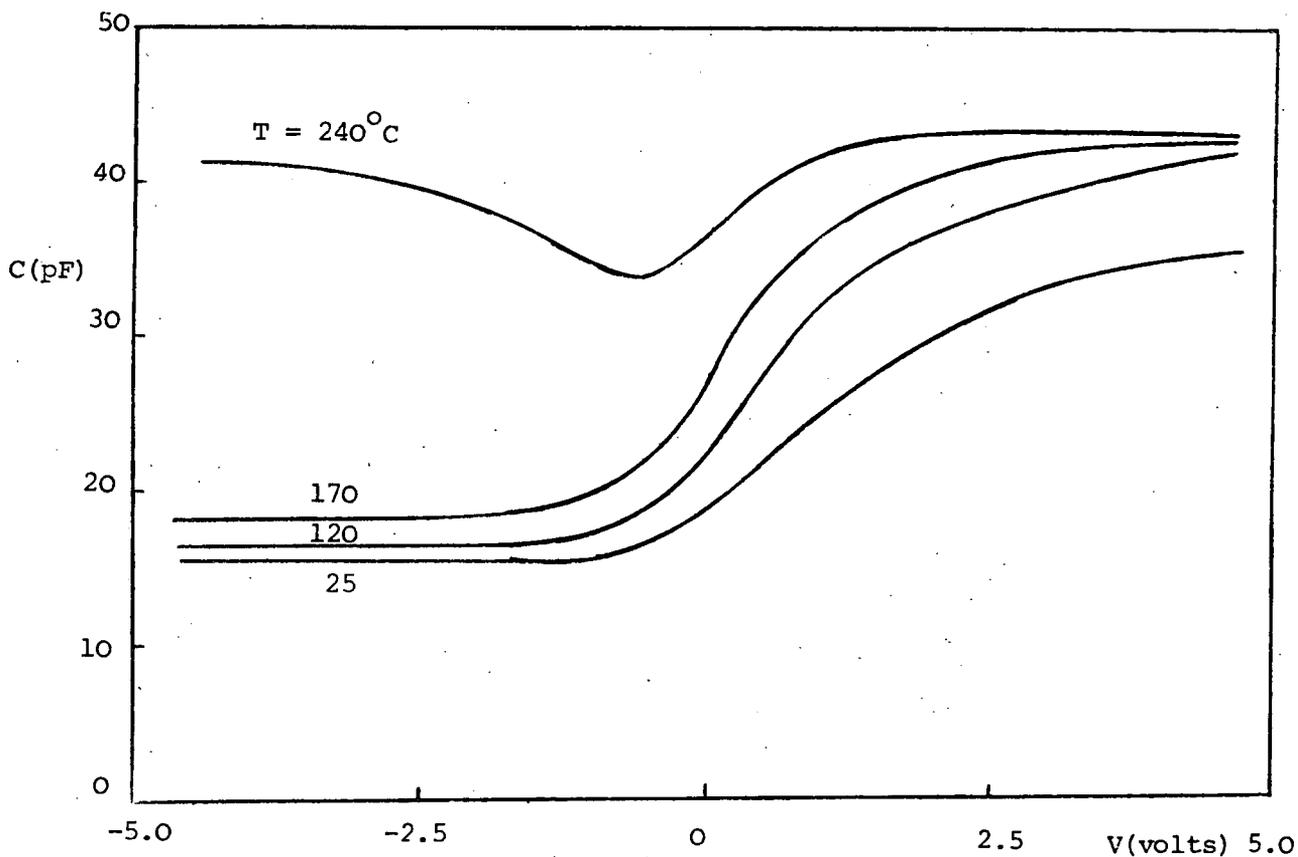
Fig 5.10    C-V curves of a composite structure measured at increasing

temperatures.  Prior to measurements a negative voltage

was deliberately applied to acquire a positive flat-band
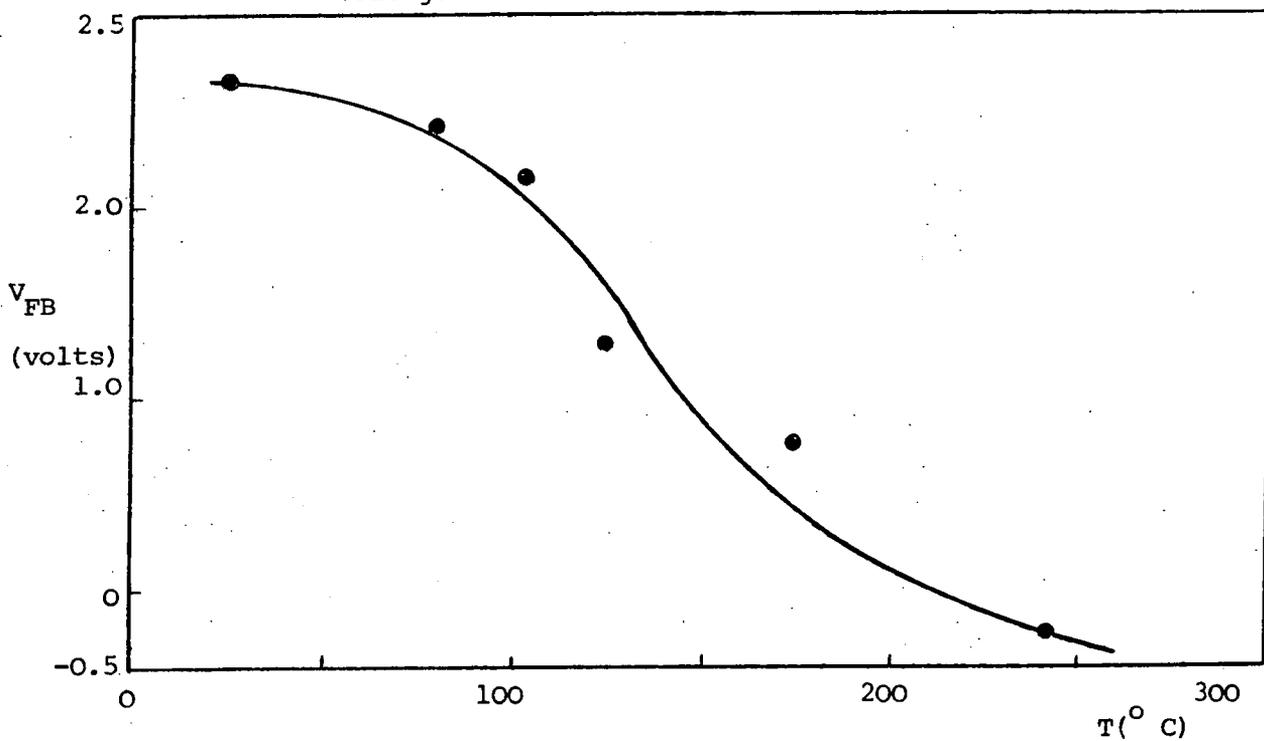
voltage.



Fig 5.11    Recovery in flat-band voltage of C-V curves with increase

in temperature for the composite structure.  Structure has

been negatively pre-stressed to achieve  a positive flat-

band voltage.

The following is an example of an experiment on flat-band voltage recovery by means of a positive stress. The composite structure was negatively stressed to achieve a +3.0v change in flat-band voltage, after which increasing positive stress voltage steps were applied consecutively to the structure for 1 sec. The result is shown in Fig.5.9 where the recovery in flat-band voltage is almost proportional to the applied voltage. However, this recovery does not happen as readily as the shifts in the opposite direction since the slope of Fig. 5.9 is only 0.088 as compared to 0.517 for Fig. 5.6. These results indicate that Type-B willemite is capable of losing some of the negative space-charge that it had previously acquired unlike Type-A willemite.

A more pronounced effect can be observed from Fig 5.10 where C-V measurements were taken at elevated temperatures. Prior to the measurements, the composite structure was stressed with a negative voltage in order to give a positive flat-band voltage value, as depicted by the $T = 25^{\circ}C$ curve. At high temperatures, the curves are seen to be pulled back towards the zero voltage axis and there seems to be a corresponding increase in the depletion region slopes. As described in Section 3.4 of Chapter 3, the increase in $C_{min}$ at high temperatures is due to the increase of the carrier generation rate in the silicon. At $240^{\circ}C$ the negative bias capacitance approaches $C_{max}$ as it would for a low frequency C-V curve at room temperature. The recovery of the flat-band voltage with temperature is shown in Fig. 5.11 where the initial value was about 2.65v. The change is more rapid above about $100^{\circ}C$. These results show that temperature has the effect of assisting the reduction of negative space-charge that has been separated within the composite film by negative voltage stressing.

B. Composite Structures with dw < do

Results in this category are from slice SL4. From Table 5.1 it can be seen that the thicknesses of the composite and residual films

were 861 and 636 Å respectively resulting in a ratio of (dw/do) < 1. This implies that the composite film is mainly made up of the residual film material rather than willemite. From the $C_{max}$ values and film thicknesses, the average dielectric constants for the composite and residual films are found to be 3.40 and 5.13 respectively. The value of the willemite film dielectric constant $\kappa_w$ work out to be 1.94, which is rather small. Inaccuracy may result from such calculation because of the extremely thin willemite film. These values are quite the reverse of the previously discussed results. Another difference is in the relatively small value of $C_{min}$, about 13.1 pF, measured for the composite structure.

Fig. 5.12 shows typical C-V plots for the composite structure which are really very different from the cases discussed previously. Firstly, the C-V curves are capable of being shifted by positive as well as negative stress voltages in this case. Also, the negative stress produces a comparatively small shift compared with the earlier samples of both Type-A and Type-B willemite. A -10.0V stress voltage applied for 3 minutes now results in a flat-band change of only + 0.20 V. On the other hand, positive stress voltages produce considerable C-V shifts towards more negative flat-band voltages in this type of sample. A further difference is that the negative stress does not result in any appreciable decrease in the slope of the C-V curves although positive stresses give a considerable lowering.

The changes of flat-band voltage due to positive stress, obtained from such C-V curves, are plotted for both the composite and residual films in Fig 5.13. Surprisingly, the change for the residual film does not differ much from that for the composite, which indicates that the composite structure characteristic is largely determined by the residual film. This would be expected because of the much thicker residual film as compared to the overlying willemite layer. With
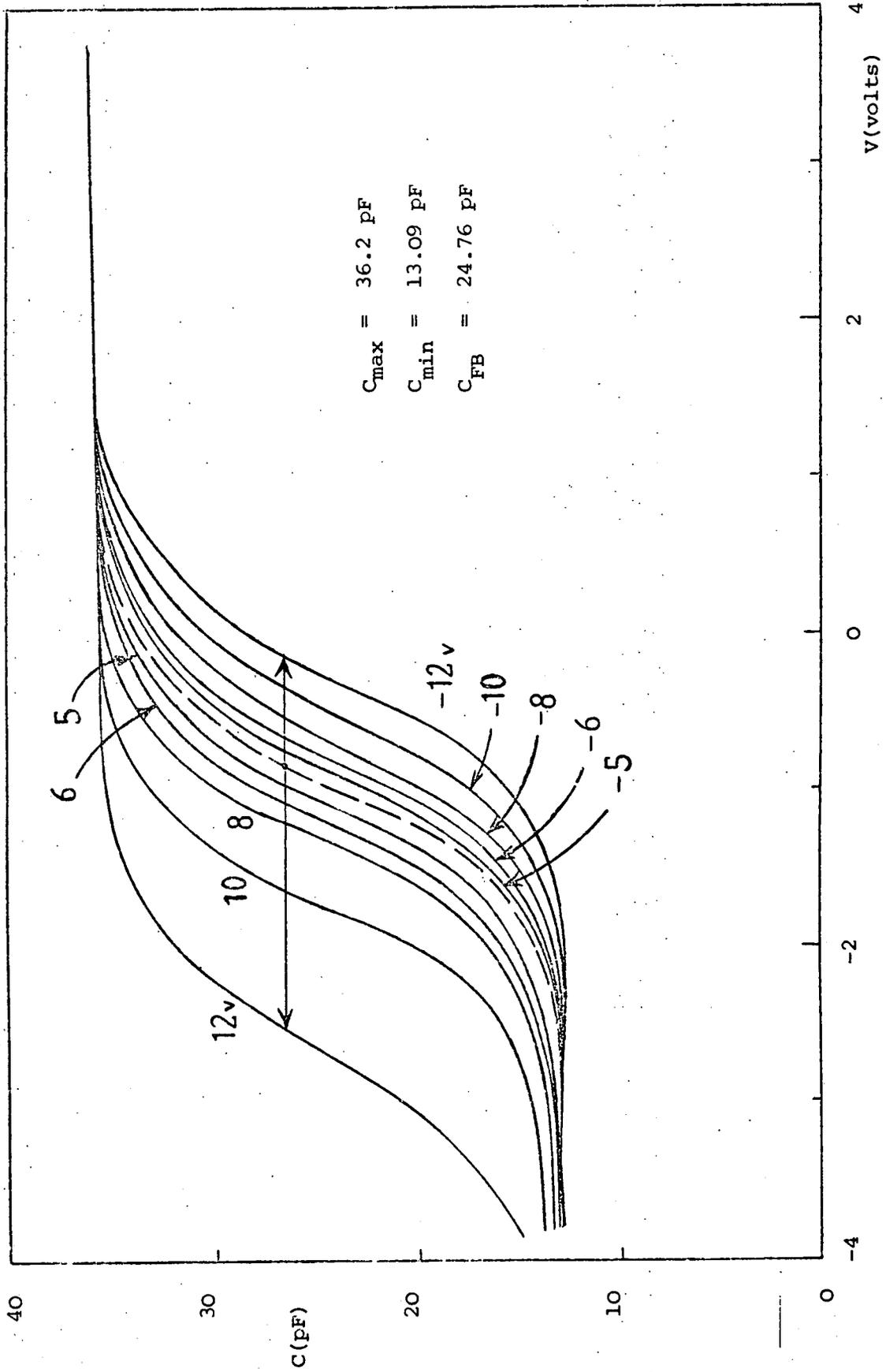
Fig 5.12    C-V curves with both positive and negative stress voltages applied to composite structure of Type-B willemite for the case, dw < do. Dashed line is initial curve. Stress time, 3 min for each step.
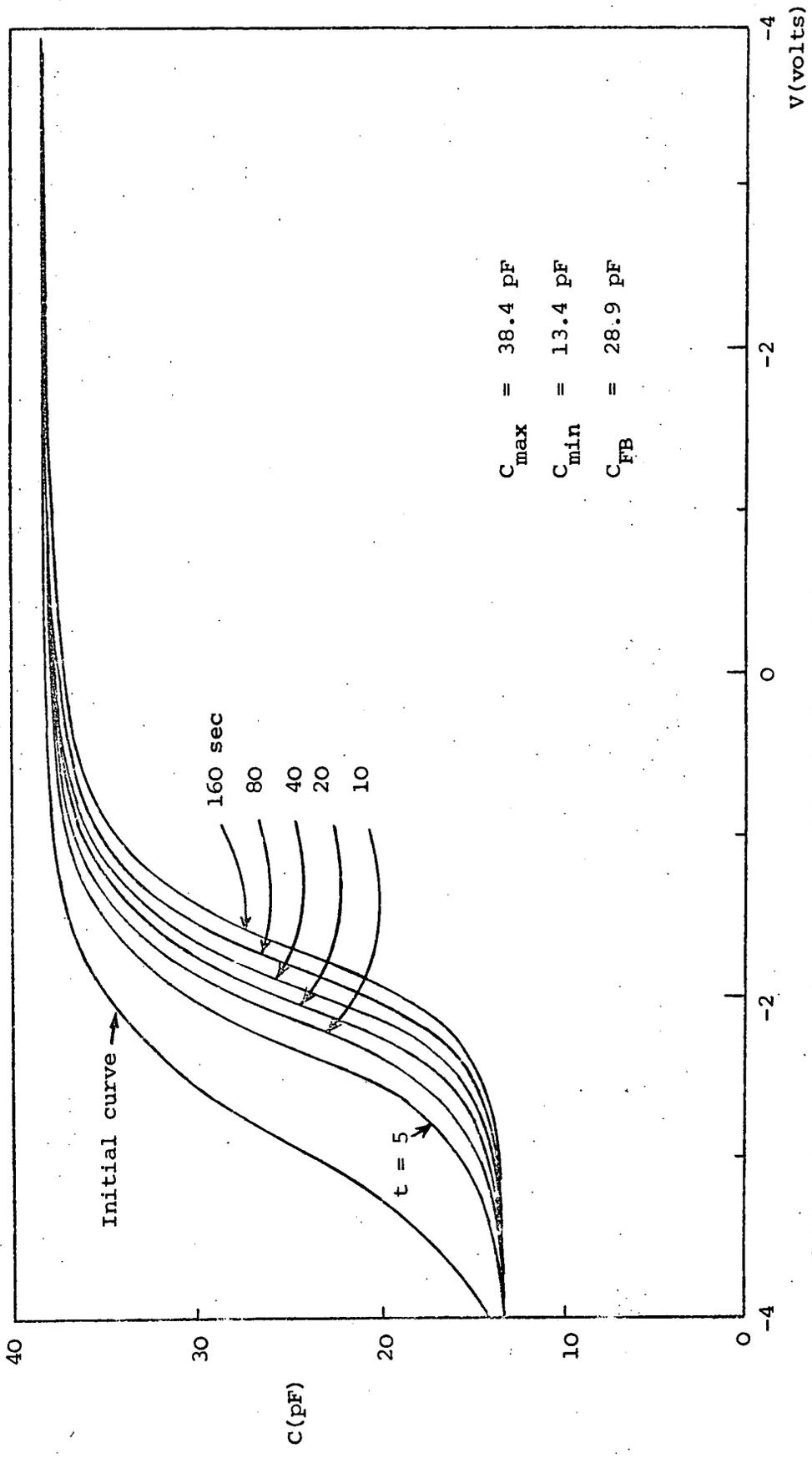
Fig 5.14    Recovery of C-V curves with time by applying a recovery voltage of -10.0v.
The curve for t = 0 is achieved by positive stressing of virgin structure.
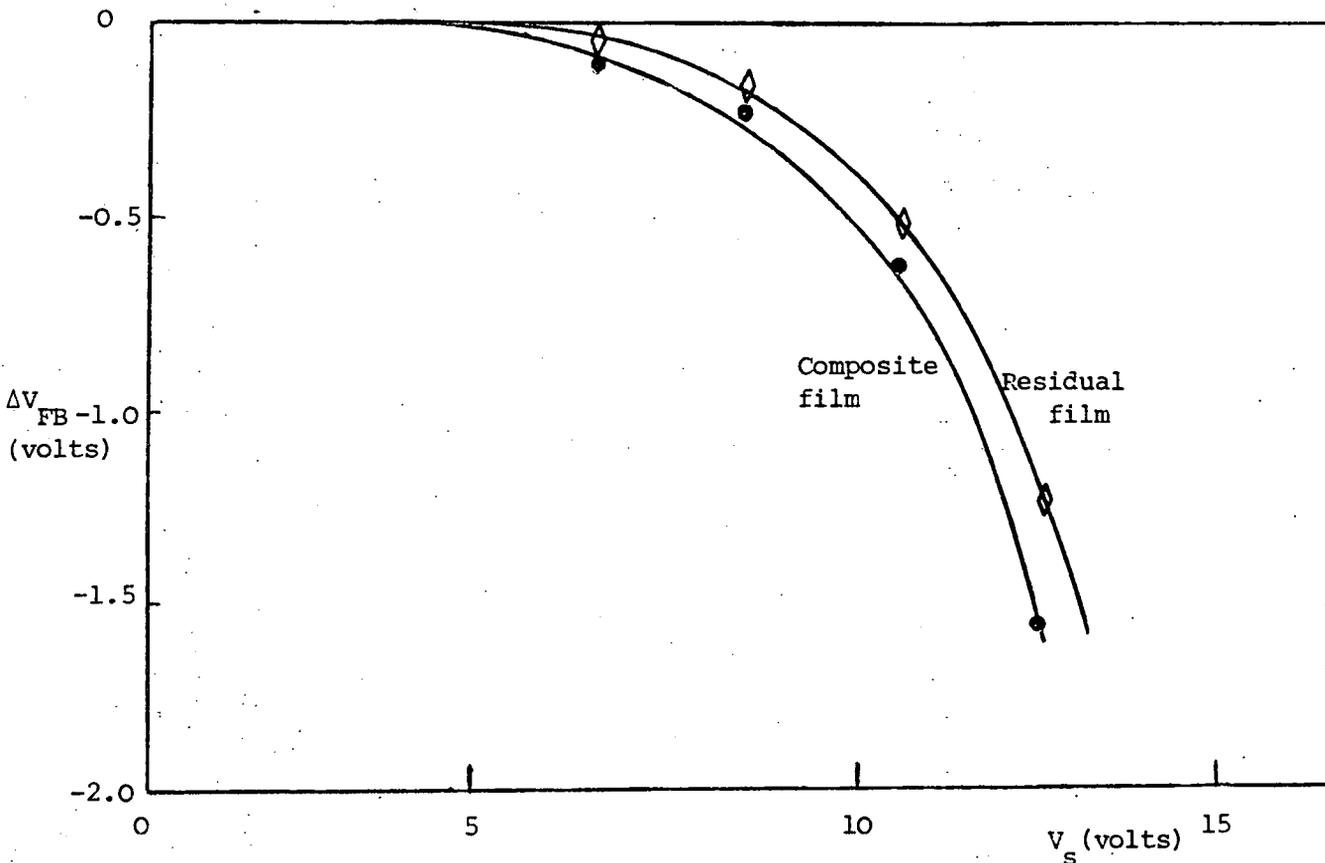
**Fig 5.13**    Change in flat-band voltage with positive stress voltages
for composite and residual film structure.
Stress time, 3 min.
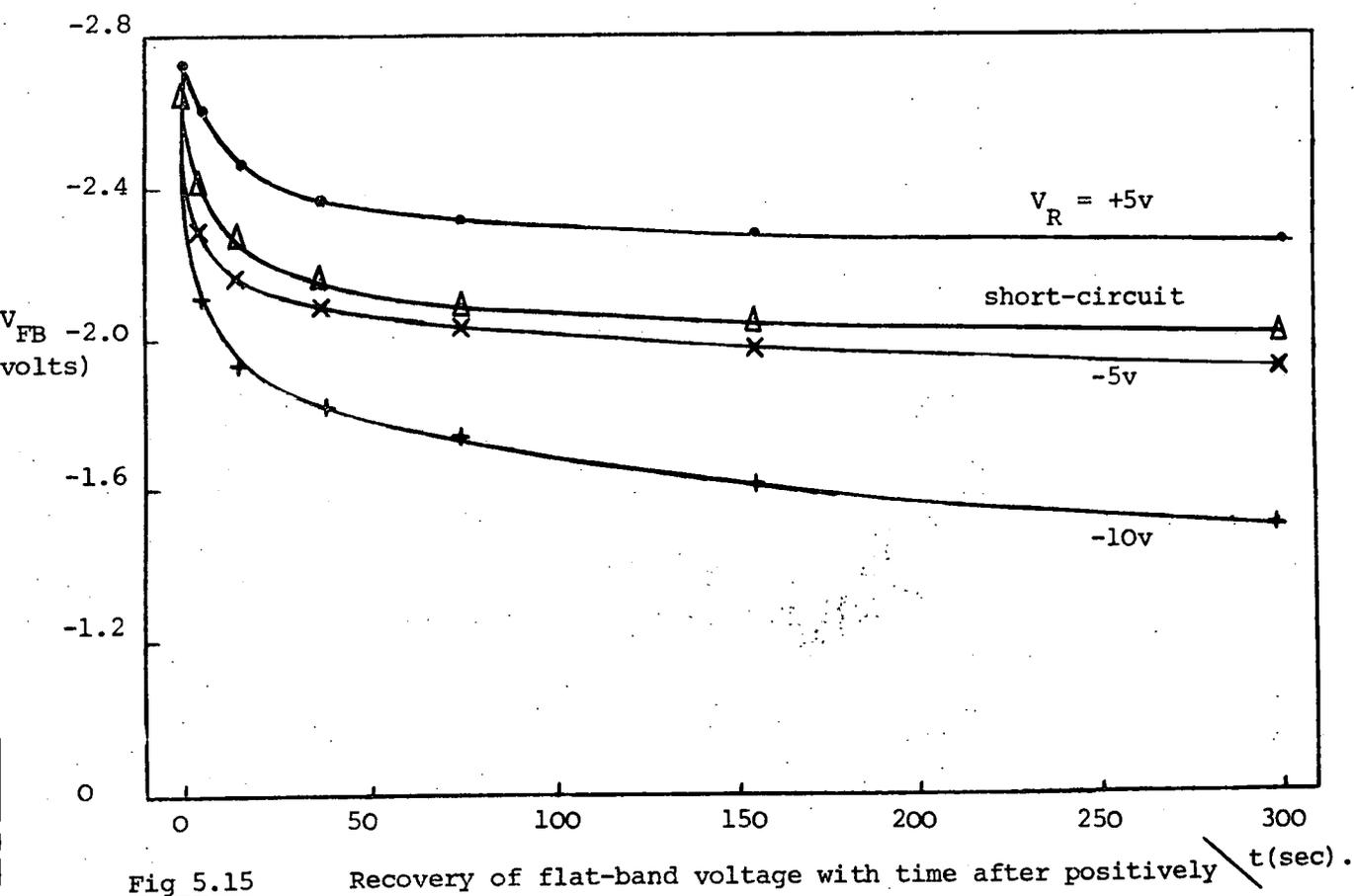


**Fig 5.15**    Recovery of flat-band voltage with time after positively
stressing the composite structure. Voltage applied during
recovery is as indicated.

positive values of $V_S$ up to about 7.0v, the flat-band change is very small but this rises rapidly from 8.0v up to about 12.0v although higher voltages were not tried.   Compared to the previous composite structures, the change in flat-band voltage occurs at considerably higher voltages so that the measuring voltage in the range $\pm$ 4.0v makes an insignificant contribution towards the shifts.  Furthermore, the stress voltages require to be applied for longer time to have an appreciable effect ; 3 mins in this case compared to 1 sec. in the previous. Instead of separating negative space-charge within the composite films, it seems here that positive space-charge  is more important.   From Fig 5.13, one can also infer that the positive space-charge occurs within the residual film and/or at its interface with the silicon rather than in the willemite itself.

Another feature of this type of composite structure is the comparatively rapid recovery of its flat-band voltage.   For example, if the composite structure is stressed so as to achieve a large negative flat-band voltage then a fast recovery is observed on applying a negative voltage.   In Fig 5.14, a positive stress has resulted in a flat-band voltage of -2.66v and then consecutive applications of -10.0v for increasing times are seen to shift the flat-band voltage towards less negative quantities again.  Simultaneously there is also a recovery in the slope of the C-V curves towards that of the initial curve.   The effect of voltage on recovery is shown in Fig· 5.15.  The initial shift in flat-band voltage was acquired by applying +12.0v for 3 min.   The recovery of flat-band voltage is most rapid in the first 20 sec, following which there is only a gradual recovery depending on the magnitude of the applied voltage $V_R$.   It can be seen that with -10.0v across the structure the recovery is largest, about 1.0v in 100 sec., while with +5.0v some recovery also occurs in the first 100 sec after which it almost

saturates. Comparison of the curves for +5 and -5v shows that the
latter has only a small effect compared with the short-circuit case.
The results presented indicate that for this type of sample the recovery
in flat-band voltage is very dependent on the magnitude and polarity of
the recovery voltage $V_R$, with very rapid recovery occuring in the first
ten seconds.

5.4     Analysis of Results

        The results described in Section 5.3 will now be discussed,
starting with those on the silicon and proceeding to the composite and
residual films of the two types.

        The Schottky barrier $1/C^2$-$V_r$ plot has shown the existence
of acceptor-type traps in the silicon (see Fig. 5.1) after etching off
the willemite. This deduction is made on the basis that the experi-
mental points all lie above the ideal curve, contrary to the donor-type
case described in the last chapter. Since the two possible metallic
atoms that can get into the silicon from the initial $ZnF_2$:Mn are zinc
and manganese, it is reasonable to expect that they can be responsible
for the deep trapping levels. Zinc is an acceptor and manganese a donor
in silicon. Although manganese makes up a very small proportion of the
total metallic atoms, for the short reaction-bake time it appears that
manganese predominates in the silicon. But for the long baking-time of
the present willemite, zinc dominates the electrical characteristics of
the silicon rather than the manganese. Zinc has two acceptor-type levels
in silicon (3) at 0.31 eV and 0.55 eV from the valence band. The
theoretical curve presented in Fig.5.1 assumes that only the upper level
is active for calculations made using the Sah-Reddi theory for deep-
levels as in equation (3.5). The trapping concentration is also
assumed to be uniform and the theoretical case is the high frequency one
only ; reasonable enough considering that the measuring frequency was
5 MHz.

The best theoretical fit for the experimental points gives a trapping concentration of $9.6 \times 10^{14}$ cm$^{-3}$ for zinc and this value is the net trap concentration. It may include a contribution from manganese levels but their effect, being of opposite sign, is neutralized by the larger zinc concentration. Chang and Tsao (4) have reported work on zinc-diffused MOS structures and they indicated that the value of $C_{min}$ in n-type silicon will be reduced because of the existence of zinc atoms in the silicon. This is indeed found to be the case for the composite structures, where $C_{min}$ for SL7 and SL10 are found to be 18.5 pF and 17.3 pF respectively as compared to the calculated value of 19.8 pF neglecting the traps.

As mentioned in Section 5.2, the dendritic features in the silicon are due to material rather than topographical differences. Pohl (5) has reported that zinc diffusion into crystals occurs irregularly depending on preferred orientations with different rates. The preferred penetration channels for zinc in silicon may provide a possible explanation for these dendritic features. This would support the Schottky barrier results which are explained by zinc atoms providing the deep acceptor-type traps. However, from the ECP observation, the crystallinity of the silicon surface still exists and this is important when considering for later discussion of the electrical results which will assume that the silicon is non-degenerate.

The discussion of the composite and residual film results will consider the two cases as in Section 5.3.

A. Case of dw > do

In general, composite structures of Type-B willemite in this category behave similarly to Type-A, especially for the moderate field case of Region I. In Section 5.4 the flat-band capacitance $C_{FB}$ was calculated using $C_{max}$, $C_{min}$ and equation (3.10) so that the corresponding

initial flat-band voltage $V_{FBO}$ could be extracted from the C-V plot.

The initial concentration of charges within the films concerned can then be estimated using equation (4.2) by inserting the values of $V_{FBO}$. Taking $\phi_{ms}$ = -0.7 v (3) and results for SL10 from Table 5.2, the initial charges within both the composite and residual films are found to be positive, with concentrations of $1.25 \times 10^{11}$ cm$^{-2}$ and $1.37 \times 10^{10}$ cm$^{-2}$ respectively. The difference between these two quantities, i.e. $5.13 \times 10^{10}$ cm$^{-2}$, is therefore the positive charge concentration in the willemite film itself and/or at its interface with the residual film.

It is appropriate at this point to attempt an analysis of the residual film before discussing the more complicated composite structure. Since the reaction-bake process was carried out for a long time it is reasonable to expect that the 200 Å -thick initial silicon oxide must have been completely used up during the reaction. Hence the non-willemite component of the composite film, which is defined as being resistant to acetic acid and non-cathodoluminescent, must be the result of further oxidation of the silicon plus other constituents probably from the zinc fluoride. Further oxidation is very likely since oxygen should diffuse through the voids in the silicate structure of willemite and find its way to the silicon. It is a well established fact that the thermal oxidation of silicon proceeds by the passage of oxygen through the growing oxide so that movement through willemite, being made up of a loose structure, should be even easier. The existence of lattice defects and impurities in the residual film may also have contributed to the trap density calculated earlier.

Although the directions of the flat-band shifts with negative stresses are the same for both composite and residual film structures, the magnitude for the residual film is much smaller than for the composite structure (see Fig 5.5). This may be interpreted in terms of two

different types of polarization phenomena occurring in the residual film and the willemite, with the composite structure characteristic being predominantly from the willemite. One type of polarization phenomenon has been discussed in Section 4.7. It was due to the movement of metallic cations within the silicate network of the willemite after dissociation from the anions . Another type of polarization phenomenon which was proposed by Snow and Deal (6), causes a smaller degree of shift in the C-V curves. Instead of there being relatively unlimited migration of ions within the film, corresponding to an infinite polarizability, the polarization is limited to a finite value. Snow and Deal suggested that this polarization could be due either to the orientation of permanent dipoles uniformly distributed in the bulk, or to interfacial polarization between conducting inclusions and the bulk material ; as shown in Fig 5.16. They called both effects 'dipolar polarization' compared with the inter-facial space-charge polarization discussed in Chapter 4.

The slope of the $\Delta V_{SAT}$ against $V_s$ plot (Fig. 5.6) for the residual film is 0.15. According to Snow and Deal (6), if the polariza-tion is dipolar than a theoretical limit on the slope can be calculated. For phosphosilicate glass, their theoretical value was 0.18. This is contrary to the prediction for space-charge polarization due to ionic movement where the slope is usually found to be in excess of 0.50. It therefore seems likely that the residual film has the smaller dipolar polarization property.

From the residual film C-V curves of Fig. 5.2 (b) a lowering of the slope is observed and it is very likely that this is due to the inhomogeneous distribution of the polarizing effect (7), Of the two types of dipolar polarization, the one most likely to be inhomogenous is the mechanism due to conducting inclusions existing within the residual film, particularly if those inclusions are non-uniformly distributed.

Metal | Residual Film | Silicon



(a)



(b)
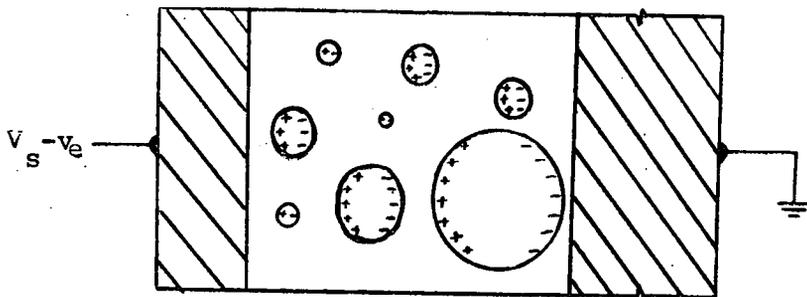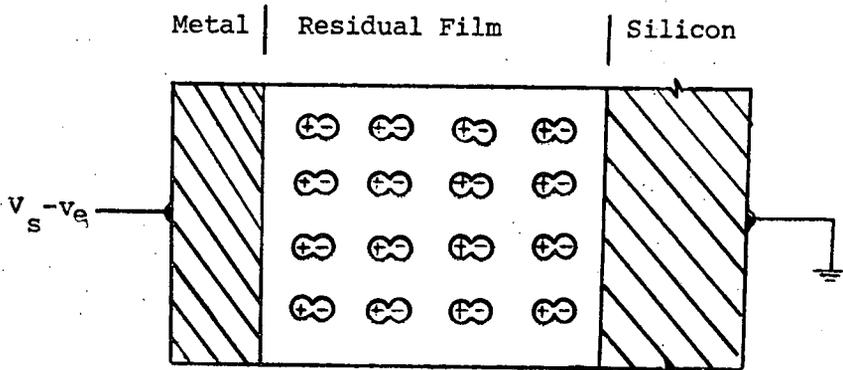
Fig 5.16    Schematic illustration of the possible dipolar
            polarization processes giving finite polarizability.

            (a) the orientation of permanent dipoles,

            (b) interfacial polarization of conducting
                inclusions.

            (after Snow and Deal (5)  ).
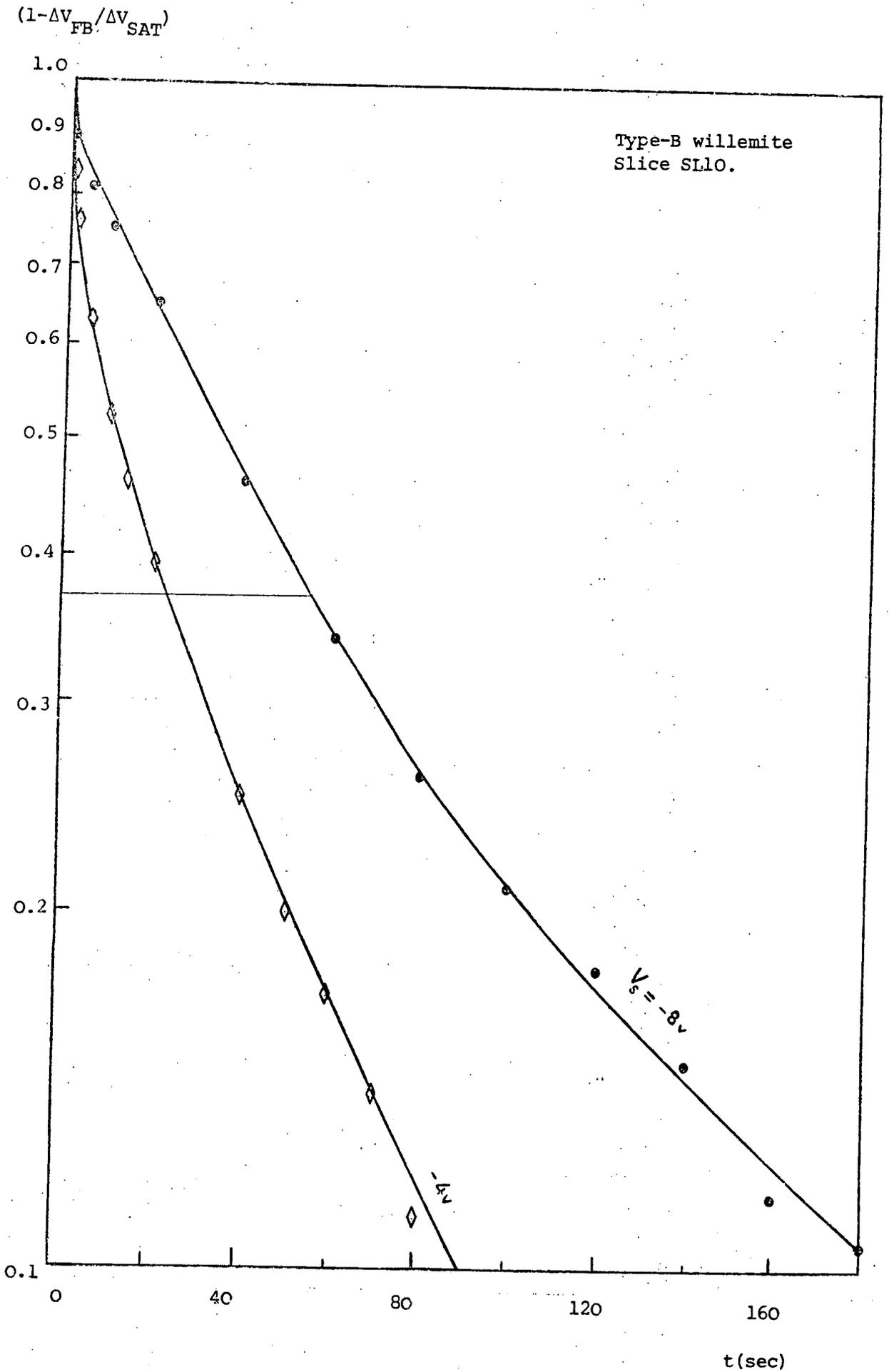
**Fig 5.17** The rate at which the flat-band shift approaches its saturation value for two different stress voltages. Data are derived from Fig 5.6.
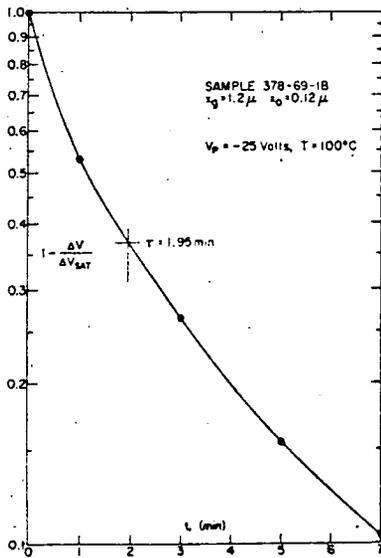
Fig 5.18
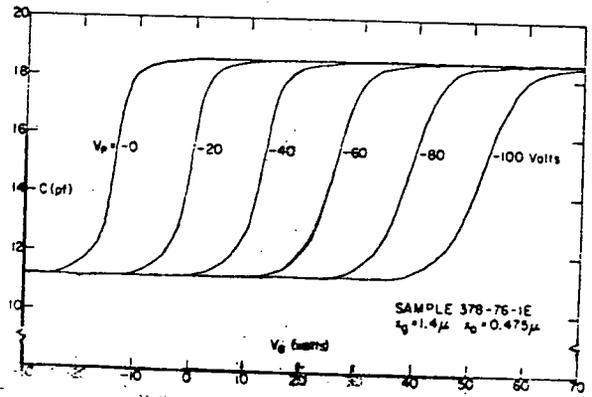


Fig 5.20
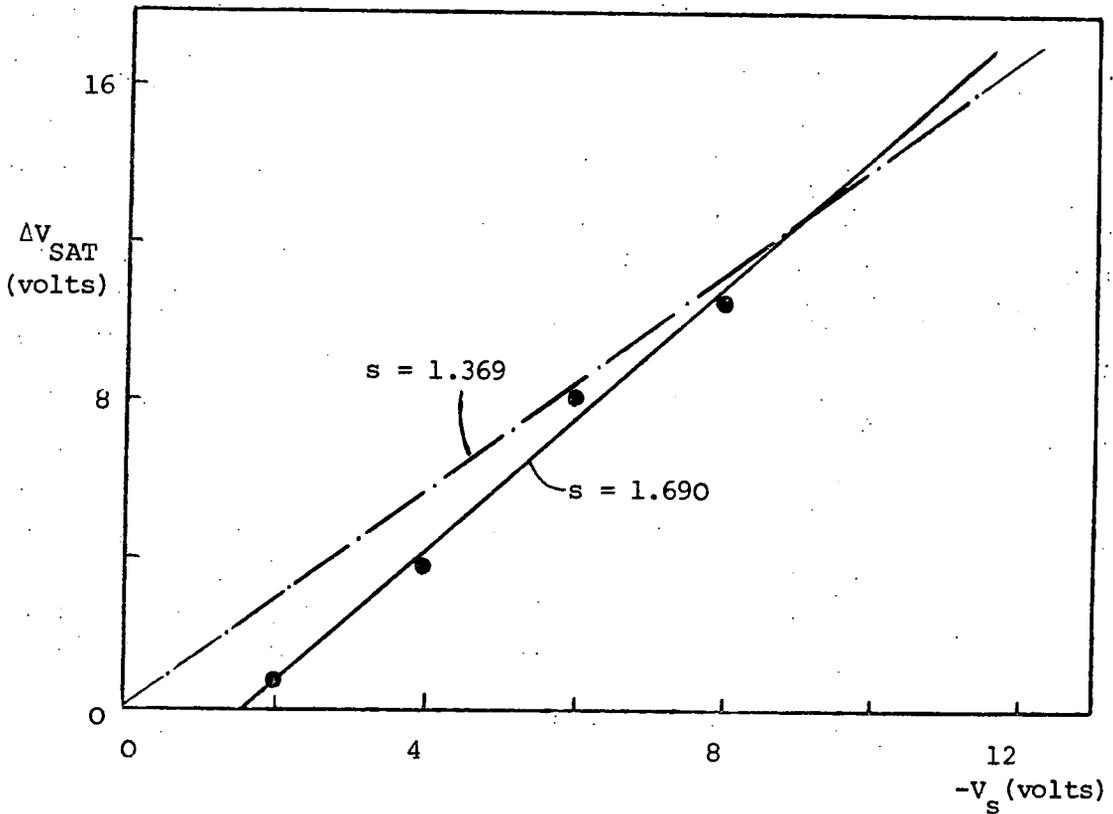


Fig 5.19

Fig 5.18    A plot of $(1-\Delta V_{FB}/\Delta V_{SAT})$ $V_s$ t for borosilicate glass/
silicon dioxide/silicon structure (after Snow & Dumesuil).
Note non-linearity of curve.

Fig 5.19    Comparison between experiment and theory for $\Delta V_{SAT}$ versus
$V_s$ for Type-B willemite structure. Dashed line is for theory
using $\kappa_o$ and $\kappa_T$.

Fig 5.20    C-V curves of borosilicate glass on n-type silicon showing
positive going shifts with negative stress voltages
(after Snow and Dumesuil).

Such conducting inclusions can arise from the dendritic features

clustering in preferred directions as observed.  It is possible that

these inclusions are of zinc and/or manganese.

However, the polarization phenomenon in the residual film only

accounts for a small shift of flat-band voltage, and therefore any treat-

ment of the composite structure as a whole can neglect this effect,

especially in Region I fields.  In other words, analysis of the composite

structure at moderate fields will, apart from the initial concentration

of positive charges, assume that the residual film plays a passive role,

i.e. the polarization is due to the willemite only.  The slope of the line

in Fig 5.6 for the composite structure is 0.517 which is too large to be

interpreted as due to dipolar polarization.  Because the present composite

structure results are similar to those for Type-A willemite, the analysis

that is to follow will be the same.  Here again, the model will neglect

the initial positive charges in the composite film and assume that the

willemite film consists of a concentration of N immobile negative ions

compensated by an equal number of mobile positive ions.  The equations in

Section 4.7 as derived by Snow and Dumesnil (8) will be used with the

experimental values for the change in flat-band voltage against stress

time.

From Fig 5.5, a plot of $(1 - \Delta V_{FB}/\Delta V_{SAT})$ against stress time

can be made.  The values of $\Delta V_{SAT}$ for - 4.0 v and -8.0 v, stress voltages

are taken as 2.37 v and 6.00 v respectively.   The result, plotted in

Fig 5.17, is found to be comparable to that for borosilicate glass on

silicon oxide by Snow and Dumesnil (see Fig 5.18).  As in their case,

the graph is curved rather than the linear prediction of equation (4.6),

and a similar explanation to theirs seems to be possible.  The non-

linearity is attributed either to a distribution of ionic mobilities or

to field-dependent mobility.  As the polarization builds up the field

in the bulk of the willemite decreases from about $10^5$ v/cm to zero.

Thus, if the mobility decreases with the decreasing field the graph will

be curved in the direction found.

The rate of change of $V_{FB}$ here is slower than for Type-A

willemite. For $V_s = -4.0$ v, the time constant from Fig 5.17 is 22.5 sec.,

while for the previous willemite it was approximately 1.15 sec at -3.0v.

This indicates that the present willemite has a more stable structure.

This is separately supported by C-V measurements made to investigate ageing

effects. Formerly, all Type-A willemite composite structures lost their

MIS-type characteristics after storage for a few weeks in a dessicator

but in the present structures the characteristics are still retained

after more than four months.

A theoretical plot of the flat-band saturation voltage against

the stress voltage(Fig 19) can be made using equation (4.5). With values of

$\kappa_o = 3.22$ and $\kappa_T = 5.62$ calculated from the $C_{max}$ value for SL10, the

theoretical slope should be 1.369. From theory, the line should pass

through the origin but this does not occur if the best straight line is

drawn through the experimental points. Also, the experimental slope is

1.690. The shift in the experimental line along the voltage-axis may be

accounted for by some voltage drop across the silicon and/or the inhomo-

geneous polarization of the films. Especially at low negative bias, some

of the stress voltage is taken up by the depletion region in the silicon

while this is neglected in the theory. The effect of inhomogeneous

polarization can be seen by the lowering of the C-V slopes of Fig 5.3.

Snow and Dumes$\overset{n}{\text{y}}$il also proposed this explanation for similar effects

in their composite borosilicate glass-oxide films on silicon, although

to a lesser degree (see Fig 5.20).

The analysis so far has neglected field-enhanced electronic

conduction because the fields concerned are not sufficiently high. At

high negative voltages, i.e. corresponding to Region II, where the fields

are in excess of $10^6$ v/cm, conduction in the form of electrons tunnelling from the metal into traps in the willemite is possible (9). This may happen because traps are very likely in the band-gap since willemite is a very disordered material (glassy). The two known charge exchange mechanisms between the metal electrode and traps in the insulator band-gap are the Poole-Frenkel and hopping processes. In the former, fields well in excess of $10^5$ v/cm are required at room temperature with moderate concentrations of trapping states (10), while the latter has to have a high density of states ($\geq 10^{18}$ cm$^{-3}$) although the field at room temperature can be as low as $5 \times 10^4$ v/cm (11). As a consequence of electronic trapping in addition to the polarization effect, the net negative space-charge in the willemite is expected to be very much increased. In fact, this is found to be the case, as can be seen from Fig.5.4. The change in flat-band voltage in Region II is more drastic than in Region I. With increasing negative bias, electron trapping continues occuring simultaneously with polarization until saturation in $\Delta V_{FB}$ occurs. This saturation may be due to either the filling up of all the traps and/or a maximum in the polarizability of the willemite for the given stress and time. However, with any further increase of the stress voltage above 18.0v, there is a reduction of $\Delta V_{FB}$ which can be explained as follows. Due to the creation of negative space-charge within the willemite, the built-in field becomes very intense so that the bands in the willemite and the residual film at the interface must be extremely bent. The trapped electrons could be released into the willemite conduction band and these electrons in turn could directly tunnel into the conduction band of the residual film. Hence there is a net loss in negative space-charge due to the detrapping of electrons from the willemite. Such a phenomenon cannot be explained in terms of the polarization effect. This is because the rely negative space-charge comes about from immobile negative ions and, there least up to this field strength, it may be the smaller dipolar polariza-

is no means of losing some of these anions at very high fields.

Similar effects may account for the recovery characteristics. Application of positive voltages in order to speed up the loss of the negative space-charge acquired with negative stressing seems to be possible (see Fig 5.9). Here, detrapping of electrons from the willemite into the metal seems to be the probable mechanism rather than the movement of positive ions back into the bulk of the willemite, although the latter cannot be totally excluded. Especially with high positve recovery voltages, the emptying of electrons from the trapping states into the conduction band of the willemite would be much easier than trying to move the larger and more massive positive ions. This is supported by the fact that the activation energy for ions is usually much larger than for electrons (12), although the line of distinction between the two has never been established (14). However, at elevated temperatures both mechanisms may be comparable and recovery of the flat-band voltage is enhanced. There is also a certain amount of restoration in the inhomogeneous polarization of the willemite as can be seen from the partial regaining of the original slope of the C-V curves in Fig 5.10.

B. Case of $d_w < d_o$

As described in the last section, the prominent difference between composite films in this category and the previous is the residual film being much thicker than the willemite. It was also shown in Fig 5.13 that the shift of flat-band voltage in the composite film is predominantly due to the residual film. For these reasons, a different line of approach from the previously discussed case may have to be taken when analyzing the results.

From Fig 5.12, a strong symmetry was observed in the C-V curves for stresses up to $\pm$ 8.0v corresponding to a field of approximately $9.3 \times 10^5$ v/cm. If polarization is responsible for these shifts, at least up to this field strength, it may be the smaller dipolar polariza-

tion mechanism because of the very small shift magnitudes. Such a polarization mechanism has already been cited for the residual films in the previous category. In the present case, however, the symmetry in the C-V curves could probably be due to the electrical characteristics of the composite film being dominated by the thicker residual film rather than by the willemite.

Further stress voltages above $\pm$ 8.0 v, however, produce non-symmetrical shifts in the C-V curves. The negative going flat-band shifts with positive stressing are considerably larger than the corresponding positive going shifts, and, especially in the former, partial recovery of the initial flat-band voltage is quite rapid (see Fig 5.14). The recovery could be made very fast (Fig 5.15) depending on the magnitude of the recovery voltage; e.g. about + 1.0 v in 20 sec. when $V_R$ = -10.0v. Such a fast recovery at room temperature is unusual if the mechanism is dielectric polarization of the type described and/or ionic movement, since both mechanisms are only appreciable at elevated temperatures (14).

An alternative to polarization could probably be an explanation in terms of electron injection. It should be remembered that the stress voltages of interest are $\pm$ 8.0v or greater, implying field strengths of greater than $10^6$ v/cm. Field-enhanced electronic trapping or detrapping is possible in such fields. The space-charge, as observed from the flat-band shifts, is positive indicating one of two possible electronic effects, (i) the emptying of electrons from the composite film into the metal or (ii) the tunnelling of holes into traps at the silicon-composite film interface. Since no appreciable d.c. conduction current was observed, then the former, which is a bulk effect, can probably be dismissed, leaving the second alternative, i.e. the tunnelling of holes from the silicon into interfacial traps, although the source of these traps is not fully understood. The stretching out of the C-V curves with

negative flat-band shifts probably gives some support to the interfacial traps model. When positive interfacial charges are present, it is much easier to accumulate the silicon surface with electrons than to invert it with holes. Similar observations on MNOS structures were made by Jeppson and Svensson (13).

With the limited amount of experimental evidence it does not seem to be possible to choose between polarization and electronic processes in these films.

5.5     Discussion

Both film examination and the electrical results have shown the existence of additional impurities in the underlying silicon after making Type-B willemite. Since baking occurs at such a high temperature for about 20 hrs, it is reasonable to expect metallic zinc and manganese to be able to diffuse into the silicon. The Schottky barrier plot of Fig 5.1 has shown that the deep-level impurities are acceptor-like in the silicon, implying that the net impurity contribution comes from zinc rather than manganese, since the latter is donor-like in silicon. Both zinc and manganese must eventually diffuse into silicon. Even if the manganese diffuses faster it must eventually be overwhelmed by the larger zinc concentration. This is consistent with the finding of manganese in the silicon following the Type-A willemite reaction but of a considerable zinc concentration in the silicon after the long reaction-bake process for Type-B. Due to the lack of information in the literature, on the diffusion of either zinc or manganese in silicon oxide or silicon, it is difficult to be more precise on the mechanisms involved in the diffusion processes.

Other forms of centre can be expected to exist in the residual film, possibly from the presence of zinc and manganese, crystal defects and vacancies. It has already been pointed out in the previous section that the residual film may be primarily made up of silicon oxide because

of the continuous exposure of the silicon surface to oxygen during the reaction. However, such an oxide would be very impure, due to products of the various other chemical processes going on simultaneously. Presumably on completion of the reaction, a certain proportion of zinc and manganese must remain in the residual film because they have also found their way into the silicon. This might be related to the observation of dipolar polarization as well as dendritic precipitates in the residual film. If zinc and manganese are able to form clusters of a conducting phase (perhaps crystalline precipitates) in the oxide, they would result in the type of dielectric polarization found (Fig 5.16b). Because of the built-in field arising from such polarization, the residual film is not expected to be electrically neutral after the application of a high field, especially at $10^6$ v/cm or greater. Also, the non-uniform polarization could be due to the random distribution of the conducting inclusions throughout the residual film.

The analysis on the composite structure in the last section has neglected the much smaller polarization and charge of the residual film but it is limited to the moderate fields of Region I, i.e. less than $10^6$ v/cm. However, the electrical results for the composite structures give sufficiently reasonable agreement when fitted to the Snow and Dumesnil space-charge polarization model (7) for this range of field strengths. This shows that space-charge polarization in the willemite dominates.

The space charge polarization mechanism in the Type-B willemite films can also be expected to be the same as in Type-A willemite. Again, the immobile negative ion is considered to be an $(SiO_4)^{4-}$ radicals which is derived from the silicate tetrahedra while the mobile cations are metallic zinc or manganese. With the application of a negative bias on the metal electrode, the cations are drawn towards the willemite surface

101
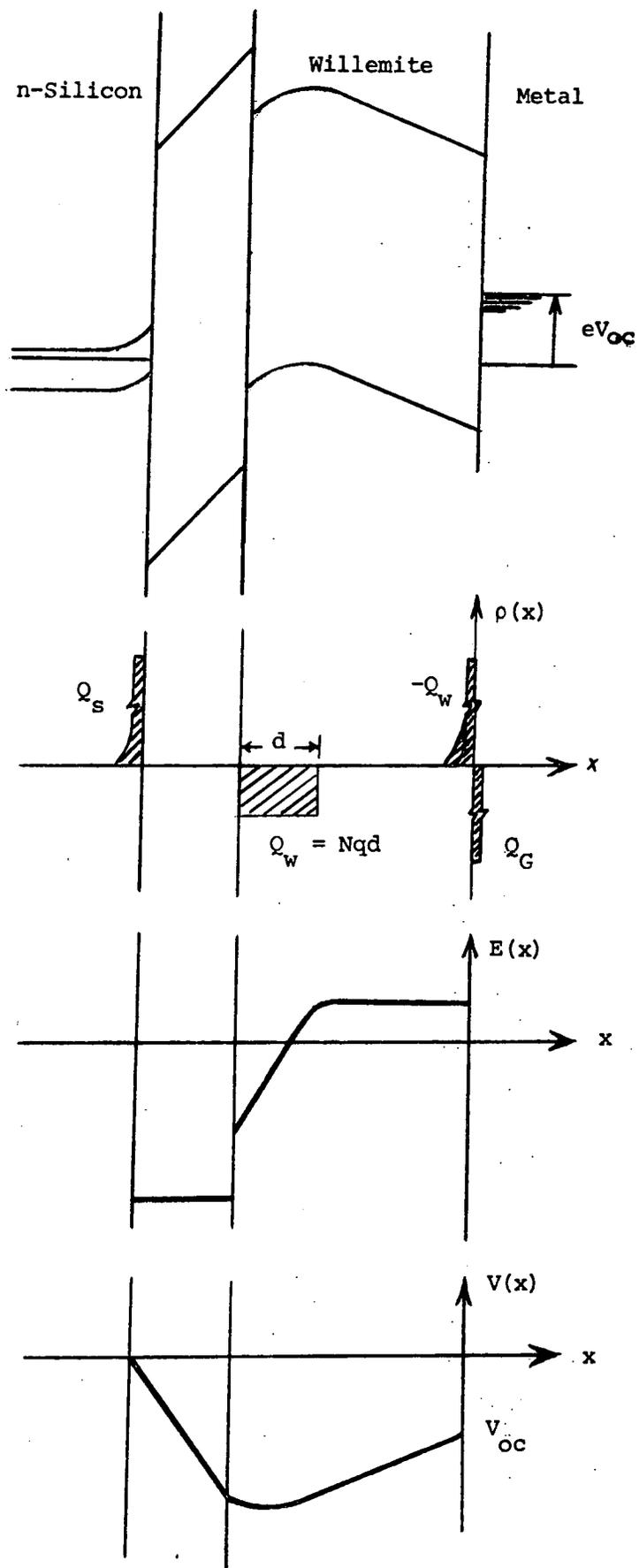
Fig 5.21    The band-diagram, charge, field and potential
            distributions deduced for the composite structure
            of Type-B willemite after removing the stress voltage.
            $V_{oc}$ is the open circuit.

leaving behind an uncompensated negative space-charge. The positive

metallic ions are either piled up in a narrow layer or discharged into

the metal but in either case, the potential drop at the metal-willemite

interface is negligible. The distributed negative space-charge, however,

will induce part of its image in the metal and part in the silicon,

forcing the silicon surface into depletion. In equilibrium the field in

the bulk of the willemite would fall from about $10^5$ v/cm to near zero.

Fig 5.21 illustrates the situation in the energy bands, charge

distribution, electric field and potential in the composite structure

after removal of the stress voltage causing polarization. The energy

bands of the residual film are here assumed to be those of silicon

dioxide, for simplicity. It should also be noted that the residual

film is assumed to be neutral. In Type-A willemite, the presence of

positive centres in the residual film resulted in a strong curvature of

the plot of flat-band voltage against time ; very much deviating from

the linear relationship predicted by theory. But in the case of the

present willemite, the slight curvature of Fig 5.17 could indicate an

almost neutral residual film.

Another important aspect arising from the polarization of the

willemite is the formation of an internal field after removal of the stress

voltage. Ionic build-up at both the interfaces,i.e. willemite-residual

film and metal-willemite, is very unsymmetrical because of the immobile

negative ions and the mobile positive ions. As a result there is a non-

uniform internal field in the willemite film (see Fig 5.21). Similar

results for fused silica have been reported by Cohen (15). With a large

degree of polarization, considerable reverse potentials can result when

the stress voltage is removed (14). The effect of this potential is

depicted in the present willemite by the open-circuit voltage $v_{oc}$, as

shown in the band diagram in Fig 5.21.

5.6       Conclusions

In this chapter the preparation and examination of Type-B willemite films have been described. The reaction-bake conditions imposed were 20 hrs. at $1000^{\circ}C$ in an atmosphere of 10% $O_2$ in $N_2$. Physical examination of the composite structures revealed residual films, slightly over 200 Å thick which are both non-luminescent and resistant to glacial acetic acid. Dendritic features which are believed to be due to zinc diffusion, were observed in both the residual film and the underlying silicon. However, ECP tests on the latter showed that it was still crystalline.

Schottky-barrier type C-V measurements on the underlying silicon showed the existence of deep acceptor-like traps, believed to be due to zinc. The residual films gave typical MIS-type C-V curves which could be shifted towards more positive flat-band voltages, with high field negative stresses. These shifts, although smaller than for the composite structures, were attributed to conducting inclusions in the insulating residual film.

The composite films showed similar electrical properties as for Type-A willemite. The stability of the present willemite films, however, seems to be better i.e. they require higher stress voltages for longer durations to achieve a given shift. The model of Snow and Dumesgil (8) has been used to analyze the electrical results in terms of interfacial space-charge polarization of the Type-B willemite. The polarization may be due to the dissociation of loosely bound $Zn^{2+}$ ions from the silicate tetrahedral network at the willemite-residual film interface.

Further discussion, relating Type-B willemite to the other two types, will be given in Chapter 7.

# REFERENCES

## CHAPTER 5

1.  G.D.Davies- M.Phil. Thesis, ~~Durham~~ London University, 1975.

2.  J. M. Hurd and R.E.Johnston  - private communication.

3.  S. M. Sze _'Physics of Semiconductor Devices', John Wiley and Sons (1969).

4.  C. Y. Chang and K.Y.Tsao - Sol.St.Elect.,12, 411-415 (1969).

5.  R. Pohl - Z. Physik, 155, 120 (1959).

6.  E. H. Snow and B. E. Deal- J. Electrochem.Soc., 113,263-269 (1966).

7.  J. R. Brews and A.D.Lopez- Sol.St.Elec., 16, 1267-1277 (1973).

8.  E.H.Snow and M.E.Dumesvil - J.Appl. Phys., 37, 2123-2131 (1966).

9.  W.C.Johnson - IEEE. Trans.Nucl.Sc.19, 33-40 (1972).

10. J.J.Chang - Proc. IEEE, 64, 1039-1059 (1976).

11. R. M. Hill and A.K.Jonscher - Thin Sol.Films, 8, 169-249 (1975).

12. R. A. Abott and T.I.Kamins - Sol. St. Elec., 13, 565-576 (1970).

13. K.O.Jeppson and C.M.Svensson - J.Appl.Phys.,48,2004 (1977).

14. P.M.Sutton - J.Am. Ceram. Soc., 47, 188-197 (1964).

15. J. Cohen - J. Appl. Phys. 28, 795-800 (1957).

# CHAPTER 6

## INVESTIGATION AND DISCUSSION OF TYPE-C WILLEMITE
### (Long Reaction Time - $N_2$)

## 6.1    Introduction

The type of willemite films to be discussed in this chapter is

called Type-C willemite following the growth technique as suggested by

Hurd and Johnston (1).    Previous workers on willemite films on silicon

have mostly investigated films prepared with a reaction-bake time ranging

from a few minutes to about an hour in a furnace ambient which was not

entirely oxygen-free.    Auger profiling work carried out by Hurd and

Johnston on such films revealed a non-uniform distribution of the

$Zn_2SiO_4$: Mn constituents, especially the presence of excess zinc in the

surface of the film and its depletion towards the vicinity of the film-

silicon interface.    Following these findings Hurd and Johnston carried

out tests involving a long reaction-bake time (about 24 hrs) in an ultra-

pure nitrogen ambient in the furnace.    Films prepared in this way were

found from Auger profiling to have a more uniform distribution of their

constituents.    Apart from a slight non-uniformity in a narrow region at

the interface, almost the entire thickness of the film had about the right

proportions of zinc, oxygen and silicon.

It is the purpose of this chapter to describe some of the

preparation, examination and electrical measurements that were carried

out on this type of willemite film.    Section 6.2 describes the conditions

required in the reaction of the constituent oxide and zinc fluoride to

produce this Type-C willemite.    Some of the visual and SEM observations

on these films are given in Section 6.3.    Section 6.4 presents the results

of various electrical measurements that were carried out and this is

followed by a section on the analysis and discussion of the results.

## 6.2    Reaction-bake Process

In order to achieve an ultra-pure nitrogen ambient in the willemite furnace, an Oxisorb gas purifier was added in the gas line between the nitrogen cylinder and the gas-inlet side of the furnace.

The Oxisorb purifier is capable of purifying white-spot nitrogen to contain less than 0.1 vpm (volume per million) of oxygen and 0.5 vpm of water. One cartridge has the capacity to purify 320 cu.ft. of gas. To ensure a one-way flow of the purified nitrogen in the furnace, a slightly higher than normal flow-rate ($\sim$ 500 cc/min) was set at the furnace gas-inlet side. At the same time the gas-outlet from the furnace was restricted to a small opening. As usual, the furnace temperature was set to give a flat zone at $1000^{\circ}C$ and left to stabilize for at least a day.

Sample preparation prior to the reaction-bake process was carried out in similar ways as for Type-A and Type-B willemite. Before the silicon slice, which had been oxidized and coated with zinc fluoride, was introduced into the furnace, the tube was flushed with a nitrogen flow of 1500 cc/min. The slice was pushed in to the furnace over a period of about 10 min. The reason for this gradual introduction was to allow sufficient time for heat redistribution within the films and the silicon. This precaution is important in trying to reduce cracking and uneven reaction effects. A period of 24 hrs was allowed for the reaction-bake process after which the slice was slowly extracted from the hot zone. The slice was allowed to cool to room temperature at the furnace mouth before removal. Similar techniques for defining capacitor areas, metallization and ohmic back contacts were carired out as previously.

Since the residual oxygen content is extremely critical in the growth of Type-C willemite films, two slices were processed, one using a nylon and the other a stainless steel pipe between the Oxysorb purifier

and the furnace.  It was thought that nylon might contain more adsorbed

water than the steel and hence it was expected that there would be some

differences in the electrical characteristics of the two slices.

A separate test was carried out to check the concentration of

oxygen in the purified nitrogen in the furnace.  A piece of silicon,

etched with HF and cleaned with IPA, had its natural oxide thickness

measured on the ellipsometer.  It was then left in the willemite reaction

furnace at $1000^{\circ}$C for 24 hrs in exactly the same conditions as for the

willemite formed using the steel gas pipe.  The oxide thickness increased

by 21 Å during this treatment.  This indicates a residual oxygen concen-

tration of 0.2 vpm in the nitrogen.

## 6.3    Film Examination

All the Type-C willemite films that were prepared had the same

initial thicknesses of zinc fluoride and silicon dioxide.  The resulting

composite film had a thickness of about 70% of the total for the two

constituents.   As usual, some of the test samples were assessed for

cathodoluminescence and all showed green emission.  The emission spectrum

for this type of willemite films, measured at Newcastle Polytechnic (2),

was found to be comparable to that of Type-A willemite having a peak of

5200 Å.

Under the optical microscope, fine grains of Type-C willemite

could be observed but only at a very high magnification of approximately

450x.  The grain size is much smaller than for Type-A willemite and signs

of localized clustering occur to a lesser extent.  The main similarities

between Type-C and Type-B willemite are in the dendritic and cellular

features which are distributed throughout the films (see Plate 6.1).

This was also observed by Hurd and Johnston (1) who thought that they

might be due to the preferential diffusion of zinc in certain directions

within the film.
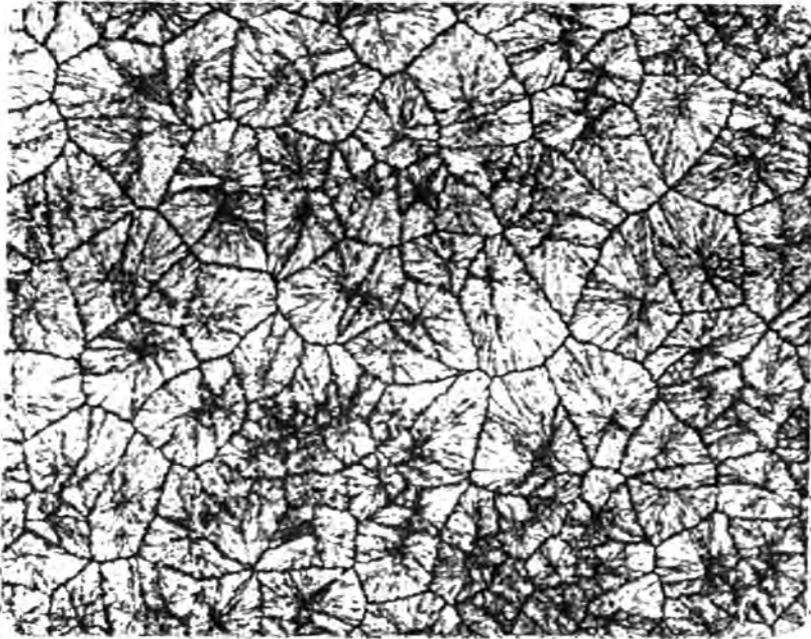
Plate 6.1    A 320x photo micrograph showing the
             grain structure in Type-C willemite
             (after Hurd and Johnston (1) ).

| Etchant | Cathodoluminescent Test after Etching | Relative Proportion of Residual Powder Remaining |
|---|---|---|
| $HNO_3$ acid | No | Small |
| HCl acid | No | Small |
| $H_2SO_4$ acid | No | Moderate |
| Orthophosphoric acid | No | Large |
| Glacial Acetic acid | Yes | Large |
| $H_2O$ (control) | Yes | Large |

TABLE 6.1   Etching tests on commercial willemite powder. The strength of acid is 25%. The last column indicates the relative quantities of the initial amount of powder left after etching.

| Experimental Slice | SL12 (Nylon gas pipe) | SL13 (Stainless steel gas pipe) |
|---|---|---|
| Initial Oxide | 489 | 572 |
| Zinc Fluoride | 482 | 492 |
| Composite film, $d_T$ | 734 | 765 |
| Acid-resistant thickness Left-over, $d_x$ | 629 | 638 |
| Thickness reduction in acetic acid etch $d_r = d_T - d_x$ | 105 | 127 |

TABLE 6.2   Film thickness in $\overset{o}{A}$ for the two experimental slices of Type-C willemite.

Investigations using the SEM revealed similar observations as above. Generally, the films are very uniform, with no distinctive topographical features to be seen even when tilting the slice at an angle. Contrast in the secondary emission mode at 15 keV is poor, which may imply that the film is very insulating i.e. it charges up with the bombarding electrons. At 25 keV, a slightly better contrast was achieved and under very high magnification, similar fine grain crystallites distributed in the dendritic network could be observed. When switched to the cathodoluminescent mode, there was a rapid darkening of the image.

Probably the most unique feature of the Type-C willemite is the inability of locating the residual film, that is if it exists. Generally, the 'residual' film below the willemite is defined as that is left behind when the composite structure is etched with weak acetic acid, leaving a non-cathodoluminescent layer. The type-C willemite, however, had rather different properties. After the acetic acid etch, the underlying film still contained randomly distributed spots of green emission when tested for cathodoluminescence. Also there was only a reduction of about 100 Å in the total film thickness, implying that the normal definition of the residual film is not applicable in this case. Even prolonged etches for 24 hrs in very concentrated acetic acid and in 10% hydrochloric acid did not alter the situation, although dilute hydrofluoric acid totally removed the film.

To compare the chemical reactivity of commercial willemite powder with that of the film, some etching tests were carried out. Small amounts of willemite powder in glass tubes had various acids of 25% concentration added and left for about an hour. Afterwards, the residue was dried and tested for cathodoluminescence. The results in Table 6.1 show that apart from glacial acetic acid and water the other four etchants virtually destroy the luminescent property of the powder.

Nitric and hydrochloric acids dissolve most of the willemite powder while the other three acids attack only part of the powder. The HCl acid etch contradicts the findings for the Type-C willemite films described above. This may be because the willemite crystallites in the film are embedded in a silicon oxide matrix, preventing them from being attacked by the acid, although why this should occur for Type-C but not for Type-B willemite is not clear. It must be concluded that there is no clear evidence for a non-luminescent residual film under Type-C willemite. This made it impossible to do separate measurements and to build up a model for the electrical characteristics of this type of film as had been done for Types-A and B willemite.

Table 6.2 gives the film thicknesses for the two electrical test samples of Type-C as measured by the ellipsometer. Instead of the 'residual film', there is an acid-resistant film remaining after the acetic acid etch, the thickness being denoted by $d_x$. The reduction of the composite film due to this etch has its thickness denoted by $d_r$. It can be seen that the film thicknesses are very similar so that there seems to be an improvement in the control of processing for the present willemite films. The refractive indices of the composite films of both slices are also 1.58 from ellipsometer measurements. The replacement of the nylon by the stainless steel gas pipe therefore seems to have had little effect on the non-electrical properties.

6.4     Electrical Results for Type-C Willemite

Typical C-V characteristics of Type-C willemite composite structures are shown in Fig 6.1 and Fig 6.2 for slices prepared using the nylon gas-line (SL12) and steel gas-line (SL13) respectively. A notable feature is that the C-V characteristics can be shifted towards more positive as well as more negative flat-band voltages. With negative stress voltages, the flat-band voltage becomes more positive while with positive
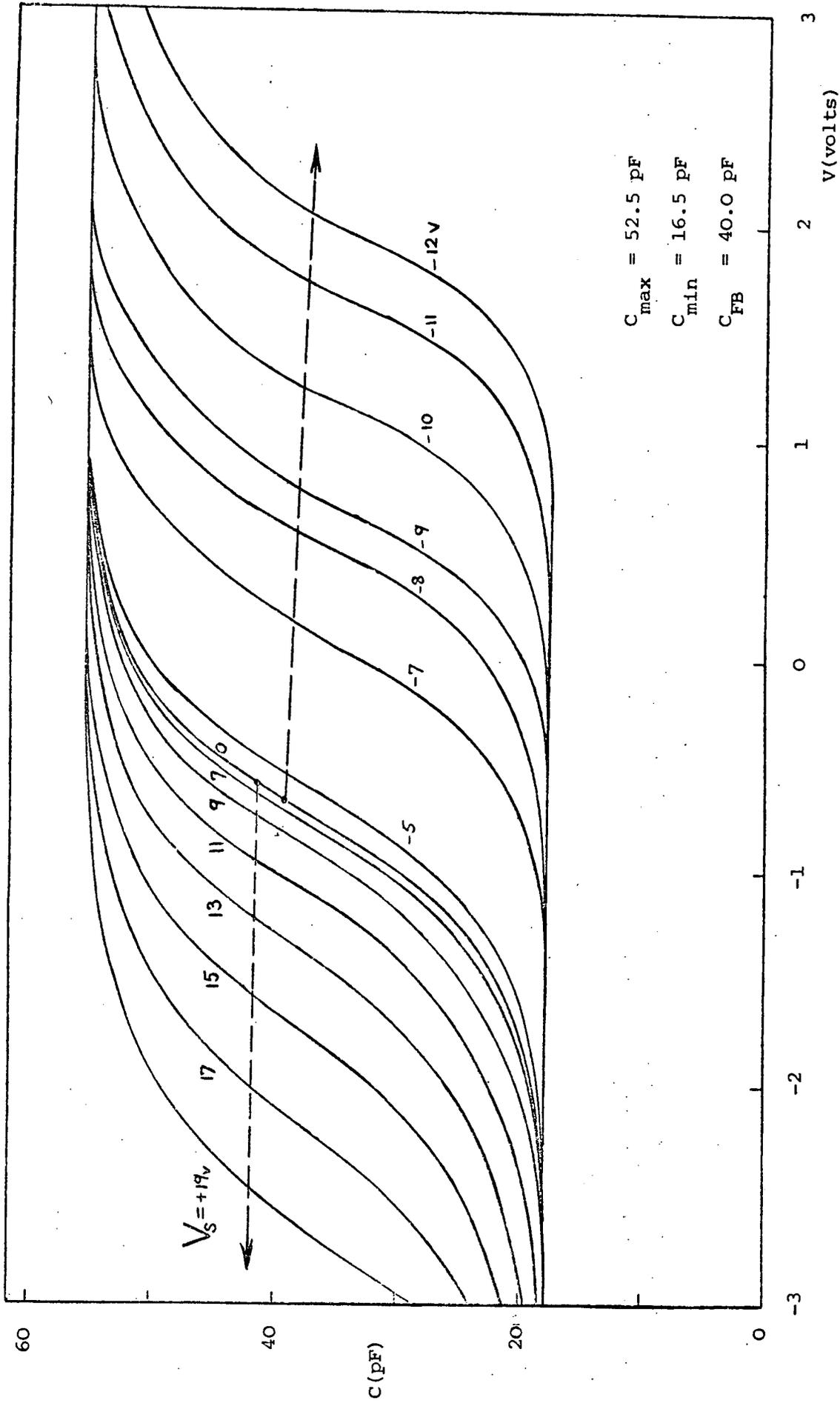
Fig 6.1    C-V curves of composite structures from Type-C willemite showing the effect of both positive and negative stress voltages.  Stress time, 1 min.  f = 100 kHz.  Slice SL12.
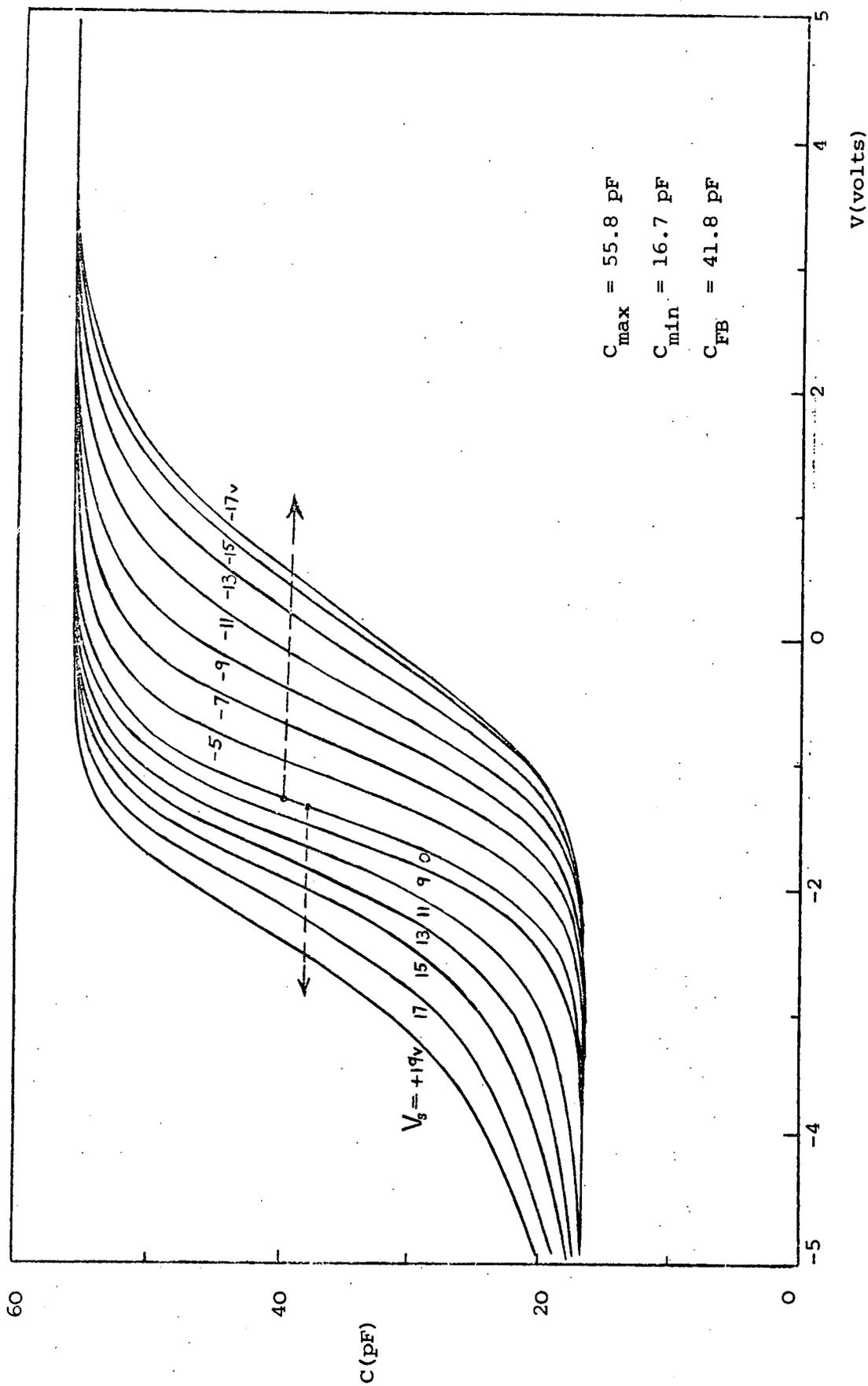
Fig 6.2    C-V curves of composite structures from Type-C willemite showing the effect of both positive and negative stress voltages.    Stress time, 1 min.    f = 100 kHz.    Slice SL13.
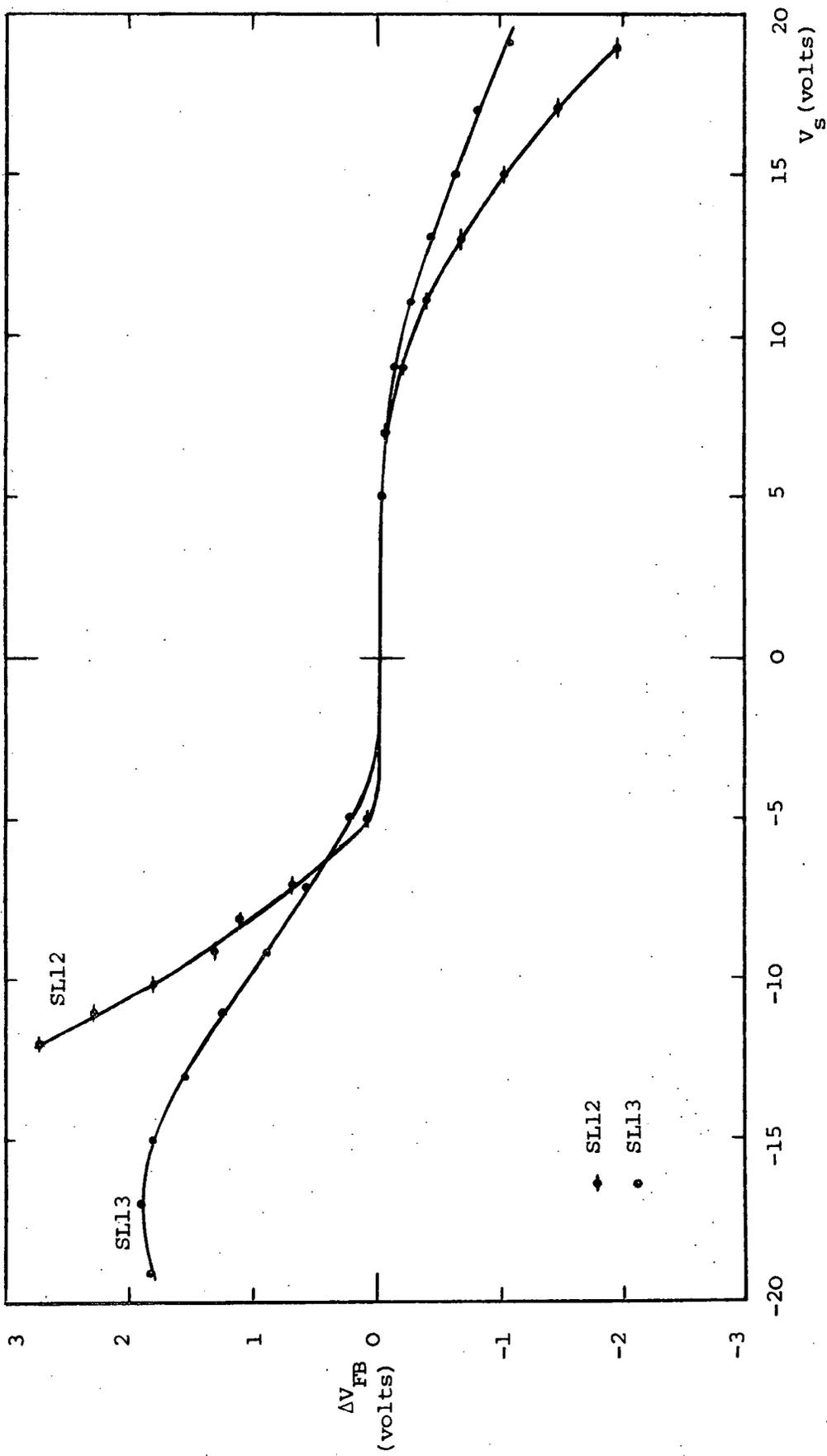
Fig 6.3    Plot of the change in flat-band voltage against stress voltage.  Stress time, 1 min.

voltages, it becomes more negative. In general this could be due to the negative voltage creating negative space-charge in the films close to the silicon, and positive voltage creating positive space-charge. The possible mechanism for such space-charge formation will be discussed in more detail in the next section.

The stability of the flat-band voltage of the present willemite is better than for either Type-A or Type-B willemite. A larger negative stress voltage and a longer time is therefore required to achieve a given magnitude of the flat-band shift. It should be noted that the stress time in Fig 6.1 and Fig 6.2 is 1 min. instead of the 1 sec applied to former types of willemite for similar measurements. Generally both slices show a lowering of the slope of the C-V curves with the shift of the flat-band voltage for both directions of shift but again the reduction of the slope is not as drastic as for the other two types of willemite. In slice SL12, positive going flat-band shifts produce only a slight lowering of the C-V slope but negative going flat-band shifts have a large reduction of slope due to the inversion voltage stretching out more than the corresponding change in flat-band voltage. For slice SL13 the flat-band shift are similar but less (Fig 6.2), except that the slope is reduced more for curves with positive going flat-band shifts unlike SL12.

A more convenient way of looking at the shifts of the C-V curves is by plotting the change in flat-band voltage $\Delta V_{FB}$ against the stress voltage $V_s$. The results for both slices are presented in Fig 6.3. It can be seen that negative stresses have a larger effect than positive, or in other words, it is easier to form negative rather than positive space-charge. This is also shown by the 'threshold' in the stress voltage which for positive stress has a value of about 5.0v and, for negative, about -3.5v. Fig 6.3 also shows that slice SL13 (grown using the steel gas pipe) is more stable than slice SL12, since the film thick-

nesses are approximately the same.

The effect of stress duration has been important in assessing previous willemite films but time only allowed a preliminary investigation for Type-C willemite with negative stresses. The change of flat-band voltage with time is plotted in Fig 6.4 for three stress voltages. It is obvious that the formation of negative space charge within the composite film depends upon the duration of stress. At 100 sec., the value of $\Delta V_{FB}$ due to stressing with -5.0v is hardly appreciable but a voltage twice this yields a value of $\Delta V_{FB}$ close to 2.0v. Within the duration of stress that was investigated, i.e. a maximum of about 1.5 hr., there is hardly any sign of $\Delta V_{FB}$ saturating at room temperature. Again, these results illustrate the stability of the present willemite films when compared to those grown previously.

Since the C-V curves for Type-C willemite can be shifted in both directions, it was decided to make some measurements of the recovery process. Two tests were carried out, one for the recovery of a structure that had been negatively stressed (see Fig 6.5(a) ) and the other for one positively stressed (see Fig 6.5 (b) ). For the structure that had been negatively stressed to give $\Delta V_{FB}$ of 6.84 v, the recovery, using a recovery voltage of +5.0v applied for 1 min. at room temperature, is very slight. But when the same stress conditions were applied at a temperature of $109^{\circ}C$, the recovery of the C-V curve was almost complete. This shows that the positively attained flat-band voltages are very stable, and recovery at room temperature take hours or even days. This may be a useful memory effect.

The recovery process for structures that have been subjected to positive stress voltages is entirely different. At room temperature and for a recovery voltage of -5.0v, the process is very rapid, occurring in times of seconds (see Fig 6.5 (b) ) for a structure previously positively
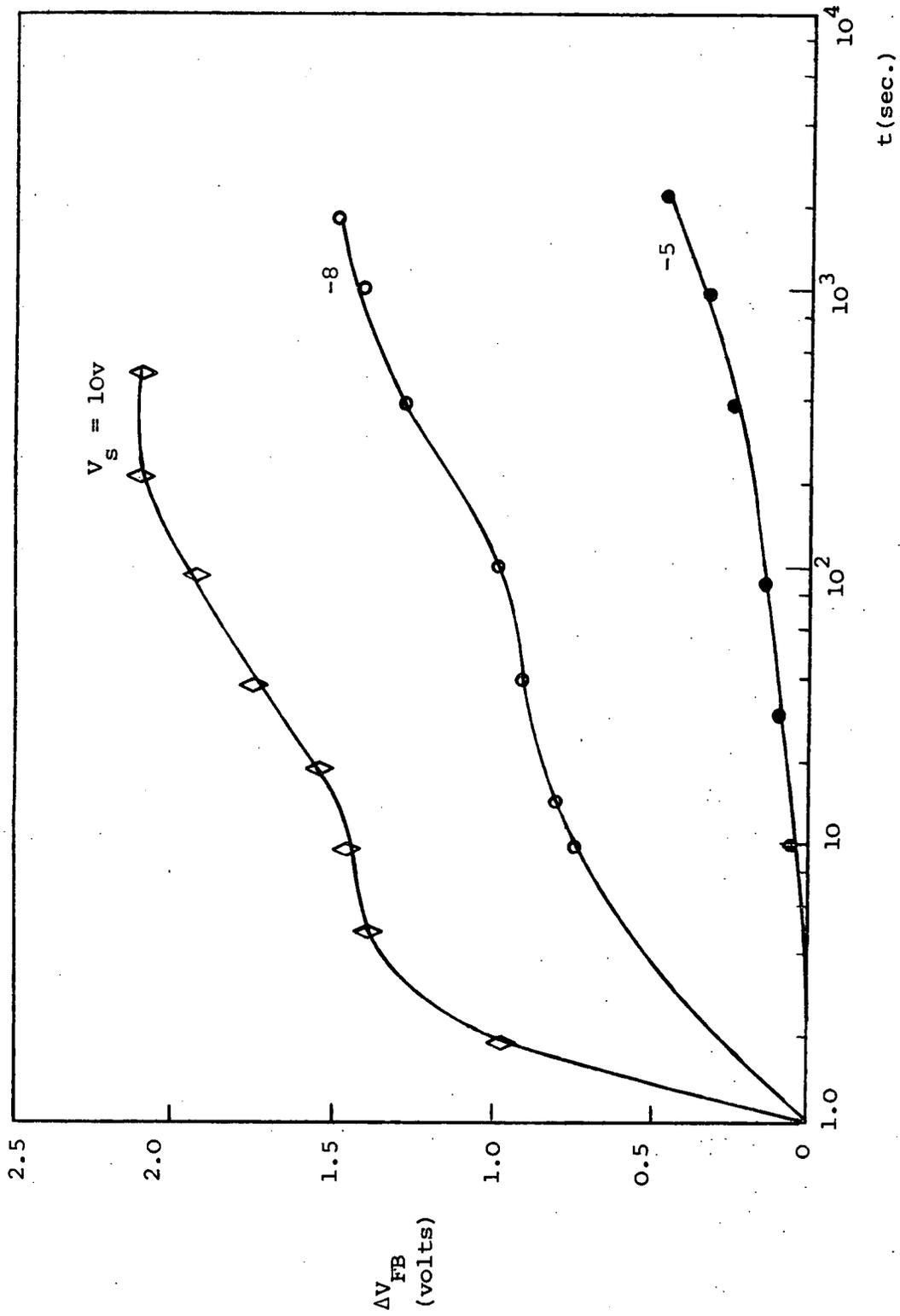
Fig. 6.4    Plot of change in flat-band voltage with stress duration for three
different negative stress voltages.    Slice SL12.
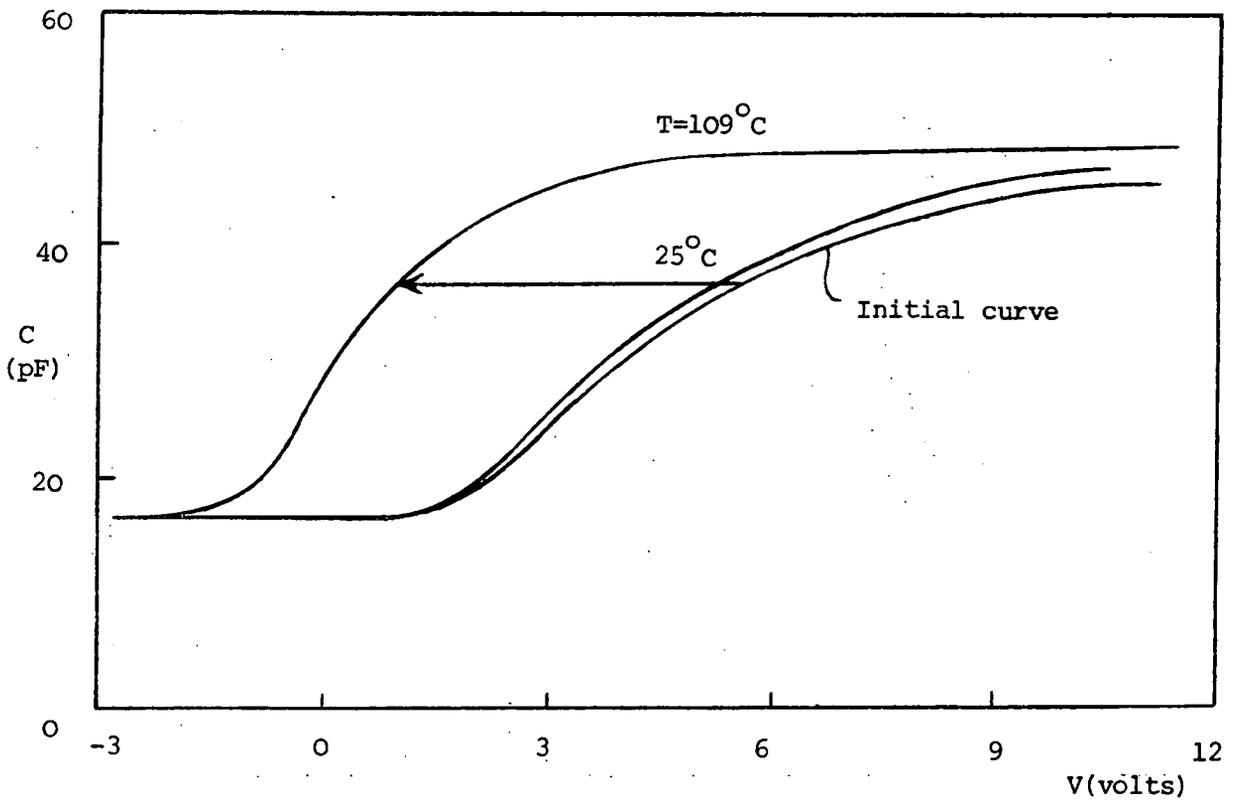
**Fig 6.5(a)**      Recovery of composite structure C-V curve at elevated temperatures. Initial curve has been negatively stressed to achieve $\Delta V_{FB} = 6.84v$. Voltage for recovery is +5.0v at 1 min.
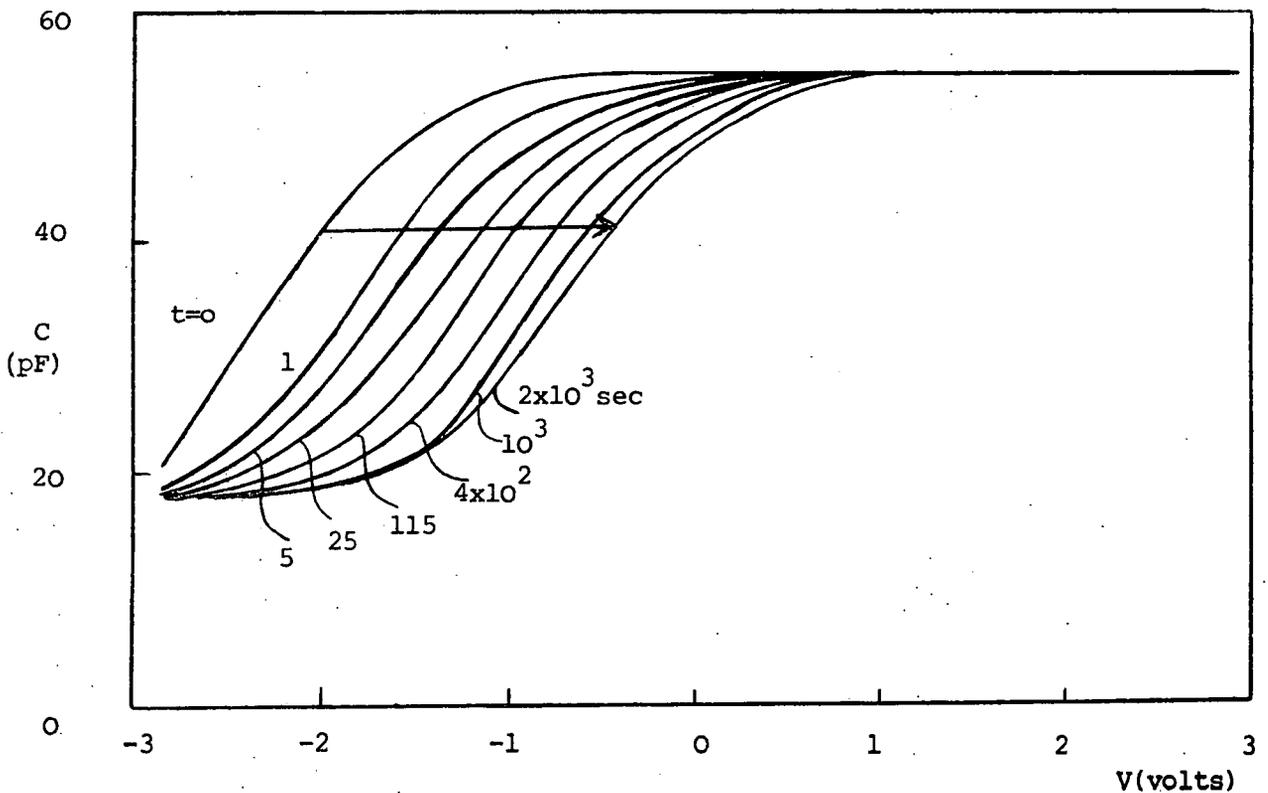


**Fig 6.5(b)**      Recovery of composite structure C-V curve with time. Prior to measurements sample has been positively stressed to achieve $\Delta V_{FB} = -1.45v$. Voltage for recovery, -5.0v.
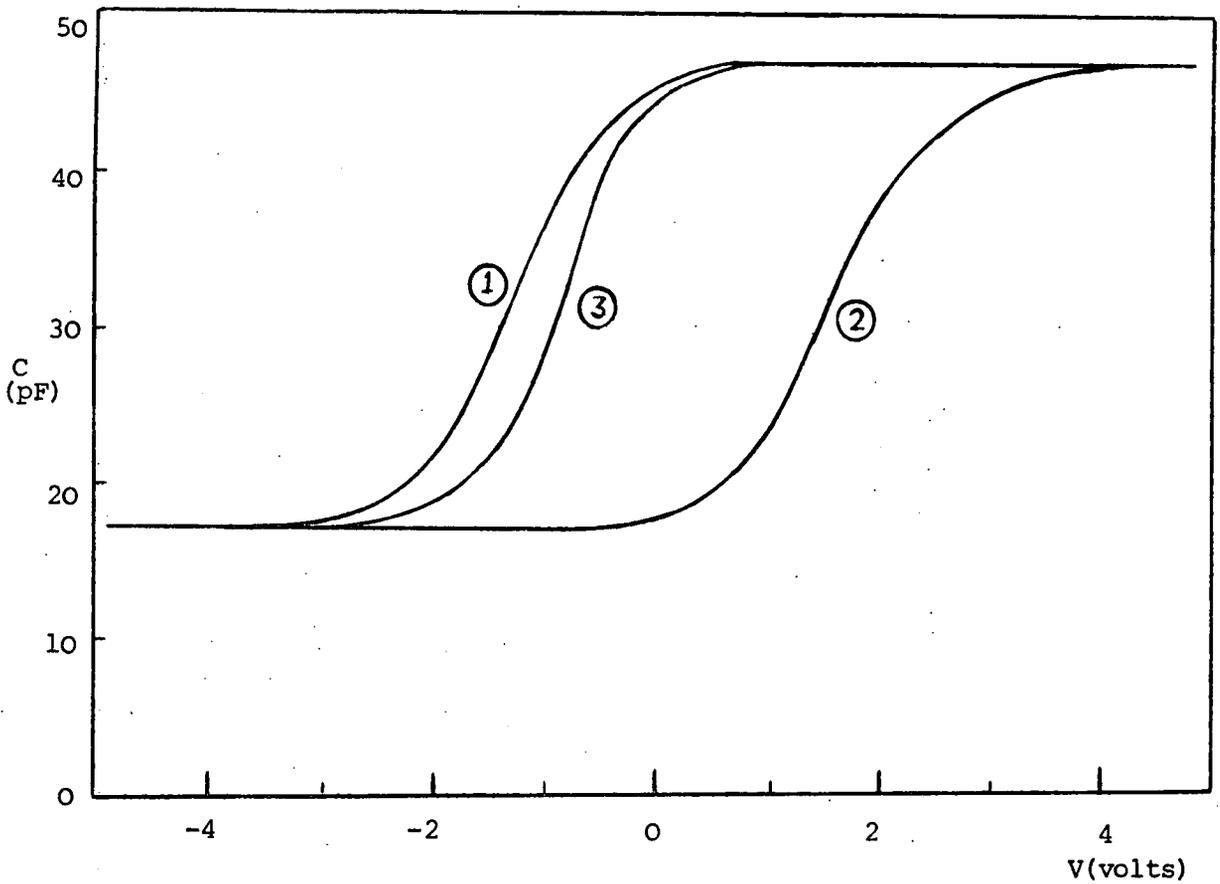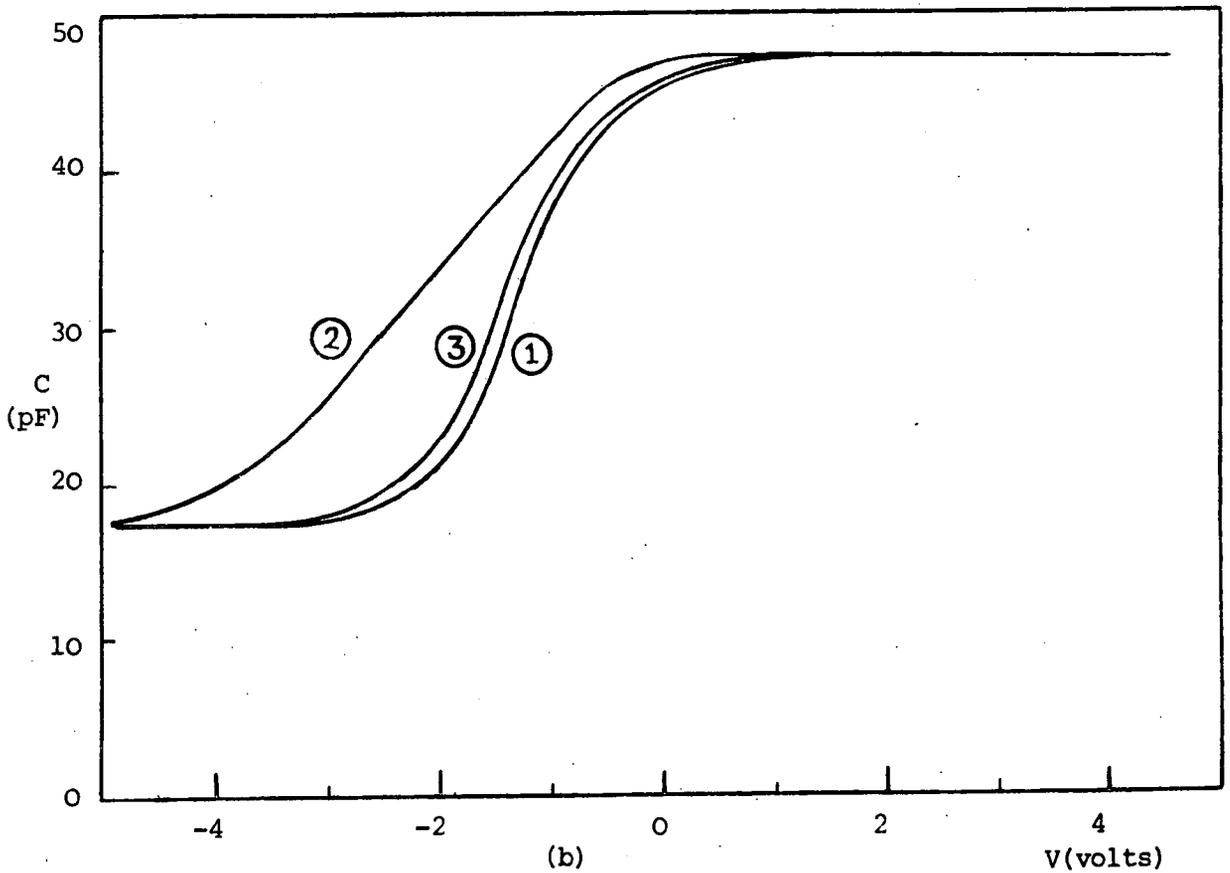
Fig 6.6    Effect of annealing the composite structure at 400°C for 10 min., and in $N_2$ after being (a) negatively and (b) positively stressed. Curves (1), (2) and (3) are for measurements done initially, after stressing and after annealing respectively. Stress voltages, -5.0v and +5.0v, stress time 1 min.

stressed to give $\Delta V_{FB}$ = -1.45v. This indicates that the positive space-charge formed within the composite film by positive stress voltages can be easily neutralised by applying a negative voltage (or an opposite field) at room temperature. These two results show that the neutralisation of negative and positive space-charges may occur by different processes.

It was next decided to investigate whether high temperature alone can lead to the recovery of C-V curves. Two composite structures were stressed with voltages of opposite polarities so as to give positive and negative $\Delta V_{FB}$ values. They were then annealed in a $N_2$ atmosphere at a temperature of $400^{\circ}$C for 10 min. The C-V measurements were made prior to the application of stress, after stressing and after annealing. The results are shown in Fig 6.6 (a) and 6.6(b) for the negative and positive stresses respectively. It can be seen that the original C-V character-istics are partly restored showing that most of the space-charge formed by voltage stressing can be eliminated by a short period at high temperatures.

6.5    Analysis and Discussion

The electrical results for Type-C willemite are somewhat different from those for the other two types of willemite discussed in previous chapters. The present willemite seems to be more stable as illustrated in Fig 6.4 where it can be seen that appreciable flat-band shifts are only produced by voltages higher than $\pm$ 5.0v. If the field required for the onset of electronic injection is taken to be $10^6$ v/cm, the corresponding voltage for the composite structures would be around 7.5v. The other noticeable feature of the present composite structure is that its C-V curves can be shifted in both directions. This has never occurred in previous willemite structures, except when $d_w < d_o$ for Type-B willemite.

Since the stress voltages causing appreciable changes in $V_{FB}$ give the same order of field as for electron injection, the analysis of the results becomes more complicated. The problem of separating electron

injection and dielectric polarization effects again arises.   Unless

electrical measurements are carried out at reduced and elevated tempera-

tures, which has not been possible here, the two mechanisms are

inseparable.   However, from similarities with the other two types of

willemite, it is reasonable to assume that dielectric polarization still

predominates in the present willemite.   The amount of polarization is

thought to be less because of the better stability of Type-C material.

The stability is also improved by increasing the purity of the nitrogen

used in the processing.   For slice SL12, the gas was passed through a

nylon pipe which probably gave off more water than the stainless steel

pipe used for SL13.   The improved stability of the latter is shown by

Fig 6.3.   It is possible that this could also have contributed to the

better symmetry of the C-V characteristic of slice SL13 compared with

slice SL12 (see Fig 6.1 and Fig 6.2).   Symmetrical C-V characteristics

arising from dielectric polarization in MAOS structures have also been

reported by Iida et al (3).

The type of polarization in Type-C willemite films could be

either the dipolar polarization proposed by Snow and Deal (4) or the

interfacial (space-charge) polarization of Snow and Dumesｨil (5).   It

is difficult to distinguish between the two effects because the results

of $\Delta V_{FB}$ against stress duration for negative stresses (Fig 6.4) cannot

be fitted on to the Snow and Dumesｨil model, as was done for Type-A and

B willemite, since no saturation in $\Delta V_{FB}$ was observed during the stressing

time used.

Furthermore, the lack of recovery of the positively-shifted

flat-band voltages at room temperature shows the stability of the stress-

induced negative space-charge, (see Fig 6.5(a) ).   Recovery is rapid only

at elevated temperatures.   One possible explanation is by assuming that

polarization is caused by the $Zn^{2+}$ ions moving towards the metal electrode,

where the cations are then trapped.   As to how the trapping really occurs

is not known, but the cations have definitely got to overcome some considerable activation energy before it can be transferred back into the bulk and reducing the space-charge (6). Such activation energy can be supplied thermally thus possibly explaining the recovery of flat-band voltages at temperatures higher than room temperature.

The discussion in the last paragraph has so far been confined to negative stress voltages. With positive stress voltages, there is a shift towards more negative values of $V_{FB}$ in Type-C willemite. This could be due to the formation of positive space-charge within the composite film close to the silicon surface. The field to give appreciable negative values in $\Delta V_{FB}$ is around $10^6$ v/cm (Fig 6.3). Apart from dielectric polarization, electronic injection processes or even the formation of interfacial traps are also possible at this field strength. However, unlike the positive-going $\Delta V_{FB}$, negative going flat-band voltages have a rapid recovery at room temperature, which is clearly illustrated in Fig 6.5(b). It may be possible that the polarization effect, with positive bias, is probably swamped by another more dominant mechanism.

The more likely explanation for the negative-going flat-band shifts is in terms of electronic processes. Since no appreciable d.c. current has been observed, it can be deduced that such processes are not in the bulk of the material. An alternative model, which seems more likely, is to assume that electron transfer takes place in a small region of the composite film near the vicinity of the silicon-film interface. The positive space-charge causing the flat-band shifts could thus be due to the injection of holes from the silicon into this interfacial layer. Hole injection from silicon into silicon nitride has been widely reported (7,8). It is also possible that the stress voltage could itself create further traps in the interfacial region of the composite film as in MNOS structures (8). The effect of annealing at $600^{\circ}$C for 10 min.(Fig 6.6(b) ) could then empty those traps and reduce their numbers. The high

113

temperature annealing-out of traps has been reported for MAOS structures by Salama (9).

Fig 6.7 shows the change in the flat-band voltages with field for the normal Type-C willemite composite structure and for a structure that has been etched with glacial acetic acid. It should be noted that the acid-resistant film has a much reduced change of $V_{FB}$ with negative stress. This implies that the surface of the composite film, around 105 $\overset{o}{A}$ thick, has stronger polarization features than the bulk of the willemite.

Because of the trapping and polarizing effects found in the composite film structure of Type-C willemite, hysteresis is expected with continuous cyclic stress voltages. Fig 6.8 depicts such results where the effect of hysteresis can be clearly seen. The initial flat-band voltage was $V_{FB_O}$ and the stressing was first done with an increasing positive voltage up to +20.0v, in steps of 5.0v for 1 min each. The stress then decreased towards negative $V_S$ etc. It can be seen that the return positive stress has a decreasing effect on $\Delta V_{FB}$ while the return negative stress does not. This implies a more rapid response for the processes occurring with positive stress compared to those for negative stress. This agrees with the results on the recovery of the flat-band voltage discussed above. After the cycle of stress shown in Fig 6.8, the complete C-V curve at the point X had a considerably distorted and stretched depletion regime although the accumulation and strong inversion capacitance were unchanged (see Fig 6.9). This result could be due to a combination of the two mechanisms discussed earlier.

A proposed model based on the electrical results discussed so far is illustrated in Fig 6.10. The uppermost layer of the composite film is probably made up of willemite having a loosely bonded structure, which is strongly polarizable. The underlying layer, which constitutes
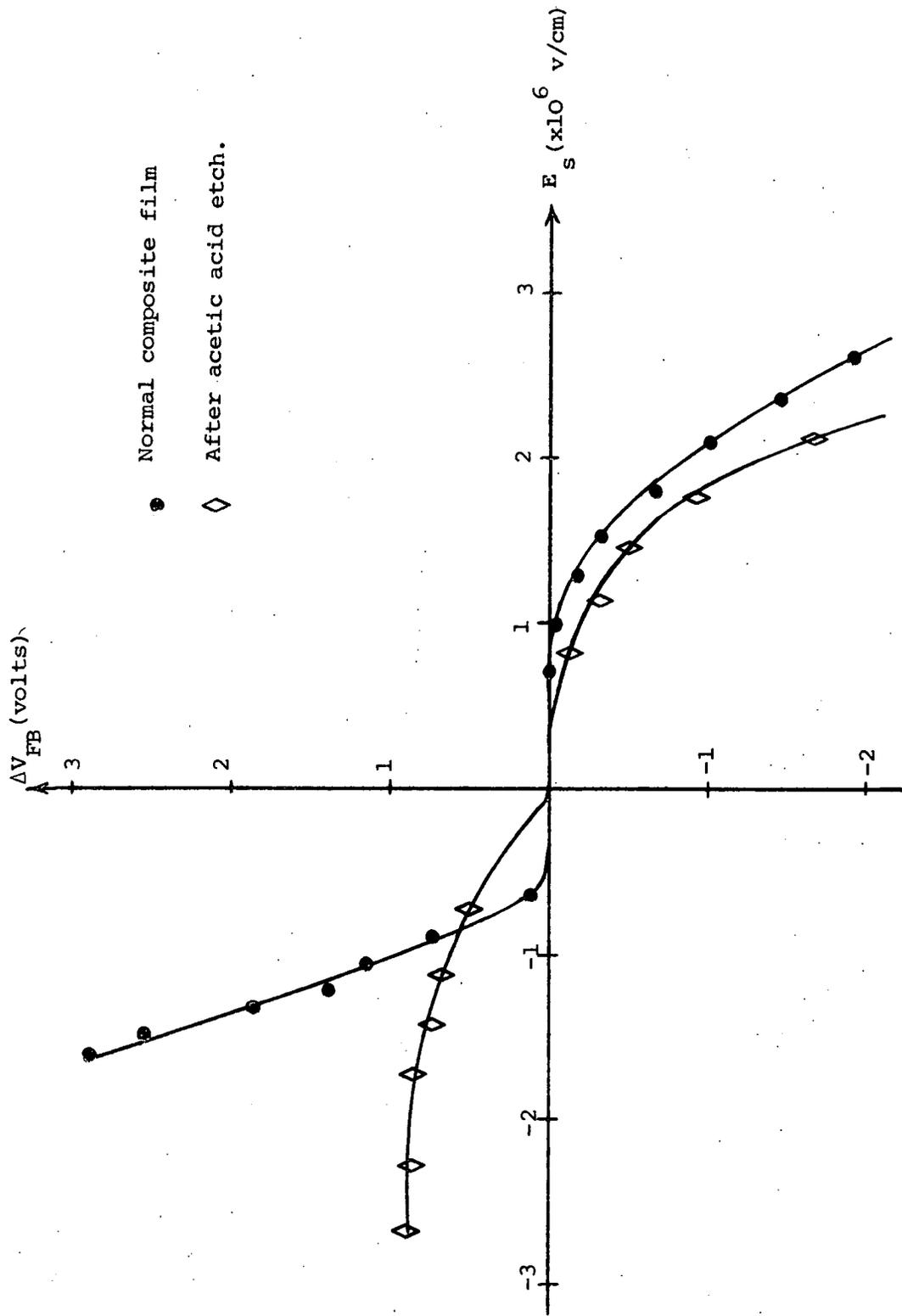
**Fig 6.7**   A plot of $\Delta V_{FB}$ against the stress field for a composite film structure of Type-C willemite showing the effects of acetic acid etching. Stress time, 1 min.
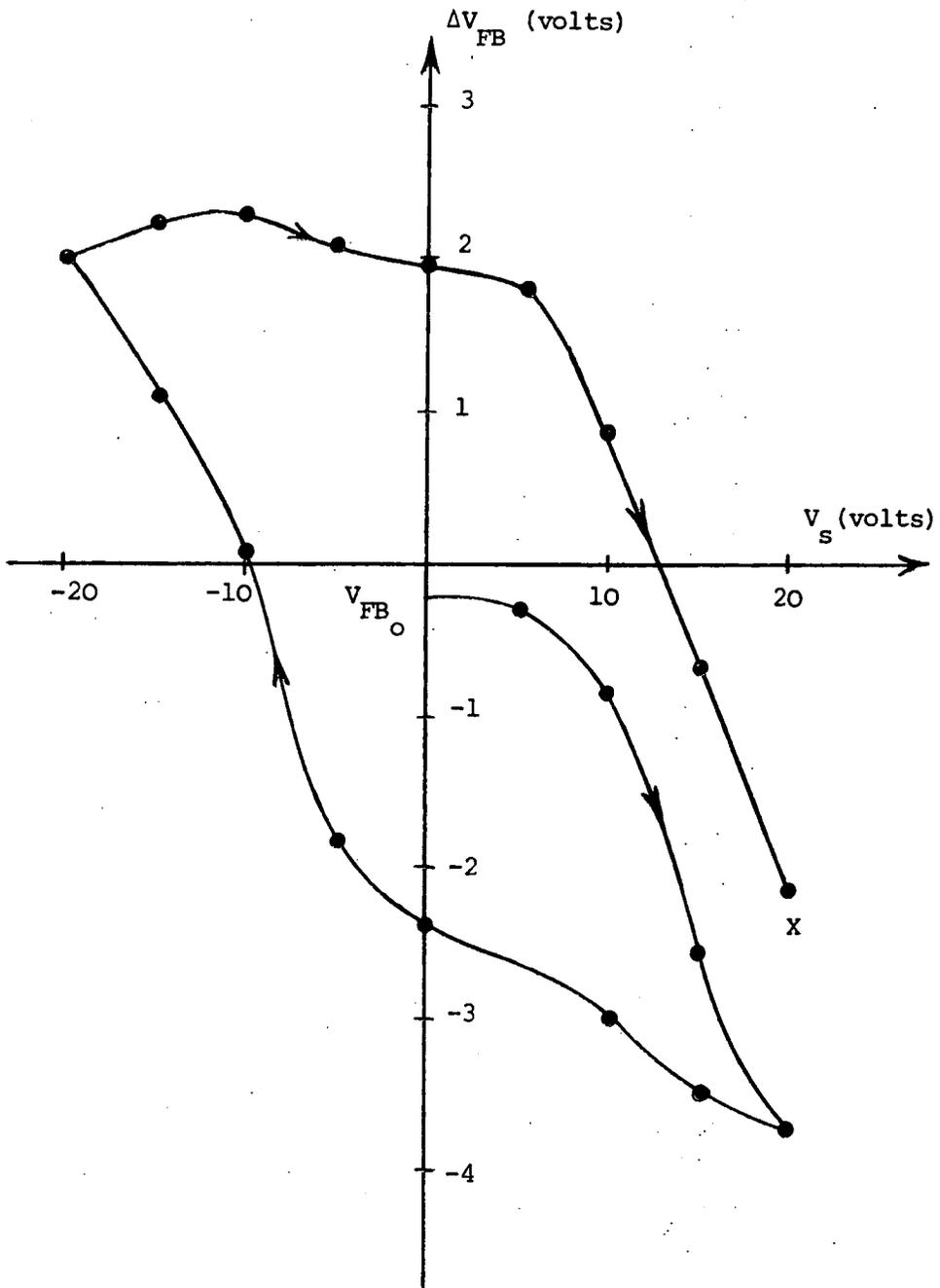
**Fig 6.8**     Hysteresis effect due to cyclic stressing.

$V_{FB_O}$ is initial flat-band voltage.  Stress time, 1 min.
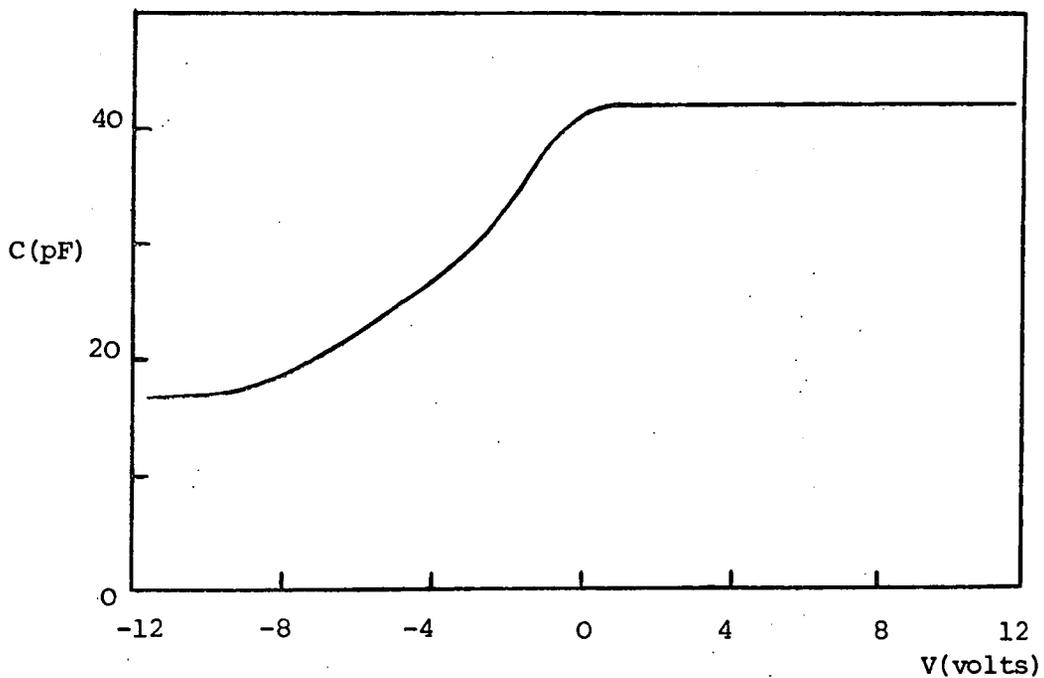
**Fig 6.9**    The C-V curve taken after the composite structure of Type-C willemite has been subjected to cyclic stressing as in Fig. 6.8.
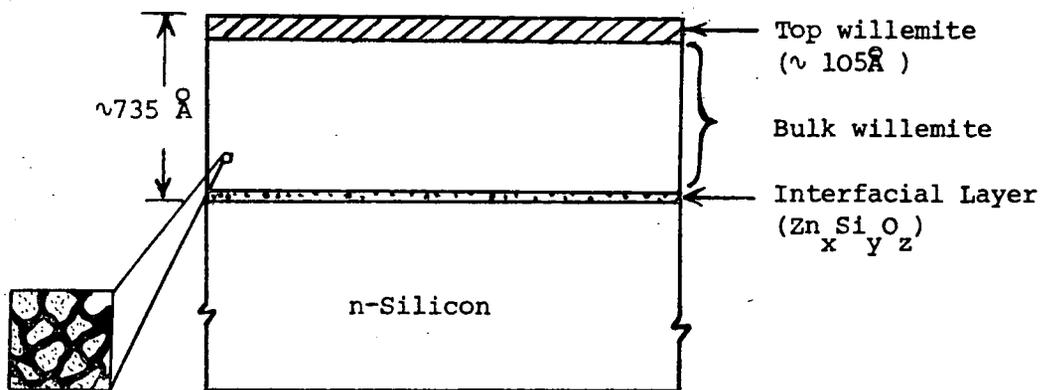


**Fig 6.10**    Proposed model for the Type-C composite willemite film. Top willemite is non-resistant to glacial acetic acid. Inset shows grains of willemite crystallites separated by very thin layers of silicon oxide. Diagram not drawn to scale.

the major part of the composite film, is probably made up of fine-grained crystallites of willemite which are separated by thin layers of silicon oxide. The structure of the silicate network is probably much more complete, hence the better electrical stability shown by the results. Lastly it is proposed that there is an interfacial layer between the willemite and the silicon, and this may contain all the elements present in the reaction, $Zn_x Si_y O_z$. Such an interfacial layer was also proposed by Iida et al (3) to explain the instability found in MAOS structures. It is believed that the $Zn_x Si_y O_z$ interfacial layer could have a large trap concentration which could be further increased by positive stresses. The results show that these could be traps for holes rather than electrons.

6.6    Conclusion

The technique for growing Type-C willemite, as proposed by Hurd and Johnston, has been described in the early part of this chapter. Etching tests on this type of willemite shows that it is largely resist-ant to most acids, except HF.  Cathodoluminescence is still found after the normal etching with glacial acetic acid so that the definition of a 'residual' film becomes vague.

The electrical properties of the present films showed better stability than Type-A or B willemite ; a larger stress voltage and/or a longer time is required to achieve any appreciable shift of flat-band voltage.  Polarization is thought to occur throughout the entire range of negative stresses, while hole injection from the silicon into inter-facial traps in the film is thought to dominate with positive stresses larger than 5.0v.

On the whole the present composite film is thought to be more uniform than the previous, except for a narrow interfacial region at the

silicon and a slightly more open structure at the surface.  The model

proposed is that crystallites of willemite are uniformly distributed

within the film and separated by very thin silicon oxide, with the correct

average composition for $Zn_2SiO_4$ as found by Hurd and Johnston (1).

The properties of Type-C willemite will be compared with those

of Types A and B in more detail in Chapter 7.

REFERENCES

## CHAPTER 6

1.    J.M. Hurd and J.E.Johnston - private communication.

2.    J.F.B.Hawkes - private communication.

3.    K. Iida, T. Tsujide and M.Nakagiri - Jap.J.Appl.Phys.,11, 1153 (1972).

4.    E.H.Snow and B.E.Deal - J.Electrochem.Soc., 113, 263 (1966).

5.    E.H.Snow and M.E.Dumesuil - J.Appl.Phys.,37, 2123 (1966).

6.    P.M.Sutton - J.Am.Ceram.Soc., 47, 188 (1964).

7.    S.M.Hu, D.R.Kerr and L.V.Gregor - Appl.Phys.Letts.,10, 97 (1967).

8.    K.O.Jeppson and C.M.Svensson - J.Appl.Phys., 48, 2004 (1977).

9.    C.A.T. Salama - J.Electrochem.Soc., 117, 913 (1970).

## CHAPTER 7

## UNIFIED DISCUSSION OF THE PROPERTIES

## OF THE THREE TYPES OF WILLEMITE

### 7.1    Introduction

In Chapters 4,5 and 6, three different methods of forming

willemite films and some of their physical properties have been described.

In each chapter, the electrical results have also been presented with

some discussion, but due to the lack of precise information on properties

such as the nature of traps, the carrier mobilities, transport mech-

anisms, etc., a detailed analysis is impossible.   In general, the analysis

of the electrical results uses ordinary electrostatics, especially the

flat-band voltage in the MIS C-V characteristics, for detecting the polarity

and concentration of space-charge within the films.   However, conclusions

of the nature of the space-charge brought about by the application of

electric fields have to be treated with some reservations because of the

lack of information about the material properties.

It is the primary objective of this chapter to attempt to bring

together the explanations proposed for the various willemite films.   This

must be highly speculative although there should be some unifying factors

to be found to correlate the growth and electrical properties of the three

types of willemite, especially concerned with the nature of the space-

charges formed within the films.

The factors affecting the mechanism for the solid-state reactions

in the growth of willemite films on silicon are discussed in Section 7.2,

while Section 7.3 will be devoted with trying to relate the resulting

properties to the growth conditions.    Section 7.4 describes the possible

mechanisms of dielectric polarization and electronic injection in willemite

composite films with emphasis on the conditions in which each might be

observed. A general discussion of the electrical properties of the composite films, with particular attention to the willemite, is presented in Section 7.5. The main differences between the three types of willemite are pointed out and an attempt is made to relate the observed physical properties and the corresponding electrical properties.

7.2      Solid-State Reactions in the Formation of Willemite

Detailed studies of the structural properties of willemite films grown on silicon were made by Edwards and Rushby (1). Later, Davies (2) found that the final film is inhomogeneous with an outer insulating layer on the willemite, and an inner interfacial film between the willemite and the silicon. The outer film is easily removed, but the interfacial (or 'residual') film is far more important as it can substantially reduce the efficiency of electron injection from the silicon into the willemite. This consideration led Errington (3) into a detailed investigation of willemite growth, varying the parameters of gas ambient, temperature and time.

Possible mechanisms for the formation of silicates by solid-state reactions are illustrated in Table 7.1 (4). There are several alternatives to the simple direct reduction of silicon dioxide and zinc fluoride molecules. The rate-limiting factor in the formation of silicates is generally the electroneutrality of the ionic fluxes arising from the mobility of the $Si^{4+}$ and $O^{2-}$ ions (4). However, in the presence of loosely bound metallic cations, the rate-limiting factor is due to the mobility of the cations, $Zn^{2+}$ ions in this case, in the growing silicate (Table 7.1(a) ). At the high reaction temperature ($\sim 1000^{\circ}$C), the zinc fluoride is assumed to be molten with loosely bound zinc, possibly in the form of mobile $Zn^{2+}$ ions. The diffusion of molecular zinc fluoride itself is not likely because of the comparative sizes of the zinc fluoride and zinc silicate molecules. It is more likely that the zinc fluoride is partially

$X_2SiO_4$                                          $SiO_2$

(a)

$2X^{2+}$

$2O^{2-}$

$2X^{2+} + 2O^{2-} + SiO_2$

$= X_2SiO_4$

(b) $Si^{4+} + 4XO$

    $= X_2SiO_4 + 2X^{2+}$

$2X^{2+}$

$Si^{4+}$

$2X^{2+} + 2SiO_2$

$= X_2SiO_4 + Si^{4+}$

(c)

$2X^{2+}$

$2O$

$4h^{\cdot}$

$2X^{2+} + 2O + SiO_2$

$= X_2SiO_4 + h^{\cdot}$

(d)

$2X^{2+}$

$O_2(g)$

$4h^{\cdot}$

$2X^{2+} + O_2(g) + SiO_2$

$= X_2SiO_4 + 4h^{\cdot}$
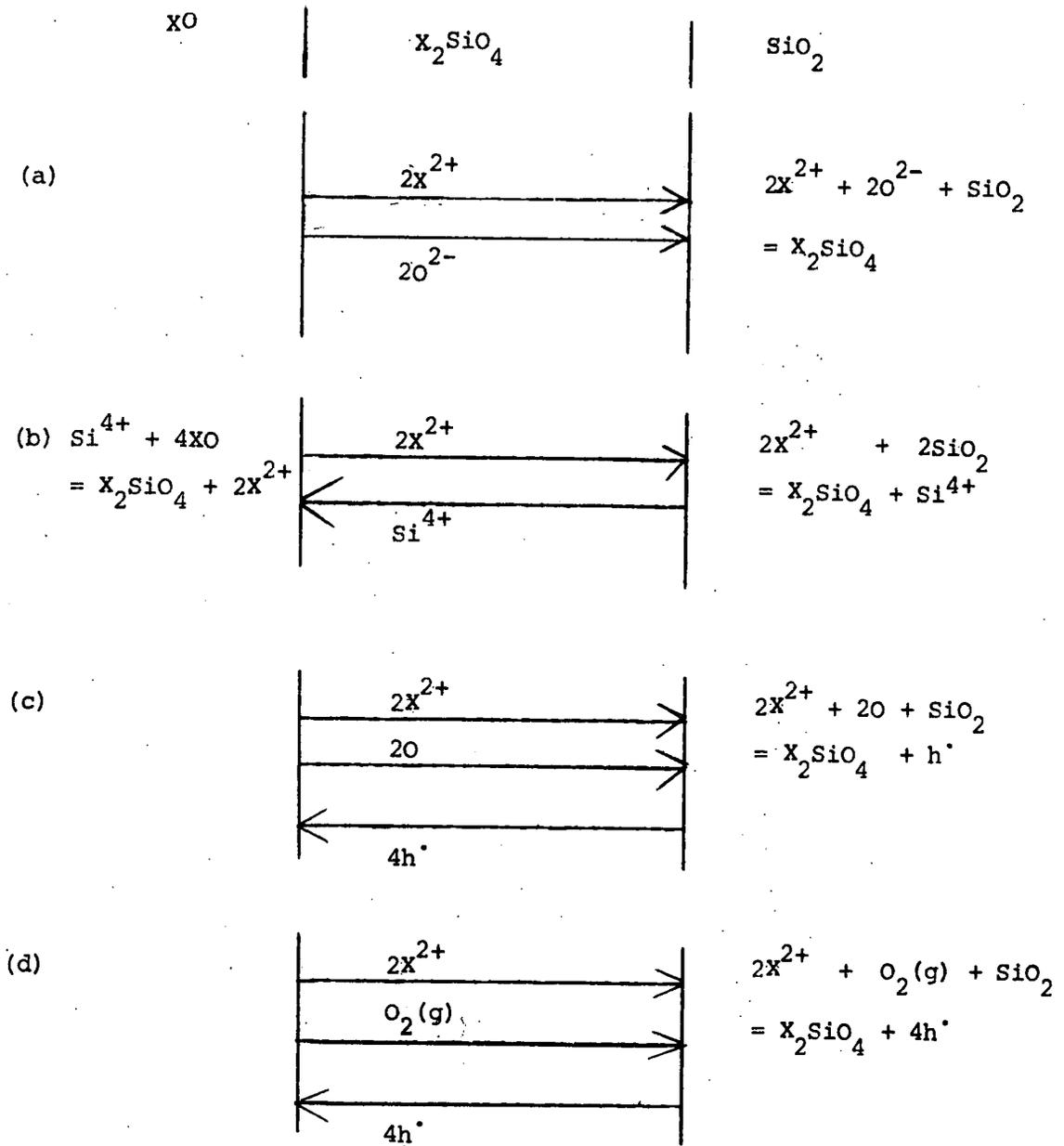
TABLE 7.1    Possible reactions in the formation of a silicate
by the reaction of a metallic oxide (XO) and silicon
dioxide (after ref.(4) ) h = hole, $O_2(g)$ = oxygen gas.

dissociated into its respective ions, i.e. $ZnF_2 \rightleftharpoons Zn^{2+} + 2F^-$, allowing

the $Zn^{2+}$ ions, which are only about 1/19 of the size of a zinc silicate

molecule to diffuse easily between the silicate tetrahedra. This model

is slightly different to that proposed by Errington (3), who concluded

that the formation of willemite was limited by the rate of dissolution of

molten zinc fluoride in silicon dioxide. This is more likely in the initial

stages of the reaction, where the zinc fluoride and silicon dioxide are

in direct contact with each other, rather than at later times in the

reaction process.

For the $Zn^{2+}$ ion diffusion model, Errington proposed a theoretical

relationship for the willemite thickness

$$d_w = \left( \frac{2\ C\ D\ t}{n} \right)^{\frac{1}{2}} \tag{7.1}$$

where C is the concentration of $Zn^{2+}$ ions at the willemite

surface,

D is the diffusion coefficient of $Zn^{2+}$ ions in willemite,

n is the number of $Zn^{2+}$ ions incorporated in a unit

volume of willemite, and

t is the reaction time.

Some evidence for a relationship of this form was obtained from

experiments carried out by Errington which gave a reasonable value of

about $10^{-16}$ cm$^2$/sec at 900°C for D. The value of C was found to be

dependent on the availability of $Zn^{2+}$ ions, or in other words the thick-

ness of the evaporated zinc fluoride. The final thickness of the willemite

film was therefore also dependent on the thickness of zinc fluoride.

This has been confirmed by the experimental observations presented in

Table 4.1. An excessively thick zinc fluoride film will result in a

large amount of unreacted products in the top-layer while too thin zinc

SAMPLE-107"
 -2000Å ZnF₂ 2000Å SiO₂
 -10min @1000°C

OXYGEN X2

ZINC X2

SI X5

AUGER PEAK TO PEAK HEIGHT (APPH)

SPUTTERING TIME (MIN)
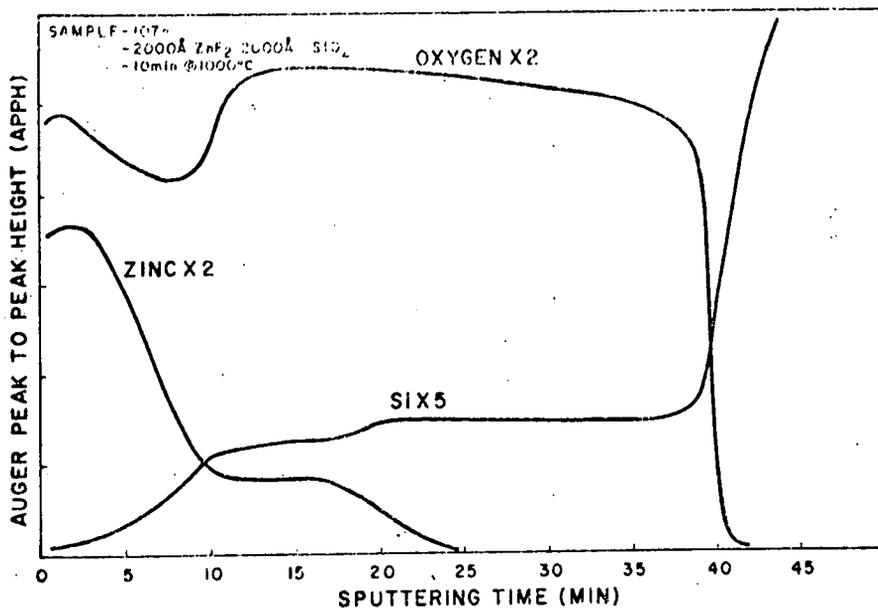
**Fig 7.1(a)**    Auger profile of a willemite film formed at 1000°C for 10 min.

Similar to Type-A Willemite (After Hurd & Johnston).



SAMPLE -107d
 - 2000A° ZnF₂ 2000A° SiO₂
 - 24hr @1000°C

OXYGEN X I

ZINC X 2

SILICON X I

AUGER PEAK TO PEAK HEIGHT (APPH)

SPUTTERING TIME (MIN)
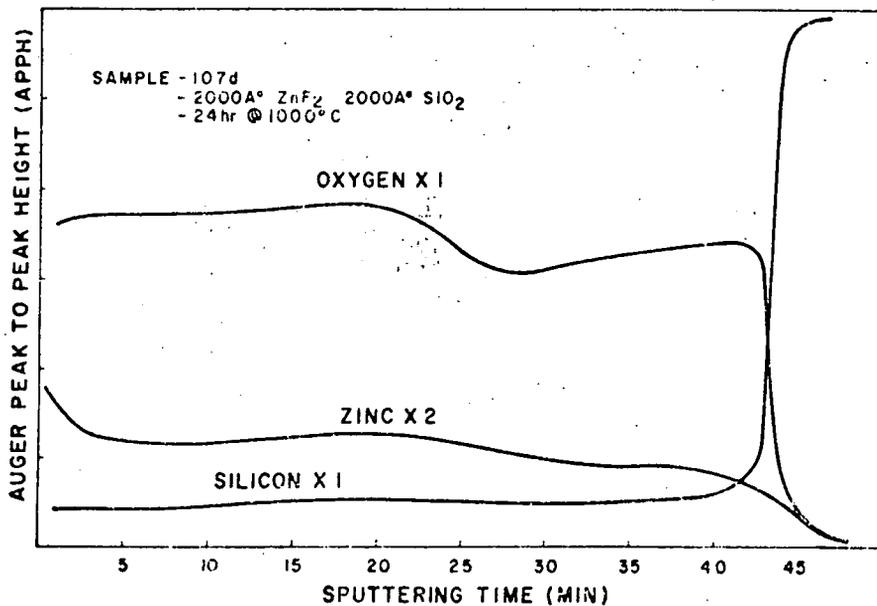
**Fig 7.1(b)**    Auger profile of a willemite film formed in $N_2$ at 1000°C for 24 hrs. Similar to Type-C Willemite. (After Hurd & Johnston).

fluoride film leaves a considerable thickness of residual film. For this reason, a balance in the ratio of initial oxide to zinc fluoride thicknesses is important and in most cases, this ratio is between 1:1 and 1:3.

An important parameter in the growth of willemite films is the length of time for which the reaction-bake process is carried out. The reaction time used by most previous workers was one hour or less, typical of Type-A willemite, and Errington found out that the relationship given by Equation (7.1) is only applicable for reactions taking longer than 2 minutes. Hurd and Johnston (5), however, concluded that such short reactions are incomplete resulting in a high concentration of zinc piling up near the surface of the film as shown in Fig 7.1 (a), while regions near the silicon-film interface are depleted of zinc. They argued that $Zn^{2+}$ ions are unlikely to diffuse right through the willemite to the silicon dioxide in such a short time. On the other hand, manganese, which has a relatively smaller mass than zinc, is likely to find it easier to diffuse through the $SiO_2$ compared to zinc. This conclusion is supported in the present work by the presence of manganese, rather than zinc, as deduced from Schottky-barrier measurements on the silicon below willemite formed by a 20 min. reaction in $N_2$.

By extending the reaction-bake time to about 24 hrs., Hurd and Johnston obtained a more uniform zinc concentration in the final film. This is shown in Fig 7.1 (b) which gives their results for an Auger profile of the materials. It is believed that in this case, sufficient time has been allowed for the $Zn^{2+}$ ions to be transferred from the surface right through the willemite to the silicon dioxide. In fact, as shown in Chapter 5, the prolonged reaction time enables a concentration of $9.6 \times 10^{14}$ $cm^{-3}$ of zinc to diffuse into the surface of the underlying silicon. Hence the technique of prolonging the reaction process gives a more uniform willemite film which is a feature of Type-B and Type-C willemite films discussed in Chapters 5 and 6 respectively.

The ambient in which the reaction-bake process takes place also has a strong influence on the final willemite film. Zinc is well known to be easily oxidized so that even a slight presence of oxygen in the ambient might alter the reaction mechanism in the film. Zinc oxide is also an insulator and is also thought to be one of the constituents of the top layer. Also, oxygen, whether in molecular or ionic form, has a very high diffusivity in silicon dioxide (6) with a diffusion coefficient of about $10^{-9}$ $cm^2$/sec approximately at $100°C$. The unit cell of a silicate structure being relatively larger and more open than silicon dioxide, might be expected to have an even higher diffusivity for oxygen. Oxygen in the furnace gas can therefore lead to further oxidation of the silicon during the reaction leading to an increase in the residual film thickness. This was shown to occur by Errington (3) and it has been proved to be the case here when oxygen was deliberately introduced into the ambient during the preparation of Type-B willemite as described in Chapter 5 (see Table 7.1 (c)& (d)). In order to prevent oxygen from interfering with the reaction-bake process, ultra-pure nitrogen with less than 0.1 vpm of oxygen, was therefore used in the preparation of Type-C willemite.

From Table 7.1, it can be seen that all four possible reactions forming a silicate involve ionic movement. If the reaction is incomplete, an accumulation of ions can be expected at the surface and/or at the interface of the silicate film, which may lead to lack of electrical neutrality of the final film. This effect has been observed in the initial flat-band voltages of composite structures which prove that positive charges exist within the film. It has also been suggested in the literature that the partial pressure of oxygen in the reaction ambient plays an important role in determining the electrical properties of silicates (4) and this is confirmed by the differences between the three types of willemite investigated here.

The three types of willemite prepared during the course of this research might be related to the four reactions shown in Table 7.1. Reaction (d) seems most likely for the formation of Type-B willemite due to the role of oxygen which was deliberately added to this reaction. When there is no oxygen present reaction (b) seems to be more likely if the metallic ion source is $x$ instead of $xo$ corresponding to Type-C willemite. For Type-A willemite, with a very short reaction time and small oxygen concentration, any of the reactions would seem to be possible.

7.3     Physical Properties of Films

Due to the differences in the reaction-bake conditions the various types of willemite have slightly different physical properties and it is rather difficult to categorize these properties.    Some general features have already been presented in Table 2.1 of Chapter 2, and an attempt will be made in this section to relate other physical properties to the method of forming the willemite.

Film Thicknesses

As described in Chapter 2, film thicknesses are measured with the ellipsometer to an accuracy of $\pm$ 20 $\mathring{A}$ for $SiO_2$ films on silicon. However, both willemite and residual films are very different from $SiO_2$ in that they are probably inhomogeneous and their interfaces are much more diffuse.    These two factors can easily give rise to inaccuracy in the ellipsometer measurements, the simple theory of which assumes a homogeneous film and a sharp film-substrate interface.    Furthermore in the measurements of composite films, the double-dielectric nature of the film gives only an effective or apparent value for the thickness, rather than the actual sum of the willemite and residual films thicknesses. In the case of Types-B and -C willemite, the existence of zinc channels in the silicon is also bound to alter the reflectivity value of the silicon from the value of 4.05-0.028i assumed in the program used to calculate the thickness.    Overall, the thickness measurements are,

therefore, expected to be very much less accurate than for $SiO_2$ on silicon.

Some simple calculations can be made of the thickness of initial oxide $t_{ox}$ required to produce a thickness, $t_w$, of willemite. Consider a volume of $SiO_2$ film, of thickness $t_{ox}$ and area A. The total number of silicon atoms is

$$N_{Si} = \frac{t_{ox}A}{t'_{ox}a} \qquad (7.2)$$

where $t'_{ox}$ is the thickness of a unit cell of $SiO_2$ and

a is its area.

If $M_{ox}$ is the molecular weight of $SiO_2$, which is 60.09, and $\rho_{ox}$ is its density, then

$$t'_{ox}a = \frac{M_{ox}}{\rho_{ox}} \qquad (7.3)$$

The same expressions can be applied to $Zn_2SiO_4$ where $t_w$ and $t'_w$ are the thicknesses of the final film and the unit cell of $Zn_2SiO_4$ respectively. Since each unit cell of $SiO_2$ and $Zn_2SiO_4$ contains one silicon atom, $N_{Si}$ is the same for both materials, so that

$$\frac{t_{ox}}{t_w} = \frac{M_{ox}/\rho_{ox}}{M_w/\rho_w} \qquad (7.4)$$

where $M_w$ and $\rho_w$ are the molecular weight and density of $Zn_2SiO_4$. This assumes no loss of silicon during the reaction.

Substituting the values $\rho_{ox} = 2.27$, $\rho_w = 4.103$ and $M_w = 222.85$ gives

$$\frac{t_{ox}}{t_w} = 0.487 \qquad (7.5)$$

This shows that to produce a willemite film of thickness $t_w$ an initial oxide of thickness 0.487 $t_w$ is required.

For Type-C willemite the experimental values of the initial oxide thicknesses are 489 Å and 572 Å for slices SL12 and SL13 respectively, giving values of 1004 Å and 1175 Å from Equation (7.5). However, the measured values were 734 Å and 765 Å respectively, indicating a discrepancy of something over 300 Å. Results for Type-A willemite deviates more than for Type-C willemite in that the measured willemite thickness is only half of the calculated value. This could be due to any of the following factors :-

(i) Error in ellipsometer readings as discussed earlier.

(ii) The value of $\rho_w$ used is for willemite powder rather than of the thin film.

(iii) It is possible that not all the $SiO_2$ has been used up.

## Film Examination

In the three previous chapters, film examinations using both the optical microscope and the SEM have been described. The use of the optical microscope is straight forward, where the points of interest are features like crystallite size, defects, coloration, etc. The SEM has been used in the secondary emission and cathodoluminescent modes for the examination of the films, while tests for crystallographic features on the underlying silicon have been made by the Electron Channelling Pattern (ECP) technique.

For the purpose of comparison, the three types of willemite will be discussed together, based on the examination of the underlying silicon, the residual film and the willemite film.

(a) The underlying silicon :-

The silicon surface of Type-A willemite, under the optical microscope appeared to be smooth with no distinctive features. However,

dendritic features forming crazed patterns are obvious for silicon

surfaces from Types-B and C. This feature has been associated with zinc

diffusion into the silicon surface during the long reaction time. An

explanation for this seems to be that zinc diffuses through $SiO_2$,

because of its random tetrahedral network, in certain preferential

regions within the oxide. It was also thought that the crystalline

structure of the silicon might have been lost because of this feature

and ECP tests were carried out. The resolution of this technique is

within 50 $\overset{o}{A}$ of the surface. The patterns, only slightly diffuse at the

edges, were still observed in the underlying silicon of Types-B and C

willemite indicating that the crystalline structure is still retained in

spite of the disruption seen in the optical microscope.

(b) The residual film :-

Such films are well-defined for Types-A and B willemite by

being non-cathodoluminescent when bombarded with electrons. In the case

of Type-C willemite, the definition is more vague because the cathodo-

luminesce remains after the composite film has been washed with normal

acids but HF removes the entire film. Under the optical microscope, the

residual film of Type-A willemite appears to be free from any distinctive

features, while for Type-B willemite the dendritic features are obvious,

superimposed with very fine crystallites. The dendritic features appear

dark brown while the crystallites are almost colourless. Secondary

emission imaging in the SEM proved to be fruitless because of the charging

of the film.

(c) The willemite film :-

The Type-A willemite films show very coarse crystallites,

observed even at a magnification of 250X under the optical microscope.

The crystallites appear violet in colour and embedded in a tan background.

They could be crystallites of willemite embedded in a silicon oxide matrix

as pointed out by Edwards (1). If white specks are seen at points of defects then this may indicate that the starting oxide is not defect-free and of good quality. The crystallites get more coarse towards the edge of the slice as well as uneven, possibly due to the outward flow of the reacting constituents when in the molten form.

Types-B and C willemite films appear more fine grained than Type-A and with bluish crystallites rather than violet. The distribution of the crystallites is more uniform and film surfaces are almost defect-free. The crystallites seem to be more numerous than in Type-A willemite.

The observed differences in grain-sizes between Type-A willemite and those of Types-B and C can probably be explained as follows. During the reaction process, willemite crystallites that are formed during the initial stages of the reaction are assumed to spread out and allow further reaction to take place between the zinc and the silicon oxide. In the case of Type-A willemite before this could occur the reaction is stopped, hence leaving behind coarse grains of willemite crystallites intermingled with other constituents in the final film. On the other hand, the long reaction times of Types-B and C willemite ensure that the growth process is not interrupted. After the initial willemite crystallites are formed, they spread out and more of the zinc is allowed to continue reacting with the oxide. This continuous spreading out effect may be responsible for the formation of the fine-grained structure over relatively larger areas.

## 7.4     Electron Injection and Dielectric Polarization

The shifts in C-V curves along the voltage axis for willemite MIS-type structures were observed right from the early work of Edwards (1) and later, Davies (2).    In other materials C-V shifts have always been associated with the creation of interface states (7), movement of mobile impurity ions (8), or the formation of space-charges arising from either dielectric polarization (9) or electronic trapping (10,11,12). One or more of these mechanisms can occur simultaneously in an MIS structure, depending on factors such as the electric field strength, material, temperature, time and the polarity of the top electrode.    In the present work, the extremely large shifts in the C-V curves of willemite composite structures could not be explained in terms of surface states and mobile impurity ions as pointed out in Chapters 4, 5 and 6. An attempt is made in this section to try to obtain a better understanding of the other two mechanisms, electronic injection with trapping and dielectric polarization, in order to distinguish between them.

### Electron Injection

Electron injection into willemite films of MIS-type structures, especially from the silicon, has always been the objective of the present work.    Unfortunately, willemite being a wide band-gap material ($\sim 5.5$ eV) and having a very open structure, is likely to have considerable concentrations of traps in the band-gap, although their nature and energy levels relative to the band edges are not known.    Unlike the case of crystalline solids, conduction in glasses or disordered materials faces two difficulties, as pointed out by Mott (14) and Jonscher and Hill (15).    These are the lack of a rigorous theory and great uncertainty about their detailed structure.    For these reasons, the use of concepts such as conduction and valence bands is not as rigorous as in the crystalline case.    The problem arises because of the absence of long-range order that is a

distinguishing characteristic of crystalline solids. Nevertheless the short-range order in non-crystalline materials is basically like that in the corresponding crystal and this is expected to give rise to some of the same important properties as for the crystalline state, most notably the existence of conduction and valence bands separated by a gap. However, the disordered solid also has many localized states near the band edges and caused by the imperfections. The electron energy levels are schematically illustrated in Fig 7.2.

The energy levels of the extended states within the conduction and valence bands are not localized, i.e. an electron in one of these states is free to move through the solid with a finite mobility. In the localized states an electron is restricted to a small volume and it therefore has a very low mobility (16). Such states are sometimes classified into "shallow" (near a band edge) and "deep" (near mid-gap) states and they are often loosely referred to as "traps". On the other hand, the states caused by a definite atomic impurity is illustrated by a single energy level $E_t$ in the band-gap (see Fig 7.2).

Charge injection into insulators can take various forms, depending on factors such as the band-gap, nature of traps, dielectric constant etc. For simplicity, only one-carrier (i.e. electron) injection into an insulator will be considered here. The three possible processes by which electrons can be injected from a metal or semiconductor are :- (a) by surmounting the potential barrier into the conduction band, (b) by emission into trapping levels, and (c) by tunnelling into the conduction band. In the case (a), the activation energy required to surmount the barriers in wide band-gap insulators are usually very large, possibly a few electron volts. This makes it most unlikely unless photo-or thermal-excitation is used. Case (c), also called Fowler-Nordheim tunnelling, usually requires very high electric fields, close to $10^7$ v/cm. Most of the discussion of
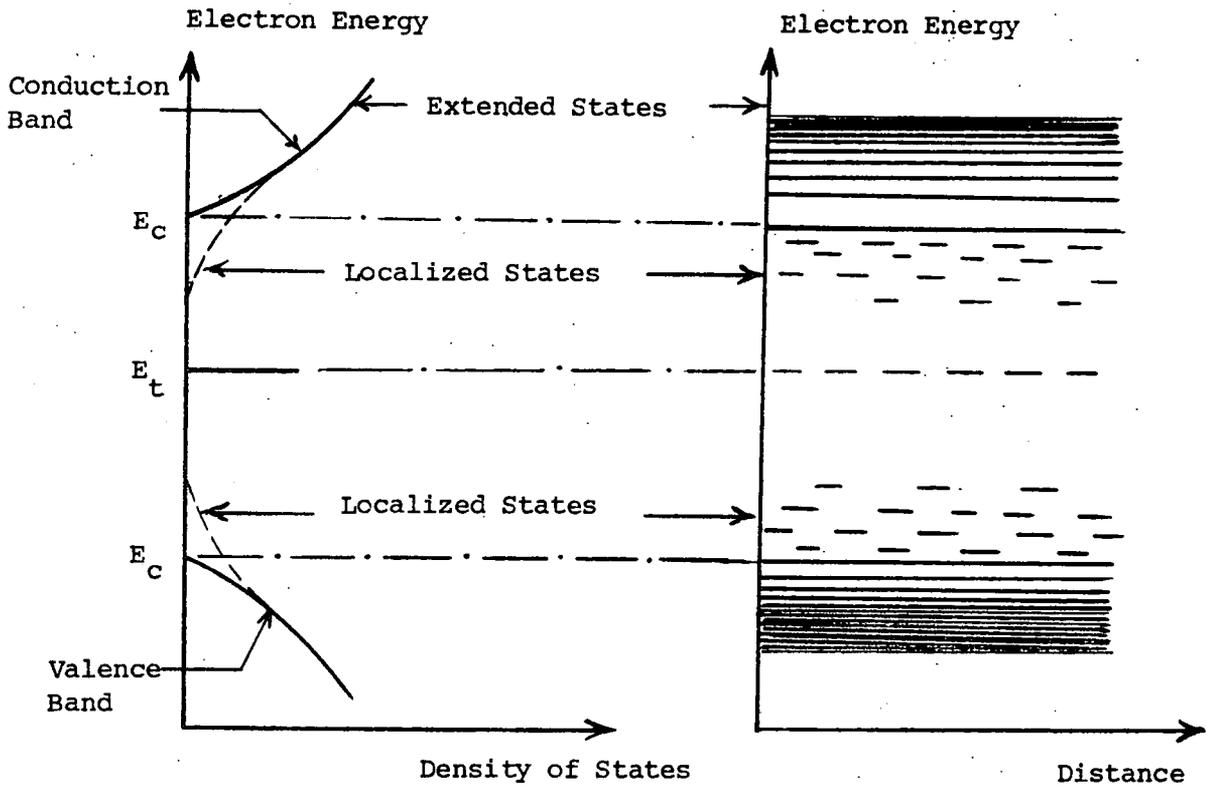
Fig 7.2    Density of electron states and energy band diagram
           of a disordered solid showing the location of electron
           states.
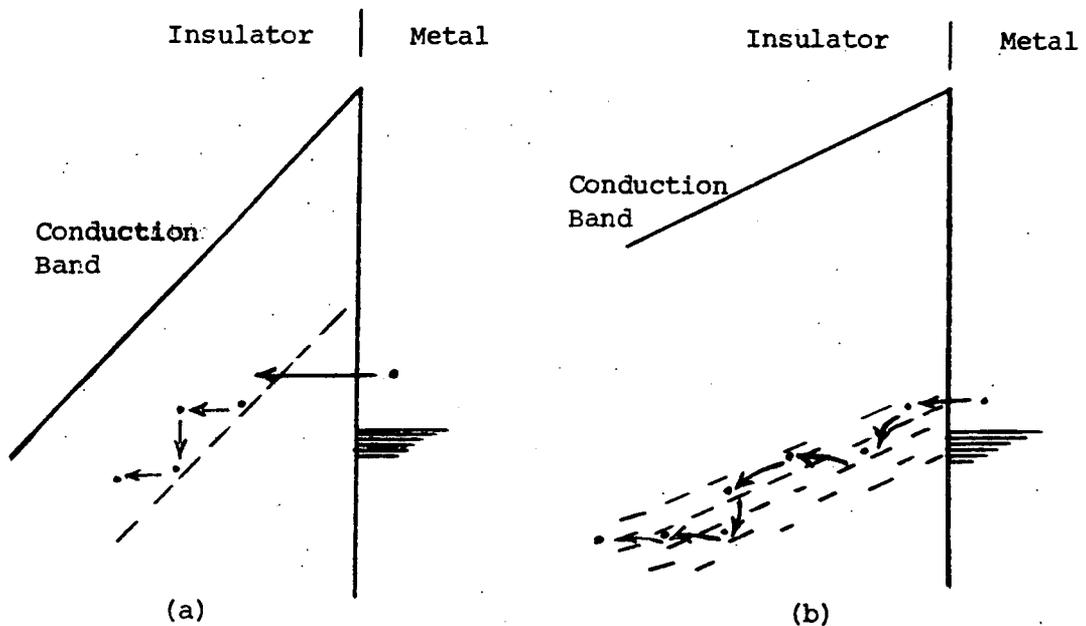


Fig 7.3    Two possible forms of conduction via traps in wide
           band-gap materials :-

           (a) Poole-Frenkel process via traps

           (b) Hopping process via localized states..

(a)                                    (b)
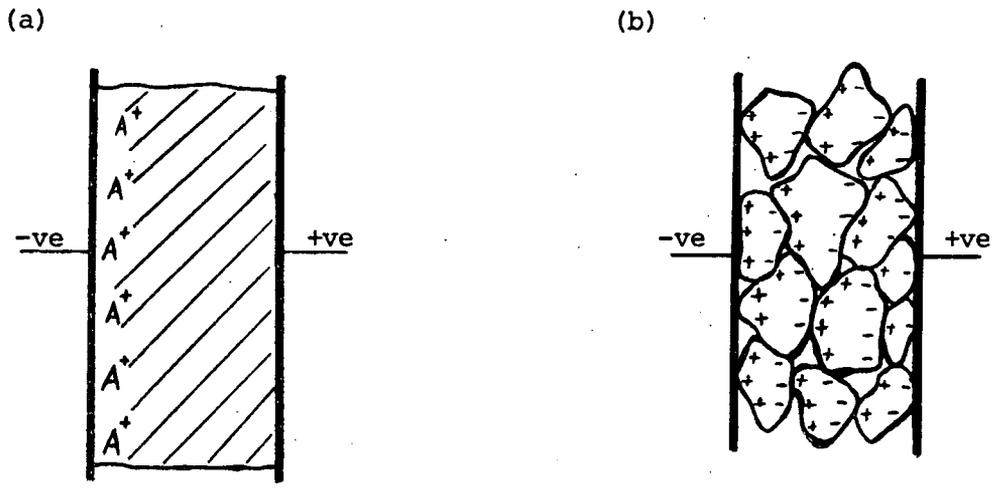


Fig 7.4      Interfacial polarization

             (a) at electrodes

             (b) in crystallites.


(a)                                    (b)



● Silicon

○ Oxygen
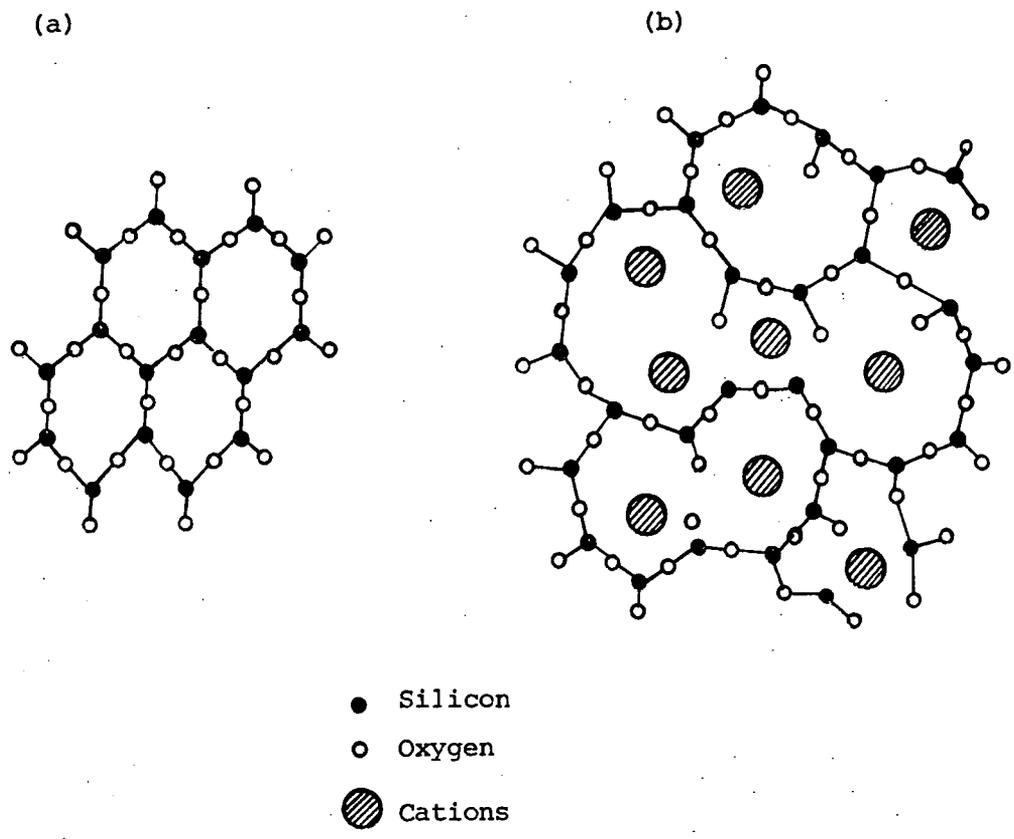
▨ Cations

Fig 7.5      Schematic representation in two dimensions of
             the structure of :-

             (a) crystalline glass

             (b) the corresponding glass structure with network
                 modifier cations
                 (after Sutton    (24) ).

electron injection in Sec. 7.5 is therefore centred around mechanism(b).

Electronic conduction via traps in insulators can be in the form of either Poole-Frenkel conduction or hopping conduction. In the former, electrons injected from an electrode into traps in the insulator are emitted into the insulator conduction band (as shown in Fig 7.2(a) ) before being retrapped at the next site. For this field strengths of $10^6$ v/cm or greater are required, e.g. as reported for $Si_3N_4$ (11) and $Al_2O_3$ (12). On the other hand, hopping conduction, never involves the insulator conduction band. With a high density of localized states in the band-gap, electrons injected into the insulator are transported by by hopping between these energy states which form a sort of a quasi-conduction band (see Fig 7.3(b) ). It has been pointed out by Jonscher (16) that this process requires less field strength than the Poole-Frenkel process, e.g. an estimated $2 \times 10^5$ v/cm when the density of localized states is approximately $10^{17}$ $cm^{-3}$ (15) at room temperature.

Studies of charge trapping effects in insulators using MIS-type structures have been successful in explaining the properties of $Si_3N_4$ (17,18) and $Al_2O_3$ (19,20). In both cases, charge injection and transport have been found to be by the Poole-Frenkel mechanism.

Dielectric Polarization

Polarization in insulators refers to the limited displacement of charge by an electric field. Although polarization can be an electronic or ionic process, the discussion here will be confined to the case for ions, where the build-up of the polarization is a slow process and the degree of polarization is large.

Two of the most common forms of polarization by the displacement of ions in an electric field are illustrated in Fig 7.4 (21). The interfacial polarization shown in Fig 7.4(a) could be due to either mobile impurity ions present in the dielectric or native ions which are dissociated

from the lattice site of the dielectric itself. The second form of polarization, Fig 7.4(b), is for the case where ions are clustered along the boundaries of crystallites or conducting inclusions in the dielectric. Both types of polarization give rise to space-charge in the dielectric and hence to a non-uniform internal field. A theoretical description of the space-charge and changes in the internal field has been given by Sutton (22) for experimental observations made on lead borosilicate glass. The space-charge formed was due to the displacement of mobile cations from immobile anions in this case.

The charging and discharging currents due to the orientation of permanent dipoles or to the movement of ions always decay with time but there is no means of distinguishing the two (23). Consequently when one speaks of conduction in insulators, which almost always decays with time, one usually has in mind a transport process involving the bodily transport of charges rather than polarization, although one can rarely test whether one is correct. In certain glasses, electrolytic conduction by cations has been observed at room temperature and above (24). The variation of conductivity with temperature at moderate fields can usually be expressed by

$$\sigma = A \exp\left(\frac{-b}{T}\right) \qquad (7.6)$$

A and b being empirical constants. The glassy network formed by silicate tetrahedra is relatively rigid and the modifying alkali or metallic cations reside in large cavities. They are loosely bonded to the network and the energy barrier which has to be overcome for movement to a neighbouring cavity is low. With sufficient thermal energy, the cation can leave its stable position and migrate, for short periods of time, through the silica framework. In the presence of a field, these

cations will drift thorugh the cavities finally building up polarization effects. Thus the conduction current, as seen from equation (7.6), is tremendously increased at elevated temperatures. A theoretical description of the polarization and diffusion of alkali cations in silicates has been clearly presented by Charles (25).

7.5    The Electrical Properties in General

In the last three chapters, individual discussions of the electrical properties of the various films have been given. The electrical results showed certain similarities as well as differences depending on the reaction conditions. It is the objective of this section to try to relate the growth conditions to the properties of the films in general.

(i) Initial Constituent Films:-

The quantity and quality of the initial constituents $ZnF_2$:Mn and $SiO_2$ for the formation of willemite could easily affect the final properties. The purity of $SiO_2$ in MOS structures is well-known to have an important influence on the stability of its flat-band voltage (7). This was also shown by the initial flat-band voltage $V_{FBO}$ of the present composite structures. The first batch of test capacitors, which had dry-oxidation carried out in the same furnace used for wet-oxidation, showed $V_{FBO}$ varying over a considerable voltage range, which could be due to impurities. However, later capacitors, which had the initial oxide grown in a separate dry-oxidation furnace, have values of $V_{FBO}$ which are constant within $\pm$ 0.2v. This showed that the quality of the initial oxide has a direct influence on the electrical characteristics final composite willemite films.

The thickness of $ZnF_2$:Mn required for the reaction has been the subject of study by Errington (3) who showed that an excess could lead to an unreacted top-layer while insufficiency results in a thicker residual film. Davies (2) showed that the unreacted top-layer is insulating which

could prevent any direct metal-to-willemite contact. However, the residual film in Type-A willemite is quite conducting with a field-enhanced tunnel-hopping conduction process, which therefore depends on thickness. In Type-B willemite the residual film is very insulating but it was shown to have a polarization effect at high fields due to the displacement of charges on conducting inclusions, possibly of zinc and/or manganese within the film. If the $ZnF_2$:Mn is very thin ( $\sim$ 200 $\AA$), the final residual film is thicker than the willemite film. This was shown in Chapter 5, i.e. the case for $d_w < d_o$, which showed that the electrical characteristics of the composite films are then dominated by the residual film.

(ii) Film Stability:-

All composite structures measured immediately after processing displayed good MIS-type C-V characteristics. However, ageing effects were observed on the composite films from Type-A willemite. After 2/3 weeks in a dessicator, the structures showed the 'breakdown' phenomenon mentioned in Chapter 4. Such deterioration was not observed in either Types-B or C willemite composite films, where even after four months, MIS-type C-V characteristics were still obtainable.

This ageing effect in Type-A willemite might be explained by its Auger profile measured by Hurd and Johnston (5). In this short-reaction case, the excess zinc concentration in the surface region of the film could have modified the silicate network and weakened the bonds. Furthermore, as indicated by Sutton (24), the structure at the surface of the glass although not well understood, appears to be frequently affected by the surrounding environment. Therefore, some form of chemical reaction may have taken place between the Type-A willemite and the atmosphere so as to alter its electrical properties. The detailed mechanism involved is, however, not understood.

The 'breakdown' phenomenon was also observed after the prolonged application of negative stress applied to the Type-A willemite composite structures. The cause of this has been attributed to the high built-in electric field resulting from the polarization effect. If this develops in localized areas it could result in conducting channels formed by broken bonds. Since this phenomenon is absent in both Types-B and -C willemite, it can be deduced that the latter films are more uniform in nature so that the localized conduction did not occur.

(iii) Effect of Stress Voltages :-

The effect of the stress voltage on the flat-band shift and shape of the C-V curves, has been the main method used for studying the charge movement within the insulator of other MIS systems (8,18,19). The same method was used here for the MIS-type composite willemite structures. The main characteristics observed in the three types of composite willemite films were as follows :-

|  | Type-A | Type-B | Type-C |
|---|---|---|---|
| (a) Negative Stress | $\Delta V_{FB}$ positive | $\Delta V_{FB}$ positive | $\Delta V_{FB}$ positive |
| (b) Positive Stress | No shift | No shift except when $d_w < d_o$ | $\Delta V_{FB}$ negative |
| (c) Residual Film | Tunnel-hopping | Dipolar Polarization | – |

Negative voltages shift the flat-band voltage towards more positive values, while positive voltages, have no effect, except for Type-C willemite. The negative space-charge arising from negative stressing has been explained in terms of the movement of $Zn^{2+}$ cations away from the willemite-residual film interface, leaving behind the immobile silicate radical $(SiO_4)^{4-}$. This explanation is justified in the case of Types-A and B willemite where the residual films are clearly defined.

However, for Type-C willemite, the movement of the loosely bound $Zn^{2+}$ cations was believed to be confined to the surface region of the willemite film, i.e. about 150 Å thick, since there is no well defined residual film in this case.

One of the important features of the electrical properties of glass is that it can act as an electrolyte (22,24) with ionic conductivity depending on temperature according to $\sigma \sim \exp(^{-W}/kT)$ where W is the activation energy. Since most metallic cations occupy interstitial positions in the network, the activation energy may be very low. The composite film of Type-A willemite has a room temperature resistivity of about $10^{12}$ Ω-cm which, from the above expression, is expected to decrease at elevated temperatures. Furthermore, at room temperature the resistivity of glass varies from $10^5$ Ω-cm. to about $10^{19}$ Ω-cm. (24) depending on the chemical composition. Willemite seems to be similar and the activation energy of the cations at interfacial regions could therefore be low, although no measurements were carried out. In Type-A willemite, the short reaction-bake, which was thought to leave the reaction incomplete, may be responsible for the loosely bonded $Zn^{2+}$ cations at the willemite-residual film interface. For Type-B willemite, the continuous passage of oxygen during the reaction may have caused the $Zn^{2+}$ cations to form some oxide of zinc rather than making stronger bonds with the interfacial silicate network. The complete reaction and oxygen-free ambient used for Type-C willemite may have confined such loosely bonded structures to the surface region of the composite film ($\sim$ 150 Å thick) as described in Section 6.5.

Both Types-A and B willemite showed no shift in flat-band voltage when positive stresses were applied. In both cases, the residual films are thought to be an oxide of silicon containing gross impurities and defects. The residual film of Type-A willemite is probably unreacted

silicon oxide while for Type-B willemite it was thought to result from the further oxidation of the silicon during the reaction. Oxides of silicon, are more close spaced and compact in their structure than the silicates (26) because they have fewer non-bridging oxygen atoms in their structure. Furthermore, the presence of cations acting as network modifiers in silicates tends to weaken the bonds while this does not occur in oxides of silicon which are more crystalline (Fig. 7.5). For this reason, it is suggested that the $Zn^{2+}$ cations cannot penetrate the residual film at room temperatures so preventing any appreciable space-charge occuring at the dielectric-dielectric interface. This could explain the stability of flat-band voltage with positive stressing in Types-A and B willemite.

It is proposed that the bulk of the Type-C willemite film is made up of well distributed $Zn_2SiO_4$ crystallites separated by very thin layers of $SiO_2$. Hence the movement of ions is confined to the individual crystallites rather than throughout the entire thickness of the film so that the effects of space-charge formation with stressing are less drastic than in the earlier types of willemite. The polarization in this case is of the smaller dipolar type as illustrated in Fig 7.4(b).

When very high positive fields are applied to Type-C willemite the resulting positive space-charge is thought to be due to the injection of holes into interfacial traps. Such traps would be in a very thin interfacial layer of the form of $Zn_xSi_yO_z$. This electronic process was proposed because it only occurs at very high field strengths, in excess of $10^6$ v/cm, and it shows a very rapid recovery of the flat-band voltage at room temperature. Furthermore, the $Zn_xSi_yO_z$ interfacial layer proposed seems to be consistent with the Auger profile of Type-C willemite as measured by Hurd and Johnston (see Fig 7.1 (b) ).

(iv) Role of Residual/Interfacial Films:-

The residual film of Type-A willemite was investigated initially by Davies (2) and further work by Errington (3) showed that it could not

be totally eliminated in the processing. It was thought earlier that the residual film played a very important role in reducing the efficiency of electron injection from the silicon into the willemite and even possibly in making the whole structure non-conducting. However, as described in Section 4.5, if sufficiently high fields are applied to the residual film, electrons can pass through it by tunnel-hopping through localized states. For thicknesses greater than 300 $\overset{o}{A}$ , where direct quantum tunnelling is not possible, the tunnel-hopping process was achieved by applying a field in excess of $10^4$ v/cm. at room temperature. Even though conduction is possible in the residual film, electrons from the silicon may be prevented from passing right through the composite film by repulsion from the negative immobile anions near the willemite-residual film. Another possibility is that there are insufficient localized states available around the centre of the willemite band-gap for tunnel-hopping to occur. The overall conduction in composite films of Type-A willemite is therefore thought to be due to the movement of ions. This may explain how it is possible to observe good MIS-type C-V characteristics in Type-A willemite composite structures, which have at the same time a d.c. conduction giving a current of approximately $10^{-9}$ A. at fields of around $10^5$ v/cm. D.C. conduction, confined within the willemite film only, is an ionic process while the high frequency strong inversion C-V characteristic is electronic.

The residual film of Type-B willemite is less conducting than for Type-A. As discussed earlier the formation of the residual film is different in the two cases. In Type-B willemite the further oxidation of the silicon during the reaction probably provides the residual film with a better and more compact silica network although zinc inclusions were thought to be still present. The measurement of $C_{max}$ against frequency for this film (Fig. 5.8 of Chapter 5) shows a variation with

frequency between about $10^3$ Hz and $2 \times 10^5$ Hz.    Normal silicon dioxide

has a constant value of dielectric constant over this range of freq-

uencies (27). The frequency variation could therefore be due to the zinc

inclusions, which may be seen from visual examinations of the film. The

Schottky-barrier measurements on the underlying silicon also show the

presence of zinc. This could also account for the residual film of Type-B

willemite having the dipolar type of polarization characteristics which

were found.

The presence of the residual films, in the case of Types-A and

-B willemite, or of the interfacial film, in the case of Type-C willemite,

must reduce the electron injection from the silicon into the willemite

films. The presence of space-charges, impurities and defects in these

films further reduces the efficiency of electron injection into the wille-

mite. Hence the probability of electroluminescence by impact collision

with the $Mn^{2+}$ centres is greatly decreased. Lattice scattering, reducing

the energy of injected electrons, further reduces the probability of

impact ionisation and light emission from the willemite. Space-charge

arising from polarization would also affect the electron injection process

particularly by forming a layer of negative immobile anions at the inter-

face of the willemite.

Former workers on willemite thin films on silicon (1,2,28) have

obtained only weak electroluminescence, even at ~~very~~ field strengths very

close to those for dielectric breakdown. No electroluminescence at all

was observed in the present work probably due to the factors discussed

above.

# REFERENCES

## CHAPTER 7

1. G.S.Edwards - Ph.D Thesis, Durham University (1970).

   G.S.Edwards and A.N.Rushby - J.Mat.Sci., 6, 225 (1971).

2. G.D.Davies - M.Phil.Thesis, Durham University (1975).

3. D. Errington - unpublished.

4. M. Schmalzried - 'Solid-state Reactions', pp 94-95, Academic Press (1974).

5. J.M.Hurd and R.E.Johnston - private communication.

6. A.S. Grove - 'Physics and Technology of Semiconductor Devices' John Wiley & Sons (1967).

7. A.S.Grove, B.E.Deal, E.H.Snow and C.T.Sah - Sol.St.Elec., 8, 145-163 (1965).

8. R.A.Abbot and T.I.Kamins - Sol.St.Elec., 13, 565-576, (1970).

9. E.H.Snow and B.E.Deal - J.Electrochem.Soc., 113, 263-269 (1966).

10. B.Swaroop and P.S.Schaffer - J.Phys. D:Appl.Phys., 3, 803-806 (1969).

11. S.M.Sze - J.Appl.Phys., 38, 2951-2956 (1967).

12. C.A.T. Salama - J.Electrochem.Soc., 118, 1993-1999 (1971).

13. P.M.Sutton - J.Am.Ceram.Soc., 47, 188-194 (1964).

14. N.F.Mott - J.Non-Cryst.Sol., 8-10, 1-18 (1972).

15. A.K.Jonscher and R.M.Hill - Thin Sol.Films, 8, 169-249 (1975).

16. A.K.Jonscher - Thin.Sol.Films., 1, 213-234 (1967).

17. G.W.Taylor and J.G.Simmons - Sol.St.Elec., 17, 1-10 (1973).

18. S.M.Hill, D.R.Kerr and L.V.Gregor - Appl.Phys.Letts., 10, 97-99 (1967).

19. T.Tsujide, S.Nokanuma and Y.Ikushima - J.Electrochem.Soc., 117, 703-708 (1970).

20. P.Balk and F.Stephany - J.Electrochem.Soc., 118, 1634-1638 (1971).

21. P.J.Harrop - 'Dielectrics', Butterworth (1972).

22. P.M.Sutton - J.Am.Ceram.Soc., $\underline{47}$, 219-230 (1964).

23. R.W.Sillars - 'Electrical Insulating Materials and their Applications', IEE Monograph Series 14, pub.Peter Peregrinus (1973).

24. R.M.Sutton - Prog.Dielec., $\underline{2}$, 115-165 (1960).

25. R.J.Charles - J.Appl.Phys., $\underline{32}$, 1115-1126 (1960).

26. W.H.Zachariasen - J.Am.Ceram.Soc., $\underline{54}$, 3841 (1932).

27. A.E.Owen and R.W.Douglas - J.Soc. Glass Tech., $\underline{43}$, 159T-178T (1959).

28. M.R.Husain - Ph.D.Thesis, Durham University (1973).

CHAPTER 8


CONCLUSION


## 8.1    Conclusions of the Present Research

The work described in this thesis has concentrated on the growth

and electrical properties of thin films of willemite on silicon as formed

from the solid-state reaction of $ZnF_2$:Mn and $SiO_2$ at a high temperature.

The research was divided into phases corresponding to three types of

willemite film, called Type-A, Type-B and Type-C willemite.  Each phase

involved a study of the growth technique, physical appearance, electrical

measurements and analysis of the results, in order to achieve some cor-

relation between the growth conditions and the properties of the resulting

films.  Results for the three types of willemite were presented in their

individual chapters, 4, 5 and 6.

Earlier work on willemite thin films on silicon (1,2,3) has

always been plagued by non-reproducible electrical results which has been

attributed to the contamination of the films due to imperfect processing

techniques.  The use of integrated circuit techniques for fabricating

the electrical test structures in very clean conditions has considerably

increased the reproducibility in the electrical results.  Very small

capacitors with well defined edges and reduced fringing field probably

avoided the defects in earlier, larger structures.  Also, the silicon

was oxidised in a special dry-oxidation furnace capable of producing high

quality MOS devices.  The $ZnF_2$:Mn was always evaporated in a vacuum of

$\sim 10^{-6}$ torr, and every precaution was taken to prevent contamination at

all stages of processing.  As a result the initial flat-band voltages of

the composite willemite MIS-type C-V curves had a scatter of less than

$\pm$ 0.2v and in the case of Type-A willemite, the negative bias d.c. cond-

uction measurements produced a constant current of about $10^{-9}$ A in almost

all capacitors.  Such reproducibility, specifically for Type-A willemite, had never been achieved before.  With the reproducibility it was worthwhile to investigate various ways of producing the films to try to find an optimum structure for injection electroluminescence.

In general the structure of silicates is well understood (4) and there is no doubt about the dependence of their electrical properties on the structure as shown, for example, in work on alkali silicates by Charles (5).  The different conditions for growing the three types of willemite resulted in composite films with widely differing properties. The excessive zinc concentration in the surface of Type-A willemite films and its reduction towards the interior gave a residual film, consisting mainly of silicon and oxygen.  Because of the relatively short reaction time, zinc diffusion through the entire thickness of the underlying silicon oxide was not possible although the Schottky barrier C-V measurements on the underlying silicon showed that manganese was able to diffuse through during the reaction.  This indicates a very much larger diffusion coefficient for manganese than for zinc.  In Types-B and -C willemite, however, the zinc was able to diffuse right into the underlying silicon because of the much longer reaction time.  Types-B and C willemite are, therefore believed to have a far more uniform zinc concentration, than Type-A.

The most important factor common to Types-A and -B films is the residual film. The residual film for Type-A willemite was attributed to the incomplete reaction of the $SiO_2$ film while for Type-B it was due to the oxidation of the silicon during the reaction.  In both composite films, the formation of a negative space-charge with a negative stress was explained by ionic movement due to the weak silicate bonds near the willemite residual film interface.  This proposal was made in view of the fact that $Zn_2SiO_4$ has a much more open structure than $SiO_2$ with many voids and loosely

bound cations (1,4), while the residual film, which is approximately $SiO_2$, has a more compact structure (6). For this reason, chemical non-stoichiometry of the willemite is to be expected near the willemite-residual film interface. The $Zn_2SiO_4$ at this interface has a relatively large number of non-bridging oxygen atoms which are electrically compensated by zinc, acting as the network modifier, fitting interstitially within the silicate network. The effect of this is that some of the ions are loosely bound at the interface (7).

Type-C willemite had the additional new property that most of it could not be etched in normal acids. It was therefore impossible to isolate a 'residual' non-luminescent film. The lack of chemical reactivity was probably due to each crystallite being surrounded by protective silicon oxide. However, the film probably still had a very narrow interfacial layer below the fully reacted willemite, and with a very thin loosely bound film, similar to Types-A and B willemite on the surface. The thickness of this surface layer was measured by etching in the normal way. The bulk of the Type-C willemite film is thought to be made up of crystallites of willemite separated by very thin layers of silicon oxide, while the interfacial film, $Zn_xSi_yO_z$, is due to the constituent atoms not being in the right proportions for any definite compound to form. This feature also exists in MNOS (8) and MAOS structures (9).

In general, the electrical properties of the three types of willemite film are dominated by the effects of polarization. In most cases, polarization is due to the displacement of the mobile $Zn^{2+}$ cations from the immobile $(SiO_4)^{4-}$ radicals, so as to leave a negative space-charge following the application of a negative bias on the electrode. This polarization is favoured by the modified structure of the silicate lattice near the dielectric-dielectric interface. The $Zn^{2+}$ cations are in interstitial positions in voids in the silicate network, where they are loosely bound and easily displaced. This picture is consistent with the work

of Sutton (10,11) who showed that silicate glasses have ionic conduction with the cations as the mobile carriers in most cases.

The electrical results for the composite films of Types-A and B willemite have been fitted to the Snow and Dumesńil double-dielectric polarization model (12) showing that the above type of interfacial space-charge polarization, was responsible for the formation of negative space-charges, with negative stresses, in these films. The residual film of Type-A willemite has field-enhanced tunnel-hopping properties where the localized states were provided by defects and/or interstitial atoms in the silicon oxide due to the incomplete reaction. On the other hand, the residual film of Type-B willemite showed dipolar polarization effects which required high electric fields, and this phenomenon has been attributed to the presence of conducting inclusions in the predominantly silicon oxide. Type-C willemite, being the most uniform, has mainly dipolar polarization properties. The bulk of this willemite is thought to become polarized by charge accumulation at the crystallite interfaces. However, the thin outer layer may have the same interfacial space-charge polarization as in Types-A and B willemite. Injection of holes into traps within the interfacial $Zn_xSi_yO_z$ layer is believed to occur with very high positive applied fields.

As mentioned in Chapter 1, the long-term objective of the present investigation is to try to achieve electroluminescence by the injection of electrons, possibly from the silicon, into the film. The results show, that such a process is not very likely, even though it may have occurred previously with fields almost sufficient to cause dielectric breakdown. The reason is that the polarization with negative bias reduces the field in the willemite to almost zero. The negative space-charge near the silicon prevents the injection of electrons and greatly reduces the number capable of impact collision with the $Mn^{2+}$ centres. Also, the low field in the willemite would increase the probability of trapping and reduce the

141

probability of them acquiring high energies. When high positive voltages are applied, electrons are prevented from being accelerated from the silicon into the willemite film by two factors. Firstly, the electrons will be scattered within the comparatively thick residual film, and secondly, they will be repelled by the negative immobile $(SiO_4)^{4-}$ radicals at the dielectric-dielectric interface. In Type-C willemite, the field of the trapped holes, will also prevent the acceleration of electrons into the bulk willemite film when a positive bias is applied. All these factors complicate the ideal suggested process of electron injection followed by impact collision with $Mn^{2+}$ centres in the willemite films and explain the negligible electroluminescent properties of the present willemite films.

## 8.2  Suggestions for Further Research

On the whole, the present work on willemite films has provided only a partial understanding of its electrical properties. If more information on the dielectric is required, then a.c. capacitance measurements would probably be of greatest help. This is because the physics of polarization is well understood, and the a.c. capacitance technique has been extensively studied for numerous materials over a wide frequency spectrum, thus providing the relaxation time constants. In most silicate glasses, relaxation processes are observed in the lower frequency range (10), i.e. at about $10^4$ Hz and less.

Complex problems arising from material inhomogeneity, interfacial films, loosely-bonded structures, etc., have been encountered in the present work. Auger profiling, as done by Hurd and Johnston (13), could possibly provide more information on the distribution of the constituent materials, and electron diffraction studies could be used to investigate the structure of the crystallites, especially for the long reaction-bake willemite films. It is hoped that from such studies, the film quality could be improved, trapping and polarization effects could possibly be

reduced, and electron injection processes into the willemite films enhanced.

However, other methods for depositing thin films of willemite, which might yield higher quality films, are still possible. There is of course the direct thermal evaporation of $Zn_2SiO_4$ : Mn powder in a high vacuum although there is some doubt as to whether the manganese atoms could be deposited simultaneously in this process. The other possible deposition technique is by sputtering, where the vapour pressures of the constituents may be less important. With recent advances in ion implantation techniques and their progressive application in semiconductor technology, might encourage them to be used for forming homogeneous willemite films. The $SiO_2$ film on a silicon substrate could be bombarded with zinc and manganese atoms, and the depth of penetration into the films could be varied by controlling the energy at which the atoms are accelerated. Heat treatment could then be applied to crystallise the disrupted lattices.

Although electroluminescence has hardly ever been achieved in the present willemite films, cathodoluminescence is always a prominent feature which can be achieved with ease. For this reason, a deeper theoretical study of cathodoluminescence should be able to provide a clearer picture of the mechanisms involved. Consequently, this might provide information relevant to the electroluminescence properties and the parameters by which it could be achieved.

# REFERENCES

## CHAPTER 8

1. G.S.Edwards - Ph.D. Thesis, ~~Durham~~ *London* University, (1970).

2. G.D. Davies - M.Phil.Thesis, ~~Durham~~ *London* University (1975).

3. M.R. Husain - Ph.D. Thesis, Durham University (1973).

4. W.H. Zacheriasen - J.Am.Chem.Soc., $\underline{54}$, 3841 (1932).

5. R. J. Charles - J.Am.Ceram.Soc., $\underline{45}$, 105-113 (1962).

6. J.M. Stevels - Phillips Tech.Rev. $\underline{22}$, 300-311 (1960/61).

7. E.U.Condon - Am.J.Phys., $\underline{22}$,43-53 (1954).

8. M. Pepper - Inst.Phys.Conf. Proc."Insulating Films on Semiconductors", Durham (1979).

9. K. Iida, T.Tsujide and M.Nakagiri - Jap.J.Appl.Phys., $\underline{11}$, 1153-1160 (1972).

10. P.M. Sutton - Prog.Dielec., $\underline{2}$, 113-164 (1960).

11. P.M.Sutton - J.Am.Ceram.Soc.,$\underline{47}$, 188-194 (1964).

12. E.H.Snow and M.E.Dumesuil - J.Appl.Phys,$\underline{37}$,2123-2131(1966).

13. J.M.Hurd and R.E.Johnston - private communication.

# APPENDIX I

## CLEANING PROCEDURE FOR SILICON SLICES

All silicon slices were cleaned by a standard procedure before any further processing was carried out. The procedure, using Ultrar chemicals, is as follows:-

(1)     Boil three times in trichloroethane

(2)     Rinse in isopropyl-alcohol (IPA)

(3)     Rinse in deionized water

(4)     Heat for 30 min. in concentrated nitric acid

(5)     Wash in flowing deionized water for 30 min.

(6)     Wash in IPA, then blow dry

(7)     Etch in 10% hydrofluoric acid

(8)     Rinse in deionized water for 30 min.

(9)     Wash in IPA and blow dry.

# APPENDIX  II

## ELLIPSOMETRY  THEORY

Ellipsometry is the measurement of the effects of reflection on
the state of polarization of polarized light.  The state of polarization
is characterized by the phase and amplitude relationships being resolved
into two plane wave components, i.e. normal and perpendicular to the plane
of incidence, of the electric field vector.  The wave components are
designated by  p, in the plane of incidence, and s, normal to the plane
of incidence.
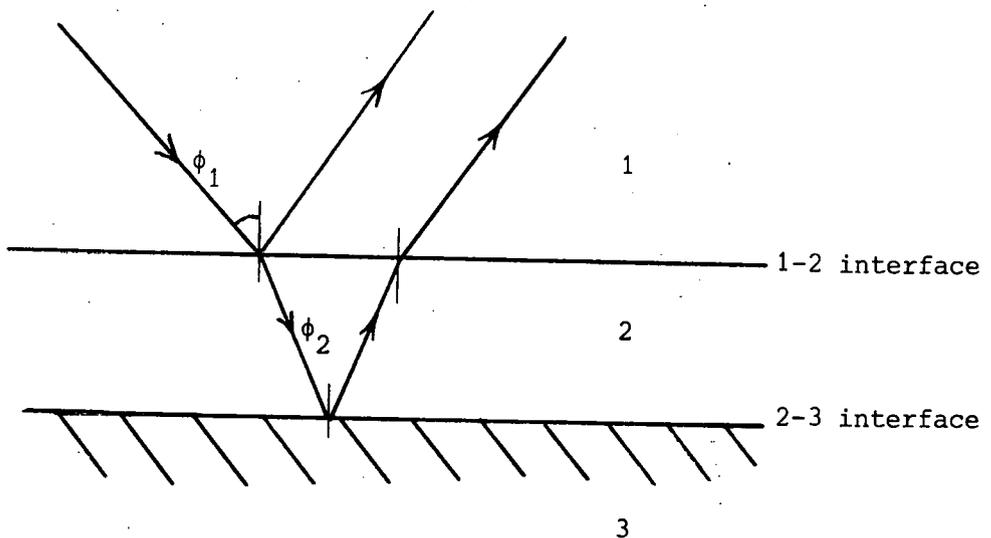


In the case of reflection from the surface of a medium x into
a medium y, at the x-y interface, the general formulae for the Fresnel
reflection coefficients are

$$r_p = \frac{n_x \cos\phi_y - n_y \cos\phi_x}{n_x \cos\phi_y + n_y \cos\phi_x} \qquad \text{(A2.1)}$$

$$r_s = \frac{n_x \cos\phi_x + n_y \cos\phi_y}{n_x \cos\phi_x + n_y \cos\phi_y} \qquad \text{(A2.2)}$$

Consider the situation at which the light has to traverse a measurement medium 1, a thin film 2 and reflected from a substrate 3. Then the Fresnel coefficients for the two component waves for reflection from the surface of the film into the ambient (at the 1-2 interface) are $r_{1p}$ and $r_{1s}$. Similarly the reflection from the substrate into the film (at the 2-3 interface) produces the coefficients $r_{2p}$ and $r_{2s}$. The change in phase $\sigma$, of the beam of wavelength $\lambda$ caused by traversing the film of thickness d and index of refraction $n_2$ is

$$\sigma = \left(\frac{2\pi d}{\lambda}\right) \left(n_2^2 - n_1^2 \sin^2\phi_1\right)^{\frac{1}{2}} \qquad \text{(A2.3)}$$

where $\phi_1$ is the angle of incidence in the measuring ambient of index of refraction $n_1$. By representing a complex function D such that

$$D = -2\sigma i \qquad \text{(A2.4)}$$

the ratio of the parallel and normal total reflection coefficients can be written as

$$\rho = \left(\frac{r_{1p} + r_{2p} e^D}{1 + r_{1p} r_{2p} e^D}\right) \Bigg/ \left(\frac{r_{1s} + r_{2s} e^D}{1 + r_{1s} r_{2s} e^D}\right) \qquad \text{(A2.5)}$$

Now the value of $\rho$ can also be represented in terms of the relative attenuation and phase shift of the parallel component with respect to the perpendicular component by the azimuthal angle $\Delta$, and relative

phase shift $\psi$ .     This is expressed by

$$\rho = \tan\psi \; e^{\Delta i} \tag{A2.6}$$

Knowing the value of the complex index of reflection for the substrate $\eta_3$ and inserting into equations (A2.1) and (A2.2), the values of $\eta_2$ and d can be obtained by equating (A2.5) and (A2.6), where $\psi$ and $\Delta$ are derived from measurements.  The final expression is in the quadratic form

$$C_1 (e^D)^2 + C_2 (e^D) + C_3 = 0 \tag{A2.7}$$

where $C_1$, $C_2$ and $C_3$ are complex functions of the refractive indexes, angles of incidence, $\Delta$ and $\psi$ .  Equation (A2.7) gives two solutions for $e^D$ but only the real part gives the true value of d.  Otherwise, if both $\eta_2$ and d are unknown, a series of refractive index values are assumed and the corresponding thicknesses are calculated.  Using these values for $\eta_2$ and d, a reverse technique is used in calculating $\psi$ and $\Delta$ , which will result in a certain amount of error, $\delta\psi$ and $\delta\Delta$, from that of the measured values.  The final value of $\eta_2$ and d is chosen for the condition where $\delta\psi$ and $\delta\Delta$ are both minimal.  The value of $\delta\psi$ and $\delta\Delta$ has to be within experimental error.

## CAPACITANCE CALCULATION FOR SCHOTTKY BARRIER

## WITH DEEP DONOR-TYPE TRAPS

Deep donor-type levels are assumed
to be present in a n-type semiconductor
at an energy level $E_T$ and with uniform
doping concentration $N_T$.  Such levels
when below the Fermi-level, are filled
with electrons and regarded as electri-
cally neutral.  When above the Fermi-
level the traps lose their electrons to
be electrically positive.  A similar
approach to that of Sah and Reddi for
acceptor levels yields a stair-case
charge distribution such that the
following conditions hold.

$$\rho_1 \ (0 < y < y_t) \ = \ q(N_D + N_T) \qquad\text{(A3.1)}$$

$$\text{(A3.1)}$$
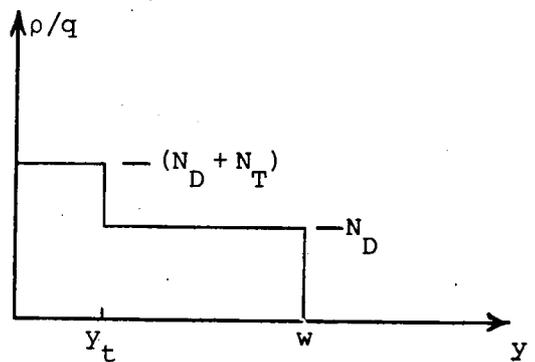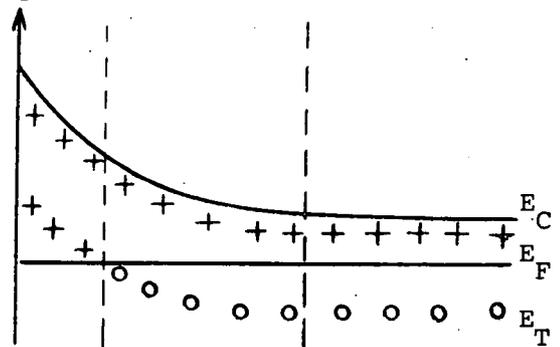
$$\rho_2 \ (y_t < y < w) \ = \ qN_D$$

Using Poisson's equation gives

$$\frac{d^2 y}{dx^2} \ = \ \frac{-1}{K\varepsilon_o} \ (\rho_1 + \rho_2) \qquad\text{(A3.2)}$$

and integrating over the voltage range from $V_D$ to $V$ results in

$$V_D - V \ = \ \frac{q}{2K\varepsilon_o} \left[ N_D w^2 + N_T y_t^2 \right] \qquad\text{(A3.3)}$$

or
$$V_D - V = \frac{q}{2\kappa\epsilon_o} \left[ N_D (w - y_t)(w + y_t) + y_t^2 (N_D + N_T) \right] \tag{A3.4}$$

Substituting
$$w - y_t = \sqrt{\frac{2\kappa\epsilon_o \phi_t}{q N_D}} \tag{A3.5}$$

where
$$\phi_t = (E_F - E_T)/q$$

into equation (A3.4) results in

$$V_D - V = \phi_t \left(\frac{N_o}{N_D}\right) \left[ 1 - \left(\frac{N_T}{N_D + N_T}\right) \right] + \frac{q}{2\kappa\epsilon_o} (N_D + N_T) \left[ w - \left(\frac{N_T}{N_D + N_T}\right)(w - y_t) \right]^2 \tag{A3.6}$$

and solving for the depletion width of the space-charge region this gives

$$w = \left(\frac{N_T}{N_D + N_T}\right)(w - y_t) + \sqrt{\frac{2\kappa\epsilon_o}{q} \left[ V_D - V - \left(\frac{N_T}{N_D + N_T}\right)\phi_t \right] / (N_D + N_T)} \tag{A3.7}$$

From Sah and Reddi, the high frequency capacitance is defined by

$$C_{ac} = \frac{\kappa\epsilon_o}{w} = \sqrt{\frac{\kappa\epsilon_o q}{2}} \left/ \left\{ \left(\frac{N_T}{N_D + N_T}\right)\sqrt{\frac{2\kappa\epsilon_o \phi_t}{q N_D}} + \sqrt{\frac{2\kappa\epsilon_o}{q} \left[ V_D - V - \left(\frac{N_T}{N_D + N_T}\right)\phi_t \right] / (N_D + N_T)} \right\} \right. \tag{A3.8}$$

As $N_T \rightarrow 0$, equation (A3.8) approaches the ideal capacitance relationship

$$C_{ac} = \left(\frac{\kappa\epsilon_o q N_D}{2}\right)^{\frac{1}{2}} (V_D - V)^{-\frac{1}{2}}$$

which is the normal expression for the trap-free case.